THE UNIVERSITY *of* EDINBURGH

Seismic interferometry and non-linear tomography

Erica Galetti

BSc Hons Geophysics & Meteorology
University of Edinburgh, 2010

BSc Geology
University of Turin, 2007

Thesis submitted in fulfilment of
the requirements for the degree of
Doctor of Philosophy

School of GeoSciences
University of Edinburgh
2015

A mamma e papà

“A journey of a thousand miles begins with a single step”

Laozi

Acknowledgements

This thesis would not have been possible without the help and support of several people. I would like to thank my supervisor Andrew Curtis for giving me this unique opportunity and for his continuous advice and encouragement over the years. His contagious enthusiasm, energy and sharp scientific intuition have been incredibly inspiring and motivating throughout the project.

I am also incredibly grateful to my second supervisor Giovanni Angelo Meles for keeping his door always open for me, for his helpful advice and his amazing sense of humour, and for his efforts to answer my questions on theoretical and practical aspects of my work.

A number of undergraduate and postgraduate students have completed their projects and dissertations with me over the last few years. Thanks to David, Laura, Richard and Helen for spotting problems with the codes and data, and for their helpful input into my own project.

During my studies I had the opportunity to take part in two internship programmes in which I learned way beyond the projects' topics. Thanks to Ed Kragh, David Halliday, Ivan Vasconcelos and Johan Robertsson in Schlumberger, and to Baishali Roy, Chuck Mosher, Mike Brhlik, Arcangelo Sena and Ali Tura in ConocoPhillips for welcoming me to their teams and for their continuous guidance and advice. Special thanks also go to Janet, Roy and Judith in Cambridge, and Abbie and Stacy in Houston for providing me with a home away from home.

I also wish to thank Malcolm Sambridge, Thomas Bodin and Nick Rawlinson for giving me access to their codes and for many helpful discussions on transdimensional methods. Thanks also to the sponsors of the Edinburgh Interferometry Project (EIP) for providing me with inspiring ideas and insightful comments on my work.

Some of the most fun memories of my PhD experience come from field trips and from times spent with the colleagues and friends in my research group. Thanks to Sophie, Carlos, Matteo (and his espresso maker!), Katrin, Claire, Zara and Craig for the

enlightening discussions and the good company. A special thank you goes to Lizzie: I still find myself laughing when I think of our funny roadtrip moments!

Apart from my studies, my life in Edinburgh has been full of many other activities and wonderful friendships. A big thank you to all my friends in Edinburgh, who have filled my life with warmth and smiles. Thank you also to the Edinburgh University Tango Society and to the African and Arabic Dance Society for the fun and excitement (and good amount of distraction!) that they have given me since the start of my studies.

A massive thank you goes to all my friends in Italy and Canada, who have been sticking by me all these years despite the distance and my not-so-regular visits. And to Loretta, Alessandro, Valentina, Monica: thank you for the adventures, the laughs and, of course, all the amazing dinners!

A special thank you goes to Paris for filling my days with peace and cheerfulness, and for giving me support during the most challenging months of my PhD.

Finally, I would like to thank my mum and dad for their unconditional support and encouragement throughout my studies in Italy and Scotland. All of this would not have been possible without all the love and opportunities you have given me – grazie di cuore!

Declaration

I declare that this thesis has been composed solely by myself and that it has not been submitted, either in whole or in part, in any previous application for a degree or professional qualification. Except where otherwise acknowledged, the work presented is entirely my own.

Parts of this work have been published in Galetti & Curtis (2012), Galetti et al. (2013c), Entwistle et al. (2015), Galetti et al. (2015b).

Erica Galetti
February 2015

Summary

Seismic records contain information that allows geoscientists to make inferences about the structure and properties of the Earth's interior. Traditionally, seismic imaging and tomography methods require wavefields to be generated and recorded by identifiable sources and receivers, and use these directly-recorded signals to create models of the Earth's subsurface. However, in recent years the method of seismic interferometry has revolutionised earthquake seismology by allowing unrecorded signals between pairs of receivers, pairs of sources, and source-receiver pairs to be constructed as Green's functions using either cross-correlation, convolution or deconvolution of wavefields. In all of these formulations, seismic energy is recorded and emitted by surrounding boundaries of receivers and sources, which need not be active and impulsive but may even constitute continuous, naturally-occurring seismic ambient noise.

In the first part of this thesis, I provide a comprehensive overview of seismic interferometry, its background theory, and examples of its application. I then test the theory and evaluate the effects of approximations that are commonly made when the interferometric formulae are applied to real datasets. Since errors resulting from some approximations can be subtle, these tests must be performed using almost error-free synthetic data produced with an exact waveform modelling method. To make such tests challenging the method and associated code must be applicable to multiply-scattering media. I developed such a modelling code specifically for interferometric tests and applications. Since virtually no errors are introduced into the results from modelling, any difference between the true and interferometric waveforms can safely be attributed to specific origins in interferometric theory. I show that this is not possible when using other, previously available methods: for example, the errors introduced into waveforms synthesised by finite-difference methods due to the modelling method itself, are larger than the errors incurred due to some (still significant) interferometric approximations; hence that modelling method can not be used to test these commonly-applied approximations.

I then discuss the ability of interferometry to redatum seismic energy in both space and time, allowing virtual seismograms to be constructed at new locations where receivers may not have been present at the time of occurrence of the associated seismic source. I present the first successful application of this method to real datasets at multiple length scales. Although the results are restricted to limited bandwidths, this study demonstrates that the technique is a powerful tool in seismologists' arsenal, paving the way for a new type of 'retrospective' seismology where sensors may be installed at any desired location at any time, and recordings of seismic events occurring at any other time can be constructed retrospectively – even long after their energy has dissipated.

Within crustal seismology, a very common application of seismic interferometry is ambient-noise tomography (ANT). ANT is an Earth imaging method which makes use of inter-station Green's functions constructed from cross-correlation of seismic ambient noise records. It is particularly useful in seismically quiescent areas where traditional tomography methods that rely on local earthquake sources would fail to produce interpretable results due to the lack of available data. Once constructed, interferometric Green's functions can be analysed using standard waveform analysis techniques, and inverted for subsurface structure using more or less traditional imaging methods.

In the second part of this thesis, I discuss the development and implementation of a fully non-linear inversion method which I use to perform Love-wave ANT across the British Isles. Full non-linearity is achieved by allowing both raypaths and model parametrisation to vary freely during inversion in Bayesian, Markov chain Monte Carlo tomography, the first time that this has been attempted. Since the inversion produces not only one, but a large ensemble of models, all of which fit the data to within the noise level, statistical moments of different order such as the mean or average model, or the standard deviation of seismic velocity structures across the ensemble, may be calculated: while the ensemble average map provides a smooth representation of the velocity field, a measure of model uncertainty can be obtained from the standard deviation map.

In a number of real-data and synthetic examples, I show that the combination of variable raypaths and model parametrisation is key to the emergence of previously-unobserved, loop-like uncertainty topologies in the standard deviation maps. These uncertainty loops surround low- or high-velocity anomalies. They indicate that, while the velocity of each anomaly may be fairly well reconstructed, its exact location and size tend to remain uncertain; loops parametrise this location uncertainty, and hence constitute a fully non-linearised, Bayesian measure of spatial resolution. The uncertainty in anomaly location is shown to be due mainly to the location of the raypaths that were used to constrain the anomaly also only being known approximately. The emergence of loops is therefore related to the variation in raypaths with velocity structure, and hence to 2^{nd} and higher order wave-physics. Thus, loops can only be observed using non-linear inversion methods such as the one described herein, explaining why these topologies have never been observed previously.

I then present the results of fully non-linearised Love-wave group-velocity tomography of the British Isles in different frequency bands. At all of the analysed periods, the group-velocity maps show a good correlation with known geology of the region, and also robustly detect novel features. The shear-velocity structure with depth across the Irish Sea sedimentary basin is then investigated by inverting the Love-wave group-velocity maps, again fully non-linearly using Markov chain Monte Carlo inversion, showing an approximate depth to basement of 5 km. Finally, I discuss the advantages and current limitations of the fully non-linear tomography method implemented in this project, and provide guidelines and suggestions for its improvement.

Lay summary

In medicine, doctors commonly study the human body using X-rays. These are high-frequency waves which easily pass through soft tissues like muscles, but not so readily through hard tissues like bones. As they behave differently when traversing diverse tissues, X-rays can therefore be used to produce images of a patient's interior in a non-invasive manner. In the same way, geoscientists often wish to scan specific geological formations inside the Earth, very much like doctors utilise X-rays to see inside patients. The Earth consists of many different types of rocks, and each rock type can be identified and classified on the basis of its characteristics and properties, such as its composition and mass density. However, direct access to certain geological structures is often limited or impossible due to their location hundreds or thousands of meters below the surface, so geophysicists rely on non-invasive imaging techniques and generally use seismic waves to study and produce images of the Earth's interior.

Seismic waves are generated within or on the Earth's surface by sources of seismic energy such as earthquakes. They travel through the Earth at speeds depending on the type of rock they pass through, and are commonly recorded on or just below the surface using sensors known as seismometers or geophones. Unfortunately, earthquakes do not occur uniformly across the planet and the exact time of their occurrence is hard to predict with accuracy, which generates considerable challenges for geophysicists. However, a new seismological technique known as seismic interferometry has recently helped to overcome this problem by creating 'virtual' recordings of earthquakes that have not happened in reality. Because these recordings can be treated just as real earthquake seismograms, this method enables geophysicists to carry out detailed studies of the Earth's interior even in areas where earthquakes do not normally take place.

The method leading geophysicists from earthquake seismograms (either real or from seismic interferometry) to images of the Earth's subsurface is known as seismic tomography. It is based on the fact that seismic waves travel at different speeds in diverse rocks (depending on their composition and structure), and its aim is to produce models

(images) of seismic velocity inside the Earth. This provides geophysicists with clues on the shape and location of various geological formations in the subsurface. In its simplest form, seismic tomography uses the distance separating two locations and the measured time of travel of seismic waves between them to calculate the point-to-point seismic velocity in a process called inversion. When traveltimes are available amidst many different locations within the area of interest, a detailed map of seismic velocity can be obtained.

The methods of seismic interferometry and seismic traveltime tomography are the core subjects of this project. In the first part of this thesis, I provide a detailed overview of seismic interferometry explaining how and why it works, and outline the historical background behind its emergence and the different approaches to the derivation of its mathematical theory. I then expose a series of examples where this technique is applied to synthetic and real datasets, and analyse its advantages and limitations. In the second part of this thesis, I present a recently-developed method for traveltime tomography, and apply it to a seismic dataset recorded across the British Isles. Lastly, I show the resulting maps of seismic velocity under the British Isles, discuss their significance with respect to the surface geology of the area, and analyse theoretical and computational aspects related to the inversion method used.

Contents

CHAPTER 0

Introduction

Just as X-rays are commonly used in medicine to study the human body, seismic waves are used in geophysics to study the interior of the Earth. Seismic waves are generated within and on the Earth's surface by impulsive or finite sources of energy of either natural or man-made origin. These waves travel through the Earth's subsurface, are transmitted, reflected, diffracted and refracted by inhomogeneities in the different materials that they encounter, and cause the particles of the medium of propagation to vibrate as they pass. Such vibrations are generally referred to as the *medium response*, and they can be recorded using seismic sensors located either beneath or on the Earth's surface. These sensors may measure ground displacement, velocity or particle acceleration with time, and seismologists can analyse the recorded medium responses to infer the properties and structure of the portion of Earth through which the waves have propagated.

Traditionally, seismologists in both academia and industry study the Earth's interior by analysing source-to-receiver records obtained from active energy sources, such as earthquakes or explosions. However, over the last decade, the field of seismology has been revolutionised by the advent and development of a new method known as *seismic interferometry*. Contrary to traditional seismology, which uses the directly-recorded medium response to deduce the properties of the Earth's subsurface, seismic interferometry can be used to construct previously unrecorded Green's functions (i.e., impulse responses) by applying either cross-correlation, convolution or deconvolution to recorded wavefields. Through this method, a *virtual seismic source* can be created at the location of any real seismic receiver (inter-receiver interferometry – see e.g. Wapenaar & Fokkema (2006) and van Manen et al. (2005); van Manen et al. (2006)) and a *virtual seismic receiver* can be placed at the location of any real seismic source (inter-source

interferometry – see e.g. Curtis et al. (2009)), where the word *virtual* is used in the sense of *imagined* (as in virtual reality). This is done using boundaries of seismic sources or receivers which surround the real receiver or source, respectively. Using a combination of source and receiver boundaries, a previously unrecorded Green's function can also be constructed between a *virtual source* and a *virtual receiver* (source-receiver interferometry – Curtis & Halliday (2010a)). In addition, seismic sources on the surrounding boundaries need not be active or impulsive (i.e., earthquakes in crustal seismology, dynamite or vibroseis in exploration seismology) but may be of passive origin (i.e., wind, oceanic waves, microseismic and anthropogenic activity). In fact, seismic waves generated by passive noise sources travel through the Earth's interior just like those that originate from active sources and, because such noise sources are widespread, may even sample areas that are not usually probed by waves of active origin. Hence, thanks to seismic interferometry, what was previously referred to as contaminating 'noise' and was commonly removed from recorded datasets to enhance the quality of coherent signals, can now be decoded to extract useful information on the Earth's subsurface by creating new, artificial seismograms. Such seismograms can then be treated just like active-source records to image the real Earth's interior using more or less traditional imaging methods.

Within this introductory chapter, I provide a description of the contents of this thesis as a guide to the reader. Most chapters in the main body of the thesis either correspond or are part of separate papers which are either already published or currently in preparation. However, such chapters have not been left in paper format but have been edited in order to fulfil thesis requirements.

This thesis can essentially be divided into two main parts, corresponding to separate studies which I carried out throughout my PhD:

- In Part I (Chapters 1–4) I focus on the theory of seismic interferometry by first providing an extensive overview of the field covering both interferometric theory and its applications (Chapter 1). I then present an acoustic modelling code which I created and optimised for applications to seismic interferometry and which is currently widely used within the Edinburgh Interferometry Project (EIP) research group (Chapter 2). This chapter also includes a number of examples of the application of inter-receiver interferometry to simple geometries in the acoustic domain. Finally, in Chapter 3 I discuss the application of source-receiver interferometry to synthetic and real datasets, particularly focusing on a small-scale experiment conducted in the field adjacent to Schlumberger Gould Research (Cambridge). Part I concludes with a discussion highlighting advantages and limitations of the modelling code described in Chapter 2, and practical aspects and possible future applications of source-receiver interferometry.

- In Part II (Chapters 5–8) I use Green's functions obtained from ambient-noise interferometry to perform Love-wave tomography of the British Isles in different

frequency bands. Traveltime tomography was carried out using a fully non-linear version of the reversible-jump Markov chain Monte Carlo algorithm (Bodin & Sambridge, 2009), which is described in detail in Chapter 5. In Chapter 6 I discuss the emergence of new uncertainty topologies when this fully non-linear inversion method is used, and the results of UK Love-wave tomography in different frequency bands are then presented in Chapter 7. Part II terminates with a discussion covering various aspects of the fully non-linear tomography method used within this thesis, and providing guidelines and suggestions for future use of the tomography code.

More details on the contents and comprehensive descriptions of each chapter can be found in the next section.

0.1 Thesis overview

Chapter 1 provides an introduction to the theory of seismic interferometry by showing how it can be thought of as a generalisation of conventional receiver functions analysis. A description of the theory and method of inter-receiver, inter-source and source-receiver interferometry is presented, with particular attention given to the three different approaches that have been used to derive the principles of inter-receiver interferometry. The method of coda-wave interferometry is also described and presented as a time-dependent technique to monitor the properties of the Earth's interior. Together with the theoretical and historical background, several published examples of the application of seismic interferometry are given, as well as insights on more recent results. As this chapter has been published as a review paper in *Tectonophysics* (Galetti & Curtis, 2012), the future of seismic interferometry and its implications for tectonophysics are also discussed.

Chapter 2 presents a new Matlab code that models directly-propagating and scattered parts of a wavefield using the theory of multiple scattering developed by Leslie L. Foldy in 1945 (Foldy, 1945). This code was produced as part of my PhD to test new theory in seismic interferometry, and has been made available to the public as a paper and code package in the *Geophysical Software & Algorithms* section of *Geophysics* (Galetti et al., 2013c). The code produces theoretically-exact results which include all multiple-scattering interactions, avoiding numerical dispersion or boundary-condition errors that are typical of, for example, finite-difference or finite-element numerical modelling schemes, and is therefore ideal when exact wavefield modelling results are needed to test the validity of new algorithms. I use this code to produce a first example of seismic interferometry in which results obtained using the exact and the approximate interferometric formulae are compared. A second example is presented to benchmark the results of interferometry obtained using the Foldy modelling method against those

obtained from a good finite-difference code. The most up-to-date version of the Foldy modelling code is included in this thesis in Appendix C (enclosed CD).

In *Chapter 3* I describe the theory of source-receiver interferometry in detail and present examples of its application to real datasets. Specifically, after providing a first synthetic example which uses a canonical geometry of sources and receivers, I describe a form of retrospective seismology which makes use of source-receiver interferometry (SRI) to construct previously unrecorded Green's functions. In the first stage of SRI, a boundary of active or passive sources is used to construct surface-wave Green's function estimates between pairs of seismic receivers. These Green's functions are then used to redatum the energy of a seismic source from an array of receivers to new receiver locations, hence creating an entirely new set of seismograms. This method of retrospective seismology is applied first to a small-scale dataset acquired in a field adjacent to Schlumberger Gould Research, and then to a large-scale dataset recorded by the USArray network. Both examples are included in a paper of which I am a co-author and which has recently been published in *Journal of Geophysical Research* (Entwistle et al., 2015).

Chapter 4 discusses the issues and challenges that have emerged from the studies in Part I of this thesis. In particular, I focus on the current uses, benefits and limitations of the Foldy modelling code, and on practical aspects of retrospective seismology at various scales.

Chapter 5 introduces the concept of inversion in geophysics and, specifically, how this can be used to obtain information on seismic velocity from a set of traveltime measurements. I first describe the various steps that I took, in collaboration with other researchers and previous PhD and undergraduate students, to produce a set of inter-station traveltimes from recordings of ambient noise in the British Isles. I then describe a fully non-linear tomography method which combines the reversible-jump Markov chain Monte Carlo (rj-McMC) algorithm with an eikonal raytracer. This method was implemented in a Fortran code to invert UK traveltime data and produce the Love-wave group-velocity and uncertainty maps presented in Chapters 6 and 7. The code and associated manual have been made available through the Edinburgh Interefrometry Project (EIP) website (`http://www.geos.ed.ac.uk/eip`), and are also included in this thesis in Appendix C (enclosed CD).

In *Chapter 6* I discuss loop-like topologies that dominate uncertainty in traveltime tomography when this is performed using a fully non-linear method, and which can not be generated using linear or linearised wave physics. These structures appear to dominate in around a third of the UK's seismic velocity structure and provide entirely new information, changing the interpretation of observed tomographic anomalies. This chapter has recently been published in *Physical Review Letters* (Galetti et al., 2015b).

In *Chapter 7* I present the first Love-wave group-velocity maps of the British Isles from fully non-linear ambient-noise tomography. I first discuss the importance of an accurate estimation of data noise (i.e., traveltime uncertainties) when inversion is performed in a

transdimensional framework, and then present the results of transdimensional UK tomography in various frequency bands. All inversions were performed using variable model parametrisation with Voronoi cells and assuming data noise to be unknown, hence both the number of model parameters and the noise in the data were estimated during the inversion. I then consider possible interpretations of the main features visible in the tomographic maps and draw correlations with previous geological and geophysical studies of the area. Finally, I provide an insight on preliminary results obtained from surface-wave dispersion inversion for shear-velocity structure in the Irish Sea basin. The work presented in this chapter is currently being prepared for submission as Galetti et al. (2015a).

Chapter 8 discusses a number of aspects and issues that emerged while I was developing the fully non-linear inversion method which was used to perform the inversions discussed in Part II of this thesis. I also discuss the current limitations of the code and provide guidelines and suggestions for its improvement and future use.

Finally, in *Chapter 9* I summarise the main conclusions that can be drawn from this thesis, consider possible future research that is suggested by this project, and highlight the main contributions of this project to the field of research.

0.2 Publications

The following publications have resulted from this study:

- Galetti, E. & Curtis, A., 2012. Generalised receiver functions and seismic interferometry, *Tectonophysics*, **532–535**, 1–26. This publication is included in this thesis as *Chapter 1*.

- Curtis, A., Behr, Y., Entwistle, E., Galetti, E., Townend, J., & Bannister, S., 2012. The benefit of hindsight in observational science: Retrospective seismological observations, *Earth and Planetary Science Letters*, **345–348**, 212–220.

- Galetti, E., Halliday, D., & Curtis, A., 2013c. A simple and exact acoustic wavefield modeling code for data processing, imaging, and interferometry applications, *Geophysics*, **78**(6), F17–F27. This publication is included in this thesis as *Chapter 2*. The code and associated user manual can be downloaded from the *Geophysics* source-code archive at `http://software.seg.org` (original version) and from the EIP website at `http://www.geos.ed.ac.uk/eip` (up-to-date version), and are also included in this thesis in Appendix C (enclosed CD).

- Entwistle, E., Curtis, A., Galetti, E., Baptie, B., & Meles, G. A., 2015. Constructing new seismograms from old earthquakes: Retrospective seismology at multiple length scales, *Journal of Geophysical Research*, **120**(4), 2466–2490. Parts of this publication

are included in this thesis as edited sections of *Chapter 3*. My contribution to this publication is explained in detail in the relevant sections of this chapter.

- Galetti, E., Curtis, A., Meles, G. A., & Baptie, B., 2015b. Uncertainty loops in travel-time tomography from nonlinear wave physics, *Physical Review Letters*, **114**(14), 148501. This publication is included in this thesis as *Chapter 6*.

- Galetti, E., Curtis, A., & Baptie, B., 2015a. Transdimensional Love-wave tomography and depth inversion of the British Isles from ambient-noise interferometry, in preparation. This publication is currently in preparation as an edited version of *Chapter 7*.

The following conference abstracts have also resulted from this study:

- Galetti, E., Jenkins, D., Nicolson, H., Curtis, A., & Baptie, B., 2013e. Transdimensional Love-wave tomography of the British Isles, *EGU General Assembly, Vienna*.

- Galetti, E., Halliday, D., & Curtis, A., 2013d. An Exact Modelling Method for Data Processing, Imaging and Interferometry Applications in Scattering Acoustic Media, *EAGE, Extended Abstracts, 75th EAGE Conference & Exhibition*.

- Galetti, E., Curtis, A., & Halliday, D., 2013b. An exact wavefield modelling method for data processing, imaging, and interferometry applications in scattering acoustic media, *SEG Technical Program Expanded Abstracts 2013*, pp. 3330–3334.

- Galetti, E., Curtis, A., Baptie, B., Jenkins, D., & Nicolson, H., 2013a. Novel Uncertainty Structures Observed in UK Ambient Noise Tomography, *AGU Fall Meeting, San Francisco*.

Part I

Seismic interferometry

CHAPTER 1

Generalised receiver functions and seismic interferometry[1]

Classical seismological receiver functions are correlational or deconvolutional combinations of vertical and horizontal component seismometer recordings of earthquake waves that focus information on near-receiver subsurface Earth structure and properties. We show that seismic interferometry can be thought of as a generalisation of receiver functions analysis to cases where recordings at pairs of receivers are considered simultaneously, and where either the same or different component recordings are combined. Further, seismic interferometry uses any of deconvolution, convolution and cross-correlation, and energy from either impulsive or random noise sources. We show both how receiver functions can logically be extended to a new, convolutional form, and that the now little-used correlational form of receiver functions contains more intuitive information than previously realised.

Seismic interferometry has provided other extraordinary extensions to seismologists' arsenal. Passive noise recordings can be converted into seismograms from virtual (imagined) earthquakes that in turn can be used to image the real Earth. Active sources (e.g., earthquakes or man-made sources) can be redatumed into new, virtual sources elsewhere, or can be converted into virtual sensors (seismometers) that record seismograms from other real earthquakes, man-made sources or noise sources that occur either in the future or in the past. And the ability to construct virtual sources and sensors at desired times and locations (rather than having to wait for earthquake sources that

[1] This chapter has been published as Galetti & Curtis (2012). Full derivations of the acoustic interferometric formulae can be found in Appendix A.

occur at uncontrollable locations) promises more repeatable monitoring of changes in Earth subsurface properties over time. Indeed, so-called coda wave interferometry offers unprecedented accuracy in detecting such changes. Finally, existing theoretical extensions to other regimes such as electromagnetic, electrokinetic and diffusive energy propagation may lead to future revolutions in other domains of science.

1.1 Introduction

Seismic interferometry loosely refers to a range of methods within which seismograms that were not physically recorded, are estimated by cross-correlation, convolution or deconvolution and summation of other recorded wavefields (Campillo & Paul, 2003; Claerbout, 1968; Duvall et al., 1993; Lobkis & Weaver, 2001; Rickett & Claerbout, 1999; Shapiro & Campillo, 2004; Snieder, 2004; van Manen et al., 2005, 2006, 2007; Wapenaar, 2004; Wapenaar & Fokkema, 2006; Wapenaar et al., 2010a,c; Weaver & Lobkis, 2001). This apparently benign ability has had profound implications for seismology.

For example, it is now possible to create estimates of inter-receiver surface waves (surface waves that would have been recorded at one receiver location if there had been a source at the location of the other) using passive or ambient seismic noise – the part of seismic recordings that until recently were filtered out of data to be analysed. This is of great interest to seismologists since passive noise sources can thus be used to create seismic velocity maps or profiles in global, regional or industrial scale seismology using human-designed, inter-receiver networks of wave propagation or ray paths (Gerstoft et al., 2006; Halliday & Curtis, 2008; Moschetti et al., 2007; Sabra et al., 2005; Shapiro & Campillo, 2004; Shapiro et al., 2005; Snieder, 2004; Snieder et al., 2006; Yang et al., 2007). It is also possible to obtain inter-receiver body wave estimates from ambient noise fields, but this is far more difficult due to the low body wave energy in naturally occurring ambient noise (Draganov et al., 2006, 2007, 2009; Forghani & Snieder, 2010; Miyazawa et al., 2008; Ruigrok et al., 2010; Tonegawa & Nishida, 2010; Tonegawa et al., 2009; Zhan et al., 2010).

Actively induced or impulsive source signals can also be cross-correlated to synthesise new, inter-receiver wavefield estimates (Bakulin & Calvert, 2006; King et al., 2011; Lu et al., 2008; Slob et al., 2007). For example, Curtis et al. (2006), Dong et al. (2006), Halliday et al. (2007); Halliday et al. (2010b) propose that similar inter-receiver surface wave estimates to those above can be used as part of a ground-roll (surface-wave) removal method in exploration seismology. Halliday et al. (2008) demonstrate that it is possible to recover both fundamental and higher-mode inter-receiver surface waves, with specific geometrical dependencies predicted by Halliday & Curtis (2008). Similar techniques can produce novel schemas for computational full-wavefield modelling (van Manen et al., 2005, 2006, 2007), and King et al. (2011) show that active-source

interferometry offers new approaches to subsurface velocity analysis. More recently, *interferometry by deconvolution* (Vasconcelos & Snieder, 2008a,b; Wapenaar & van der Neut, 2010; Wapenaar et al., 2011) has been proposed as an alternative technique to cross-correlational interferometry in cases where the recorded wavefields present a strong source signature, or where the distribution of sources is not uniform in space.

By using two different forms of interferometry, Hong & Menke (2006) and Curtis et al. (2009) show that it is also possible to estimate inter-source seismograms (as though one of a pair of sources had been a seismometer that recorded the other source) using earthquake sources as subsurface seismometers. The latter method was applied by Tonegawa & Nishida (2010) to find body wave travel times between earthquakes in the slab subducting beneath Japan.

As can be seen from the references cited above, while this field has its origins in a handful of papers from before 2000, it has expanded dramatically in terms of both theoretical development and practical use since only 2003. In that year both the first solid-Earth application was demonstrated (Campillo & Paul, 2003), and the first comprehensive 3-dimensional mathematical theory was published (Wapenaar, 2003). The field may therefore still be in its infancy. Nevertheless, advances are already such that it is timely for Earth scientists in a variety of fields to become familiar with these techniques, and to investigate what they offer in these various fields of application.

This chapter begins by showing how seismic interferometry can be thought of as a generalisation of conventional seismological (deconvolutional and cross-correlational) receiver function analysis. It then gives a more detailed review of interferometric theory and applications. Finally, it explores implications of seismic interferometry for future tectonophysical studies.

1.2 Classical receiver functions

In order to understand the near-surface (e.g., crustal and uppermost mantle) structure beneath a seismometer, it is common to calculate so-called receiver functions (Phinney, 1964; Vinnik, 1977). If waves emanating from some distant source impinge on a subsurface interface between layers of different elastic properties (the Moho for example), the energy both refracts and converts from P to S energy or vice versa as it crosses the interface. This energy may then be recorded at a seismometer. If the energy source is far from the seismometer, the path of propagation at and below the seismometer is usually reasonably close to vertical due to refraction in near-surface, low-velocity layers. In that case the P energy appears dominantly on the vertical-component recording, shear energy on the horizontal components (Fig. 1.1(a)).

A receiver function is a quantity derived from the P (or vertical-component $V(t)$) and S (horizontal-component $H(t)$) seismograms designed such that it focuses information on

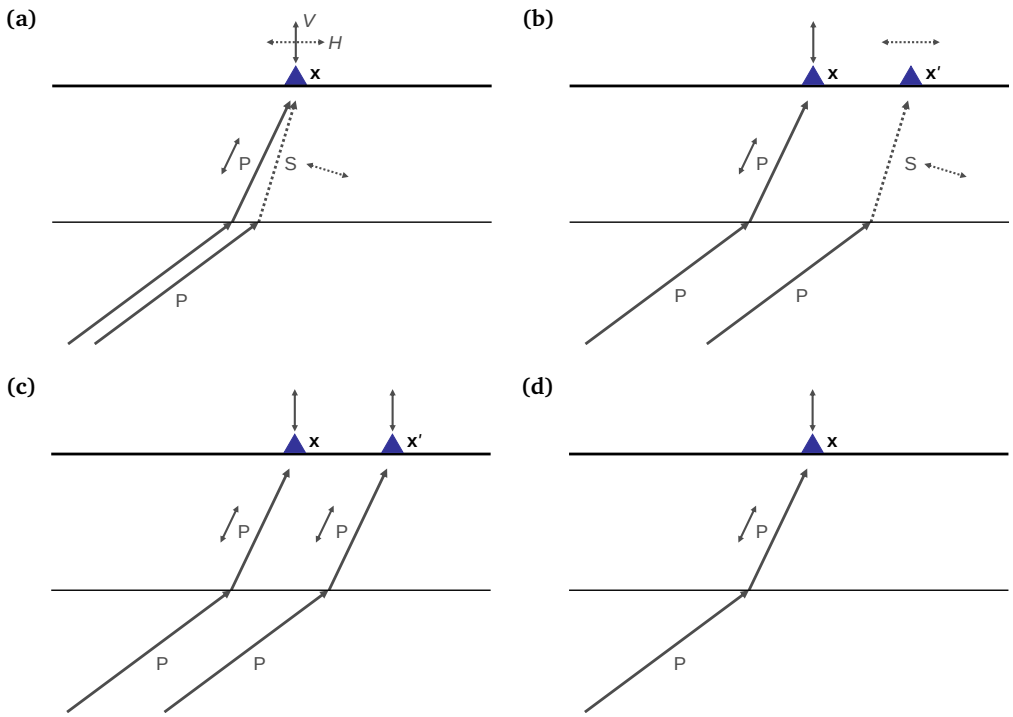

Figure 1.1. Non-classical receiver function analysis. (a) A vertical and a horizontal sensor are placed side by side and record P and S arrivals. (b) The two sensors are moved apart. (c) The horizontal sensor is replaced by a vertical sensor. (d) The two vertical sensors are moved back side by side.

the propagation path between the interface and the seismometer, diminishing sensitivity to Earth properties along the rest of the path of propagation. Usually this involves transforming the vertical and horizontal components into the frequency domain and dividing one by the other for each frequency – an operation known as deconvolution:

$$R(\mathbf{x}, \omega) = \frac{H(\mathbf{x}, \omega)}{V(\mathbf{x}, \omega)}\,, \tag{1.1}$$

where ω is angular frequency and $\mathbf{x}$ is the location of the recording. Intuitively, parts of the data that are common to both the vertical and horizontal recordings will cancel out between numerator and denominator. Parts that are approximately common correspond to the propagation path before the interface was intercepted by the wavefield (lower left in Fig. 1.1(a)). Hence, what remains after this division is a quantity R that is dominantly sensitive to the structure at and above the reflector. R is known as a receiver function, and would subsequently be used to infer the distribution of properties of the near-surface approximately beneath the receiver location (Gurrola et al., 1994; Heit et al., 2008; Langston, 1979; Ryberg & Weber, 2000; van Manen et al., 2003; Vinnik, 1977).

In reality the division is stabilised to avoid problems with division by zero for any frequency. For example, the water level method of Langston (1979) simply sets the magnitude of the denominator equal to some fixed, small number e if it is ever less than

e. In addition, many alternative methods of receiver function retrieval exist such as plain summation without deconvolution (Kumar et al., 2010), and the deconvolution technique may simply be employed to enhance signal-to-noise ratios. Nevertheless, equation (1.1) represents the essential elements of a receiver function and provides a natural link to the theory of seismic interferometry.

To this end, notice that a receiver function can be thought of in a slightly different way by multiplying numerator and denominator by the complex conjugate of the denominator:

$$\frac{H(\omega)}{V(\omega)} = \frac{H(\omega)V^*(\omega)}{V(\omega)V^*(\omega)} = \frac{1}{|V(\omega)|^2}H(\omega)V^*(\omega)\,, \tag{1.2}$$

where we have omitted the $\mathbf{x}$-dependence for the moment. The final term includes the cross-correlation of H and V (since cross-correlation of two time-series is defined in the frequency domain as the multiplication of one with the conjugate of the other for each frequency), and thus we see that receiver function R is nothing more than a cross-correlation of H and V, weighted by a set of real numbers $1/|V(\omega)|^2$. Indeed, the cross-correlation includes all phase information in the receiver function, and it is interesting to note that some earlier work on receiver functions used the cross-correlation rather than the deconvolution of H and V (Kind & Vinnik, 1988). From hereon we will therefore consider a classical receiver function R_C to be simply a (perhaps weighted) cross-correlation of a vertical and a horizontal component record:

$$R_C(\mathbf{x},\omega) \cong H(\mathbf{x},\omega)V^*(\mathbf{x},\omega)\,. \tag{1.3}$$

1.3 Non-classical receiver functions

We now introduce a *non*-classical extension to receiver functions analysis. Within every multi-component seismometer there are multiple sensors, each measuring the displacement (or time-derivatives thereof) in different directions. Instead of encasing them all within one seismometer, let us imagine them as each having separate casings. If we put a vertical-component sensor beside a horizontal-component sensor and make a recording of the situation in Fig. 1.1(a) we will obtain essentially identical records to those discussed above. However, we are then free to move these two sensors apart from each other as in Fig. 1.1(b).

We can still calculate the cross-correlation of the two recordings

$$R^{HV}(\mathbf{x},\mathbf{x}',\omega) = H(\mathbf{x},\omega)V^*(\mathbf{x}',\omega)\,, \tag{1.4}$$

but in this case the non-classical receiver function R^{HV} depends on both locations $\mathbf{x}$ and $\mathbf{x}'$ (van Manen, 2006). It is not obvious that it will be any easier to interpret R^{HV} than it would the original recordings of V and H: the portion of the path up to the interface is

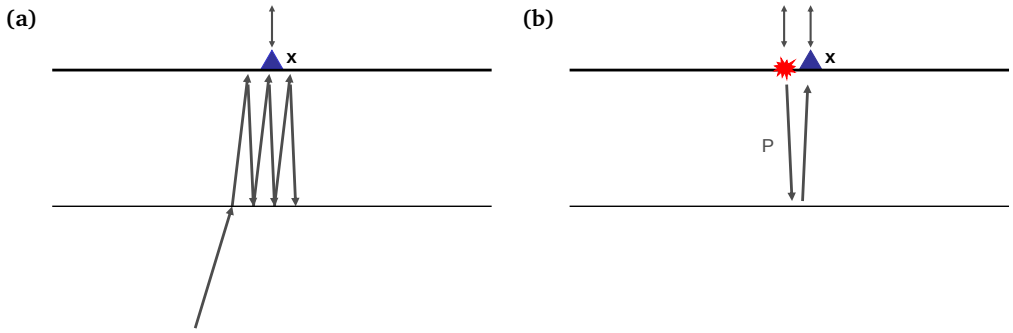

Figure 1.2. From transmission to reflection response: (a) the transmission response is given by the arriving P wave and all of its reverberations in the subsurface. (b) The reflection response is obtained from the autocorrelation of the transmission response.

now not necessarily even approximately the same, and hence it is not obvious that R^{HV} contains information that is focussed on the portion of the subsurface that is close to the two receivers. Nevertheless we can still choose to calculate R^{HV} and below we will show that in fact R^{HV} can be converted into something that is as easy to interpret as a standard seismogram.

Given that R^{HV} is calculated between two separate seismometers, it is also possible to replace the right-hand horizontal component sensor with another vertical component sensor as in Fig. 1.1(c), and calculate the cross-correlation,

$$R^{VV}(\mathbf{x}, \mathbf{x}', \omega) = V(\mathbf{x}, \omega)V^*(\mathbf{x}', \omega) \tag{1.5}$$

and indeed it is possible to move the two vertical-component sensors side by side as in Fig. 1.1(d) and calculate

$$R^{VV}(\mathbf{x}, \omega) = V(\mathbf{x}, \omega)V^*(\mathbf{x}, \omega)\,. \tag{1.6}$$

The right side of equation (1.6) is the autocorrelation of the vertical record with itself.

To get to this point it has been necessary to take steps that are not usually taken in receiver functions analysis, yet the result is remarkably similar to the classical formula in equation (1.3). However, in retrospect we now recognise equation (1.6) as the first published example of seismic interferometry: if $V(\mathbf{x}, \omega)$ is a recording of the arriving P wave and all of its subsequent reverberations (multiples) within the medium (the Earth) as shown in Fig. 1.2(a), then the recording is an approximation to the so-called *transmission response* of the medium – the measurement one would obtain on one side of the medium of waves transmitted from a temporally impulsive source on the far side of the medium. Claerbout (1968) proved that the autocorrelation of the acoustic transmission response in Fig. 1.2(a) is equal to the so-called *reflection response* depicted in Fig. 1.2(b) – the seismogram that one would have recorded if the impulsive source was instead placed on

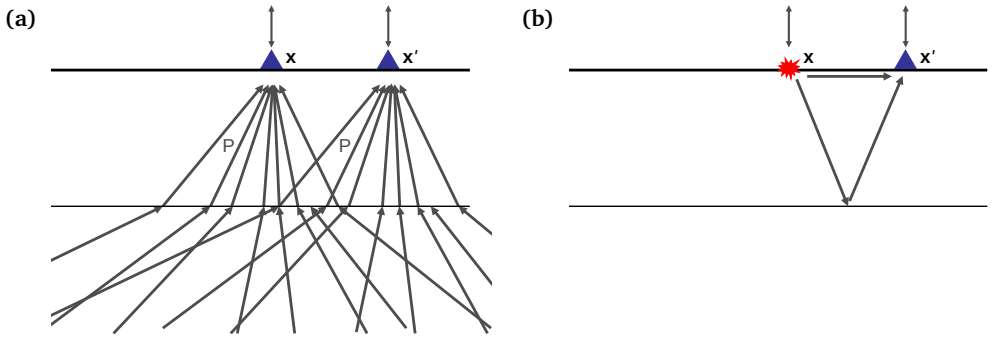

Figure 1.3. Principle of seismic interferometry. (a) Two receivers record P-wave arrivals from sources within the medium. (b) Cross-correlation of these recordings turns one of these receivers into a virtual source, whose signal is recorded at the other receiver.

the near side of the medium. That is, by autocorrelation we obtain a real seismogram from a source that never actually existed; we now call such sources *virtual* (imagined) sources.

The far-reaching importance of this result was embodied within a conjecture made by Claerbout, quoted by Cole (1995) and Rickett & Claerbout (1999): that in the geometrical case depicted in Fig. 1.1(c) it would be possible that the cross-correlation of the recordings made at the two receivers in equation (1.5) would also result in a seismogram from a virtual source at the surface. This result was subsequently demonstrated by Rickett & Claerbout (1999) for the sun, and by Campillo & Paul (2003) for the Earth, and was eventually proved to be true mathematically by Wapenaar (2003); Wapenaar (2004). Wapenaar showed that the conjecture is true provided that the transmission response is recorded from sources that (in a sense made strict below) surround the portion of the medium that contains the two receivers as in Fig. 1.3(a). Intuitively, by recording at two points the energy from this set of impulsive sources that surround this portion of the medium, and by cross-correlating and summing over all of those recordings, we obtain the real seismogram from a virtual source, and Wapenaar proved that the virtual source would be at the location of one of the two receivers as in Fig. 1.3(b).

We think of this simple data processing operation of cross-correlation and summation, now called seismic interferometry, as having turned a real receiver into a virtual source, from which we obtain a real seismogram. What is more, Wapenaar (2003); Wapenaar (2004) proved that this would also hold approximately true if instead of being impulsive the sources were uncorrelated ambient noise sources that possibly fire contemporaneously, and hence which are already summed within the recordings. In principle then, by recording at two points the background noise in the Earth from diverse uncorrelated sources throughout and around the Earth, then cross-correlating these two recordings, a seismogram is obtained that approximates what one would have recorded if a real source had existed at the location of one of the seismometers. Thus we obtain real, earthquake-like seismograms without the need for an earthquake to occur.

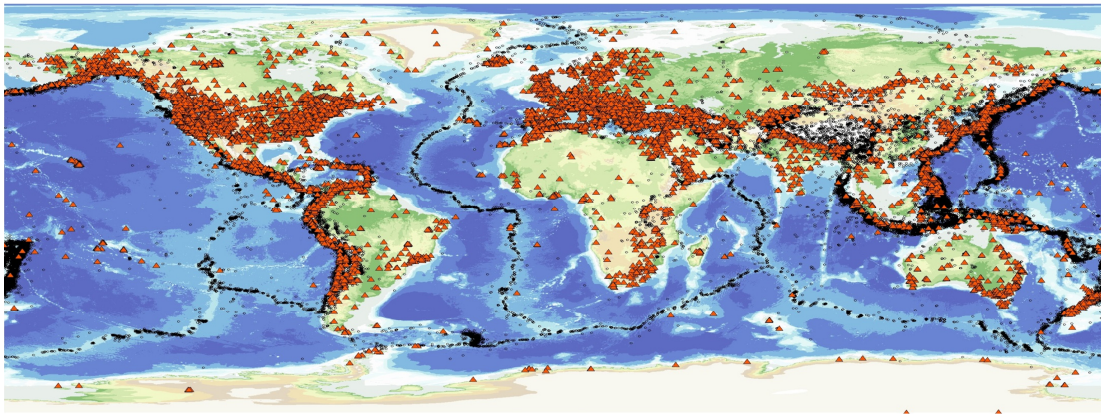

Figure 1.4. Global distribution of National Earthquake Information Center (NEIC) seismometers (triangles) and earthquakes of magnitude > 5 since 1973 (circles). Map courtesy of Brian Baptie (British Geological Survey).

The implications for seismology have been profound. Most of the Earth has virtually no large local earthquakes (Fig. 1.4). Such areas can not easily be imaged in detail using conventional seismological methods other than by classical receiver functions analysis as in equations (1.1) and (1.3), and even then only approximately vertically beneath each individual receiver. Local tomography or imaging between receiver locations is difficult because while we can install local seismometer arrays, such areas have no local sources so that all recorded seismograms have very long source-to-receiver ray paths. Discriminating only the local component of such recordings is difficult. On the other hand, by using seismic interferometry, if long recordings of background noise are taken at any set of local receivers, and for every pair of receivers these recordings are then cross-correlated, we convert each receiver in turn into a virtual source and obtain real seismogram recordings of that source at all of the other receivers. Thus we obtain a local array of source-to-receiver records that can be analysed for detailed structure both beneath and between receivers in the array, and in principle we can do this anywhere that we can put receivers on the surface of the dominantly aseismic Earth.

The remainder of this chapter explores the historical background of seismic interferometry, and presents the mathematical results that form a necessary foundation of knowledge in order to understand and apply this theory robustly. It then explores the consequences of this theory which, in the space of only eight years since the first mathematical proof, has revolutionised the imaging of much of the Earth's crust and upper mantle, and has led to the creation of methods to monitor temporal changes in the Earth that are so exceptionally accurate as to be unimaginable only a decade ago. We have already shown that seismic interferometry can be thought of as a generalisation of receiver functions analysis, and we will show later that interferometry expands the field of receiver functions analysis from only correlation and deconvolution to a third form, involving convolution of records. The result is a theory that has revolutionised Earth

imaging while still in its infancy, and which will certainly have many significant consequences still unimagined today.

1.4 Background to the theory of seismic interferometry

The first derivation of seismic interferometric theory was published for 1D media by Claerbout (1968), and extended using modal theory by Weaver & Lobkis (2001) and Lobkis & Weaver (2001). It was eventually proved for fully 3D acoustic media (Wapenaar, 2003; van Manen et al., 2005, 2006; Wapenaar et al., 2010a,c), elastic media (Wapenaar, 2004; Snieder et al., 2006; van Manen et al., 2006; Wapenaar & Fokkema, 2006) and electromagnetic media (Slob et al., 2007; Slob & Wapenaar, 2007), and a unified approach allows application to other wave phenomena such as seismoelectric wave propagation and diffusive wavefields (Wapenaar et al., 2006; Snieder et al., 2007; Vasconcelos, 2008). Although they can be quite complex, we explore some of these different derivations here as they shed light on the generality of interferometric theory, provide intuition about *why* interferometry works, and highlight the approximations made when interferometry is applied in practice. The latter is particularly important for robust interpretation of results of interferometric studies.

Let us now consider the 1D configuration shown in Fig. 1.5(a): a homogeneous, lossless acoustic layer of thickness Δz and propagation velocity c, is sandwiched between a stress-free surface (like the Earth's surface) and a homogeneous lossless half-space. The upwards-travelling transmission coefficient across the subsurface interface is τ. A vertically upward-propagating wave is emitted by an impulsive unit source in the lower half-space, and arrivals are recorded at a point on the free surface. These arrivals are shown in Fig. 1.5(b): the first arrival occurs at time t_0 and has amplitude $a_0 = \tau$; the second arrival, resulting from the wave being reflected downwards by the free surface (with reflection coefficient -1) and then upwards by the interface (with reflection coefficient r), occurs at time $t_0+\Delta t$ (with $\Delta t = 2\Delta z/c$) and has amplitude $a_1 = -r\tau$; subsequent arrivals occur at regular time intervals Δt, and have amplitudes $a_2 = r^2\tau$, $a_3 = -r^3\tau$, etc. If we denote the global transmission response by $T(t)$ and its time-reverse by $T(-t)$, then the autocorrelation of the global transmission response (i.e., the convolution of the signal with its time-reverse) yields the global reflection response:

$$T(t) \otimes T(-t) = \delta(t) - R(t) - R(-t)\,, \tag{1.7}$$

where the symbol $\otimes$ denotes convolution, $\delta(t)$ is the impulse obtained from autocorrelation for zero lag time, and $R(t)$ and $R(-t)$ are the so-called causal and acausal parts of the autocorrelation, respectively (Wapenaar, 2003; Wapenaar et al., 2010a). An intuitive representation of all terms in equation (1.7) is given in Fig. 1.5(c).

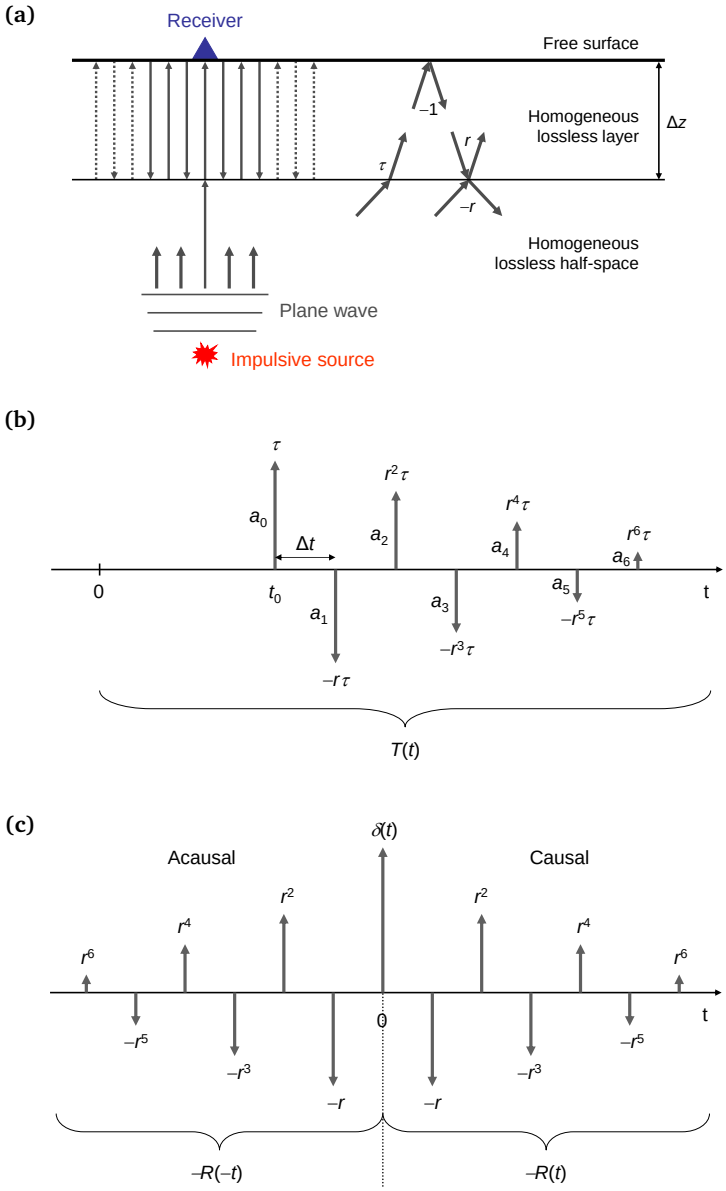

Figure 1.5. From transmission to reflection response in 1D as conceived by Claerbout (1968). (a) Simple layered medium consisting of a homogeneous, lossless layer sandwiched between a lossless half-space and a free-surface. The transmission coefficient at the subsurface interface is τ, the reflection coefficient is r; the reflection coefficient at the free surface is -1. (b) Transmission response $T(t)$ as observed at a point on the free surface. (c) Autocorrelation of the transmission response $T(t) \otimes T(-t)$ yields, apart from a negative sign, the reflection response $R(t)$ (causal part of the autocorrelation) and the time-reversed reflection response $R(-t)$ (acausal part of the autocorrelation). Redrawn after Wapenaar et al. (2010a).

By rearranging the terms in equation (1.7), we obtain the so-called *Kunetz equation* (Claerbout, 1976):

$$R(t)+R(-t)=\delta(t)-T(t)\otimes T(-t)\,. \tag{1.8}$$

According to equation (1.8), the Earth's reflection response (from a plane wave source at the surface, a source which did not exist) can be constructed by taking either the positive- or negative-time part of the autocorrelation of its transmission response.

In the case of transient, non-impulsive sources (e.g., ambient noise), equation (1.8) can be modified as follows (Claerbout, 1968):

$$\{R(t)+R(-t)\}\otimes S_N(t)=S_N(t)-\langle u(t)\otimes u(-t)\rangle\,, \tag{1.9}$$

where $N(t)$ is the noise signal emitted by the source in the lower half-space, $u(t)=T(t)\otimes N(t)$ is the recorded wavefield at the surface and $S_N(t)=N(t)\otimes N(-t)$ is the autocorrelation of the noise source time function. According to equation (1.9), an approximation to the Earth's reflection response can be obtained from the autocorrelation of passive noise transmission records. The theory can be proved to hold for arbitrarily layered media (Claerbout, 1968).

Claerbout conjectured that the method could be extended to 2D and 3D varying media and wavefields, but it was not until 1993 that this was shown to be applicable in reality: Duvall et al. (1993) and Rickett & Claerbout (1999) applied cross-correlation to records of solar surface noise to obtain the first helioseismological pseudo-impulsive shot records.

Mathematical proofs of 3D seismic interferometry based on representation theorems were derived subsequently by Wapenaar (2003); Wapenaar (2004), van Manen et al. (2005); van Manen et al. (2006), Wapenaar & Fokkema (2006), Wapenaar et al. (2006), Slob et al. (2007), Snieder et al. (2007), Vasconcelos (2008), and Wapenaar & van der Neut (2010), and based on a stationary-phase approach by Snieder (2004). The theory has been independently demonstrated through time-reversal laboratory experiments by Lobkis & Weaver (2001), Weaver & Lobkis (2001), Derode et al. (2003a); Derode et al. (2003b) and Larose et al. (2005). All of these derivations have one element in common: by applying the above-mentioned techniques to the recordings obtained at a pair of receivers, a new set of data is obtained that approximates or equals that which would be recorded at one of the two receivers if the other one was instead at the location of an active source. This form of seismic interferometry is called *inter-receiver interferometry*, and it allows one of the receivers to be turned into a 'virtual' (imagined) source. However, inter-receiver interferometry is not the only type of interferometry as two additional forms have recently been developed: *inter-source interferometry* (Hong & Menke, 2006; Curtis et al., 2009), which allows a real source to be turned into a virtual receiver, and *source-receiver interferometry* (Curtis & Halliday, 2010a), which allows a (perhaps

unrecorded) recording of energy travelling between a source and a receiver to be constructed by making use of both virtual sources and virtual receivers.

The following sections of this chapter provide details of each of these three forms of interferometry, together with a number of successful examples of their application. Finally, the method of *coda-wave interferometry* (Snieder et al., 2002; Snieder, 2006) and its application to time-dependent monitoring are presented and discussed.

1.5 Theory of inter-receiver interferometry

1.5.1 Interferometry and time-reversed acoustics

There is a precise link between Green's function retrieval in seismic interferometry and wavefields in time-reversed acoustics which provides an intuitive approach to understand interferometric theory. It was clearly illustrated by Derode et al. (2003a); Derode et al. (2003b) who, starting from the principle of invariance of the wave equation under time-reversal, derive Green's function representations using physical arguments.

Consider a lossless, arbitrarily inhomogeneous, acoustic medium bounded by surface S embedded within a homogeneous surrounding medium (Fig. 1.6). Suppose a source, located at position $\mathbf{x}_A$ within the inhomogeneous medium, fires an impulse at time $t = 0$, and the response is recorded by receivers located at positions $\mathbf{x}$ all around a boundary S (Fig. 1.6(a)). In the time domain, the response to the impulsive source at $\mathbf{x}_A$, recorded at each $\mathbf{x}$ on S, is denoted by $G(\mathbf{x}, \mathbf{x}_A, t)$, and the time-reverse of this signal is denoted by $G(\mathbf{x}, \mathbf{x}_A, -t)$. If the time-reversed signals are simultaneously fed back into the medium by transducer sources at all positions $\mathbf{x}$ on the boundary (Fig. 1.6(b)), in the absence of attenuation the wavefield should exactly reverse, arriving at any arbitrary position $\mathbf{x}' \neq \mathbf{x}$ (at $t < 0$) before refocusing at the original source location $\mathbf{x}_A$ at time $t = 0$ (just as the concentric waves originating from a stone dropped into a pond would travel inwards to refocus on the stone if we played the recording of the event backwards in time).

The wavefield recorded at point $\mathbf{x}'$ inside boundary S, due to sources $\mathbf{x}$ on boundary S, can be obtained by applying the superposition principle:

$$u(\mathbf{x}', t) \propto \int_S G(\mathbf{x}', \mathbf{x}, t) \otimes G(\mathbf{x}, \mathbf{x}_A, -t)\, \mathrm{d}S\,. \tag{1.10}$$

Here, the symbol $\propto$ denotes proportionality, while the symbol $\otimes$ denotes convolution between the boundary source term $G(\mathbf{x}, \mathbf{x}_A, -t)$ (the time-reverse of the original boundary recordings) and the propagation term $G(\mathbf{x}', \mathbf{x}, t)$ which defines how the wave propagates from boundary location $\mathbf{x}$ to any interior location $\mathbf{x}'$. The integral over S ensures that the contributions from all sources on the boundary are considered simultaneously.

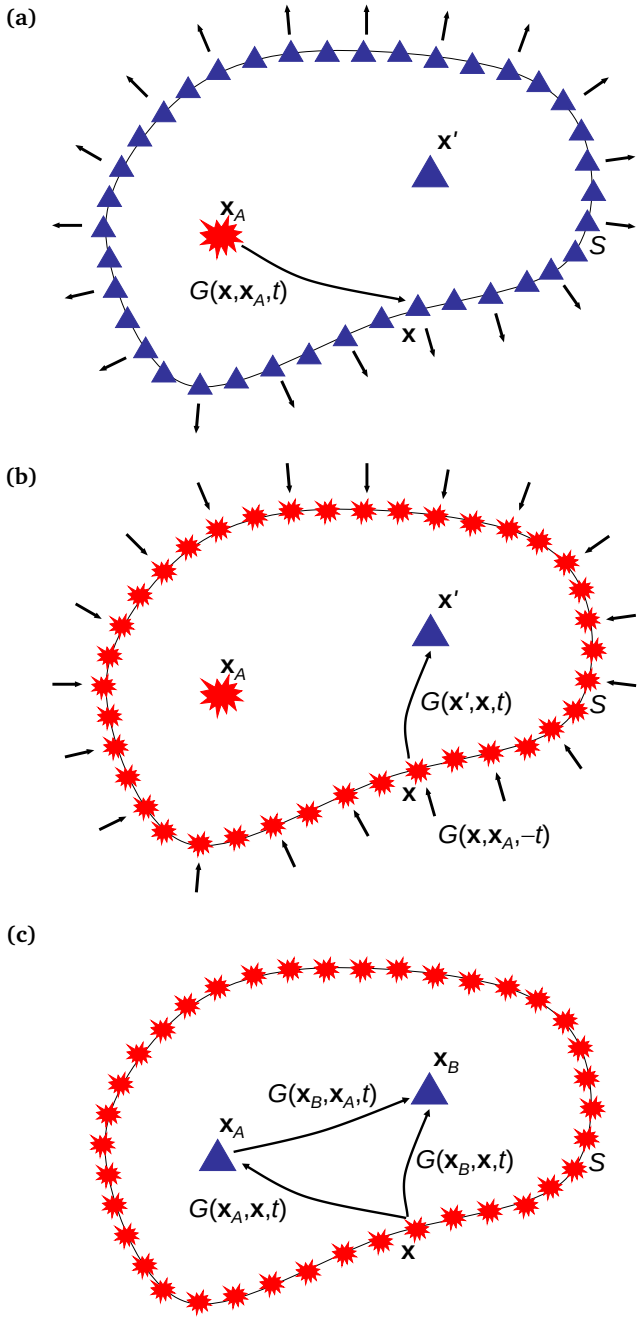

Figure 1.6. Green's function retrieval from a time-reversed acoustics experiment. (a) The response at a receiver at $\mathbf{x}$ on boundary S for a source at $\mathbf{x}_A$ is given by $G(\mathbf{x}, \mathbf{x}_A, t)$. (b) The time-reversed signal $G(\mathbf{x}, \mathbf{x}_A, -t)$ is emitted back into the medium from sources on boundary S. (c) The Green's function between $\mathbf{x}_A$ and $\mathbf{x}_B$ can be obtained by cross-correlating the wavefield recorded at these two positions and integrating over the whole boundary. Redrawn after Wapenaar et al. (2010c).

However, as energy is not taken out of the system at $t = 0$, the wavefield does not stop after refocusing at $\mathbf{x}_A$, but propagates outwards again, arriving at position $\mathbf{x}'$ again at $t > 0$. This wavefield must be identical to the original wavefield propagating out from the source at $\mathbf{x}_A$ (since no energy has been removed or altered in the time-reversed experiment); it must also be the time-reverse of the wavefield observed at $\mathbf{x}'$ as the waves were converging towards $\mathbf{x}_A$. Hence, the wavefield $u(\mathbf{x}', t)$ that would be recorded at $\mathbf{x}'$ consists of negative-time and positive-time components

$$u(\mathbf{x}', t) = G(\mathbf{x}', \mathbf{x}_A, t) + G(\mathbf{x}', \mathbf{x}_A, -t)\,, \tag{1.11}$$

where $G(\mathbf{x}', \mathbf{x}_A, -t)$ represents the acausal contribution due to the wavefield propagating inwards from the sources on S to position $\mathbf{x}'$ before refocusing at $\mathbf{x}_A$, and $G(\mathbf{x}', \mathbf{x}_A, t)$ represents the causal contribution due to the wavefield propagating outward from $\mathbf{x}_A$ to $\mathbf{x}'$, after refocusing.

By substituting equation (1.11) for the left side of equation (1.10), applying source-receiver reciprocity (i.e., $G(\mathbf{x}, \mathbf{x}_A, t) = G(\mathbf{x}_A, \mathbf{x}, t)$) and setting $\mathbf{x}' = \mathbf{x}_B$ (the location of a receiver anywhere inside the boundary S), the following expression is obtained:

$$G(\mathbf{x}_B, \mathbf{x}_A, t) + G(\mathbf{x}_B, \mathbf{x}_A, -t) \propto \int_S G(\mathbf{x}_B, \mathbf{x}, t) \otimes G(\mathbf{x}_A, \mathbf{x}, -t)\, \mathrm{d}S\,. \tag{1.12}$$

The right-hand side of equation (1.12) gives the integral, over all boundary sources at $\mathbf{x}$ on S, of cross-correlations of wavefield recordings obtained by receivers at $\mathbf{x}_B$ and $\mathbf{x}_A$; the left-hand side of the equation shows that the result is the superposition of the signal recorded at $\mathbf{x}_B$ for an impulsive source located at $\mathbf{x}_A$ and its time-reversed version (Fig. 1.6(c)). This reconstructed Green's function contains both the direct wave from the virtual source at $\mathbf{x}_A$ to the receiver and all contributions due to scattering.

Although the derivation by Derode et al. (2003a); Derode et al. (2003b) is helpful in understanding the physical aspects of seismic interferometry, it is not mathematically precise for a general Earth-like heterogeneous medium. In the next section, exact mathematical results based on representation theorems are presented.

1.5.2 Interferometry and reciprocity

The now-standard mathematical approach to prove how Green's functions are retrieved in seismic interferometry begins with the definition of a convolutional and a correlational reciprocity theorem (theorems that relate two independent acoustic or elastodynamic states, A and B, of a medium – in this case the states being differentiated by having sources at different locations). From the reciprocity theorem of the convolution type (Rayleigh, 1878; de Hoop, 1988; Fokkema & van den Berg, 1993), by choosing impulsive point sources of volume injection rate and expressing the wavefields in terms of Green's

functions in both states A and B, source-receiver reciprocity can be proved in both the acoustic and the elastic case (see Appendix A.1 for a full derivation). For acoustic media this is stated as

$$G(\mathbf{x}_B, \mathbf{x}_A, \omega) = G(\mathbf{x}_A, \mathbf{x}_B, \omega) \tag{1.13}$$

and was actually used above in the physical argument from Derode et al. (2003a); Derode et al. (2003b). This expression states that the signal recorded at location $\mathbf{x}_B$ due to a source at $\mathbf{x}_A$ is equal to the signal recorded at location $\mathbf{x}_A$ due to a source at $\mathbf{x}_B$. This result is particularly important in the case of seismic interferometry, as it allows progress from inter-receiver interferometry to both inter-source and source-receiver interferometry by variously interchanging sources and receivers – see below.

From the acoustic reciprocity theorem of the correlation type (de Hoop, 1988; Fokkema & van den Berg, 1993), Wapenaar (2004), van Manen et al. (2005); van Manen et al. (2006) and Wapenaar & Fokkema (2006) derive exact representations of the Green's function between $\mathbf{x}_A$ and $\mathbf{x}_B$. The expression obtained by Wapenaar & Fokkema (2006) is slightly different from that obtained by van Manen et al. (2005) due to a difference in the type of source assumed: Wapenaar & Fokkema (2006) assume volume injection rate density sources (denoted by a double hat symbol $\hat{\hat{}}$ – see Appendix A.2.1), while van Manen et al. (2005) assume the change in volume injection rate density over time (denoted by an upside-down hat symbol $\check{}$ – see Appendix A.2.3). The *interferometric formula* for *acoustic* waves derived by van Manen et al. (2005) is

$$\begin{aligned} &\check{G}^*(\mathbf{x}_B, \mathbf{x}_A) - \check{G}(\mathbf{x}_B, \mathbf{x}_A) \\ &= \int_S \frac{1}{\rho(\mathbf{x})} \left[\left(\partial_j \check{G}(\mathbf{x}_B, \mathbf{x}) \right) \check{G}^*(\mathbf{x}_A, \mathbf{x}) - \check{G}(\mathbf{x}_B, \mathbf{x}) \left(\partial_j \check{G}^*(\mathbf{x}_A, \mathbf{x}) \right) \right] n_j \, \mathrm{d}S \,, \end{aligned} \tag{1.14}$$

and by Wapenaar & Fokkema (2006) is

$$\begin{aligned} &\hat{\hat{G}}^*(\mathbf{x}_B, \mathbf{x}_A) + \hat{\hat{G}}(\mathbf{x}_B, \mathbf{x}_A) \\ &= -\int_S \frac{1}{\iota\omega\rho(\mathbf{x})} \left[\left(\partial_j \hat{\hat{G}}(\mathbf{x}_B, \mathbf{x}) \right) \hat{\hat{G}}^*(\mathbf{x}_A, \mathbf{x}) - \hat{\hat{G}}(\mathbf{x}_B, \mathbf{x}) \left(\partial_j \hat{\hat{G}}^*(\mathbf{x}_A, \mathbf{x}) \right) \right] n_j \, \mathrm{d}S \end{aligned} \tag{1.15}$$

where $\iota = \sqrt{-1}$, n_j is the j^{th} component of the outward-pointing normal $\mathbf{n}$ to boundary S, $\rho(\mathbf{x})$ is the mass density of the medium at $\mathbf{x}$ (for simplicity, we drop the $\mathbf{x}$-dependence in all subsequent equations), ∂_j is the partial derivative with respect to the j^{th} coordinate at the source location $\mathbf{x}$, the asterisk * denotes complex conjugation in the frequency domain, $\mathrm{d}S$ represents integration over surface S and the different notation in the Green's function terms ($\check{G}$ versus $\hat{\hat{G}}$) arises from the difference in the source types used. In both cases, the Green's functions are given in the frequency domain and the terms G and $\partial_j G$ under the

integral represent the responses for monopole and dipole sources on S, respectively (since the latter results in a spatial derivative over the source coordinates taken in the direction perpendicular to the outer boundary of sources). Dipolar or coupled sources are familiar to tectonophysicists as earthquake source mechanisms are usually represented as a double-couple, or a pair of dipoles. The products in the integral correspond to cross-correlations in the time domain.

Equations (1.14) and (1.15) provide exact representations of the Green's function between $\mathbf{x}_A$ and $\mathbf{x}_B$. Also, unlike the time-reversal approach in equation (1.12), no assumption is made regarding the homogeneity of the medium outside of boundary S (made by Derode et al. (2003a); Derode et al. (2003b)) to ensure no waves entered the medium through surface S; instead, in equations (1.14) and (1.15) the combination of products of Green's functions for monopole and dipole sources ensures that there is no interaction between waves propagating outwards and inwards through surface S.

Wapenaar et al. (2005) show that if we assume the medium outside S is homogeneous and we approximate $n_j \partial_j \hat{\hat{G}}$ by $-\imath(\omega/c)\hat{\hat{G}}$ (where c is the propagation velocity in the homogeneous medium), equation (1.15) becomes

$$2\Re\left\{\hat{\hat{G}}(\mathbf{x}_B,\mathbf{x}_A)\right\} \approx \frac{2}{\rho c}\int_S \hat{\hat{G}}(\mathbf{x}_B,\mathbf{x})\hat{\hat{G}}^*(\mathbf{x}_A,\mathbf{x})\,\mathrm{d}S\,. \tag{1.16}$$

When converted back into the time domain, this yields equation (1.12) with proportionality factor $2/\rho c$. Hence, the expression obtained from the time-reversal approach by Derode et al. (2003a); Derode et al. (2003b) can be considered an approximation of the expression obtained from the reciprocity theorem approach.

From the elastodynamic reciprocity theorem of the correlation type, Wapenaar (2004), Wapenaar & Fokkema (2006) and van Manen et al. (2006) derive expressions for the Green's function between two receivers located at $\mathbf{x}_A$ and $\mathbf{x}_B$ in an *elastic* medium. Similarly to the acoustic case, the expressions derived by Wapenaar (2004) and Wapenaar & Fokkema (2006), and by van Manen et al. (2006) present some differences which are due to the different source terms and quantities recorded. van Manen et al. (2006) derive the following interferometric formula for elastodynamic waves:

$$\begin{aligned}&\check{G}^*_{im}(\mathbf{x}_B,\mathbf{x}_A) - \check{G}_{im}(\mathbf{x}_B,\mathbf{x}_A)\\ &= \int_S c_{njkl}(\mathbf{x})\left[\left(\partial_k \check{G}_{il}(\mathbf{x}_B,\mathbf{x})\right)\check{G}^*_{mn}(\mathbf{x}_A,\mathbf{x}) - \check{G}_{in}(\mathbf{x}_B,\mathbf{x})\left(\partial_k \check{G}^*_{ml}(\mathbf{x}_A,\mathbf{x})\right)\right] n_j\,\mathrm{d}S\,,\end{aligned} \tag{1.17}$$

where $c_{njkl}(\mathbf{x})$ is the stiffness tensor at $\mathbf{x}$ (for simplicity, we drop the $\mathbf{x}$-dependence in all subsequent equations), ∂_k denotes the partial derivative in the k-direction with respect to the source location $\mathbf{x}$, and $\check{G}_{im}(\mathbf{x}_B,\mathbf{x}_A)$ represents the *displacement* Green's function at location $\mathbf{x}_B$ in the i-direction due to a uni-directional point force in the m-direction at

location $\mathbf{x}_A$. Wapenaar (2004) and Wapenaar & Fokkema (2006) instead find

$$\begin{aligned}&\hat{\tilde{G}}^{*}_{qp}(\mathbf{x}_B,\mathbf{x}_A)+\hat{\tilde{G}}_{qp}(\mathbf{x}_B,\mathbf{x}_A)\\&=-\int_S \frac{c_{ijkl}}{\imath\omega}\left[\left(\partial_l\hat{\tilde{G}}_{qk}(\mathbf{x}_B,\mathbf{x})\right)\hat{\tilde{G}}^{*}_{pi}(\mathbf{x}_A,\mathbf{x})-\hat{\tilde{G}}_{qi}(\mathbf{x}_B,\mathbf{x})\left(\partial_l\hat{\tilde{G}}^{*}_{pk}(\mathbf{x}_A,\mathbf{x})\right)\right]n_j\,\mathrm{d}S\,,\end{aligned}\tag{1.18}$$

where $\hat{\tilde{G}}_{qp}(\mathbf{x}_B,\mathbf{x}_A)$ represents the *particle velocity* Green's function at location $\mathbf{x}_B$ in the q-direction due to an impulsive point force excitation rate in the p-direction at location $\mathbf{x}_A$. The terms $\hat{\tilde{G}}_{pi}(\mathbf{x}_A,\mathbf{x})$ and $(c_{ijkl}/\imath\omega)\partial_l\hat{\tilde{G}}_{pk}(\mathbf{x}_A,\mathbf{x})n_j$ under the integral represent the p^{th} component of particle velocity observed at $\mathbf{x}_A$ due to respectively volume force and deformation rate tensor sources at $\mathbf{x}$. Both expressions are given in the frequency domain and Einstein's summation convention for repeated indices applies.

Equations (1.17) and (1.18) provide exact representations of the elastodynamic Green's function between locations $\mathbf{x}_A$ and $\mathbf{x}_B$ as though a source had been fired at location $\mathbf{x}_A$, using only recordings of sources fired on the boundary. Thus, the receiver at location $\mathbf{x}_A$ is turned into a virtual source. Similarly to the acoustic case, these equations can be simplified by making a number of assumptions (e.g., homogeneous medium outside S) or approximations (e.g., a source boundary S that is far from the receiver pair) which result in a single correlation operation and remove the need for dipole sources in the integrand, similar to equation (1.16) (Wapenaar & Fokkema, 2006).

If noise sources are to be used, Wapenaar & Fokkema (2006) show that if noise sources distributed around the boundary S are uncorrelated, the approximate Green's function between $\mathbf{x}_A$ and $\mathbf{x}_B$ in the acoustic case is obtained from the above expressions by

$$2\Re\left\{\hat{\tilde{G}}(\mathbf{x}_B,\mathbf{x}_A,\omega)\right\}S(\omega)\approx\frac{2}{\rho c}\langle p^{obs}(\mathbf{x}_B,\omega)p^{obs*}(\mathbf{x}_A,\omega)\rangle\,,\tag{1.19}$$

where $S(\omega)$ is the power spectrum of the noise, $p^{obs}(\mathbf{x}_A,\omega)$ and $p^{obs}(\mathbf{x}_B,\omega)$ indicate the observed noise wavefields at $\mathbf{x}_A$ and $\mathbf{x}_B$, and $\langle\cdot\rangle$ denotes spatial ensemble average. This shows precisely how the Green's functions between $\mathbf{x}_A$ and $\mathbf{x}_B$ is approximated by cross-correlation of recordings of ambient noise at each of the receiver locations. Similar expressions exist for elastic media.

1.5.3 Stationary-phase approach

Analysing seismic interferometry using the method of stationary phase is particularly useful to understand the mechanisms of constructive and destructive interference that account for the emergence of the Green's function from the above cross-correlations of wavefields (Snieder, 2004; Snieder et al., 2006). Snieder et al. (2006) consider a model consisting of a single horizontal reflector with reflection coefficient r for downward-travelling waves, embedded in a homogeneous medium. The sources, located

on the free surface at $\mathbf{r} = (x, y, 0)$, with a density of n sources per unit area, are assumed to be uncorrelated, and receivers are located within the Earth at locations $\mathbf{r}_A = (x_A, 0, z_A)$ and $\mathbf{r}_B = (x_B, 0, z_B)$, as shown in Fig. 1.7(a). The cross-correlation of wavefields recorded at the two receivers in the frequency domain is given by

$$C_{AB}(\omega) = |S(\omega)|^2 n \int_{\mathbf{r}} G^{full}(\mathbf{r}_B, \mathbf{r}) G^{full*}(\mathbf{r}_A, \mathbf{r}) \mathrm{d}x\mathrm{d}y \,, \tag{1.20}$$

where $|S(\omega)|^2$ is the power spectrum of the sources, and G^{full} denotes the full Green's function consisting of the direct and singly-reflected wave in the frequency domain. The full Green's functions recorded at each of the two receivers are given by

$$G^{full}(\mathbf{r}_A, \mathbf{r}) = G(|\mathbf{r}_A - \mathbf{r}|) + rG(|\mathbf{r}_A - \mathbf{r}_{RA}| + |\mathbf{r}_{RA} - \mathbf{r}|) \tag{1.21a}$$

and

$$G^{full}(\mathbf{r}_B, \mathbf{r}) = G(|\mathbf{r}_B - \mathbf{r}|) + rG(|\mathbf{r}_B - \mathbf{r}_{RB}| + |\mathbf{r}_{RB} - \mathbf{r}|) \tag{1.21b}$$

where, on the right-hand side of both equations, the first term represents the direct wave and the second term represents the singly reflected wave. By inserting equations (1.21a) and (1.21b) into equation (1.20), an expression consisting of the sum of four terms is obtained: term $T1$ is the correlation of direct waves to both receivers; terms $T2$ and $T3$ are given by the correlation of a direct and a reflected wave to the receivers; term $T4$ is the correlation of reflected waves to both receivers. All four terms contain the Green's function for a homogeneous medium

$$G(R) = -\rho \frac{\mathrm{e}^{-\iota kR}}{4\pi R} \,, \tag{1.22}$$

where R is the distance of propagation between the source and one receiver, which contains an oscillatory integrand of the form $\mathrm{e}^{-\iota kR}$, and this term has a stationary point that depends on the expression for R in equations (1.21a) and (1.21b). For this reason, in all four terms the integral is analysed in the stationary-phase approximation. This assumes that the amplitude of the integral varies smoothly compared to the phase, in which case the dominant contributions to the integral in equation (1.20) come from points $\mathbf{r}$ where the phase is stationary (becomes constant) with respect to the boundary source position. As an example, consider term $T1$:

$$T1 = \int G(|\mathbf{r}_B - \mathbf{r}|) G^*(|\mathbf{r}_A - \mathbf{r}|) \mathrm{d}x\mathrm{d}y = \frac{\rho^2}{(4\pi)^2} \int \frac{\mathrm{e}^{-\iota k(L_A - L_B)}}{L_A L_B} \mathrm{d}x\mathrm{d}y \,, \tag{1.23}$$

where quantities L_A and L_B are defined in Fig. 1.7(a). Snieder et al. (2006) show that the phase of the integrand is stationary when $\psi_A = \psi_B$ and $y = 0$, where the angles ψ_A and

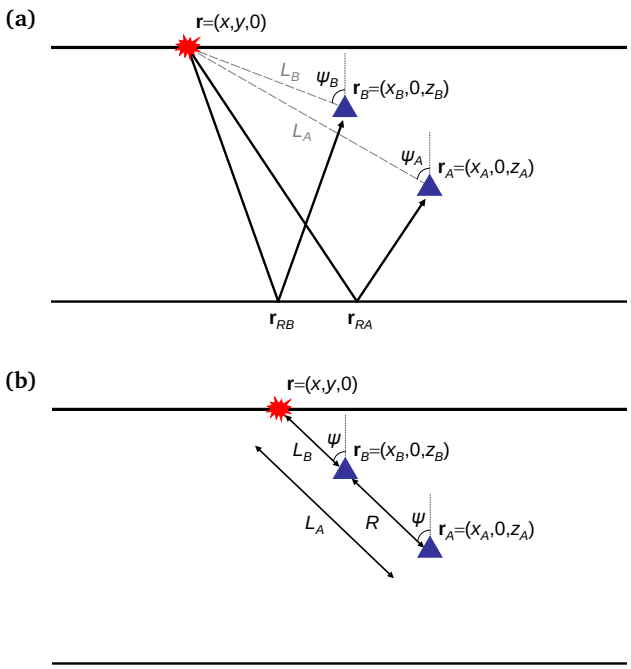

Figure 1.7. Geometry of a simple model and raypaths for a derivation of seismic interferometry based on stationary phase. (a) A source is located on the surface at $\mathbf{r}$ and two receivers are located in the subsurface at $\mathbf{r}_A$ and $\mathbf{r}_B$. Reflection points are located at $\mathbf{r}_{RA}$ and $\mathbf{r}_{RB}$. The variables used in the analysis of term $T1$ are also defined. (b) The stationary source in term $T1$ is located along the line joining the two receivers. Redrawn after Snieder et al. (2006).

ψ_B are also defined in Fig. 1.7(a). This corresponds to a source located along the line of the receivers, as shown in Fig. 1.7(b).

Snieder et al. (2006) repeat the analysis for terms $T2$, $T3$, $T4$ and determine the locations of the stationary points for each term. The source positions and ray paths corresponding to the stationary contributions in the integrals are shown in Fig. 1.8: energy travelling along the ray paths in panel (a) contribute to the causal and acausal direct waves, propagating directly between the two receivers; the ray paths in panel (b) contribute to the causal and acausal singly-reflected waves, which propagate between the two receivers via a reflection at the interface. In all four cases, the sources corresponding to the stationary points are located along the extension of the ray path joining the two receivers (in the case of reflected waves, the mirror images below the reflectors can be considered). Hence, as the phase of the correlation is stationary only for the raypaths that are aligned with the inter-receiver line, it follows that the main contribution to the Green's function emergence is given by sources at or around those that contribute to these paths, for which energy passes and is recorded by both receivers; signals resulting from sources on other ray paths interfere destructively upon integration over all the sources, due to the oscillation of the exponential in equation (1.23).

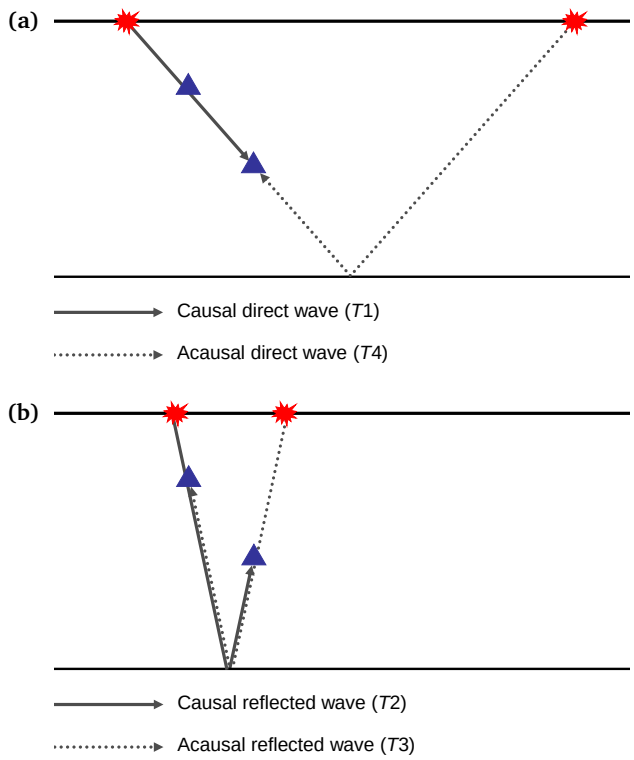

Figure 1.8. Raypaths corresponding to the four terms resulting from the cross-correlation of the full wavefields recorded at the two receivers: (a) causal direct wave from term $T1$ and acausal direct wave from term $T4$; (b) causal reflected wave from term $T2$ and acausal reflected wave from term $T3$. Redrawn after Snieder et al. (2006).

Snieder (2004) shows in a 2D model that this latter statement is also true for waves in the scattered coda in the approach of Campillo & Paul (2003): those that pass the locations of *both* receivers contribute energy that is stationary in the above sense, and hence which survives the cross-correlation process. In 3D media, Halliday & Curtis (2008) show that subsurface point sources are also necessary (even for surface waves) in order to excite all stationary-phase points and hence produce correct interferometric reconstructions.

Snieder et al. (2006) show that in the stationary-phase analysis for a medium with more than one reflector, if sources are only present on the surface the cross-terms of wavefields resulting from reflections at different reflectors may give non-zero contributions that are proportional to the product of the reflection coefficients at the reflecting interfaces. These signals, which do not correspond to physical events and would vanish in the presence of a closed boundary of sources, are therefore named *spurious multiples*. A development of the discussion of spurious multiples and their use in exploration seismology is provided by Halliday & Curtis (2009a) and King et al. (2011) (see next section), where the more general term *non-physical* contributions is used in place of spurious multiples.

An example of how Green's functions emerge from waves with stationary phase in more complex media is given by van Manen et al. (2005). Their 2D acoustic seismic

model, which includes a salt dome, is shown in Fig. 1.9(a). Sources are located along the dotted line and receivers are represented by the two triangles. Wave-propagation simulations are carried out for each source separately and the cross-correlations of the resulting traces recorded at the two receivers are shown in Fig. 1.9(b) for each source. When these traces are stacked (summed), the seismogram represented in Fig. 1.9(c) is obtained: the points in plot (b) that are stationary with respect to source position (identified as waves lying on horizontal lines in plot (b)) provide the dominant contributions, and the Green's function between the two receivers (red) emerges here as a result of constructive and destructive interference between the wavefields propagating through the medium from each source. This trace perfectly matches the reference trace obtained by direct forward modelling (blue).

Halliday & Curtis (2009a) repeat the stationary-phase analysis for scattered (rather than reflected) waves and include the effects of attenuation. Similarly to Snieder (2004) and Snieder et al. (2006), four different contributions ($T1$, $T2$, $T3$, $T4$) to the interferometric integral are obtained, defined similarly to above, and are analysed for the stationary-phase contributions. The analysis yields similar results to the study by Snieder (2004), and the stationary source points for $T1$ are found to be those aligned with the inter-receiver line. Assuming a closed source boundary, terms $T2$ and $T3$ contribute both physical and non-physical parts (Fig. 1.10), the non-physical parts of which are cancelled by term $T4$ when no attenuation is present.

In the case of attenuative media (like the real Earth), this complete cancellation does not occur since contributions $T2$, $T3$ and $T4$ may be differentially attenuated. This results in spurious or non-physical arrivals in the reconstructed seismograms. Slob et al. (2007) and Halliday & Curtis (2009a) show that this difficulty can be overcome by using seismic interferometry by convolution instead of correlation. This technique was developed by Slob et al. (2007) for electromagnetic waves which are often affected by strong attenuation. The interferometric relationship of convolution type is derived from the reciprocity theorem of the convolution type and importantly requires one of the receivers to be outside of the boundary of sources (e.g., compare Fig. 1.11(a) for correlation and Fig. 1.11(b) for convolution). This relationship only provides the causal component of the Green's function and for (an)elastic media is given in the frequency domain by the following equation:

$$\begin{aligned}&\breve{G}_{im}(\mathbf{x}_B,\mathbf{x}_A)\\&=\int_S c_{njkl}(\mathbf{x})\left[\breve{G}_{in}(\mathbf{x}_B,\mathbf{x})\left(\partial_k\breve{G}_{ml}(\mathbf{x}_A,\mathbf{x})\right)-\left(\partial_k\breve{G}_{il}(\mathbf{x}_B,\mathbf{x})\right)\breve{G}_{mn}(\mathbf{x}_A,\mathbf{x})\right]n_j\,\mathrm{d}S\,,\end{aligned}\tag{1.24}$$

where ∂_k acts on the source coordinate $\mathbf{x}$ and only one of $\mathbf{x}_A$ and $\mathbf{x}_B$ is inside the boundary of sources S. Examples of stationary-phase analysis for scattered surface waves are shown in Fig. 1.11, where the solid and dashed lines indicate the interferometric and the directly modelled waveforms, respectively. In (c), the sum of the four terms $T1$-$T4$ for the model

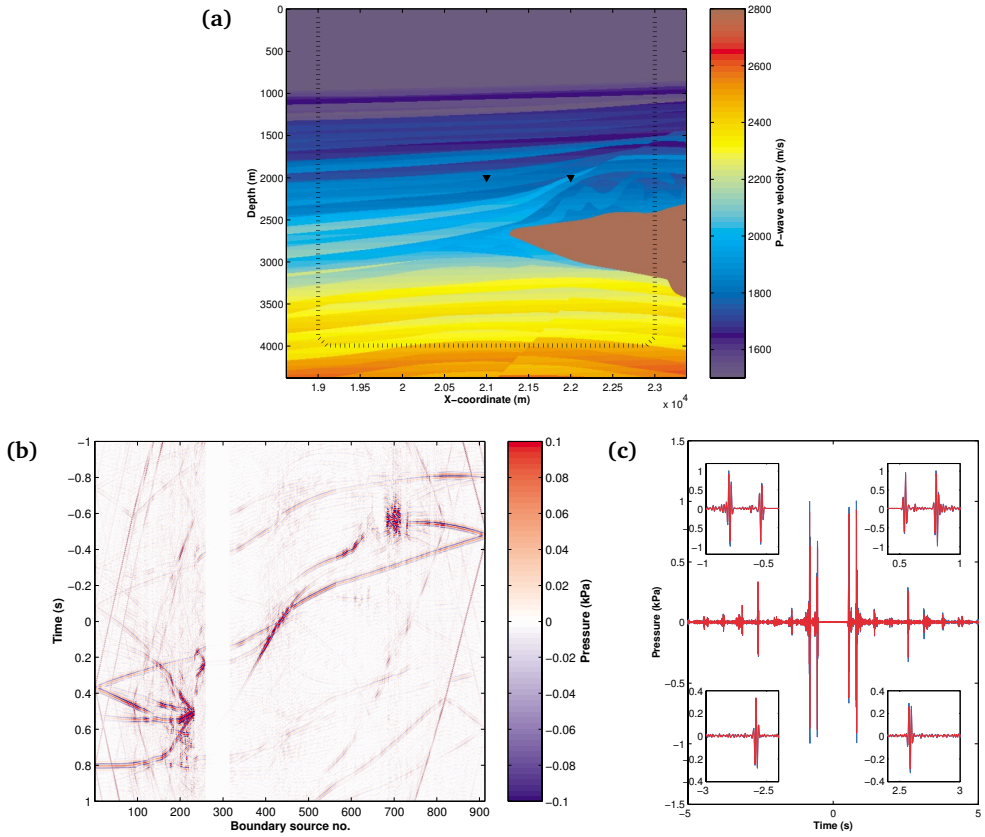

Figure 1.9. Model and simulation results from van Manen et al. (2005). (a) 2D acoustic marine seismic model including a high-velocity salt body. The boundary of 912 sources is represented by the dotted line; the two receivers are represented by the triangles. (b) Correlation gather for the two receivers shown in (a). (c) Comparison between the waveform obtained by stacking (summing) all traces from the correlation gather in (b) (red line) and that obtained from direct forward modelling (blue line). Reprinted figure with permission from van Manen, D.-J., Robertsson, J.O.A., Curtis, A., Physical Review Letters 94 (16), 164301, 2005. Copyright (2005) by the American Physical Society (http://prl.aps.org/abstract/PRL/v94/i16/e164301). Readers may view, browse, and/or download material for temporary copying purposes only, provided these uses are for noncommercial personal purposes. Except as provided by law, this material may not be further reproduced, distributed, transmitted, modified, adapted, performed, displayed, published, or sold in whole or part, without prior written permission from the American Physical Society.

shown in (a) and no attenuation is shown when correlational interferometry is used as in equations (1.14), (1.15), (1.17), (1.18). In this case, no non-physical arrivals are present, as the non-physical contributions brought by $T2$, $T3$ and $T4$ mutually cancel. In contrast, a non-physical event and strong amplitude distortions are visible in (d), which displays the sum of the four terms for the same model as (c) but with the effects of attenuation included. Instead, if convolution, rather than cross-correlation, is applied for case (b), the waveform shown in (e) is obtained: despite the amplitude mismatch in the early, low-frequency arrivals caused by the absence of sources at depth, this signal only contains a causal part and presents no non-physical arrivals. Convolutional interferometry is therefore likely to be more suitable for near surface applications, where complex

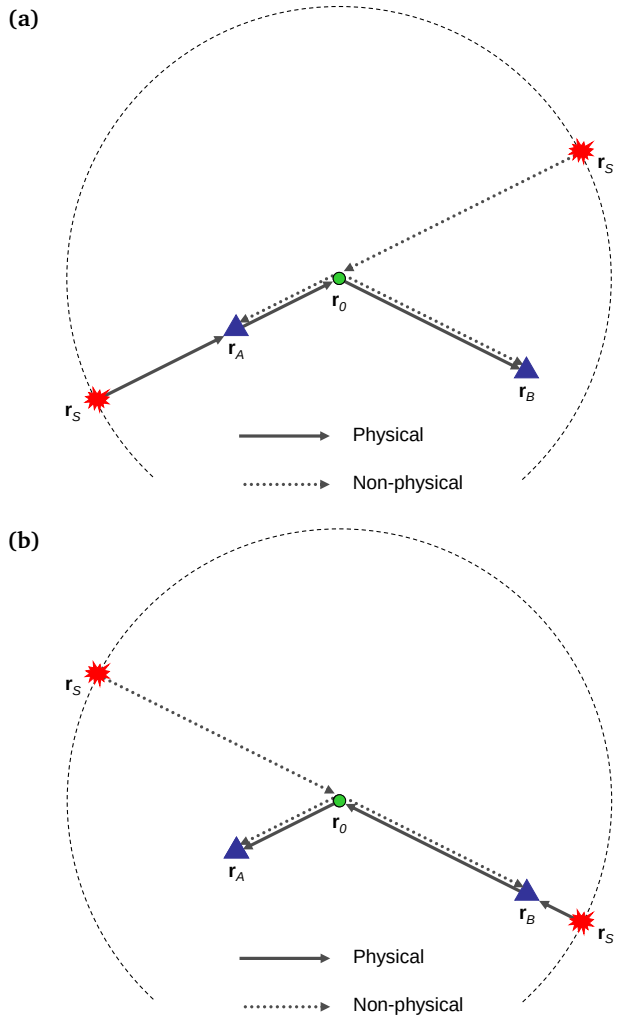

Figure 1.10. Stationary source points ($\mathbf{r}_S$) in the interferometric integral for wave propagation from receiver $\mathbf{r}_A$ to receiver $\mathbf{r}_B$, with a scatterer at location $\mathbf{r}_0$. The boundary of sources is indicated by a dashed line. (a) Physical and non-physical part of term $T2$; (b) physical and non-physical part of term $T3$. Physical events have traveltime equal to $[t(\mathbf{r}_0,\mathbf{r}_A)+t(\mathbf{r}_B,\mathbf{r}_0)]$ in (a) and $[t(\mathbf{r}_0,\mathbf{r}_B)+t(\mathbf{r}_A,\mathbf{r}_0)]$ in (b) (where $t(\mathbf{r}_0,\mathbf{r}_A)$ denotes the traveltime from point $\mathbf{r}_A$ to point $\mathbf{r}_0$), which corresponds to the traveltime of the scattered wave from one receiver to the other. Non-physical events have traveltime equal to $|t(\mathbf{r}_A,\mathbf{r}_0)-t(\mathbf{r}_B,\mathbf{r}_0)|$, which corresponds to the difference in traveltimes from the scatterer to the two receivers and has no physical meaning (see Section 2.4.1 for further details).

scattering and attenuation are likely to occur, provided an appropriate source geometry exists. However, the convolutional method only works for transient sources, hence it is not applicable in the case of ambient noise.

Halliday & Curtis (2008) use the stationary-phase approach to analyse the effect of source distribution on the construction of surface wave signals from seismic interferometry (the most common application of seismic interferometry). One of their most striking findings is that, contrarily to common opinion, sources at depth also play an important role in the interferometric construction of surface waves. In fact, the use of deep sources allows the correct amplitudes to be recovered for all surface wave modes

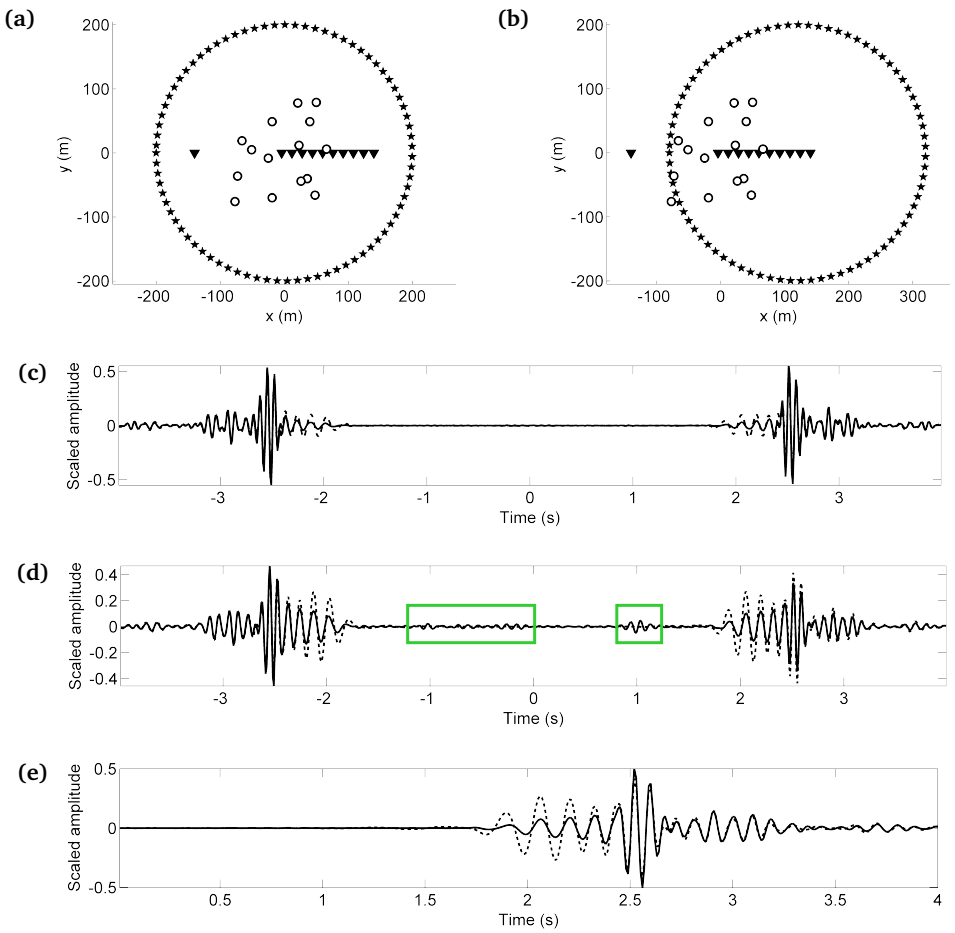

Figure 1.11. Comparison between waveforms obtained by summing the four contributions to the interferometric integral (solid lines) and those obtained from direct modelling (dashed lines) for scattered surface waves, in the case of the two models shown in (a) and (b), where triangles represent receivers, stars represent sources and circles indicate scatterers. (c) Waveform for model (a) with no attenuation; (d) waveform for model (a) with attenuation. Green boxes highlight non-physical arrivals. (e) Waveform for model (b) with attenuation. From Halliday, D., Curtis, A., 2009. Seismic interferometry of scattered surface waves in attenuative media. Geophys. J. Int. 178 (1), 419-446. Reprinted with permission from John Wiley & Sons Ltd.

without the introduction of spurious or non-physical events which otherwise result from the cross-correlation of different modes with each other (so-called modal cross-talk). If an ideal source distribution is not available, modal separation prior to cross-correlation is found to provide correct estimates of the wavefield propagating between the receivers in some practical geometries.

The discussion of physical and non-physical energy is complex but is extremely important. It explains why in practice the Green's function estimates from virtual sources derived using seismic interferometry do not necessarily look exactly like seismograms that would be recorded from real sources, and how and why they differ. Nevertheless, it should not be assumed that non-physical energy is always unwanted; on the contrary, since it is also formed by combining (e.g., cross-correlating) recorded,

physically-propagating energy, it also contains information about the medium (the Earth). For example, King et al. (2011) use non-physical energy to retrieve information about subsurface layer velocities and thicknesses, as described in the next section. Mikesell et al. (2009) also use energy in the non-physical, so-called "virtual refraction" for the same purpose. It is currently a moot point as to whether physical or non-physical energy contains most information about the medium.

Despite being the most popular and widely used form of seismic interferometry, cross-correlational interferometry presents several limitations (Curtis & Halliday, 2010b; Halliday & Curtis, 2008, 2009a; Slob & Wapenaar, 2007; Stehly et al., 2008; Harmon et al., 2010). It provides reasonably accurate Green's function estimates when the medium is lossless and the waves are equipartitioned (e.g., if the distribution of sources is regular around the receivers and the sources are transient or uncorrelated with equal autocorrelation functions and power spectra), but these assumptions seldom hold in practical applications, causing the Green's function estimate to be affected by non-physical artifacts. In addition, the Green's function retrieved from cross-correlation when these assumptions are not satisfied is proportional to the Green's function that would be generated by a spatio-temporally blurred source, the distortion being quantified by a so-called point-spread function (Wapenaar & van der Neut, 2010).

By replacing the cross-correlation operation with deconvolution (see equation (1.1)), Vasconcelos & Snieder (2008a); Vasconcelos & Snieder (2008b) showed how these assumptions may be avoided and a more accurate representation of the Green's function may be obtained. Similarly, in their so-called *directional balancing* method, Curtis & Halliday (2010b) used deconvolution to reduce the effects that an irregular distribution of sources may have on the Green's functions retrieved by cross-correlation. What is more, interferometry by deconvolution may be extended to two or three dimensions, giving rise to the method of multi-dimensional deconvolution (MDD) (Wapenaar et al., 2008; Minato et al., 2011; Wapenaar et al., 2011). The main advantages of MDD over cross-correlation include the fact that the assumption of a lossless medium is relaxed, the source is deblurred to some extent, and its signature is eliminated. On the other hand, MDD requires the inversion of a matrix and a network of receivers (rather than only a single pair of receivers as in cross-correlation), and is therefore more expensive than cross-correlational interferometry. Overall, interferometry by convolution, cross-correlation, deconvolution and multi-dimensional deconvolution present advantages and disadvantages, and one method may be preferable to another for a specific application. A detailed comparison of the latter three methods is given by Snieder et al. (2009).

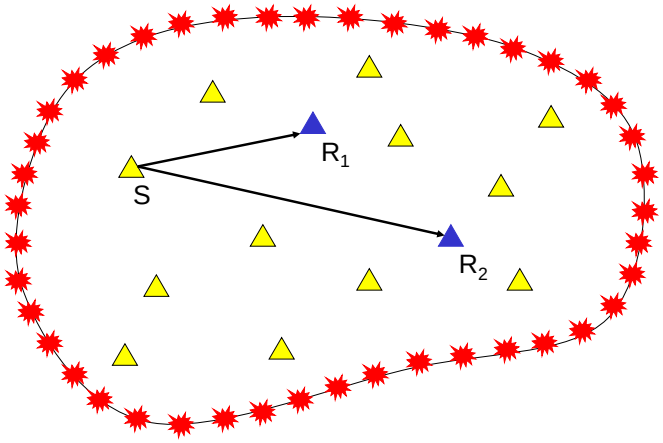

Figure 1.12. Schematic representation of the geometry used in the C^3 method developed by Stehly et al. (2008). A boundary of seismic noise sources encloses a network of receivers. The Green's function between the blue receivers R_1 and R_2 is reconstructed by cross-correlating the codas of the Green's functions obtained from cross-correlation of seismic noise records from these receivers and all the yellow receivers S in the network.

1.6 Applications of inter-receiver interferometry

The applications of seismic interferometry span a number of different fields, including crustal seismology, volcano monitoring and industrial exploration. Almost all of these applications take advantage of the fact that inter-receiver interferometry allows real receivers to be converted into virtual sources, hence increasing the number of available sources and possible source-receiver paths.

However, the first examples of Green's function reconstruction from the cross-correlation of diffuse wavefields on Earth were obtained from laboratory experiments using ultrasonic and thermal noise (Lobkis & Weaver, 2001; Weaver & Lobkis, 2001), rather than from seismograms recorded in the natural environment. It was not until 2003 that Campillo & Paul (2003) showed that in the real Earth the Green's function between a pair of receivers can be reconstructed by cross-correlating coda wave signals from an earthquake recorded at the two receivers. Seismic codas are those parts of the seismic signal that emerge after the direct arrivals, as a result of (multiple) scattering of the waves in the subsurface. Since the location of earthquakes on the Earth's surface is inhomogeneous, it may be thanks to the presence of scatterers that wavefields originating from earthquakes become sufficiently diffuse for interferometry to work in practice. By cross-correlating seismic codas of distant earthquakes recorded at a number of seismic stations in Mexico, Campillo & Paul (2003) succeeded in reconstructing the Green's function between various station pairs. These Green's functions displayed both Rayleigh and Love wave signals and were found to agree well with theoretical Green's functions computed along the same paths using a three-layer crustal model.

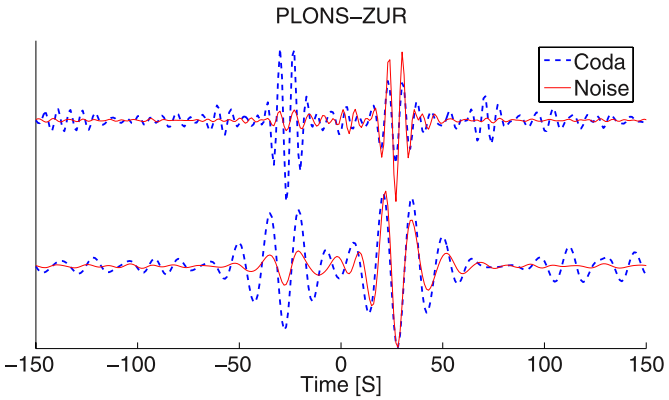

Figure 1.13. Comparison of Green's functions obtained from noise cross-correlation (solid red line) and the C^3 method (dashed blue line) in the period bands of 5–10 s (top) and 10–20 s (bottom). Reprinted from Stehly et al. (2008).

Stehly et al. (2008) developed a technique for Green's function retrieval using correlation of seismic codas obtained in turn by the correlation of seismic ambient noise records. This method can be explained by considering the configuration shown in Fig. 1.12, where R_1 and R_2 are the receivers between which the Green's function is to be calculated. Traditionally, inter-receiver interferometry allows the Green's function between these two receivers to be computed by cross-correlating long records of ambient noise obtained at the two stations. However, although they generally provide a good estimate of the Green's function, the resulting cross-correlations are usually not perfect due to an inhomogeneous distribution of noise sources. In fact, the reconstructed Green's functions may present spurious or non-physical arrivals due to incomplete cancellation upon stacking, and may also be asymmetric between positive and negative times due to the presence of directionality in the noise field. Hence, rather than cross-correlating passive noise or real codas recorded at R_1 and R_2, Stehly et al. (2008) start by computing ambient noise correlations between each of these two stations and a third station S that is varied around a neighbouring station network. The resulting seismograms correspond to those that would be recorded at R_1 and R_2 if a source had been placed at S. For each seismogram from such a receiver S, they then select the time window corresponding to the coda (at positive and negative time) of the Green's function recorded at R_1 and R_2 for a virtual source at S, and compute four cross-correlations (positive-positive, negative-negative, positive-negative, negative-positive times). Finally, these intermediate cross-correlations are separately averaged over all stations S in the network and stacked to obtain the so-called C^3 (Correlation of Coda of Correlation) function.

An example of the application of this technique to records obtained at stations PLONS and ZUR in the Swiss Alps is shown in Fig. 1.13. In this case, since the intermediate positive-negative and negative-positive cross-correlations had a very low signal-to-noise ratio which would not greatly improve the reconstruction of the Green's function, the C^3 function was calculated by stacking only the coda wave correlations for positive and

negative times. For both the 5–10 s period band (top) and the 10–20 s period band (bottom), the C^3 functions present Rayleigh wave arrivals that match those obtained by simply cross-correlating noise records from the two stations. However, the Green's function reconstructed from noise correlations is not symmetric and has a relatively low signal-to-noise ratio, and it would not normally be used in tomography studies. In contrast, the C^3 function is symmetric, and could therefore be used more reliably when performing surface wave tomography. In fact, while the amplitude of noise correlations depends on the distribution of the sources, the azimuthal dependence is eliminated when computing the C^3 function, as the use of coda waves compensates for an anisotropic source distribution. Therefore, Stehly et al. (2008) suggest that this new method has the potential to increase the number of paths contributing to Rayleigh wave tomography, improving the resolution of crustal models.

Since the work of Campillo & Paul (2003) surface wave ambient noise tomography has become common practice. Green's functions are reconstructed from the cross-correlation of ambient noise records (assumed to be diffuse, or coming from an approximately complete boundary of noise sources) for as many inter-receiver paths as possible within a network of receivers. From the resulting cross-correlograms, the surface wave (Rayleigh or Love) group or phase velocities are obtained at different frequencies and used to perform surface wave tomography. As different frequencies are sensitive to seismic velocities at different depths in the Earth (generally higher frequencies oscillate in shallower layers, lower frequencies in deeper layers), it is possible to construct velocity models of the subsurface at a range of depths that depends on the set of frequencies considered. Since in principle this method does not depend on source location but only on the location of the receivers, it is particularly useful in aseismic regions where traditional tomography using teleseismic earthquake sources is not able to provide sufficiently high resolution.

In 2005 both Shapiro et al. (2005) and Sabra et al. (2005) produced velocity maps of California which agreed well with the known regional geology (e.g., Fig. 1.14) using the correlational method. Ambient noise surface wave tomography has since been applied successfully to Europe (Yang et al., 2007), the Iberian Peninsula (Villaseñor et al., 2007), Iceland (Gudmundsson et al., 2007), Italy (Li et al., 2010a), Australia (Rawlinson et al., 2008; Arroucau et al., 2010; Saygin & Kennett, 2010), New Zealand (Lin et al., 2007), South Africa (Yang et al., 2008), China (Zheng et al., 2008; Li et al., 2009; Zheng et al., 2010), South Korea (Cho et al., 2007), the United States (Bensen et al., 2008; Liang & Langston, 2008; Lin et al., 2008), the Tibetan Plateau (Yao et al., 2006, 2008; Li et al., 2009, 2010b), the Alps (Stehly et al., 2009) and Scotland (Nicolson et al., 2012). In addition, by performing surface wave ambient noise tomography at the Piton de la Fournaise volcano, Brenguier et al. (2007) showed that this technique can be used to image volcanic edifices.

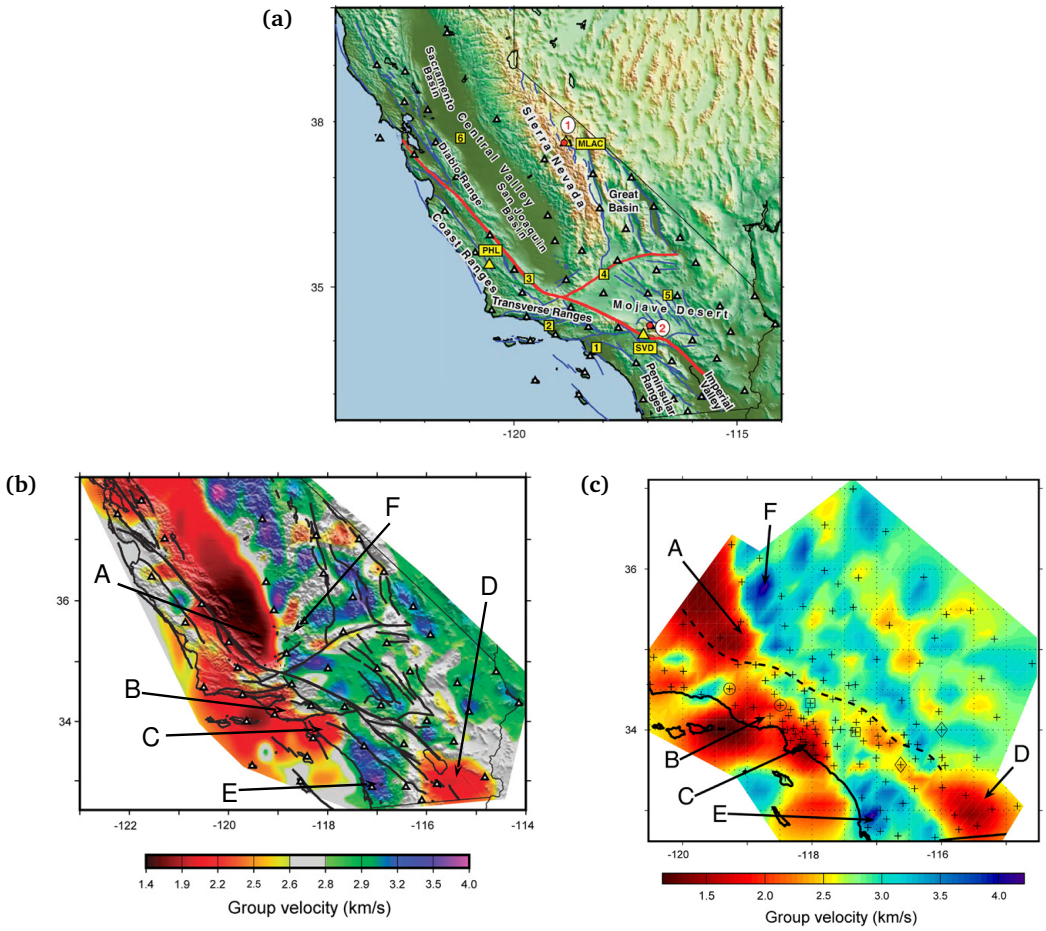

Figure 1.14. (a) Reference map of California. Group-velocity maps obtained from ambient noise tomography by (b) Shapiro et al. (2005) and (c) Sabra et al. (2005). In (a) the yellow squares with digits indicate the following features: (1) Los Angeles Basin, (2) Ventura Basin, (3) San Andreas Fault, (4) Garlock Fault, (5) Mojave shear zone, and (6) Stockton Arch. In (b) and (c) the letters indicate the following features: (A) San Joaquin Valley, (B) Ventura basin, (C) Los Angeles basin, (D) Salton Sea, (E) Peninsular Ranges, (F) Sierra Nevada. (a) and (b) from Shapiro, N.M., Campillo, M., Stehly, L., Ritzwoller, M.H., 2005. High-Resolution Surface-Wave Tomography from Ambient Seismic Noise. Science, 307 (5715), 1615–1618. Reprinted with permission from AAAS. (c) Modified with permission from Sabra et al. (2005).

In industrial exploration, some of the first applications of seismic interferometry were to perform seismic imaging and redatuming of sources to the positions of receivers. Schuster (2001) and Schuster et al. (2004) showed that by cross-correlating traces recorded in the configuration in Fig. 1.15(a) from either source, that data could be redatumed to the case where a virtual source was at the location of receiver R_1 and the resulting trace could be migrated to find the location of the reflector. They also explained how the data from a source in the lower layer as in Fig. 1.15(b) could either provide a receiver function by cross-correlating S and P waves at R_1 and R_2 which can then be used to image the reflector, or by cross-correlating P waves at each receiver the resulting time series can be used to image the source. Schuster et al. (2004) also apply interferometric

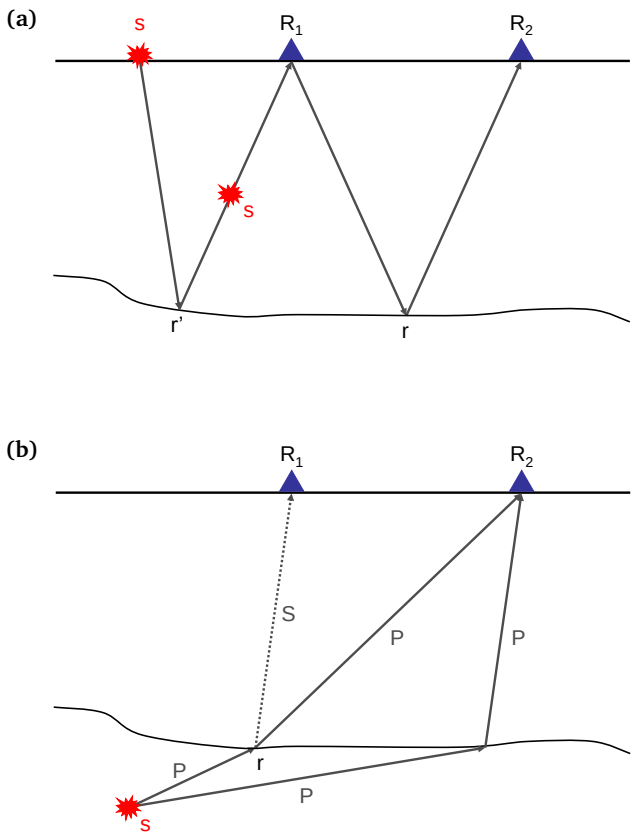

Figure 1.15. Different geometries for cross-correlation in interferometric/daylight seismic imaging: (a) cross-correlation of data recorded at receivers R_1 and R_2 from either source gives the trace that would be recorded at R_2 if a source were placed at R_1; (b) cross-correlation of data from a source in the lower layer can be used to image either the reflector or the source. Redrawn after Schuster et al. (2004).

imaging to a number of case studies and show how this method has the potential to image reflectivity distribution and source location from passive seismic data, without knowing either the approximate source location or source wavelet.

Surface wave retrieval from seismic interferometry has also proved useful in industrial exploration settings, where ground-roll (the industrial term for surface waves) often negatively impacts the quality of acquired seismic data. In industrial settings, ground-roll travels within the shallowest layers of the Earth and hence contains no relevant information about deeper layers. Significantly, due to its high amplitude, ground-roll often masks the deeper-reflecting arrivals which are of interest in seismic exploration. While ground-roll propagating directly from the source to a receiver is relatively easy to remove using standard frequency-wavenumber (f-k) filters, scattered ground-roll (surface waves that have scattered from heterogeneities in the subsurface) is particularly difficult to remove because it may occupy the same part of f-k space as the body wave reflections or refractions of interest.

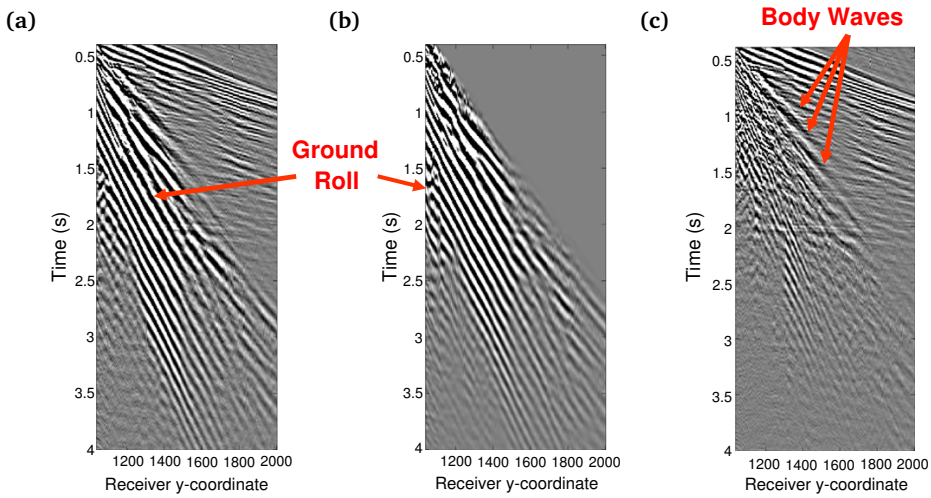

Figure 1.16. Example of scattered ground-roll removal through seismic interferometry. (a) Raw data. (b) Ground-roll predicted from seismic interferometry. (c) Data obtained by subtracting the adaptively filtered ground-roll obtained through seismic interferometry from the raw data. Modified after Halliday (2010).

Curtis et al. (2006), Dong et al. (2006), and Halliday et al. (2007); Halliday et al. (2010b) use cross-correlational and convolutional interferometry to predict scattered surface waves between receiver locations within an industrial seismic data set. For sources with neighbouring receiver locations this prediction may be adaptively subtracted from real-source to receiver records, leaving the body wave energy untouched. Their method allows better quality data to be obtained, as it successfully attenuates the effects of ground-roll while preserving the reflection signals. An example of this technique is given in Fig. 1.16 (Halliday, 2010): the scattered surface waves predicted from seismic interferometry are shown in (b); these signals, after being adaptively filtered, are subtracted from the raw data in (a), giving the cleaner data set shown in (c) in which body waves are clearly visible.

However, the application of seismic interferometry in the industrial domain is not restricted to the removal of surface waves. From the principles of time-reversed acoustics, Bakulin & Calvert (2004); Bakulin & Calvert (2006) developed a method that allowed them to image below the complex surface overburden by turning real downhole receivers into virtual sources. Their so-called *virtual source method* (VSM) is illustrated in Fig. 1.17: by cross-correlating the signals recorded at two different downhole receivers in a near-horizontal well, one of the receivers is turned into a virtual source, whose signal is recorded at the other receiver. Hence, many of the distortions caused by the complex near-surface are eliminated, providing much cleaner and distortion-free data, without any knowledge of the complex overburden.

Mehta et al. (2007) show that this method can be improved significantly by cross-correlating wavefields that have been decomposed into up- and down-going components prior to interferometry. Correlating the downwards-propagating field at one location with

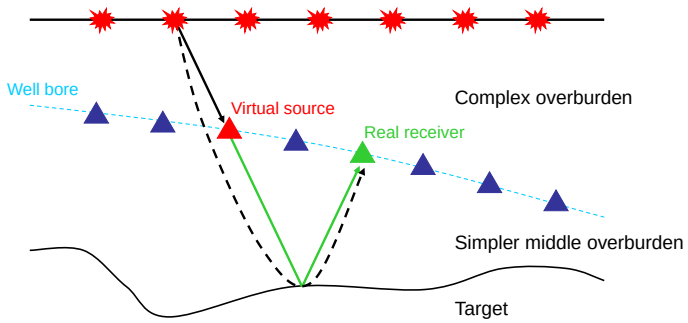

Figure 1.17. Geometry of the so-called virtual source method of Bakulin & Calvert (2006). Receivers are located in the borehole, and record both the down-going wavefield through the complex overburden and the up-going reflected wavefield. By cross-correlating the waveforms recorded at two receivers, one receiver (red triangle) is turned into a virtual source, whose signal (green line) is recorded at the other receiver (green triangle).

the upwards-propagating part at another location eliminates many of the non-physical arrivals that otherwise occur. Bakulin et al. (2007) and Mehta et al. (2008) suggest how the VSM may also be used as a time-dependent reservoir monitoring technique thanks to its ability to eliminate the effect of temporal variations in the overburden.

Another application of inter-receiver interferometry in exploration settings is the method of *interferometric velocity analysis* (King et al., 2011), which allows layer velocity and thickness to be retrieved using non-physical as well as physical energy. The method is presented and applied in an acoustic velocity model using cross-correlational interferometry, although it could just as easily be applied with interferometry by deconvolution. The method uses an acquisition geometry consisting of an array of sources and receivers such as that shown in Fig. 1.18(a) for a marine setting. Cross-correlations are computed for each source position using the approximate acoustic interferometric integral equation of Wapenaar & Fokkema (2006) (equation (1.16)), and the resulting traces are sorted into a correlation gather (like that in Fig. 1.9(b)). When each Green's function in the integral is considered as the sum of a direct and reflected component, a sum of four terms is obtained from equation (1.16), similarly to the case described by Snieder et al. (2006). Among these four terms, interferometric velocity analysis makes use of term $T4$, which is obtained from the cross-correlation of multiply-reflected waves, having the same (Fig. 1.18(b)) or different (Fig. 1.18(c)) numbers of bounce points from the reflector, at both receivers. King et al. (2011) call energy located to the left of the stationary points indicated by the green arrows in Fig. 1.18(c) *non-physical* (np) *energy*, since from an interferometric point of view it contains no stationary points and hence does not contribute to the physical energy that would propagate from one receiver location to the other. They use this non-physical energy to constrain layer thickness and root-mean-square (rms) velocity.

In the 1-layer case, traveltime difference curves between waves recorded at two receivers (receiver 1 and receiver 151) are calculated for different layer depths (D_1),

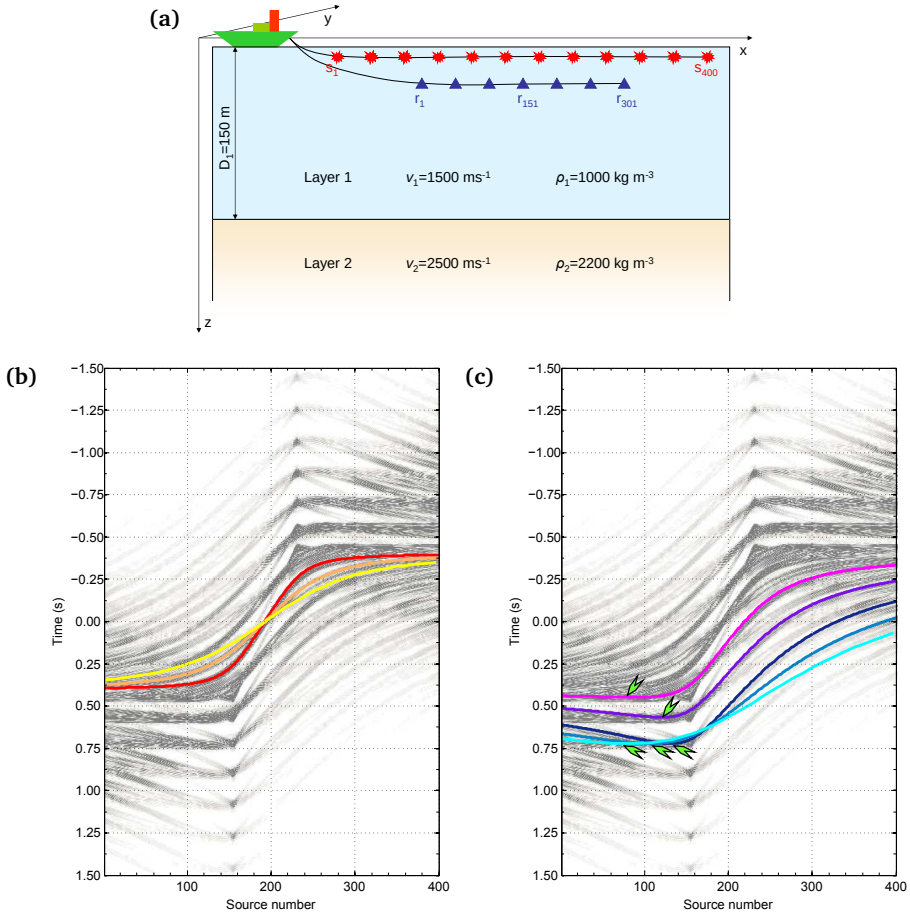

Figure 1.18. (a) Schematic illustration of the 1-layer model used by King et al. (2011) for interferometric velocity analysis. Correlation gathers between receiver 1 and receiver 151 and traveltime curves of reflected waves having (b) the same and (c) a different number of bounce points. Plots courtesy of Simon King.

velocities (v_1) and number of bounce points at the interface. The coherency between the calculated traveltime difference curves and the curves in the correlation gather is assessed using the semblance measure (Neidell & Taner, 1971). Fig. 1.19 shows velocity-layer thickness spectra computed up to the 3rd order multiple using (a) all 400 sources, and (b) only the first 80 sources which are all located at far offsets from both receivers. Both spectra provide a layer thickness and velocity value which is close to the actual value (shown by the arrow). However, King et al. (2011) show that the maximum coherency value for 80 sources is three times larger than that for 400 sources, and suggest how better velocity and layer thickness estimates can therefore be obtained by using fewer sources that provide only non-physical arrivals.

King et al. (2011) then repeat the same procedure for a multi-layer model. In this case, they suggest computing and subtracting terms $T1$, $T2$ and $T3$ from the correlation gather, in order to be left purely with term $T4$. A 'layer-stripping' approach is then used in order to obtain estimates of the rms velocity and thickness of each layer. With this

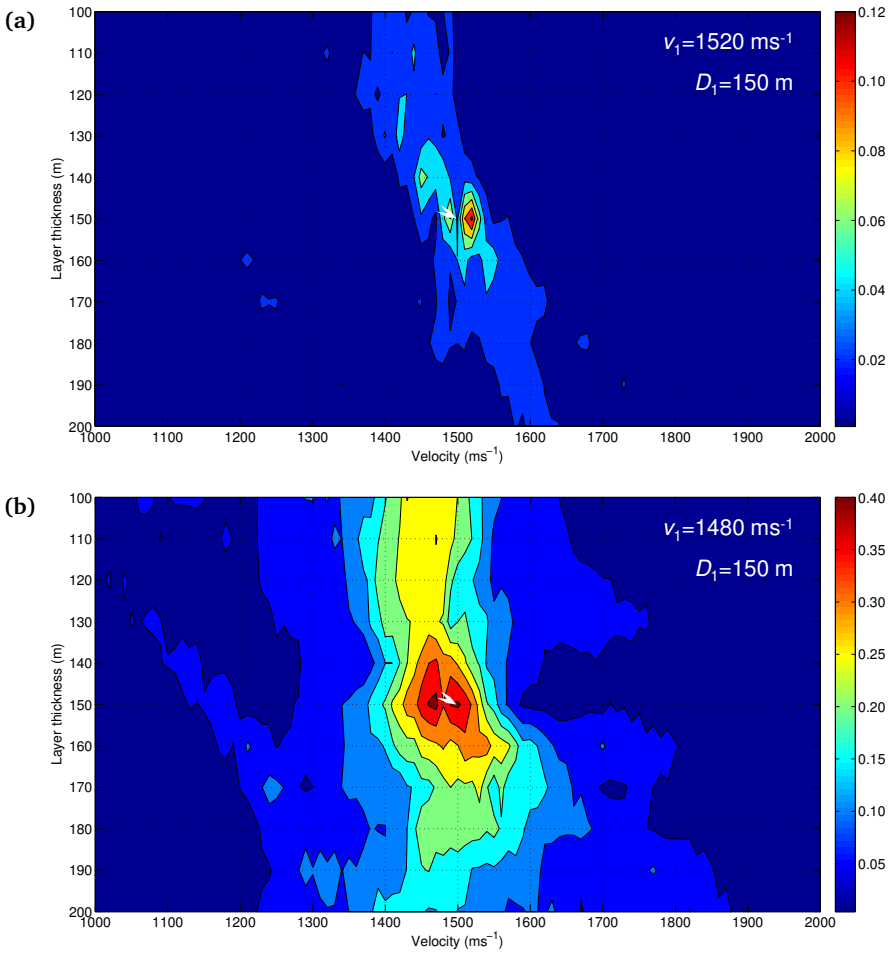

Figure 1.19. Velocity-layer thickness spectra computed up to the 3rd order multiple for the 1-layer model shown in Fig. 1.18(a), using (a) all 400 sources, and (b) only the first 80 sources. The values of semblance are given by the colour scales on the right of the plots; white pointers indicate the true layer thickness and velocity, while the root-mean-square velocity and layer thickness values with higher coherency are indicated in the top-right corner. Plots courtesy of Simon King.

technique, rms velocity and thickness are obtained first for the top layer, by using the same method as for the 1-layer case, and then progressively for each deeper layer in turn, by using the results obtained for the layers above to 'strip-off' their effects. Hence, compared to traditional velocity analysis, which may wrongly treat multiples as primaries, interferometric velocity analysis presents several advantages: multiples are correctly handled and used constructively in order to retrieve information on the subsurface, rather than being removed from the data; in addition, since only two receivers can be considered at a time, the procedure can be repeated for many receiver pairs, providing a large number of estimates of layer thickness and velocity. However, as in all layer-stripping methods, errors during the initial stages may propagate and expand throughout the process, and prior geological knowledge is required in order to constrain the initial velocity and layer thickness values to a plausible range. In addition, the method is not applicable in the case of dipping layers. The important conclusion of this work is

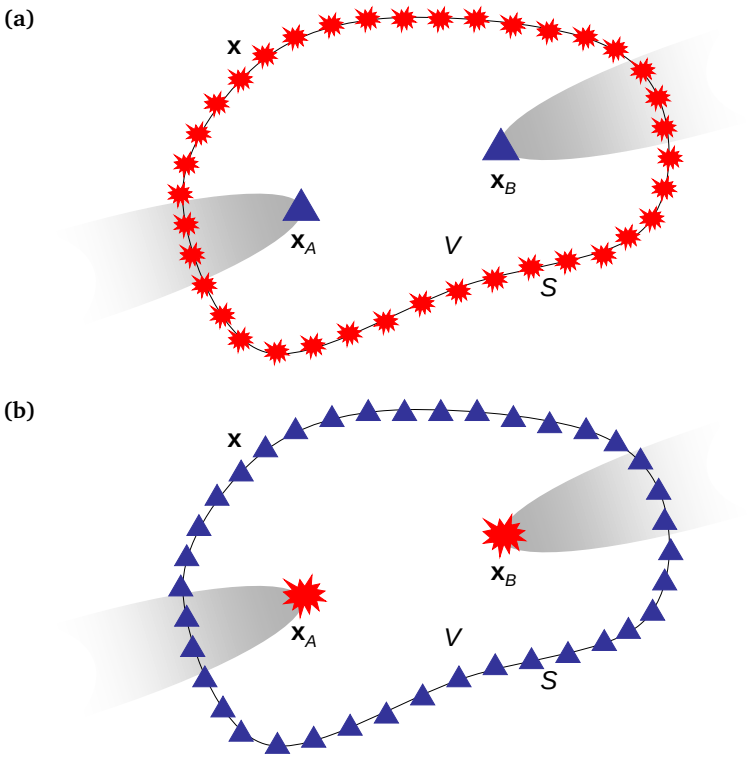

Figure 1.20. Schematic geometries for seismic interferometry. (a) Inter-receiver interferometry by cross-correlation requires receivers to be placed within a boundary of sources. (b) Inter-source interferometry by cross-correlation requires sources to be placed within a boundary of receivers. In both cases, the stationary-phase approach shows that the Green's function can be approximated by only considering boundary sources (receivers) located along the extension of the line connecting the receivers (sources) – within the shaded areas.

therefore that in some situations so-called non-physical energy may contain more information about the subsurface than physical energy.

1.7 Inter-source interferometry

The theory of inter-source interferometry arises directly from that of inter-receiver interferometry, by applying source-receiver reciprocity (equation (1.13)) to the interferometric integrals in Section 1.5.2 (Curtis et al., 2009). The starting points in the derivation are the source-receiver geometries shown in Fig. 1.20 and the interferometric integral by van Manen et al. (2005); van Manen et al. (2006), for either the acoustic (equation (1.14)) or the elastodynamic (equation (1.17)) case.

Consider the geometry shown in Fig. 1.20(a): two receivers, located at $\mathbf{x}_A$ and $\mathbf{x}_B$, are surrounded by a boundary of sources $\mathbf{x}$ on S, and the shaded areas highlight those sources contributing constructively to the interferometric integral, as demonstrated by Snieder (2004). According to source-receiver reciprocity, the acoustic signal recorded at $\mathbf{x}_A$ ($\mathbf{x}_B$) for a source at $\mathbf{x}$ is equal to the signal recorded at $\mathbf{x}$ for a source at $\mathbf{x}_A$ ($\mathbf{x}_B$): $G(\mathbf{x}_A, \mathbf{x}) = G(\mathbf{x}, \mathbf{x}_A)$

and $G(\mathbf{x}_B, \mathbf{x}) = G(\mathbf{x}, \mathbf{x}_B)$ – equation (1.13). It is therefore possible to interchange sources and receivers and still record the same data. Interchanging sources and receivers results in the geometry in Fig. 1.20(b): two sources located at $\mathbf{x}_A$ and $\mathbf{x}_B$ are surrounded by a boundary of receivers $\mathbf{x}$ on S. Applying source-receiver reciprocity to the interferometric integral equations, the following expressions are obtained in the frequency domain:

$$\begin{aligned} &\check{G}^*(\mathbf{x}_B, \mathbf{x}_A) - \check{G}(\mathbf{x}_B, \mathbf{x}_A) \\ &= \int_S \frac{1}{\rho} \left[\left(\partial_j \check{G}(\mathbf{x}, \mathbf{x}_B) \right) \check{G}^*(\mathbf{x}, \mathbf{x}_A) - \check{G}(\mathbf{x}, \mathbf{x}_B) \left(\partial_j \check{G}^*(\mathbf{x}, \mathbf{x}_A) \right) \right] n_j \, \mathrm{d}S \end{aligned} \tag{1.25}$$

in the acoustic case, and

$$\begin{aligned} &\check{G}^*_{im}(\mathbf{x}_B, \mathbf{x}_A) - \check{G}_{im}(\mathbf{x}_B, \mathbf{x}_A) \\ &= - \int_S c_{njkl} \left[\left(\partial_k \check{G}_{li}(\mathbf{x}, \mathbf{x}_B) \right) \check{G}^*_{mn}(\mathbf{x}, \mathbf{x}_A) - \check{G}_{ni}(\mathbf{x}, \mathbf{x}_B) \left(\partial_k \check{G}^*_{lm}(\mathbf{x}, \mathbf{x}_A) \right) \right] n_j \, \mathrm{d}S \end{aligned} \tag{1.26}$$

in the elastodynamic case (Curtis et al., 2009), where ∂ acts on the receiver coordinate $\mathbf{x}$. In both cases, the reconstructed Green's function corresponds to the signal that would be recorded at $\mathbf{x}_B$, due to a source at $\mathbf{x}_A$, if a receiver, rather than a source, were placed at $\mathbf{x}_B$. Hence, in contrast to inter-receiver interferometry, these two equations allow the Green's function between two sources, $\mathbf{x}_A$ and $\mathbf{x}_B$, to be obtained from wavefields recorded on a surrounding boundary of receivers S, by turning one of the sources into a virtual receiver. In addition, by using the stationary-phase approach as earlier, it can be shown that receivers need not necessarily be placed all along boundary S, but only near the extension of the ray path connecting the sources (shaded area in panel (b)).

Just as inter-receiver interferometry obviates the need for seismic sources in aseismic areas, inter-source interferometry between two earthquake sources allows virtual receivers to be created within seismic areas that may not be well covered by receiver networks (e.g., Central Africa, the Tibetan and Andean Plateaux). What is more, since earthquakes are by definition in the Earth's subsurface, so are the virtual receivers. Curtis et al. (2009) show that the resulting measured seismograms constructed in this way are actually records of the dynamic strain caused by passing waves from the other earthquake (rather than measures of displacement as obtained from normal seismometers). The components of strain measured are precisely those represented in the original earthquake source mechanisms: virtual sensors constructed from thrust or normal fault earthquakes measure the strain difference in the vertical and horizontal plane; those constructed from strike-slip earthquakes measure shear strain in the horizontal plane, and, finally, those constructed from explosions or implosions measure the volumetric expansion or contraction of the subsurface.

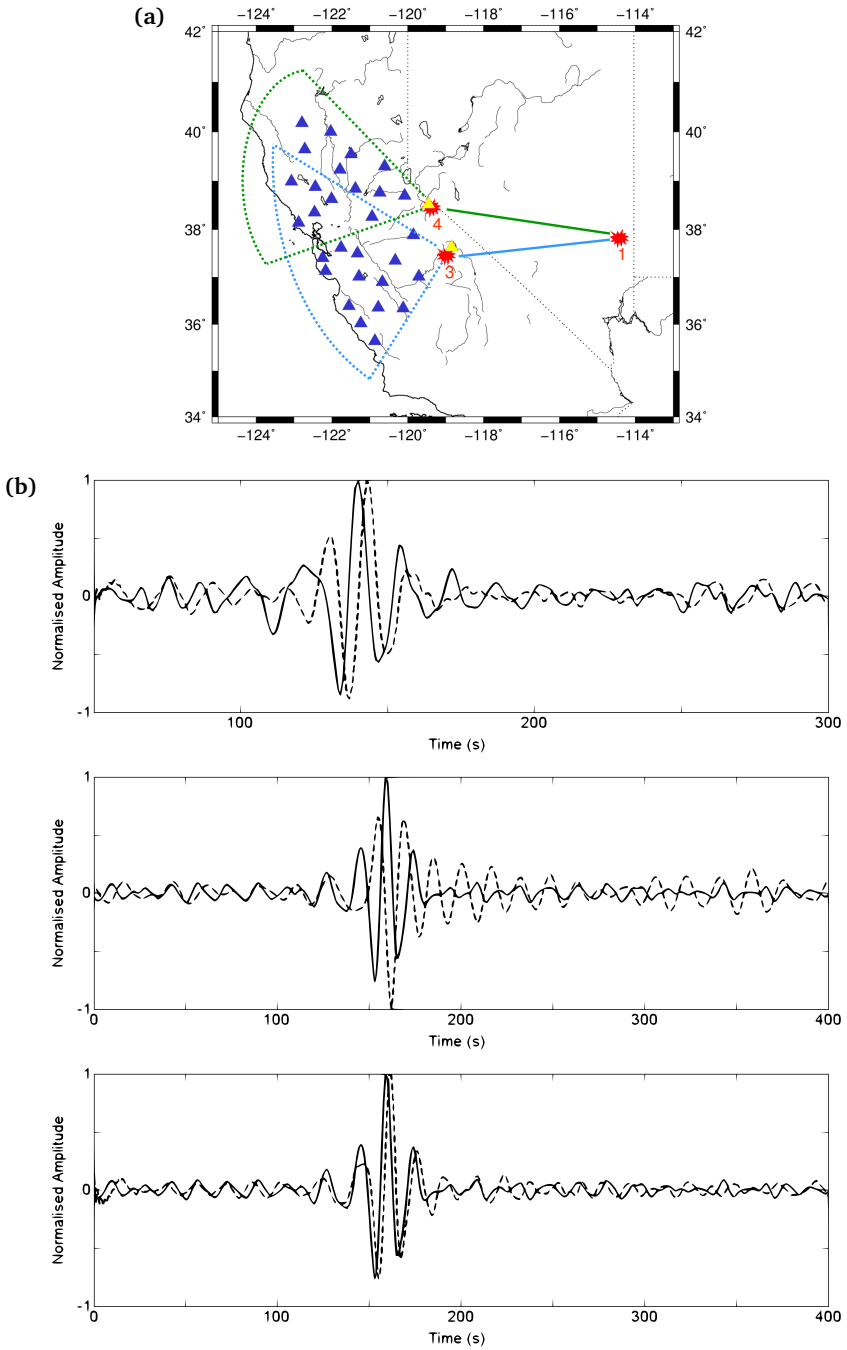

Figure 1.21. (a) Earthquakes (red stars) and seismic stations (blue triangles) used for the application of inter-source interferometry in California. The virtual receivers are indicated by yellow triangles. (b) Comparison of virtual-receiver (solid lines) and real (dashed lines) seismic records: (top) earthquake 1 recorded at sensor 3, (middle) earthquake 1 recorded at sensor 4 (difference between vertical and horizontal strain components), (bottom) earthquake 1 recorded at sensor 4 (approximation to e_{11} component of strain). Map in (a) redrawn after Curtis et al. (2009) using the GMT (Generic Mapping Tools) package; seismograms in (b) courtesy of Heather Nicolson.

Curtis et al. (2009) apply the method of inter-receiver interferometry to data recorded at the USArray and Berkeley seismic networks in California (Fig. 1.21(a)): earthquakes 3 (strike-slip) and 4 (normal) are turned into virtual sensors and used to record other earthquakes occurring in the region; these virtual records are then compared to actual records obtained at recording stations located near the virtual sensors. In the case of earthquake 1, a comparison between the sum of the horizontal strain components (solid line), from the virtual sensor at 3, and the inverted time-derivative of the radial component of velocity from actual recordings (dashed line) is shown in the top image of Fig. 1.21(b): the difference between the surface wave arrival times is less than 5 s for both the main energy envelope and individual phase arrival times, this difference being explained by the difference in location and in temporal response between real and virtual seismometers. The middle image of Fig. 1.21(b) shows a comparison between the real vertical component of particle velocity for event 1 recorded near sensor 4 (dashed line) and the difference between strain components e_{33} and e_{11} from virtual receiver 4: as in the previous case, group arrival times match, while phases do not. However, if the same virtual recording is compared with real measurements of the e_{11} strain component (approximated by the measured, inverted time-derivative of radial particle velocity measurements), an extremely good match is observed (Fig. 1.21(b), bottom image).

Hong & Menke (2006) previously used a related but different method that employs only the coda of the recorded seismograms from the earthquake pair. Similar to Campillo & Paul (2003) they appeal to the diffuse-wavefield (highly scattered) version of interferometric theory rather than to the exact representation theorems given above. However, Curtis et al. (2009) show that by using only the coda all of the main, directly-propagating energy between the two source locations is removed, and since the requirement of a strongly scattering medium may not hold this leads to errors in the results (indeed, in a non-scattering medium such a method can not work at all). Hence, using all of the recorded energy including the direct waves, and appealing to the representation theorem approach above appears to be advantageous.

Tonegawa & Nishida (2010) show that the method of Curtis et al. (2009) can also be applied to obtain inter-earthquake *body* waves. Using pairs of events within a subducting slab recorded on a neighbouring dense network of seismometers across Japan, they are able to obtain approximate Green's functions and time-versus-distance relationships for body wave propagation within the slab. This is the first time that recordings have been made on (virtual) seismometers within the subducting lithosphere, and one of the first publications to successfully extract body wave information from interferometric correlations at a regional scale.

Besides its applications in earthquake seismology where it can be used to monitor dynamic strain caused by passing seismic waves, the method of inter-source interferometry is also useful in exploration seismology. For example, active sources in a seismic survey can be turned into virtual sensors, producing many more measurement

locations (Halliday et al., 2010b). Also, the fact that virtual seismometers can also provide non-invasive measurements within the interior of the Earth means that they may be able to be created directly within resource reservoirs in the subsurface without drilling.

1.8 Source-receiver interferometry

The method of source-receiver interferometry arises from a combination of inter-receiver and inter-source interferometry (Curtis & Halliday, 2010b). It allows the wavefield between an actual source and an actual receiver to be reconstructed from only recordings obtained from surrounding boundaries of receivers and sources (i.e., without using the measured source-to-receiver wavefield). In so doing, the real source and the real receiver are converted into a virtual receiver and a virtual source, respectively. While this may not seem to be particularly useful from a practical point of view, we show below that it has several important ramifications.

So far in the geophysical literature, source-receiver interferometric integrals have been derived for the three configurations shown in Fig. 1.22, in both the acoustic and elastic case (Curtis & Halliday, 2010a). The derivations for source-receiver interferometry involve creating a unified representation theorem, obtained from the reciprocity theorems of the convolution and correlation type. In the acoustic case, the following expression is obtained in the frequency domain for the configuration shown in Fig. 1.22(a):

$$
\begin{aligned}
&\hat{\hat{G}}^*(\mathbf{x}_B,\mathbf{x}_A)+\hat{\hat{G}}(\mathbf{x}_B,\mathbf{x}_A)\\
&\quad=\frac{1}{\iota\omega\rho}\int_S\Bigg\{\Bigg[\frac{-1}{\iota\omega\rho}\int_{S'}\Big\{\hat{\hat{G}}(\mathbf{x}',\mathbf{x}_A)\Big(\partial_f\hat{\hat{G}}^*(\mathbf{x}',\mathbf{x})\Big)\\
&\qquad\qquad-\Big(\partial_f\hat{\hat{G}}(\mathbf{x}',\mathbf{x}_A)\Big)\hat{\hat{G}}^*(\mathbf{x}',\mathbf{x})\Big\}n_{j'}\,\mathrm{d}S'\Bigg]\Big(\partial_j\hat{\hat{G}}(\mathbf{x}_B,\mathbf{x})\Big)\\
&\qquad\qquad-\Bigg(\partial_j\Bigg[\frac{-1}{\iota\omega\rho}\int_{S'}\Big\{\hat{\hat{G}}(\mathbf{x}',\mathbf{x}_A)\Big(\partial_f\hat{\hat{G}}^*(\mathbf{x}',\mathbf{x})\Big)\\
&\qquad\qquad-\Big(\partial_f\hat{\hat{G}}(\mathbf{x}',\mathbf{x}_A)\Big)\hat{\hat{G}}^*(\mathbf{x}',\mathbf{x})\Big\}n_{j'}\,\mathrm{d}S'\Bigg]\Bigg)\hat{\hat{G}}(\mathbf{x}_B,\mathbf{x})\Bigg\}n_j\,\mathrm{d}S
\end{aligned}
\tag{1.27}
$$

where $\hat{\hat{G}}(\mathbf{x}_B,\mathbf{x}_A)$ represents the pressure Green's function between an impulsive source at $\mathbf{x}_A$ and a receiver at $\mathbf{x}_B$. Similar expressions can be found in Curtis & Halliday (2010a) for the source-receiver geometries represented in Fig. 1.22(b) and (c).

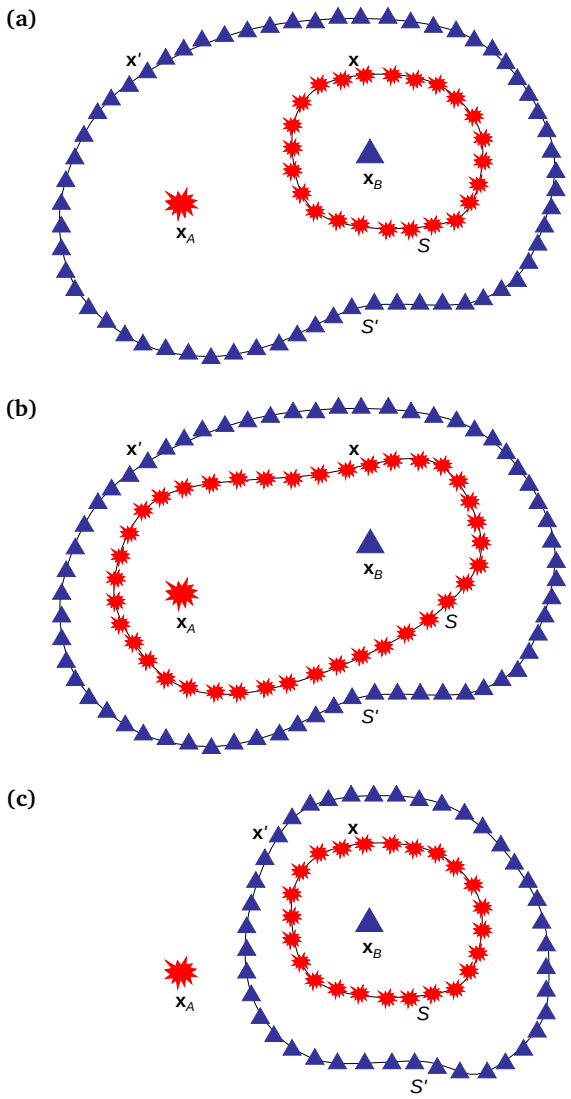

Figure 1.22. Schematic canonical geometries for source-receiver interferometry for which interferometric formulae are given in Curtis & Halliday (2010a). Receivers are represented by blue triangles and sources are represented by red explosions.

Although this expression may look complicated, its meaning can be explained by examining it in conjunction with the corresponding source-receiver geometry. The terms in square brackets use the boundary of receivers just as in equation (1.25) to turn the source at $\mathbf{x}_A$ into a virtual receiver that records each of the boundary sources $\mathbf{x}$ in turn. Cross-correlation is used for the configurations in panels (a) and (b) as the boundary of receivers surrounds all sources, while convolution is used for the configuration in panel (c) as the boundary of receivers does not surround source $\mathbf{x}_A$. Then, in the outer integral, this new virtual receiver is used to construct the Green's function between $\mathbf{x}_A$ and $\mathbf{x}_B$ by using the boundary of sources $\mathbf{x}$ on S, turning $\mathbf{x}_B$ into a virtual receiver, this latter step using equations like equation (1.24), for the geometries in panels (a) and (c), and like equation (1.15) for the geometry in panel (b).

However, dipolar sources (represented by the derivatives of the Green's functions) and closed boundaries of sources and receivers may not always be available in practical applications. Hence, in order to apply these formulae, some approximations may be needed. These approximations may include expressing dipolar sources in terms of monopolar sources ($\mp \imath k G = n_j \partial_j G$) assuming Sommerfield conditions hold (Born & Wolf, 1999), and considering only boundary sources and receivers that are located near the line connecting $\mathbf{x}_A$ and $\mathbf{x}_B$, as stationary-phase analysis shows that these are the ones that provide constructive contributions to the interferometric integral. The resulting simplified equation for the geometry in Fig. 1.22(a) is

$$\hat{\hat{G}}^*(\mathbf{x}_B, \mathbf{x}_A) + \hat{\hat{G}}(\mathbf{x}_B, \mathbf{x}_A) \approx \frac{4k^2}{(\omega\rho)^2} \int_S \int_{S'} \hat{\hat{G}}(\mathbf{x}', \mathbf{x}_A) \hat{\hat{G}}^*(\mathbf{x}', \mathbf{x}) \hat{\hat{G}}(\mathbf{x}_B, \mathbf{x}) \, \mathrm{d}S' \, \mathrm{d}S \tag{1.28}$$

(Curtis, 2009; Curtis & Halliday, 2010a). The method was demonstrated to work well in practice on a test industrial seismic data set by Duguid et al. (2011); indeed, in that application source-receiver interferometry gave improved results compared to inter-receiver or inter-source interferometry.

This new type of interferometry presents several advantages and potential applications compared to the previous two forms, and just as the equations in Curtis & Halliday (2010a) were derived by combining convolutional and cross-correlational interferometry for the geometries shown in Fig. 1.22, similar equations can be derived for many different source-receiver geometries, for deconvolutional interferometry in place of correlational interferometry, and even combining passive and active sources (Curtis & Halliday, 2010a). Examples of possible applications in exploration seismology include the creation of synthetic source-receiver records which were not directly recorded, for instance for the removal of ground-roll from reflection data sets. This application may be useful in cases where the direct recording between $\mathbf{x}_A$ and $\mathbf{x}_B$ is not available, while recordings between $\mathbf{x}_A$ and many other receivers are. For interferometric ground-roll removal, source-receiver interferometry would provide similar surface wave estimates to the inter-receiver method used by Halliday et al. (2007); Halliday et al. (2010b), but with the advantage that receivers would not be required beside each shot location, perhaps making this design more economically viable: Duguid et al. (2011) perform ground roll removal on a seismic data set to reveal underlying scattered arrivals that were otherwise hidden by the directly-propagating surface waves. Also, if real records between $\mathbf{x}_A$ and $\mathbf{x}_B$ were also available, source-receiver interferometry could be used to assess the limitations of seismic interferometry given practical conditions, by comparing the real and virtual records obtained between $\mathbf{x}_A$ and $\mathbf{x}_B$.

In other applications, Poliannikov (2011) shows that, using only receivers in a subsurface well and sources on the surface similarly to Fig. 1.17, inter-receiver interferometry usually only provides top-side reflections for reflectors below the well,

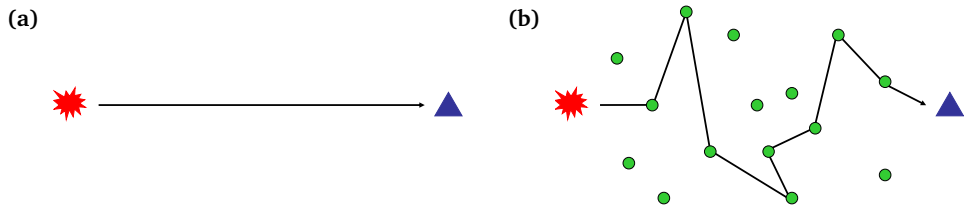

Figure 1.23. Comparison of direct and scattered coda wave raypaths from a source (red explosion) to a receiver (blue triangle). (a) A direct wave follows the shortest path between the source and the receiver. (b) A coda wave travels a longer path due to scattering off heterogeneities (green circles).

whereas a particular application of source-receiver interferometry also provides underside reflections from reflectors above the well. Additionally, King & Curtis (2012) show that the second integration in source-receiver interferometry actually corrects errors (the existence of non-physical energy) made in the first integration (which is equivalent to an application of standard inter-receiver interferometry).

However, perhaps the most fundamental result of source-receiver interferometry theory to-date is that Halliday & Curtis (2010) show that it is directly and analytically related to the imaging theory of Oristaglio (1989), a theorem that describes how many modern imaging algorithms work. This link had been postulated by authors previously (Thorbecke & Wapenaar, 2007; Wapenaar, 2007; Vasconcelos, 2008), but could not be derived analytically because either only a single boundary of sources (Fig. 1.20(a)) or receivers (Fig. 1.20(b)) were considered in inter-receiver or inter-source interferometry, respectively. Imaging theory always uses both sources *and* receivers, hence source-receiver interferometry is the first interferometric form that could be related directly to prove the link. Vasconcelos et al. (2010) use this or similar theory to perform localised velocity analysis in the subsurface using what they call "extended images", and Halliday & Curtis (2010) show precisely how source-receiver interferometry can be thought of as a new, non-linear imaging method. What is more, Halliday et al. (2010a) extend the theory of source-receiver interferometry to body waves, retrieving dynamically-correct interferometric expressions for both reflected and converted P- and S-wave responses between sources and receivers. In doing so, Halliday et al. (2010a) derive a generalised form of the PP + PS = SS equation (Grechka & Tsvankin, 2002; Grechka & Dewangan, 2003), which describes the relationship between PP (i.e., reflected P-wave), PS (i.e., S-wave generating from the reflection and conversion of a P-wave) and SS (i.e., reflected S-wave) waves. These new expressions may find application in acquisition and processing, imaging and inversion of seismic data, allowing a dynamically-correct estimate of SS waves to be made from PP and PS responses alone.

1.9 Coda-wave interferometry

Coda-wave interferometry (CWI) is a technique for subsurface monitoring which makes use of recordings of multiply scattered waves in order to infer time-dependent changes within the medium. While the directly arriving phases only sample the medium along the (perhaps virtual) source-receiver path (Fig. 1.23(a)), coda waves have a much longer propagation path due to multiple scattering (Fig. 1.23(b)) and are therefore sensitive to changes within a much larger volume of the medium. Consequently, if a perturbation in the medium (i.e., a bulk variation in velocity, scatterer positions, etc.) occurs over time, it can often be identified by a change in traveltime of the coda waves when this change is undetectable in the first arrivals (Snieder et al., 2002; Snieder & Hagerty, 2004; Grêt et al., 2005, 2006a,b; Pandolfi et al., 2006; Nagaoka et al., 2010; Zhou et al., 2010).

An example of this application is illustrated in Fig. 1.24, which shows the responses recorded on the Merapi volcano in Java due to an impulse fired by an air gun, as in the study presented by Snieder (2003). The two waveforms, recorded a year apart in time, appear to match when the early arrivals are considered (Fig. 1.24(b)). In contrast, the late coda waveforms (Fig. 1.24(c)) do not match and appear to be shifted in time, as a result of changes that occurred within the interior of the volcano.

The differences in the waveforms recorded before and after the perturbation can be quantified using the normalised cross-correlation coefficient $R(t_S)$ defined by Snieder et al. (2002). The unperturbed wavefield $u^{(u)}(t)$ (i.e., the wavefield before perturbation of the medium) and the perturbed wavefield $u^{(p)}(t)$ (that recorded after perturbation of the medium) can be respectively denoted by

$$u^{(u)}(t) = \sum_T A_T(t) \tag{1.29a}$$

and

$$u^{(p)}(t) = \sum_T A_T(t - \tau_T)\,, \tag{1.29b}$$

where $A_T(t)$ is the wave propagating along scattering trajectory T and the summation signs denote the sum of all waves scattered along all possible paths, t is time and τ_T is the time shift between waveforms propagating along trajectory T before and after the perturbation. The correlation coefficient between the coda of the unperturbed and perturbed wavefields can be defined as

$$R(t_S) \equiv \frac{\int_{t-t_w}^{t+t_w} \left(u^{(u)}(t')\right)\left(u^{(p)}(t'+t_S)\right) \mathrm{d}t'}{\left(\int_{t-t_w}^{t+t_w} \left(u^{(u)}(t')\right)^2 \mathrm{d}t' \int_{t-t_w}^{t+t_w} \left(u^{(p)}(t')\right)^2 \mathrm{d}t'\right)^{1/2}}\,, \tag{1.30}$$

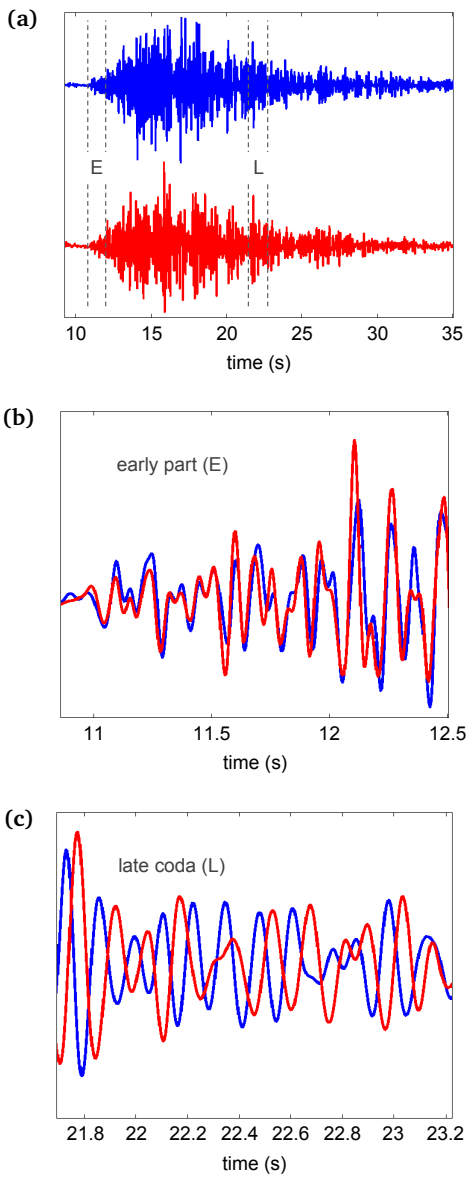

Figure 1.24. Comparison of waveforms recorded at Merapi volcano for the same source and receiver a year apart in time: (a) complete waveforms; (b) early arrivals; (c) late coda. Seismograms courtesy of Roel Snieder.

where the correlation time-window of width $2t_w$ is centred at time t, and t_S is the correlation time-shift between the unperturbed and perturbed waveforms. The correlation coefficient $R(t_S)$ attains its maximum value $R(t_{max})$ when the correlation time-shift t_S is equal to the average time-shift $\langle\tau\rangle$ of the waveforms in the correlation time-window considered:

$$t_{max} = t_S = \langle\tau\rangle \, . \tag{1.31}$$

This maximum correlation value $R(t_{max})$ is related to the variance of the traveltime perturbation σ_τ^2 according to

$$R(t_{max}) = 1 - \frac{1}{2}\bar{\omega}^2\sigma_\tau^2 \,, \tag{1.32}$$

where $\bar{\omega}^2$ is the mean-squared angular frequency of the waves arriving in the time window (Snieder et al., 2002). Hence, from the cross-correlation of coda waves, it is possible to calculate both the mean and the variance of the time-shift before and after the perturbation using equations (1.31) and (1.32).

Snieder et al. (2002) identify three types of perturbations that affect the coda: these include a change in the velocity of the medium, a variation in scatterers' locations, and the displacement of the source position. Each of these perturbation types influences the scattered wavefields in a different way and has a distinct effect on the coda: velocity perturbations can be identified by a linearly increasing magnitude of shift in t_{max}; changes in scatterers' positions instead cause the maximum cross-correlation value $R(t_{max})$ to decrease with time; finally, a variation in source location only affects the path between the source and the first scatterer, and the maximum cross-correlation value $R(t_{max})$ is independent of time.

For a constant velocity perturbation δv and fixed scatterer and source locations, the relative velocity change $\delta v/v$ can be obtained from the ratio of the time-shift $\langle\tau\rangle$, which gives the maximum cross-correlation coefficient, and the centre time t:

$$\frac{\delta v}{v} = -\frac{\langle\tau\rangle}{t} \,. \tag{1.33}$$

If the velocity of the medium does not vary with time but a change in scatterer location occurs, the root-mean-square of the scatterer displacement can be calculated provided the wave velocity v and the transport mean free path l^* (Maret, 1995; Lagendijk & van Tiggelen, 1996) are known:

$$\delta^2 = \left(1 - R(t_{max})\right) \frac{v l^*}{\bar{\omega}^2 t} \,. \tag{1.34}$$

Finally, if the variations in the coda occur as a result of a change in position of the source, the source displacement distance δ can be calculated from

$$\delta^2 = \left(\frac{2v^2}{\bar{\omega}^2}\right)\left(1 - R(t_{max})\right) \,. \tag{1.35}$$

Snieder et al. (2002) demonstrated the applicability of the theory of coda-wave interferometry by conducting laboratory experiments on a granite sample. The waveforms obtained at different temperatures show a decorrelation of the scattered coda with

increasing temperature, which corresponds to a structural change (thermal expansion and potentially cracking) occurring within the sample as the temperature increases.

Grêt et al. (2005) applied coda wave interferometry to seismic records from a number of Strombolian eruptions at Mount Erebus volcano, Antarctica. Their results showed a decreasing correlation of codas following different events as a result of changes in the scattering properties of the volcanic edifice due to an evolution of its structure. What is more, these changes could not be detected by early (more direct) arrivals, proving how the sensitivity of coda waves to structural variations within the medium exceeds that of direct waves.

Brenguier et al. (2008b) successfully combined the methods of seismic interferometry presented in the preceding sections with coda-wave interferometry described here, to create a powerful new monitoring methodology. They applied time-dependent monitoring techniques of coda-wave interferometry to seismic records obtained from virtual sources constructed between receiver pairs at Piton de la Fournaise volcano, La Réunion Island. By using inter-receiver interferometry, they constructed reference Green's functions between all possible pairs of receivers in the network using 18 months of passive noise data. Green's functions along identical paths were then repeatedly computed by cross-correlating seismic noise records from only ten-day-long windows. By moving the windows forward in time through the 18 month period and comparing the windowed Green's function estimates with the reference Green's functions, Brenguier et al. (2008b) succeeded in identifying temporal changes in seismic velocities within the volcanic edifice that resulted from structural changes in the subsurface. In particular, seismic velocities were found to decrease (up to -0.05%) before volcanic eruptions, as a result of dilatation of the edifice due to the increased pressure in the magma.

Using a similar technique based on the cross-correlation of ambient noise records, Brenguier et al. (2008a) were able to detect reductions in seismic velocity around the San Andreas fault zone before the 2003 San Simeon and the 2004 Parkfield earthquakes. The velocity perturbations were found to relax over time to initial levels and to agree with the relaxation curve of along-fault displacement obtained from GPS measurements. From these observations, Brenguier et al. (2008a) suggest that co-seismic velocity changes are related to co-seismic damage in the shallow layers and stress changes at depth, and also to post-seismic stress relaxation. Again, velocity changes of -0.04% to -0.08% were observed robustly, showing the accuracy of this new method.

What is particularly interesting about the above two applications is that the Green's function estimates used for monitoring were fairly poor due to the short time period of noise employed for their construction (10-day intervals in Brenguier et al. (2008b)). Nevertheless, the phase of the signal in the erroneous Green's functions appears stable enough to obtain robust readings of phase changes over time. Since the errors in the Green's functions may be thought of as non-physical arrivals due to an incomplete boundary of noise sources firing within each of the short time periods considered, this

again attests to the fact that non-physical energy contains a great deal of useful information, provided we can work out how to extract it.

Similar studies that applied the method of Passive Image Interferometry to monitor seismic velocity changes in the subsurface were also conducted by Sens-Schönfelder & Wegler (2006), Wegler & Sens-Schönfelder (2007), Ohmi et al. (2008) and Wegler et al. (2009). Similarly, Kraeva et al. (2009) studied changes in Green's functions obtained from cross-correlation of noise recordings, and attributed the seasonal variation pattern to microseismic activity induced by ocean storms in the deep ocean.

1.10 Discussion

While traditional seismology regards background noise as a perturbation to desired recordings of earthquake waves, seismic interferometry allows the retrieval of useful information from ambient seismic waves propagating between two receiver locations without the need for an identifiable active source of energy. The main theoretical requirement for this to be robust across different media with only monopolar or only dipolar noise sources is that the sources are both far from, and completely surround one or both of the receivers in question. However, recent developments have shown how noise sources generally need to be located only along the extension of the ray path connecting the two receiver positions, provided that the medium is not too strongly scattering off this ray path (Snieder, 2004; Snieder et al., 2006).

When noise is poorly distributed or arrives with a significantly biased amplitude from different directions, a number of techniques have been developed to compensate to varying extents for this biased directionality (Curtis & Halliday, 2010b; Douma & Snieder, 2006; Mehta et al., 2007; van der Neut & Bakulin, 2008; Wapenaar & van der Neut, 2010; Wapenaar et al., 2008, 2011). The introduction of seismic interferometry by cross-convolution has also allowed the method to account for attenuation and to be safely applied to media with losses, hence providing more accurate and realistic Green's function reconstructions (Slob et al., 2007; Halliday & Curtis, 2009a).

What is important for tectonophysical applications is that local earthquakes are no longer needed to image the crust and mantle locally. Imaging is now possible between seismic stations, in addition to below individual seismometers as was already possible using conventional receiver functions analysis. Interferometry provides a means to construct seismograms as though local sources of energy existed at receiver locations; hence, it is important that seismometers are moved in networks (not only as individual instruments) to those huge areas of the Earth over which we currently have relatively sparse information about the subsurface due to the low density of both stations and earthquakes (e.g., Africa, Siberia, ocean floors, etc. – Fig. 1.4).

By interchanging sources and receivers, it was shown how seismic interferometry could be used to create virtual seismometers out of earthquakes themselves; since earthquakes are by definition within the Earth's subsurface, so are the virtual seismometers (Hong & Menke, 2006; Curtis et al., 2009). Both Curtis et al. (2009) and Tonegawa & Nishida (2010) have shown that this allows virtual recordings of seismic waves to be made within subducting lithospheric slabs, and Tonegawa & Nishida (2010) used these to estimate body wave velocities within or around the slab. Such localised recordings in the deep subsurface have not previously been possible to observe, and it is likely that future applications of the method will lead to significantly more detailed information about slab and mantle structure and properties. In addition, the ability to use earthquakes as sensors in relatively remote areas such as the Tibetan or Andean plateaux or mid-oceanic ridges where it is difficult to place real sensors may allow more detailed information about those areas to be obtained in future. In Tibet, for example, related techniques of inter-source surface-wave phase velocity analysis have already been used (Romanowicz, 1982; Brandon & Romanowicz, 1986; Curtis & Woodhouse, 1997); interferometric analysis could extend such methods from only kinematic (travel time) information to dynamic information.

Curtis et al. (2009) showed that virtual seismometers constructed from earthquake sources measure components of dynamic strain, rather than displacement as measured by real seismometers. Recent work has shown the potential for large magnitude, remote seismic events that send powerful dynamic wavefields through an area, to change the seismogenic strength of the crust in that area (Taira et al., 2009). The change in strength is shown to be manifest as a higher propensity to earthquake failure. The ability to measure dynamic strain components of passing seismic waves within the subsurface using seismic interferometry is therefore potentially of significant benefit, both to provide quantitative data about the mechanisms of earthquake triggering implied above, and to aid prediction of future propensity to failure.

The ability to reconstruct unrecorded source-to-receiver records using only boundaries of other distant sources and receivers (Curtis & Halliday, 2010b) has several implications as yet unrealised. First, it is in principle possible to synthesise unrecorded seismograms between earthquakes and stations for stations that were not installed at the time of the earthquake. It is therefore possible to create such seismograms for stations installed after the earthquake occurred – for example, rapid-deployment arrays installed immediately after large events. While such arrays are used to locate aftershocks of large events, they are not currently able to be used to locate the main event. If seismograms for the main event can be synthesised for seismometers in these arrays, 'acausal' local event location and characterisation (acausal because the event preceded the array's existence in time) using such arrays may become a practical possibility[2].

[2]Since the time of writing of this article, Curtis et al. (2012) and Entwistle et al. (2015) (of both of which I am a co-author) have developed and tested the method of 'retrospective' seismology in small- and large-scale acquisition scenarios. This method allows previously unrecorded Green's functions to be constructed using the

Another implication of source-receiver interferometry was explored by Halliday & Curtis (2010) who showed that this form of interferometry is directly and analytically related to linearised imaging theorems (Oristaglio, 1989). They showed that a new, non-linear imaging relationship is created directly from source-receiver interferometric theory. This relationship creates a new perspective on subsurface imaging that does not require that waves scatter only once from diffractors as most current imaging algorithms assume, and which is consistent with the Optical Theorem of Physics (see below). The challenge is to translate this relationship into a practical and stable algorithm to construct images. In fact, first steps have already been taken by Sava & Vasconcelos (2009) and Vasconcelos et al. (2009a); Vasconcelos et al. (2009b). They use theory closely related to source-receiver interferometry to perform local velocity analysis around a fixed set of points in a subsurface image. This closes part of the gap between standard velocity analysis or tomography, and imaging theory. Future work will develop new ways to capitalise on the new methods to perform imaging directly[3].

Coda-wave interferometry is now used by many groups around the world to monitor changes in subsurface properties over time (Snieder & Hagerty, 2004; Grêt et al., 2005, 2006a; Pandolfi et al., 2006; Nagaoka et al., 2010; Zhou et al., 2010). This method has been shown to be up to two orders of magnitude more accurate than existing industrial time-lapse monitoring methods (e.g., seismic velocity changes detected by Brenguier et al. (2008a) appear to be robust to less than 0.005%). However, the high accuracy is achieved only for a bulk change in the average background velocity across a region, hence this method currently trades off spatial resolution in favour of increased accuracy of velocity estimates. A future challenge is to develop extensions to the existing methodology that allow this trade-off to be controlled explicitly or implicitly, such that we can choose the level of deterioration in spatial resolution that we are willing to tolerate for a certain increase in accuracy of velocity estimates.

However, what is clear from discussions with practitioners and collaborators around the world (and from our own investigations) is that many CWI studies of seismic properties do *not* show clear temporal changes during active volcanic eruptions, and that such negative results have not been widely published to-date. This 'bias-towards-positivity' creates the potential illusion that this method works well in most cases. It is important that negative results are also analysed and published in future, to clarify whether there is some underlying assumption of the method that is not fulfilled in each particular case, or whether there really is no temporal change in average velocity at the scale of the average seismic wavelengths observed.

principles of source-receiver interferometry. More details on the method and examples of its application are presented in Chapter 3.

[3]Since the time of writing of this article, fully non-linear imaging theorems based on the principles of source-receiver interferometry have been developed by Vasconcelos (2013) in the acoustic domain and by Ravasi & Curtis (2013) in the elastic domain.

There are other areas of Physics that have been extended profoundly by the development of interferometry. Snieder et al. (2008) showed that at a scatterer (diffractor) the cancellation of the $T4$ term when summed with $T2$ and $T3$ in Fig. 1.8 requires that the Generalised Optical Theorem of classical Physics be adhered to at the scatterer. The Generalised Optical Theorem describes how energy is distributed as a function of angle during the diffraction of a wave at the scatterer (Wapenaar et al., 2010b), and Snieder et al. (2008) showed that if one writes out the required cancellation between terms $T2$, $T3$ and $T4$ explicitly as an equation, it can be rearranged to create a proof or a derivation of the optical theorem directly. While Snieder et al. (2008) used this method to re-derive the Generalised Optical Theorem for acoustic waves, Halliday & Curtis (2009b) showed that the same method could be used to derive completely new optical theorems. They thus derived the first such theorem for elastic surface waves, which is also the first to exist for inhomogeneous media (some surface waves only exist in inhomogeneous media). From the structure of such derivations it is also clear that some kind of 'super-generalised' optical theorem that is valid for multiple media and wave types must emerge as a result of this theory in the near future.

The implications for Earth science are important: currently subsurface migration or imaging methods usually employ the so-called Born approximation (which implies that the physics of scattering is linearised and that only single-scattering occurs – see Wapenaar et al. (2010b)). Since true scattering is non-linear, the Born approximation results in incorrect amplitudes in the constructed images. Snieder et al. (2008) showed that interferometry is implicitly consistent with the Optical Theorem and hence with the true, non-linear scattering processes inside the Earth, and since also Halliday & Curtis (2010) showed how interferometry can potentially be used to construct new, non-linear imaging algorithms, such imaging algorithms can also be consistent with the true scattering mechanisms in subsurface diffractors. Thus, as a result of future developments Earth images should become more consistent with physical reality.

Since its origin, the field of seismic interferometry has shown great promise in many areas of seismology. In addition, because its principles are not restricted to seismic waves but can also be applied to electromagnetic, acoustic, seismoelectric and electrokinetic wavefields, and to diffusive fields, the method has promoted the collaboration of researchers from different backgrounds, allowing the rapid development of innovative techniques and applications. It is likely that this cooperation will significantly benefit many of the Earth-related sciences. Hence, the need for this review is clear: to make this, in parts complex field accessible to Earth scientists in general, and to tectonophysicists in particular.

CHAPTER 2

Exact wavefield modelling in scattering acoustic media[1]

Improvements in industrial seismic, seismological, acoustic or interferometric theory and applications often result in quite subtle changes in sound quality, seismic images or information which are nevertheless crucial for improved interpretation or experience. When evaluating new theories and algorithms using synthetic data, an important aspect of related research is therefore that numerical errors due to wavefield modelling are reduced to a minimum. We present a new Matlab code based on the Foldy method that models theoretically-exact, direct and scattered parts of a wavefield. Its main advantage lies in the fact that, while all multiple scattering interactions are taken into account, unlike finite-difference or finite-element methods, numerical dispersion errors are avoided. The method is therefore ideal for testing new theory in industrial seismics, seismology, acoustics and in wavefield interferometry in particular since the latter is particularly sensitive to the dynamics of scattering interactions. We present the theory behind the Foldy acoustic modelling method and provide examples of its implementation. We also benchmark the code against a good finite-difference code. As our Foldy code was written and optimised to test new theory in seismic interferometry, a number of examples of its application to seismic interferometry are also presented, showing its validity and importance when exact modelling results are needed.

[1]This chapter has been published as Galetti et al. (2013c).

2.1 Introduction

Testing new algorithms in acoustics or exploration and earthquake seismology normally requires a synthetic dataset to be created in order to assess the validity of the theory on virtually error-free data. A number of wavefield modelling methods and codes are currently available, allowing variously for different levels of complexity in the velocity model, and providing different levels of accuracy in the construction of direct and multiply-scattered events. Among the most popular modelling techniques, numerical grid- or cell-based schemes such as finite-differences, finite-elements and pseudospectral methods are possibly the most commonly used, enabling the user to model realistic signals or seismograms for either acoustic or elastic wave propagation through media of any desired degree of complexity. These numerical methods use 2D or 3D grids of points to track the evolution of the wavefield in a medium by approximating the time and space derivatives of the equations of motion. As both the medium and the equations are discretised, the accuracy of the results can be improved by decreasing the grid size and increasing the order of derivative approximations, at the expense of memory usage and computation time. Using coarser grids and lower-order derivatives reduces that computational burden, but can introduce numerical errors that may spread throughout any subsequent operation that is performed on the modelled data. In addition, numerical errors may be introduced by linear interpolation between staggered grid cells and by the model having finite dimensions and artificial boundaries, which constrain the size of the velocity grid (and the number of computations required), and which often produce non-physical reflections off the sides of the model in the absence of absolute energy absorption methods at the boundaries.

Given that a compromise between accuracy and computational power is always necessary in practice, when testing the reliability of any data processing or interpretation algorithm it may not be possible to assess whether errors in the results are the product of incorrect theory in the algorithm, or simply arise from the modelling method used. In such cases, a simple, fast and exact modelling scheme is extremely useful in order to reduce the impact of modelling errors on the results and eliminate numerical dispersion from the range of possible causes of errors in the results.

In this chapter, I present an exact method for acoustic modelling of direct and scattered wavefields that uses the theory of multiple scattering (or diffraction) developed by Foldy (1945). Although we do not introduce new scientific concepts herein, we bring together existing theory to produce a modelling code that is exact and can easily be adapted and applied when testing new algorithms in acoustics, seismic imaging, seismology and wavefield interferometry. We give examples of the latter here and in the code package.

The code, written in Matlab, uses multiple scattering theory to model the acoustic wavefield produced by monopole or dipole (spatial derivative) sources as it propagates

through a scattering medium and is recorded by monopole or dipole receivers. Monopole impulse-responses are calculated in the frequency domain using analytical Green's function formulae (given in Appendix B.1), with the option of adding a Ricker wavelet to the source. Dipole (derivative) Green's functions are also evaluated analytically from the frequency-domain spatial derivative of the monopole Green's functions. The Foldy method uses analytic solutions to the wave equation (Green's functions) to propagate energy through the non-scattering background medium. As analytic Green's function formulae exist in various numbers of dimensions, the code can easily perform 1D, 2D or 3D modelling by simply choosing the appropriate formula (all of these are included). A practical limitation of this analytical approach is that the Foldy method and code can only model direct and scattered wavefields in a homogeneous medium of uniform velocity. However, this prevents any numerical error due to ray tracing from propagating across the dataset and allows the modelling results to be exact and free from numerical errors (to machine precision).

The scattered part of the wavefield is modelled by including isotropic point-scatterers (i.e., diffractors that scatter spherically symmetrical waves in the 3D case) in the medium, and computing all possible interactions between them by using an exact solution to the infinite scattering series. Although such infinitely small point-scatterers do not exist in reality, they represent the scattering process while avoiding the introduction of any errors that would be produced if the diffractors had a finite size and physical properties. They can also be used to model more continuous structures like reflectors by placing them close together in a line and, because a relationship exists between wavelength and scatterer cross-section (Foldy, 1945; Snieder, 1988a,b; Groenenboom & Snieder, 1995), point-scatterers may be used to approximate real scattering bodies. In addition, as all possible combinations of scattering interactions, including multiple re-visits of the same scatterer, are taken into account, the Foldy modelling method may open up applications in diffusion, strong (Anderson) and weak localisation (Larose et al., 2004), and in the analysis of multiply-scattered wave paths (Meles & Curtis, 2013a).

Although the Foldy modelling method is not intended to substitute for the more advanced grid- or cell-based modelling schemes for practical applications, it is nevertheless a powerful tool in the acoustician's and geophysicist's arsenals: because it is exact and theoretically error-free, it can be used safely to assess the validity of data processing, imaging and interferometry algorithms, and thus to detect any errors in the theory, before moving on to more complicated and realistic cases that require grid- or cell-based modelling methods, and real data tests and applications.

Within this chapter, we first describe the theory of multiple scattering as developed by Foldy (1945). As the code was created to test new theory in seismic interferometry (and will be useful to others who develop and test interferometry algorithms in future), we then give a brief overview of interferometric theory, and illustrate the application of the code in a number of examples. Finally, we discuss the advantages and limitations of the Foldy

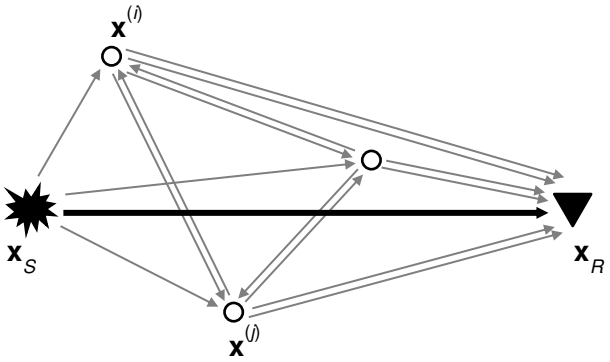

Figure 2.1. The total wavefield reaching a receiver at $\mathbf{x}_R$ from a source at $\mathbf{x}_S$, and scattered by a number of diffractors (e.g., $\mathbf{x}^{(i)}$, $\mathbf{x}^{(j)}$), is given by the sum of a direct term (black solid arrow) and a multiply scattered term (sum of all of the thin grey arrows), as indicated in equation (2.1).

method in comparison with grid-based modelling methods such as finite-differences. The monopole and dipole Green's function formulae that are used in the code are provided in Appendix B.1.

2.2 The Foldy method

Consider a source and a receiver respectively located at position $\mathbf{x}_S$ and $\mathbf{x}_R$ within a homogeneous medium containing a distribution of N scatterers. The total wavefield $\Psi(\mathbf{x}_R)$ recorded at $\mathbf{x}_R$ from the source at $\mathbf{x}_S$ is given by the sum of the direct and scattered wavefield: although the former can easily be calculated as a Green's function from the source to the receiver, the computation of the latter is more complicated as it requires the evaluation of the direct wavefield to each scatterer, wavefield scattering or diffraction, and all possible multiple-scattering interactions of that scattered field. Together these provide the total wavefield radiated by each single scatterer (Fig. 2.1). The total scattered wavefield reaching the receiver is finally obtained by summing the components of the wavefield radiated by each scatterer which then propagate to the receiver location.

By assuming the diffractors are limited to isotropic point scatterers we can reduce the multiple scattering process to a system of linear equations which can be solved numerically (Foldy, 1945; Groenenboom & Snieder, 1995). In the frequency domain, the total wavefield $\Psi(\mathbf{x}_R)$ can be expressed as follows:

$$\Psi(\mathbf{x}_R) = \Psi_0(\mathbf{x}_R) + \sum_{i=1}^{N} \Psi(\mathbf{x}^{(i)}) A^{(i)} G(\mathbf{x}_R, \mathbf{x}^{(i)}) \,. \tag{2.1}$$

Here $\Psi_0(\mathbf{x}_R)$ denotes the direct wavefield from $\mathbf{x}_S$ to $\mathbf{x}_R$, $\Psi(\mathbf{x}^{(i)})$ denotes the total wavefield (direct and scattered) reaching scatterer (i) located at $\mathbf{x}^{(i)}$, $A^{(i)}$ is the scattering amplitude of scatterer (i), and $G(\mathbf{x}_R, \mathbf{x}^{(i)})$ is the full Green's function between scatterer (i) and receiver

$\mathbf{x}_R$. Also, when the wavefield emitted by the source at $\mathbf{x}_S$ is simply a Green's function convolved with a source wavelet $s(\omega)$, the direct wavefield $\Psi_0(\mathbf{x}_R)$ can be expressed as

$$\Psi_0(\mathbf{x}_R) = s(\omega) G(\mathbf{x}_R, \mathbf{x}_S) \,, \tag{2.2}$$

where $G(\mathbf{x}_R, \mathbf{x}_S)$ denotes the full Green's function between source $\mathbf{x}_S$ and receiver $\mathbf{x}_R$.

The scattering amplitude A is a complex number whose real and imaginary components can be determined from the optical theorem following principles of energy conservation. Within our code, we assume energy loss within the medium is only due to the scattering process and ignore the effects of anelastic attenuation. In order to satisfy the requirement of energy conservation, the real and imaginary parts of A are intimately related, and the value of the imaginary component must fall within a specific range – a detailed discussion on this topic is given in Appendix B.2.

The sum in equation (2.1) essentially means that any scattered wave arriving at $\mathbf{x}_R$ must have come from one of the N scatterers; hence it must have arrived at the scatterer ($\Psi(\mathbf{x}^{(i)})$), been scattered (with amplitude and phase scaled by $A^{(i)}$), and must then have propagated to the receiver ($G(\mathbf{x}_R, \mathbf{x}^{(i)})$). The entire series of multiple scattering interactions is therefore included intrinsically within term $\Psi(\mathbf{x}^{(i)})$.

By the same reasoning, the total wavefield $\Psi(\mathbf{x}^{(i)})$ reaching scatterer (i) can be expressed as the sum of the direct and scattered wavefield, where the latter must have been scattered from any and all of the *other* scatterers:

$$\Psi(\mathbf{x}^{(i)}) = \Psi_0(\mathbf{x}^{(i)}) + \sum_{\substack{j=1 \\ j \neq i}}^{N} \Psi(\mathbf{x}^{(j)}) A^{(j)} G(\mathbf{x}^{(i)}, \mathbf{x}^{(j)}) \,, \tag{2.3}$$

where $\Psi_0(\mathbf{x}^{(i)})$ is the direct wavefield from $\mathbf{x}_S$ to scatterer (i), $\Psi(\mathbf{x}^{(j)})$ denotes the total wavefield reaching scatterer (j) located at $\mathbf{x}^{(j)}$, $A^{(j)}$ is the scattering amplitude of scatterer (j), and $G(\mathbf{x}^{(i)}, \mathbf{x}^{(j)})$ is the full Green's function between $\mathbf{x}^{(j)}$ and $\mathbf{x}^{(i)}$.

By swapping the order of terms, expressing the wavefields $\Psi(\mathbf{x}^{(i)})$ and $\Psi_0(\mathbf{x}^{(i)})$ as vectors, and arranging the terms $A^{(j)} G(\mathbf{x}^{(i)}, \mathbf{x}^{(j)})$ into a square matrix of dimension equal

to the number of scatterers, equation (2.3) can be re-written as

$$\begin{pmatrix} \Psi_0(\mathbf{x}^{(1)}) \\ \Psi_0(\mathbf{x}^{(2)}) \\ \dots \\ \Psi_0(\mathbf{x}^{(N)}) \end{pmatrix} = -\begin{pmatrix} -1 & A^{(2)}G(\mathbf{x}^{(1)},\mathbf{x}^{(2)}) & \dots & A^{(N)}G(\mathbf{x}^{(1)},\mathbf{x}^{(N)}) \\ A^{(1)}G(\mathbf{x}^{(2)},\mathbf{x}^{(1)}) & -1 & \dots & A^{(N)}G(\mathbf{x}^{(2)},\mathbf{x}^{(N)}) \\ \dots & \dots & \dots & \dots \\ A^{(1)}G(\mathbf{x}^{(N)},\mathbf{x}^{(1)}) & A^{(2)}G(\mathbf{x}^{(N)},\mathbf{x}^{(2)}) & \dots & -1 \end{pmatrix} \times \begin{pmatrix} \Psi(\mathbf{x}^{(1)}) \\ \Psi(\mathbf{x}^{(2)}) \\ \dots \\ \Psi(\mathbf{x}^{(N)}) \end{pmatrix}, \tag{2.4}$$

where the term on the left-hand side is defined to be a vector $\mathbf{\Psi_0}$ containing the direct wavefields from the source at $\mathbf{x}_S$ to each scatterer, the first term on the right-hand side is matrix $\mathbf{M}$ containing the interaction terms between all scatterers, and the second term on the right-hand side is vector $\mathbf{\Psi}$ containing the total wavefields arriving at each scatterer. In compact form, this equation thus becomes

$$\mathbf{\Psi_0} = -\mathbf{M}\mathbf{\Psi}\,, \tag{2.5}$$

and since both $\mathbf{\Psi_0}$ and $\mathbf{M}$ can be calculated using equation (2.2) and the Green's function formulae in Appendix B.1, equation (2.5) can be solved numerically by matrix inversion:

$$\mathbf{\Psi} = -\mathbf{M}^{-1}\mathbf{\Psi_0}\,. \tag{2.6}$$

Equation (2.6) gives a vector containing the total field that reaches each scatterer. When inserted into equation (2.1), this term can therefore be used to evaluate the total field that reaches the receiver at $\mathbf{x}_R$.

The equations above thus provide an exact representation of the monopole wavefield through a scattering medium of constant background velocity produced by an impulsive source at $\mathbf{x}_S$ and recorded by a receiver at $\mathbf{x}_R$, including all orders of interactions between the scatterers. The only possible sources of inaccuracy in practice are numerical, due to the finite word storage length of a real number, and any approximation in the matrix inversion in equation (2.6). In our code, the inverse problem in equation (2.6) is solved in Matlab using the `mldivide` operation, which seeks a solution by performing a general triangular factorisation that uses LU decomposition of $\mathbf{M}$ with partial pivoting (MathWorks, 2012). If

matrix $\mathbf{M}$ is singular, the solution to equation (2.6) either does not exist or it is non-unique. In all of our experiments, the inverse problem in equation (2.6) was always well-posed. In the case of dipole (derivative) sources and receivers, as used for example in acoustic time-reversal (Cassereau & Fink, 1993; Fink & Prada, 2001; Fink, 2006), in wavefield extrapolation (Berkhout & Wapenaar, 1989; Wapenaar, 1993), in seismic interferometry (Wapenaar, 2004; van Manen et al., 2005, 2006; Wapenaar & Fokkema, 2006), or in some cases in seismic acquisition (Moldoveanu et al., 2007) or imaging (Halliday & Curtis, 2010; Vasconcelos et al., 2009a, 2010), equations (2.1)–(2.3) need to be slightly modified to take into account whether differentiation is performed at the source (to obtain a dipole source) or at the receiver (to obtain a dipole receiver). When dipole sources or receivers are used, the direct wavefield in equation (2.2) becomes

$$\begin{aligned}\Psi_0'(\mathbf{x}_R) &= \partial_m \Psi_0(\mathbf{x}_R) \\ &= s(\omega)\partial_m G(\mathbf{x}_R, \mathbf{x}_S)\,,\end{aligned} \tag{2.7}$$

where $\partial_m G(\mathbf{x}_R, \mathbf{x}_S)$ is the partial derivative of the Green's function between source $\mathbf{x}_S$ and receiver $\mathbf{x}_R$ along the m-direction, evaluated at $\mathbf{x}_S$ for a dipole source and at $\mathbf{x}_R$ for a dipole receiver.

When differentiation is performed with respect to sources, from equation (2.3) we get

$$\Psi'(\mathbf{x}^{(i)}) = \Psi_0'(\mathbf{x}^{(i)}) + \sum_{\substack{j=1 \\ j\neq i}}^{N} \Psi'(\mathbf{x}^{(j)}) A^{(j)} G(\mathbf{x}^{(i)}, \mathbf{x}^{(j)})\,, \tag{2.8}$$

where $\Psi_0'(\mathbf{x}^{(i)})$ is the direct dipole-source wavefield to scatterer (i). The total dipole-source wavefield recorded by receiver $\mathbf{x}_R$ is given by

$$\Psi'(\mathbf{x}_R) = \Psi_0'(\mathbf{x}_R) + \sum_{i=1}^{N} \Psi'(\mathbf{x}^{(i)}) A^{(i)} G(\mathbf{x}_R, \mathbf{x}^{(i)})\,. \tag{2.9}$$

When differentiation is performed with respect to receivers, the total wavefield recorded by a dipole receiver at $\mathbf{x}_R$ is simply given by:

$$\Psi'(\mathbf{x}_R) = \Psi_0'(\mathbf{x}_R) + \sum_{i=1}^{N} \Psi(\mathbf{x}^{(i)}) A^{(i)} \partial_m G(\mathbf{x}_R, \mathbf{x}^{(i)})\,, \tag{2.10}$$

where $\partial_m G(\mathbf{x}_R, \mathbf{x}^{(i)})$ is the partial derivative of the Green's function between scatterer (i) and receiver $\mathbf{x}_R$ evaluated along the m-direction at $\mathbf{x}_R$. Equations (2.7)–(2.10) can therefore be used to solve a similar inverse problem to that in equation (2.6), to obtain the total wavefield from source $\mathbf{x}_S$ to receiver $\mathbf{x}_R$ when dipole or derivative Green's functions are used.

Since analytical Green's function formulae are available in all three dimensions, the calculation of the impulse response between two points is straightforward in 1D, 2D and

3D, as monopole and dipole (derivative) Green's functions can easily be calculated using analytic formulae (see Appendix B.1). Figure 2.2 shows the results of modelling monopole (black solid curves) and dipole (dark grey dashed curves) Green's functions in one, two and three dimensions, with and without a source wavelet of central frequency 10 Hz: while the shape of the analytical Green's functions (Figs 2.2(a), 2.2(c), 2.2(e)) looks somewhat odd (e.g., the Gibbs phenomenon causes 'overshoots' in amplitude at the wavefront arrival time), realistic-looking seismograms (Figs 2.2(b), 2.2(d), 2.2(f)) are obtained when the analytical Green's functions are convolved with a wavelet (Figs 2.2(g) and 2.2(h)). In this example, a total of 4096 frequencies were evaluated in the range 0.02–100 Hz in a medium of uniform velocity 1000 m s^{-1}, and for a source-receiver distance of 200 m. As expected, the arrival times in the monopole Green's functions peak at 0.2 s, while the analytical dipole Green's functions correctly reconstruct the spatial derivatives of the monopole signals (cfr. analytical derivatives obtained using the formulae in Appendix B.1 and numerical derivatives obtained using a finite-difference approximation in Figs 2.2(b), 2.2(d) and 2.2(f)).

2.3 Code description

The Foldy acoustic modelling code *model_gfs_p_scat_acoust.m* that goes along with this chapter is a well commented Matlab script that models direct and scattered wavefields generated by monopole and dipole sources of volume injection and volume injection rate, recorded by monopole and dipole receivers. The code uses the analytical Green's function formulae in Appendix B.1 to compute the impulse response of a medium of constant velocity c, with the option of applying a Ricker wavelet of a certain central frequency as source signature. In the absence of scatterers, the impulse response is evaluated only using the Green's function formulae in Appendix B.1; when scatterers are present, the code uses the above theory of multiple scattering developed by Foldy (1945) to compute the scattered part of the wavefield.

The code consists of a main Matlab function and a number of sub-functions that work in combination:

1. *model_gfs_p_scat_acoust.m*: the main modelling function, models direct and scattered acoustic pressure Green's functions in a homogeneous acoustic medium in the frequency domain, by applying the equations listed in the previous section.

2. *acoustic_p_gfs_direct_f.m*: models direct Green's functions in a homogeneous acoustic medium in the frequency domain. These Green's functions are fed into *model_gfs_p_scat_acoust.m* to evaluate the total wavefield through the medium.

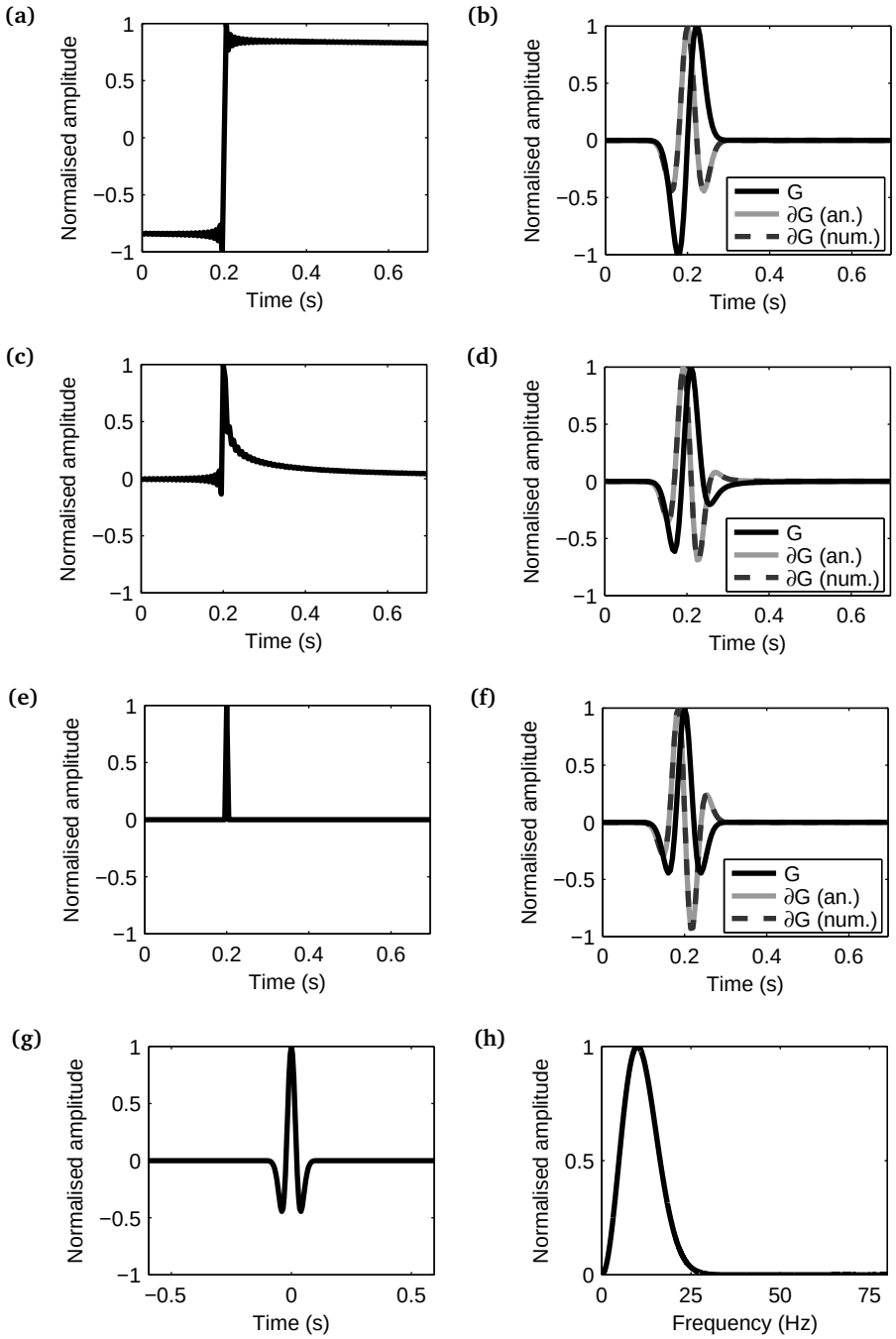

Figure 2.2. Examples of wavefield modelling in (a) 1D, (c) 2D and (e) 3D using analytical Green's function formulae. The medium has velocity 1000 m s^{-1} and the source-receiver distance is 200 m. A wavelet of central frequency 10 Hz (bottom panels: in time domain (g) and frequency domain (h)) is applied to the analytical Green's functions shown in the top-three left panels to give the corresponding seismograms in (b) 1D, (d) 2D and (f) 3D. Derivative Green's functions are calculated analytically within the code (light grey solid traces) and are compared to numerical derivatives (dark grey dashed traces) obtained by placing additional sources along the direction of differentiation and using finite-differences (Richardson's extrapolation) to calculate the derivative. The analytical derivatives obtained with the Foldy code perfectly match the numerical derivatives.

3. *rickerwavl_time.m*: computes a Ricker wavelet of any desired central frequency f_c. The length of the wavelet (in seconds) is given by

$$\frac{n_t}{2f_{max}}, \tag{2.11}$$

where f_{max} is the maximum modelled frequency and n_t is the nearest integer (towards infinity) to the ratio

$$\frac{2f_{max}}{f_c}. \tag{2.12}$$

4. *centerfreqs.m*: creates a centered frequency spectrum from the one-sided spectrum obtained from modelling.

The outputs can be given in either or both of the frequency and time domains. If scattering is included, the wavefields are given as the sum of the direct and scattered wavefields (total wavefield), with the option of including separate direct and/or scattered wavefields in the output. Standard output includes a vector of the actual frequency/time samples for which output values are given, and the actual Ricker wavelet used if a source wavelet is applied.

2.4 Application to seismic interferometry

Seismic interferometry is a relatively new field of research in seismology which has been gaining increasing importance since its mathematical basis was derived early in this millennium. Although the theory was first conceived in 1D by Claerbout (1968), and early results were obtained in helioseismology (Duvall et al., 1993; Rickett & Claerbout, 1999) and from laboratory experiments which used ultrasonic and thermal noise (Lobkis & Weaver, 2001; Weaver & Lobkis, 2001), the application of this technique currently spans a variety of fields, as interferometric theory may be equally applied to acoustic, elastic, electromagnetic, seismoelectric and electrokinetic wavefields. The term *seismic interferometry* refers to a set of methods of Green's function construction through cross-correlation (Wapenaar, 2004; van Manen et al., 2005, 2006; Wapenaar & Fokkema, 2006), convolution (Slob et al., 2007; Slob & Wapenaar, 2007) or deconvolution (Vasconcelos & Snieder, 2008a,b; Wapenaar et al., 2008; Wapenaar & van der Neut, 2010; Wapenaar et al., 2011; Minato et al., 2011) of seismic wavefields. Inter-receiver interferometry by cross-correlation uses a boundary of seismic sources (active sources such as dynamite or passive sources such as microseisms) to construct the Green's function between any pair of receivers located within the boundary as though one of the receivers had actually been a source that was recorded by the other receiver (Fig. 2.3). This has important implications in the study of the Earth's properties, as new information

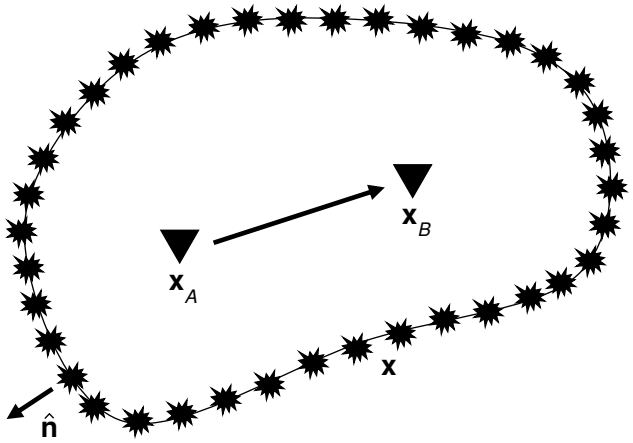

Figure 2.3. Schematic illustration of a typical geometry for correlational seismic interferometry. Two receivers (inverted triangles) are surrounded by a boundary of sources (explosions). At each source position, the boundary normal is denoted by $\hat{\mathbf{n}}$. The method of seismic interferometry uses one of the receivers (e.g., $\mathbf{x}_A$) as a 'virtual' (imagined) source, and constructs the signal (Green's function) as though this source was recorded by the other receiver (e.g., $\mathbf{x}_B$).

about the medium of propagation can be obtained without directly recording the wavefield propagating between the two receiver locations (which would otherwise require a source to be placed at $\mathbf{x}_A$ in Fig. 2.3). Within the Earth sciences, the application of seismic interferometry ranges from industrial exploration to crustal seismology and volcano monitoring: all of these applications take advantage of the fact that, in its various forms, seismic interferometry provides either new or more accessible information about the medium of propagation by converting receivers into virtual (imagined) sources of seismic energy, and vice-versa. This method has been applied to image regional and continental scale seismic velocity structures (Sabra et al., 2005; Shapiro et al., 2005), for volcano or earthquake monitoring (Sens-Schönfelder & Wegler, 2006; Wegler & Sens-Schönfelder, 2007; Brenguier et al., 2007, 2008a,b), for industrial imaging (Bakulin & Calvert, 2004, 2006; Bakulin et al., 2007), noise removal (Curtis et al., 2006; Dong et al., 2006; Halliday et al., 2007, 2008, 2010b; Halliday & Curtis, 2008, 2009a; Duguid et al., 2011), and to model synthetic waveforms (van Manen et al., 2005, 2006, 2007; Halliday et al., 2012).

Interferometry is a good area to test and demonstrate the Foldy code as it is a field in rapid development where new algorithms are being developed monthly (for reviews see Curtis et al. (2006), Wapenaar et al. (2010a); Wapenaar et al. (2010c), Galetti & Curtis (2012)). Because it is exact, the Foldy method of acoustic wavefield modelling provides a good method to test these new algorithms. Acoustic interferometric modelling formulae using wavefield cross-correlation or convolution have so far been derived by van Manen et al. (2005) and Wapenaar & Fokkema (2006) in the inter-receiver case, by Curtis et al. (2009) in the inter-source case, and by Curtis & Halliday (2010a) in the source-receiver case. Further interferometric theory that uses deconvolution or multi-dimensional

deconvolution of wavefields has been derived by Vasconcelos & Snieder (2008a), Vasconcelos & Snieder (2008b), Wapenaar et al. (2008), Minato et al. (2011) and Wapenaar et al. (2011). Because all of these formulae require traces from many combinations of boundary sources or receivers to be added or inverted using either cross-correlation, convolution or deconvolution, any errors present in the modelled data will propagate across subsequent operations. As a consequence, although the interferometric formulae are exact, the practical results of applying seismic interferometry may not be as accurate as the theory predicts.

In the following sections, we show how synthetic data produced with our Foldy Matlab modelling code can be used to test the theory of inter-receiver interferometry. In the first example, the results of interferometry performed using exact and approximate interferometric formulae (see equations (2.13)–(2.14)) are compared. In the second example, we use both the Foldy method and a finite-difference code to model signals from a boundary of sources to two central receivers. By performing interferometry with both datasets, we are then able to estimate the size of the errors produced by the two modelling schemes and to evaluate how errors in the modelling propagate through subsequent operations on the data. The code package also includes examples of inter-source and source-receiver interferometry which use similar geometries to those presented in the following examples.

2.4.1 Inter-receiver interferometry example

Classical inter-receiver interferometry uses a boundary of seismic sources to construct the wavefield that would propagate between the locations of two receivers within the medium of propagation. This is done by cross-correlating the traces recorded at the two receivers from each source on the boundary, and stacking (summing) all of those cross-correlations over the source positions. The result is a two-sided signal, each side representing energy travelling between the two receivers in one or other of the opposite directions. In mathematical form, this process can be represented by the following formula, given in the frequency domain where cross-correlation corresponds to a product when the complex conjugate of one of the factors is taken first (Wapenaar & Fokkema, 2006):

$$\begin{aligned}&\hat{G}(\mathbf{x}_B,\mathbf{x}_A)-\hat{G}^*(\mathbf{x}_B,\mathbf{x}_A)\\&=\int_S \frac{1}{\rho(\mathbf{x})}\left[\left(\partial_j\hat{G}(\mathbf{x}_B,\mathbf{x})\right)\hat{G}^*(\mathbf{x}_A,\mathbf{x})-\hat{G}(\mathbf{x}_B,\mathbf{x})\left(\partial_j\hat{G}^*(\mathbf{x}_A,\mathbf{x})\right)\right]n_j\,\mathrm{d}S\,.\end{aligned}\tag{2.13}$$

Here, $\rho(\mathbf{x})$ is the density of the medium at $\mathbf{x}$, the asterisk * denotes complex conjugation in the frequency domain (equivalent to time-reversal in the time domain, if applied to all terms in the Fourier transform of a time series), ∂_j represents partial differentiation in the

x_j-direction with respect to the source coordinate $\mathbf{x}$, n_j is the component of the boundary normal along the x_j-direction, and $\hat{G}$ and $\partial_j\hat{G}$ represent Green's functions as responses to monopole and dipole sources. Einstein's summation convention applies for repeated indices and the integral over boundary S ensures summation over all boundary sources is performed. The hat $\hat{}$ over the Green's function symbols refers to the notation used in Appendix A.2.2, where a full derivation of equation (2.13) is given.

By assuming a high frequency regime, that the surrounding surface of sources S is a sphere with very large radius, and that no energy scatters back through S once it has left, equation (2.13) can be simplified using the Sommerfeld radiation conditions to eliminate the derivatives, giving (Wapenaar & Fokkema, 2006):

$$\hat{G}(\mathbf{x}_B,\mathbf{x}_A)-\hat{G}^*(\mathbf{x}_B,\mathbf{x}_A)\approx-\frac{2\iota\omega}{\rho c}\int_S\hat{G}(\mathbf{x}_B,\mathbf{x})\hat{G}^*(\mathbf{x}_A,\mathbf{x})\,\mathrm{d}S\,, \tag{2.14}$$

where c is the propagation velocity of the medium and ι is the imaginary unit. The result of either of equations (2.13) and (2.14) is a two sided signal, at positive and negative times: the causal (positive-time) part of the signal represents the Green's function between $\mathbf{x}_A$ and $\mathbf{x}_B$, while the acausal (negative-time) part of the signal represents the negative of the Green's function between $\mathbf{x}_A$ and $\mathbf{x}_B$ (or equivalently, the negative of the Green's function travelling between $\mathbf{x}_B$ and $\mathbf{x}_A$, by acoustic source-receiver reciprocity). Both formulae assume positive volume injection sources are used, as indicated in Wapenaar & Fokkema (2006).

In practical applications, where continuous source boundaries are not available, the integration factor in equations (2.13) and (2.14) can be discretised using a summation over M sources, giving

$$\begin{aligned}&\hat{G}(\mathbf{x}_B,\mathbf{x}_A)-\hat{G}^*(\mathbf{x}_B,\mathbf{x}_A)\\&\approx\sum_{k=1}^{M}\left\{\frac{1}{\rho(\mathbf{x}_k)}\left[\left(\partial_j\hat{G}(\mathbf{x}_B,\mathbf{x}_k)\right)\hat{G}^*(\mathbf{x}_A,\mathbf{x}_k)-\hat{G}(\mathbf{x}_B,\mathbf{x}_k)\left(\partial_j\hat{G}^*(\mathbf{x}_A,\mathbf{x}_k)\right)\right]n_j\,\mathrm{d}S_k\right\}\end{aligned} \tag{2.15}$$

in place of equation (2.13), and

$$\hat{G}(\mathbf{x}_B,\mathbf{x}_A)-\hat{G}^*(\mathbf{x}_B,\mathbf{x}_A)\approx-\frac{2\iota\omega}{\rho c}\sum_{k=1}^{M}\left\{\hat{G}(\mathbf{x}_B,\mathbf{x}_k)\hat{G}^*(\mathbf{x}_A,\mathbf{x}_k)\,\mathrm{d}S_k\right\} \tag{2.16}$$

in place of equation (2.14), where $\mathrm{d}S_k$ is the source sampling interval acting as an extra weighting factor for each source k. Equations (2.15) and (2.16) are normally implemented when transient sources at known positions are used for interferometry, and their application is demonstrated in the following examples (and in all of the other examples in the code package).

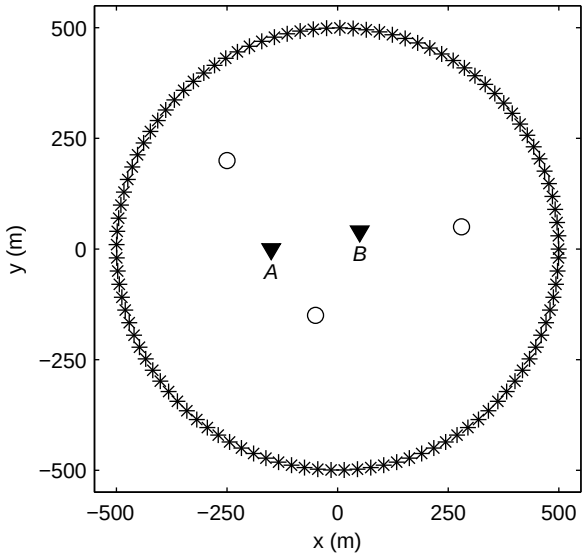

Figure 2.4. Geometry of numerical example with results in Fig. 2.5: two receivers (inverted triangles) and three scatterers (empty circles) are surrounded by a circular boundary of sources (stars). Only every sixth source is shown for clarity.

An example of the use of inter-receiver interferometry to construct the Green's function between two points within a circular boundary of sources (Fig. 2.4) is shown in Fig. 2.5. In this example we highlight the difference in the results of interferometry when the exact interferometric formula including both monopolar and dipolar sources in equation (2.15) (a discretised version of equation (2.13)) and the approximate interferometric formula involving only monopolar sources in equation (2.16) (a discretised version of equation (2.14)) are used. As expected, while the trace constructed using the exact interferometric formula in equation (2.15) (light grey dashed) perfectly matches the true Green's function (black solid), the trace constructed using the approximate formula in equation (2.16) (dark-grey thin solid) presents small errors which are due to the approximation conditions not being completely satisfied (i.e., the radius of the circle has a finite size). The latter also contains a number of artefacts that are non-physical and stationary with respect to source position (e.g., the event at ∼0.12 s). Each of these arrivals is the result of cross-correlation of the scattered monopole wavefields to A and B, and its amplitude is proportional to the energy scattered by the diffractor that produced it (Snieder et al., 2008; Wapenaar et al., 2010b). For the geometry in Fig. 2.4, each scatterer (i) contributes a non-physical arrival at time

$$t_{(i)} = \left| \frac{|\mathbf{x}_A - \mathbf{x}_{(i)}| - |\mathbf{x}_B - \mathbf{x}_{(i)}|}{c} \right|, \tag{2.17}$$

where c is the velocity of the medium and $\mathbf{x}_A$, $\mathbf{x}_B$ and $\mathbf{x}_{(i)}$ are the positions of receiver A, receiver B and scatterer (i), respectively. For the geometry shown in Fig. 2.4 and a background velocity of 1000 m s^{-1}, non-physical arrivals of this origin are expected at

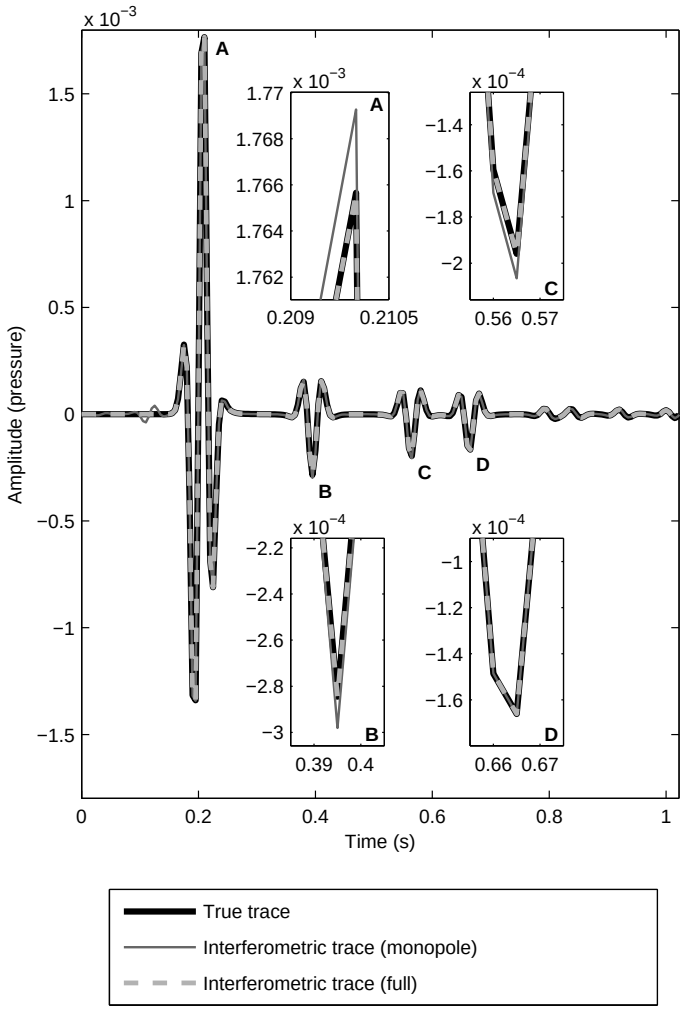

Figure 2.5. True and (positive-time) interferometric traces from receiver A to receiver B in Fig. 2.4 with four magnified panels. The light-grey dashed trace, constructed using the exact interferometric formula in equation (2.15) (discretised version of equation (2.13)), perfectly matches the true trace; the dark-grey thin solid trace, constructed using the approximate interferometric formula in equation (2.16) (discretised version of equation (2.14)), presents some errors which are due to the approximations in that formula. The arrival at ∼0.12 s on the monopole interferometry trace is non-physical, stationary with respect to the sources, and arises from the cross-correlation of scattered waves to A and B. Similarly, the error in the monopole interferometry trace shown in the top-left magnified panel is due to interference with a non-physical arrival of similar origin at ∼0.20 s.

∼0.03 s, ∼0.12 s and ∼0.20 s. Notice that, with the exception of the non-physical arrival at ∼0.12 s, most of the errors incurred by using equation (2.16) are so tiny that the modelling code must be extremely accurate to detect them and hence to test the severity of the approximation.

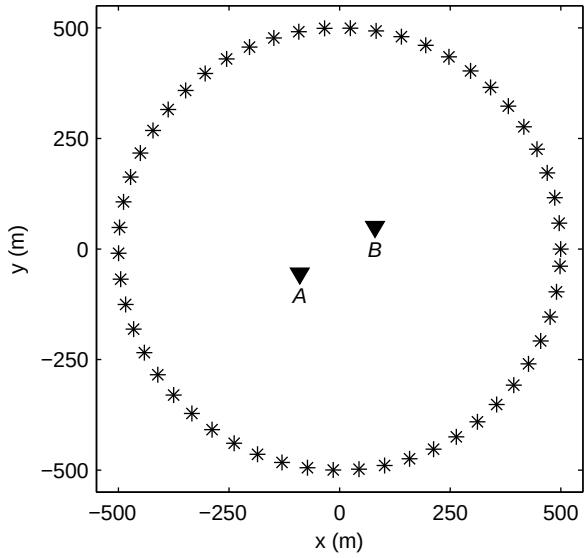

Figure 2.6. Experimental geometry used to obtain results in Figs 2.7 and 2.8: two receivers (inverted triangles) are surrounded by a circular boundary of sources (stars). Only every sixth source is shown for clarity.

2.4.2 Foldy versus FD modelling example

As outlined in Section 2.1, the main advantage of the Foldy method over grid-based schemes such as finite-differences is the fact that it produces an exact construction of direct and scattered events. Since modelling errors can be neglected, any error in the outputs of an algorithm can be attributed to errors in the theory itself rather than to the modelling method. In this section, we show how errors in modelling may propagate across any further operation (e.g., cross-correlation) that is performed on the modelled data.

We used seismic interferometry to construct the Green's function between receivers A and B by using the signals produced by a circular boundary of sources (Fig. 2.6). We produced two synthetic datasets using first our Foldy Matlab code, and second the 2D finite-difference (FD) modelling code *fdelmodc* (courtesy of Jan Thorbecke, TU Delft, and available at `http://software.seg.org/2011/0001`). A grid-spacing of 1 m and a time-step of 0.5 ms were used in the FD modelling. In order to keep the two datasets as consistent as possible, scatterers were not included, only monopole volume-injection sources were used, and for both modelling codes interferometry was performed using the approximate formula in equation (2.16).

The reference Green's functions between A and B, modelled using the two methods, are shown in Fig. 2.7. As illustrated by Thorbecke & Draganov (2011) in a similar experiment, the two Green's functions are perfectly overlapping, with a difference in the peak amplitude of less than 0.02%. However, when the Green's function between A and B is created using seismic interferometry, errors in the interferometric Green's function constructed from the

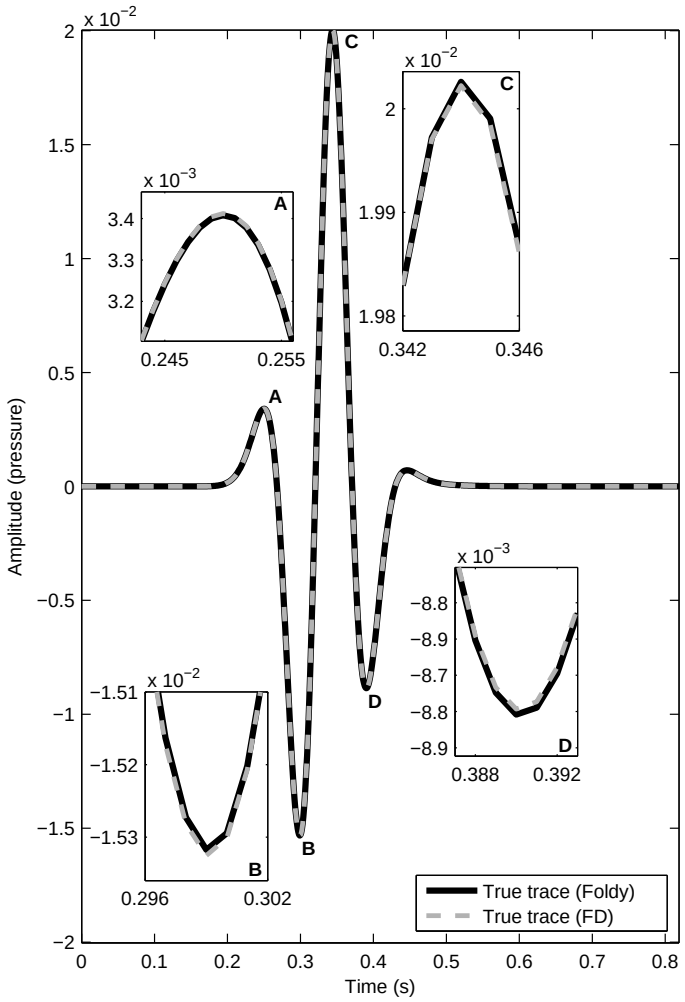

Figure 2.7. True traces from receiver *A* to receiver *B* in Fig. 2.6 evaluated using the 2D analytic Green's function formula used in the Foldy method (black solid line), and a finite-difference method (grey dashed line). The two traces overlap almost perfectly, and differences are only visible in the magnified panels.

FD data become more visible (Fig. 2.8). Since the FD interferometric trace was constructed using the approximate Green's function formula, we are not able to determine whether the errors are caused by compounded effects of small imperfections in the modelled data, or by interferometry itself. In contrast, the Green's function constructed from the Foldy-modelled data closely matches the true Green's function. After observing similar effects in the previous example, we can safely conclude that any error in the interferometric Green's function in the Foldy case is due to the use of the approximate formula in equation (2.16), and not to the use of the Foldy code.

Finally, note that because it does not require a grid, in some cases the Foldy method may be faster than traditional FD modelling. Specifically, given that the modelling function *model_gfs_p_scat_acoust.m* solves the inverse problem in equation (2.6) for each modelled source and frequency, the computation time required by the code is only

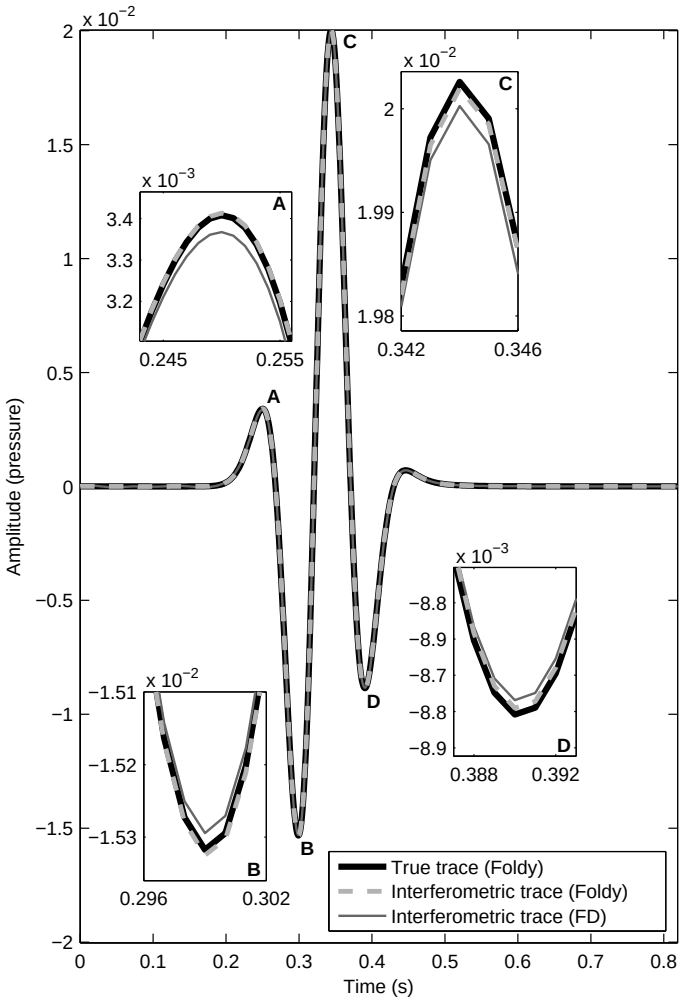

Figure 2.8. True and (positive-time) interferometric traces from receiver A to receiver B. Because interferometry was performed using the approximate interferometric formula in equation (2.14), small errors are visible in the interferometric Green's functions. The errors are larger for the trace constructed using the finite-difference modelled data. Only the availability of the Foldy solution makes clear that these errors are not due to the monopole approximation in equation (2.14), but derive directly from the tiny finite-difference errors observed in Fig. 2.7.

dictated by the complexity of the model (i.e., by the number of scatterers N in the medium) and by the number of modelled sources (n_S) and frequencies (n_f). In terms of computational cost, this implies that the complexity of the problem is $O(n_S \times n_f \times f(N))$, where f is a function that depends on the algorithm employed by Matlab to perform the `mldivide` operation in equation (2.6). While no further details are provided by MathWorks (2012) regarding the specific algorithm used to perform LU decomposition of matrix $\mathbf{M}$ in equation (2.6), the complexity of this operation is directly related to that of matrix multiplication (Bunch & Hopcroft, 1974). As an indication, if the Coppersmith-Winograd algorithm were used for matrix multiplication, then $f(N)$ would equal $N^{2.376}$. In the above examples, the computation of the Green's functions from all sources to the two receivers took ∼352 seconds with *fdelmodc* (in which case sources and

receivers were swapped to speed-up the modelling process) and ∼4.7 seconds with *model_gfs_p_scat_acoust* on a Quad-Core AMD Opteron processor with CPU running at 2.21 GHz. This increase in efficiency may also contribute to more rigorous testing (on more cases/scenarios) of novel algorithms in the future.

2.5 Conclusions

The ability to model exact data is an important requirement when testing new theory and algorithms in acoustics, seismics and seismology. At present, grid-based modelling schemes allow the user to produce synthetic seismograms for wavefields propagating through simple to very complex media. However, both time and space-domain discretisation in such modelling schemes introduce errors that may propagate inside any subsequent operation that is performed on the synthetic data. On the other hand, analytical solutions to the wave equation are not subject to numerical dispersion errors and therefore provide exact results (to machine precision).

In this chapter, I presented a Matlab code that uses analytical solutions to the wave equation in 1D, 2D and 3D to calculate Green's functions in multiply-scattering media. Although it is currently designed to work in the acoustic regime and to output monopole or dipole pressure responses, the theory behind the code could easily be transferred to an elastic modelling scheme. For example, this is possible provided that the scattering amplitudes used account for conversions between modes (e.g., P- and S-wave modes, or higher order surface wave modes). In the case of surface waves, we have also used a modified form of the 2D acoustic code that takes the dispersive nature of surface waves into account (by attributing a different velocity to each modelled frequency), and have found this is a quick and efficient way to model scattered surface waves.

In any case, because it is fast, exact and virtually error-free, this code may be an ideal choice when a synthetic dataset is needed to test the validity of new algorithms using simple geometries. If the theory in the algorithm is valid, one can then safely move on to more complex geometries that require grid-based modelling methods, or to real data tests and applications.

CHAPTER 3

Applied source-receiver interferometry[1]

One of the aims of this PhD thesis is the application of source-receiver interferometry (SRI) to a real acquisition dataset in order to test the accuracy of the method on real data. Within this chapter, I first introduce a standard workflow for SRI and present a synthetic example which uses a canonical geometry of sources and receivers. I then present results obtained when applying SRI to a small-scale exploration dataset recorded at Schlumberger Gould Research (SGR) in 2010. Finally, I provide insight on the method of retrospective seismology when SRI is applied to a large-scale dataset of earthquake and ambient-noise records. The two real-data examples are part of a recently published paper (Entwistle et al., 2015) and are here edited to fit the format of this thesis.

3.1 Theory and method

As explained in Section 1.8, the theory of source-receiver interferometry arises from a combination of inter-receiver and inter-source interferometry. This method allows one to construct the Green's function between a real source and a real receiver using recordings obtained from surrounding boundaries of receivers and sources, and is particularly useful when the true recording between the target source and receiver is not available.

This often occurs in earthquake seismology: following a large earthquake, temporary seismometers are normally deployed near the location of the earthquake's epicentre to measure any aftershocks and subsequent seismic activity. However, since such

[1]Parts of this chapter are edited versions of sections of Entwistle et al. (2015), which has recently been published in *Journal of Geophysical Research* and of which I am a co-author. My contributions to this paper are highlighted within each relevant section.

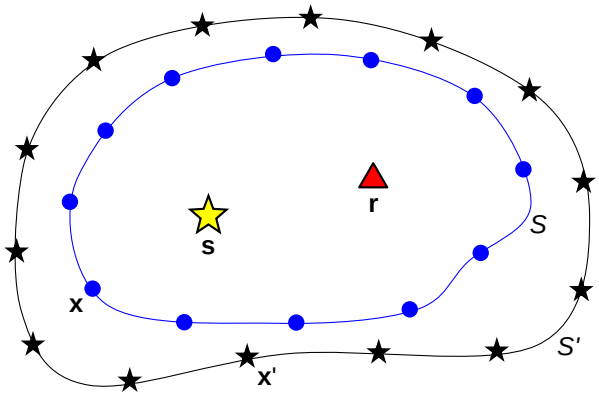

Figure 3.1. Example of a canonical geometry of sources and receivers for correlation-correlation SRI. The target source **s** and target receiver **r** are denoted by the yellow star and the red triangle, respectively. The boundary of sources S' and the boundary of backbone receivers S are denoted by black stars and blue circles, respectively.

seismometers were not installed at the time of the earthquake the temporary array fails to record the main event, and important information on the earthquake's properties tends to be lost. Thanks to SRI, a backbone of (more distant) seismometers which did record the earthquake may be used to redatum the earthquake's energy onto the temporary seismometers, and hence recover the missing seismograms. As an example, Curtis et al. (2012) used SRI to develop the method of *retrospective* seismology, by constructing virtual recordings of two earthquakes in New Zealand on a set of temporary seismometers, some of which were not installed until after the time that the events occurred.

Within this chapter, I present a series of examples of the application of SRI to construct seismograms between a seismic source and a seismic receiver, some of which had not been recorded directly. SRI is a two-step process which involves the consecutive application of inter-receiver and inter-source interferometry to wavefields generated and recorded by a boundary of sources and a boundary of receivers, respectively. A schematic canonical geometry of sources and receivers used for SRI is shown in Fig. 3.1, where a source **s** and a receiver **r** are surrounded by a boundary of receivers **x** on S, which acts as the backbone array, and a boundary of sources $\mathbf{x}'$ on S'. Since this canonical geometry was not previously discussed in Section 1.8, I now describe how it can be used to perform SRI in detail. All of the following equations are given in the frequency domain, and acoustic conditions and positive volume injection rate sources (as in Wapenaar & Fokkema (2006)) are assumed. The Green's functions notation follows that used in Chapter 1 and Appendix A.

In the first stage of SRI, inter-receiver interferometry and the boundary of sources $\mathbf{x}'$ on S' are used to use receiver **r** as a virtual source whose signal is recorded by receivers **x** on boundary S. The exact interferometric formula for inter-receiver interferometry is given in

equation (1.15), and using the notation in Fig. 3.1 becomes

$$\begin{aligned}&\hat{\hat{G}}(\mathbf{x},\mathbf{r})+\hat{\hat{G}}^{*}(\mathbf{x},\mathbf{r})\\&=-\int_{S'}\frac{1}{\iota\omega\rho(\mathbf{x}')}\left[\left(\partial_{j'}\hat{\hat{G}}(\mathbf{x},\mathbf{x}')\right)\hat{\hat{G}}^{*}(\mathbf{r},\mathbf{x}')-\hat{\hat{G}}(\mathbf{x},\mathbf{x}')\left(\partial_{j'}\hat{\hat{G}}^{*}(\mathbf{r},\mathbf{x}')\right)\right]n_{j'}\,\mathrm{d}S'\,,\end{aligned}\tag{3.1}$$

where the double hat $\hat{\hat{}}$ over the Green's function symbols refers to the notation used in Appendix A.2.1, where a full derivation of equation (3.1) is given. For practical applications, this formula is often simplified by assuming high-frequency wave propagation, that the source boundary is large and approximately circular, and that the medium outside this boundary is homogeneous. This gives

$$\hat{\hat{G}}(\mathbf{x},\mathbf{r})+\hat{\hat{G}}^{*}(\mathbf{x},\mathbf{r})\approx\frac{2}{\rho c}\int_{S'}\hat{\hat{G}}(\mathbf{x},\mathbf{x}')\hat{\hat{G}}^{*}(\mathbf{r},\mathbf{x}')\,\mathrm{d}S'\,,\tag{3.2}$$

which corresponds to that in equation (1.16) using the notation in Fig. 3.1.

Second, using the boundary of receivers $\mathbf{x}$ on S, inter-source interferometry is used to turn the virtual source at $\mathbf{r}$ back into a receiver which records the signal from source $\mathbf{s}$. The exact inter-source interferometric formula for negative volume injection sources is given in equation (1.25). When positive volume injection rate sources are used as in Wapenaar & Fokkema (2006), this equation becomes

$$\begin{aligned}&\hat{\hat{G}}(\mathbf{r},\mathbf{s})+\hat{\hat{G}}^{*}(\mathbf{r},\mathbf{s})\\&=-\int_{S}\frac{1}{\iota\omega\rho(\mathbf{x})}\left[\left(\partial_{j}\hat{\hat{G}}(\mathbf{x},\mathbf{r})\right)\hat{\hat{G}}^{*}(\mathbf{x},\mathbf{s})-\hat{\hat{G}}(\mathbf{x},\mathbf{r})\left(\partial_{j}\hat{\hat{G}}^{*}(\mathbf{x},\mathbf{s})\right)\right]n_{j}\,\mathrm{d}S\,.\end{aligned}\tag{3.3}$$

By making the same assumptions as in the inter-receiver case above (for the receiver boundary this time), equation (3.3) can be simplified to

$$\hat{\hat{G}}(\mathbf{r},\mathbf{s})+\hat{\hat{G}}^{*}(\mathbf{r},\mathbf{s})\approx\frac{2}{\rho c}\int_{S}\hat{\hat{G}}(\mathbf{x},\mathbf{r})\hat{\hat{G}}^{*}(\mathbf{x},\mathbf{s})\,\mathrm{d}S\,.\tag{3.4}$$

In the geometry illustrated in Fig. 3.1, the source and receiver boundaries surround both the target source $\mathbf{s}$ and the target receiver $\mathbf{r}$. Since both the inter-receiver and the inter-source steps of SRI involve cross-correlation of wavefields (rather than a combination of cross-correlation and convolution, or convolution only, as discussed in Section 1.8), this type of SRI will be referred to as *correlation-correlation* SRI in the rest of this chapter.

In order to further simplify equations (3.2) and (3.4), we can invoke the stationary phase approximation of Snieder (2004) and use only a subset of boundary sources and receivers, provided that the medium is not too strongly scattering. These boundary sources

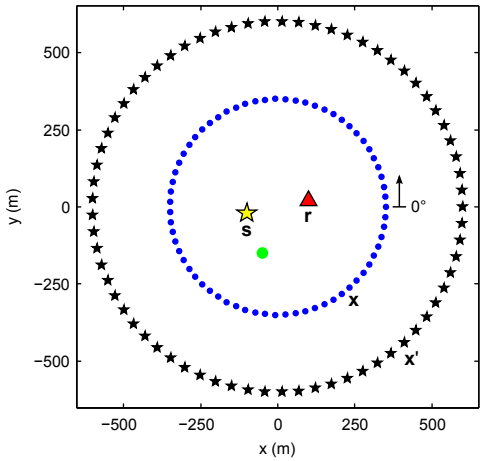

Figure 3.2. Acquisition geometry for the synthetic SRI experiment. The target source **s** (yellow star) and the target receiver **r** (red triangle) are surrounded by a circular boundary of 201 receivers (blue circles) and a circular boundary of 345 sources (black stars). A point-scatterer is denoted by a green circle. The arrow denotes the starting point from which the position of the boundary receivers is measured (i.e., the receiver angle in the gathers in Fig. 3.3). Note that only every fifth source and every third receiver on the boundaries are shown for clarity.

and receivers lie within regions of the boundaries where the phase of the integrands in equations (3.2) and (3.4) is stationary, and are located approximately along the extension of the line connecting **s** and **r** (Fig. 1.20). In addition, boundary sources $\mathbf{x}'$ need not be active seismic sources but can be mutually uncorrelated noise sources, which reduces equation (3.2) similarly to equation (1.19).

3.2 Synthetic experiment

In this section I present a simple synthetic 2D example of SRI using a dataset generated with the exact Foldy modelling code (Chapter 2) in a medium with a single isotropic point-scatterer. The acquisition geometry is shown in Fig. 3.2: a boundary of 345 sources (black stars) and a boundary of 201 receivers (blue circles) surround the target source **s** (yellow star), the target receiver **r** (red triangle) and a point-scatterer (green circle). Using the Foldy modelling code, monopole Green's functions from each source to each receiver were modelled by evaluating 256 frequencies in the range 0.39–100 Hz in a medium of uniform velocity 1000 m s^{-1}, and applying a zero-phase Ricker wavelet with central frequency 15 Hz. SRI was then performed in two separate steps by applying equations (3.2) and (3.4).

In the first step of SRI, inter-receiver interferometry was performed to construct Green's functions between receiver **r** and all receivers on boundary S according to equation (3.2). The receiver gather obtained from interferometry is shown in Fig. 3.3(a): as expected, since the source boundary completely encloses all receivers, both causal and acausal inter-

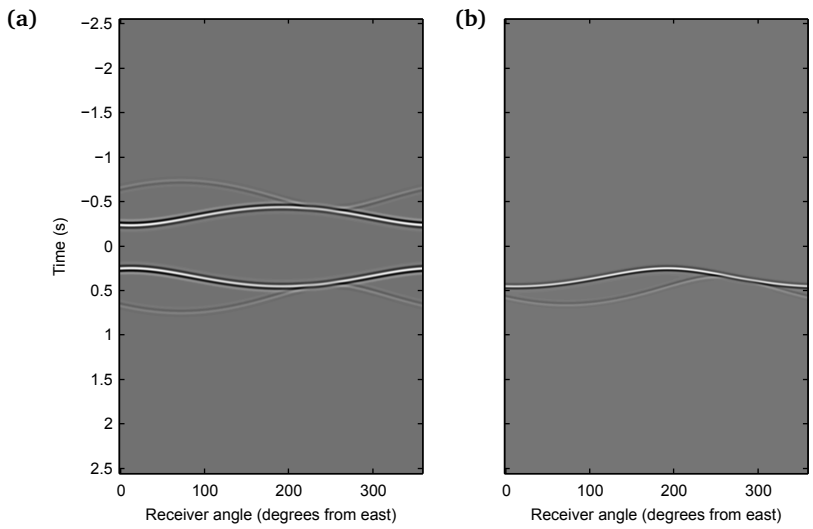

Figure 3.3. Receiver gathers for (a) the inter-receiver interferometric traces from receiver **r** to all receivers on boundary S, and (b) the modelled traces from source **s** to all receivers on boundary S. The receiver angle is measured anticlockwise from the easternmost receiver as indicated by the arrow in Fig. 3.2.

receiver Green's functions are recovered, and the direct and scattered arrivals can clearly be identified. Since the second step of SRI (equation (3.4)) only requires a one-sided Green's function between **r** and **x**, we cut the two-sided Green's functions at 0 seconds and only retained the causal part for the inter-source step of SRI.

Inter-source interferometry was then used to construct the Green's function between source **s** and receiver **r** according to equation (3.4). This involved cross-correlating the causal part of each trace in the inter-receiver gather in Fig. 3.3(a) with the corresponding trace in the receiver gather modelled from source **s** (Fig. 3.3(b)), and stacking all cross-correlations. The causal components of the SRI Green's function and of the true Green's function modelled between **s** and **r** are shown in Fig. 3.4(a). Although the two waveforms peak at the same arrival time, their shape is considerably different. This is due to the fact that the double cross-correlation operation in SRI causes the SRI Green's function to be convolved with the square of the complex conjugate of the source wavelet. Hence, the true Green's function between **s** and **r** must itself be convolved with the square of the complex conjugate of the source wavelet for a proper comparison to be made between the two traces. When this is done, the trace in Fig. 3.4(b) is obtained. In this case, the match between the two traces is almost perfect, and any difference between the true trace and the estimate from SRI (i.e., the non-physical event just before the direct arrival at ~ 0.09 s on the SRI trace) can be related to the approximations in equations (3.2) and (3.4). In fact, a similar experiment showed that no differences (to numerical precision) were present between the true and SRI traces when the exact formulae in equations (3.1) and (3.3) were used (see Section 4.2.1).

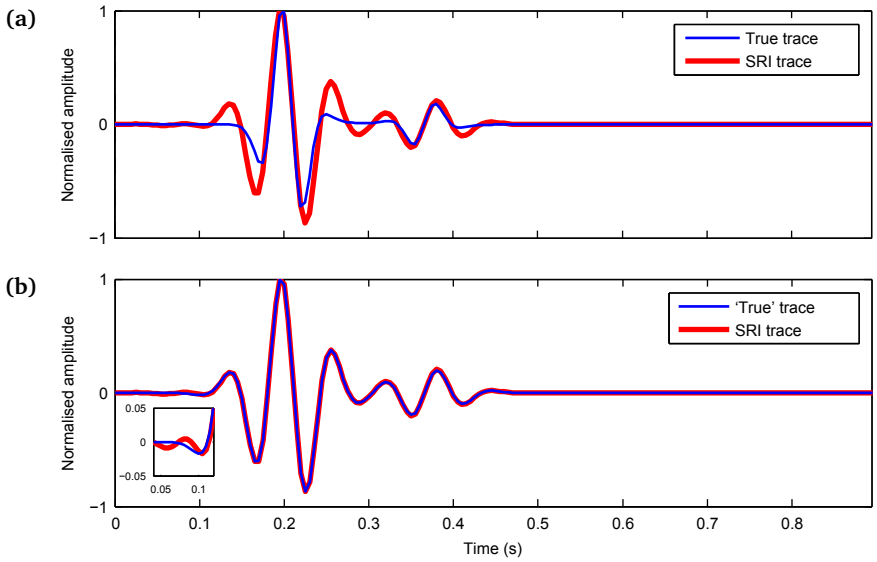

Figure 3.4. Comparison of Green's functions constructed using SRI (thick red traces) with the true Green's function (thin blue traces) from source **s** to receiver **r** as shown in Fig. 3.2. (a) The true Green's function is that obtained from the Foldy modelling code. (b) The 'true' Green's function is obtained by convolving the true Green's function from panel (a) with the square of the complex conjugate of the source wavelet. The arrival at ~ 0.09 s on the SRI trace (magnified panel in (b)) is non-physical and arises from the cross-correlation of scattered waves to **s** and **r**.

3.3 SRI at engineering seismology scale[2]

We applied correlation-correlation SRI to construct the seismogram between an active source and a number of receivers in a small exploration or engineering scale seismic experiment performed in the field beside Schlumberger Gould Research in 2010 (Duguid et al., 2011). The acquisition geometry is shown in Fig. 3.5: active seismic sources, consisting of an accelerated weight drop, were placed at intervals of 4 m along the running-track shaped boundary S'. This boundary encloses a grid of receivers at locations $\mathbf{r}_i$, some of which we use as target sensors, and a receiver line S which acted as the backbone array in this case. Active shots were also recorded at all receiver positions from a source at location **s**. Our goal is to construct seismograms from source **s** on target receivers $\mathbf{r}_i$ using SRI, and compare the results to the real recordings.

We constructed the seismograms between source **s** and receivers $\mathbf{r}_i$ by applying SRI using equations (3.2) and (3.4), and without using the direct recordings of the source on $\mathbf{r}_i$. Thus we simulate the case where the source at **s** was fired before or after the period during which the receivers at $\mathbf{r}_i$ were installed and activated, and hence where the source was only recorded on the backbone receiver boundary S. This was achieved by first using seismic energy propagating from sources on boundary S' to estimate the Green's function propagators between $\mathbf{r}_i$ and each **x** on S using inter-receiver interferometry in equation

[2]This section is an edited version of Section 3 in Entwistle et al. (2015), of which I am a co-author. All work presented in this section is entirely my own and was carried out on a dataset acquired by Craig Duguid and David Halliday at Schlumberger Gould Research in July 2010 (Duguid et al., 2011).

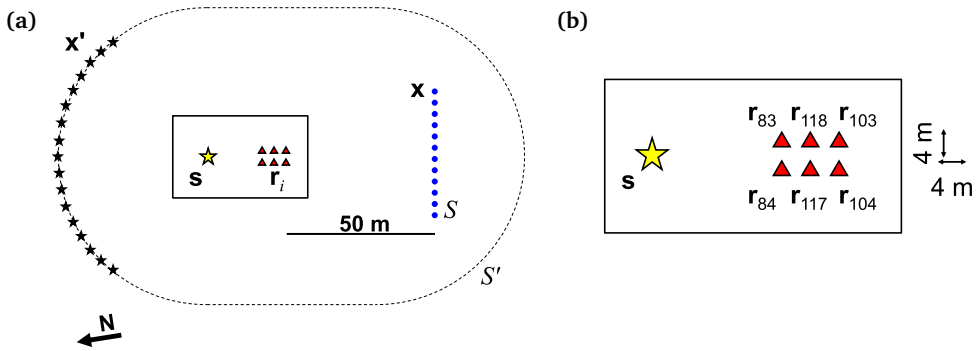

Figure 3.5. Geometry for the small-scale seismic experiment. (a) Active sources are located along the dashed boundary S' (black dashed line and black stars) and at position $\mathbf{s}$ (yellow star). Receivers are located along line S (blue circles - every second receiver is shown here for clarity) and at points $\mathbf{r}_i$ (red triangles) close to the source at $\mathbf{s}$. Only those boundary sources located approximately around the stationary-phase region of S' are used (black stars). (b) Magnified view of the active source and the target receivers marked by red triangles with receiver numbers shown in the numbering scheme of Duguid et al. (2011): results for these receivers are shown in Fig. 3.7.

(3.2), thus turning receivers $\mathbf{r}_i$ into virtual sources recorded by receivers at $\mathbf{x}$ on S. We then redatum the signals from the backbone array S to the target sensors $\mathbf{r}_i$ using inter-source interferometry in equation (3.4), turning the virtual sources at $\mathbf{r}_i$ into virtual receivers.

The active-source data was recorded at 250 Hz over a time period of 4 s in a field adjacent to Schlumberger Gould Research (SGR) in July 2010. As a variety of geophone types was deployed during acquisition (with responses centred at 4.5 Hz, 10 Hz and 14 Hz in the target sensors, and at only 4.5 Hz at receiver line S), transfer functions from 4.5 Hz to 10 Hz, and from 14 Hz to 10 Hz were estimated from the recorded data and applied to the 4.5 Hz and 14 Hz data before any subsequent processing (Duguid et al., 2011). In order to ensure coherency in the frequency content across all receivers, the data from boundary S' was filtered between 8 and 22 Hz before the inter-receiver step (Fig. 3.6(a)–(b)). In accordance with the stationary-phase principles of Snieder (2004), only a subset of boundary sources that were assumed to provide a constructive contribution to the integrand in equation (3.4), was used to construct the inter-receiver Green's functions (see the small black stars in Fig. 3.5(a)). Before the inter-source step, a second filter (8–15.5 Hz) was applied to the signals recorded by the backbone array, and to those recorded from the active source $\mathbf{s}$ at the receivers $\mathbf{r}_i$. This was the only frequency band with significant energy that overlapped between all recorded signals, which thus limits the results to a narrow frequency band (Fig. 3.6(d)–(e)). In addition, note that since the location of the boundary sources and receivers used in this experiment is one-sided, only the causal component of the inter-receiver Green's functions was generated during the inter-receiver step, while the inter-source step only produced the acausal component of the Green's function between $\mathbf{s}$ and $\mathbf{r}$.

The results of SRI for the 6 receivers $\mathbf{r}_i$ are shown in Fig. 3.7 as time-reversed acausal components: all seismograms are cut to 1.4 s in length and are normalised to their

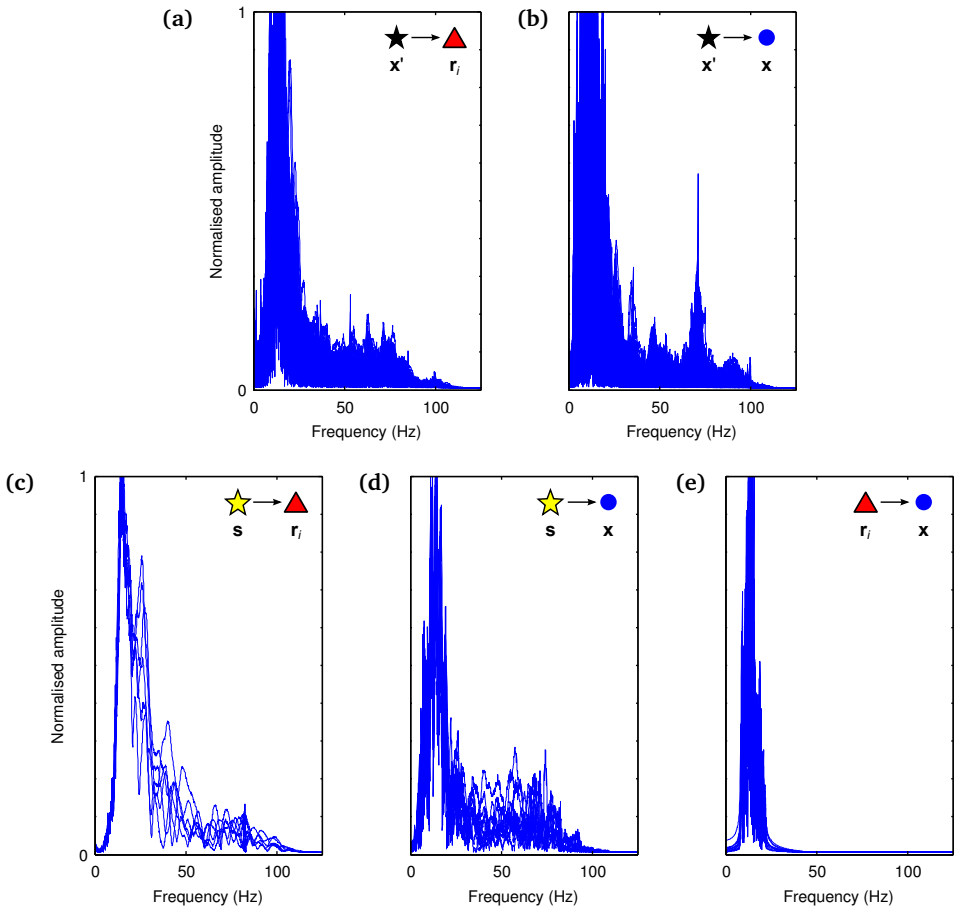

Figure 3.6. Frequency spectra from the small-scale experiment. (a) Boundary sources $\mathbf{x}'$ to target sensors $\mathbf{r}_i$. (b) Boundary sources $\mathbf{x}'$ to backbone receivers $\mathbf{x}$. (c) Active source $\mathbf{s}$ to target sensors $\mathbf{r}_i$. (d) Active source $\mathbf{s}$ to backbone receivers $\mathbf{x}$. (e) Virtual sources $\mathbf{r}_i$ to backbone receivers $\mathbf{x}$. In each stage of SRI it is necessary that the signal frequency band is common to correlated signals. Hence, the spectra in panels (a)–(b) were used to select 8–22 Hz as the pre-inter-receiver interferometry pass band, while the spectra in panels (d)–(e) were used to select 8–15.5 Hz as the pre-inter-source interferometry pass band.

absolute maximum amplitude. The dominant arrival is the emerging surface wave (ground roll) which can be seen to move out from the source for increasingly distant receivers. The match is not perfect, and this is likely partly because the equations discussed in Section 3.1 for correlational interferometry assume a non-attenuating medium which is an approximation. Also, similar weight drop sources were used at locations $\mathbf{x}'$ and $\mathbf{s}$: thus in the first step of interferometry both Green's functions on the right of equation (3.2) are in fact convolved with the source time function and the result on the left will therefore be multiplied by the source power spectrum. This extra factor is multiplied into the SRI result in equation (3.4), but will not be present in the real recording (similarly to Fig. 3.4(a)). Of course, since we have both the real recordings and the SRI seismograms at receivers $\mathbf{r}_i$ in this case, in principle we could divide one by the other to obtain the source power spectrum (Behura & Snieder, 2013). We do not

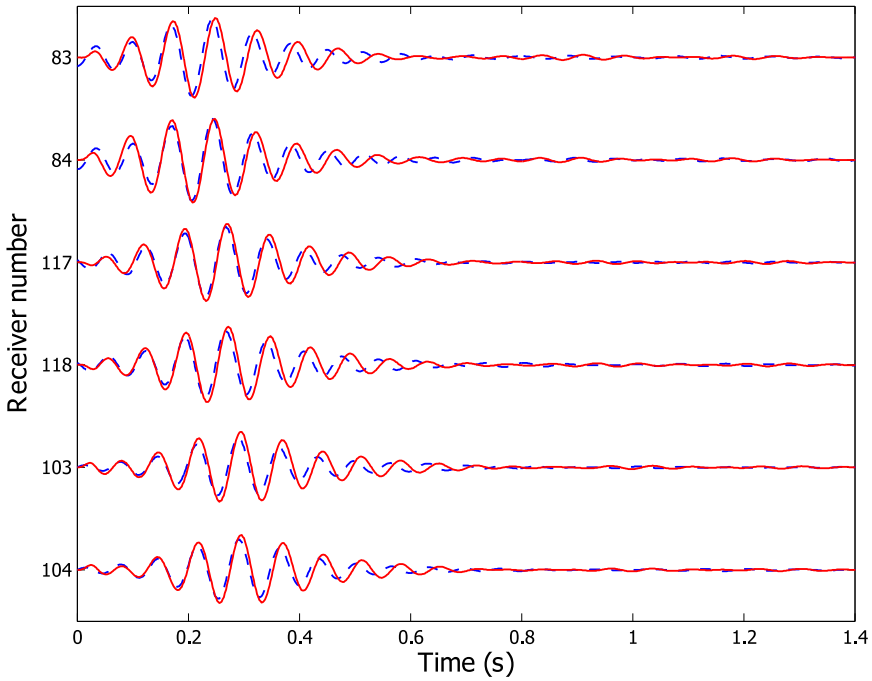

Figure 3.7. Comparison of surface wave (ground roll) seismograms constructed using SRI (red solid traces) with the real recordings (blue dashed traces) at the target sensors $\mathbf{r}_i$ shown in Fig. 3.5(b). All seismograms are bandpassed in the frequency range 8–15.5 Hz, chosen because that range contained all dominant amplitudes that were common to all recordings at $\mathbf{x}$ and $\mathbf{r}_i$ in Fig. 3.5.

implement this here as first it assumes a non-attenuative medium, and second we focus on testing the case where we do not have any direct recordings at $\mathbf{r}_i$. Finally, in this controlled small scale example the SRI reconstructions are narrow-band signals with a low frequency content compared to other industrial surveys (8–15.5 Hz). This has implications for the use of such SRI seismograms for subsurface imaging as spatial resolution will be low.

Nevertheless, in all cases the match between the real and SRI traces is reasonably good, showing the reliability of the method in a controlled experiment and when an ideal geometry of sources and receivers is available. In the next section, I discuss the application of the principles of SRI and retrospective seismology to less controlled scenarios in earthquake seismology, showing the potential of this method when the distribution of sources and receivers is far from perfect.

3.4 SRI at earthquake seismology scale[3]

In this section I describe the application of SRI in an earthquake seismology scale experiment using data recorded by the USArray seismic network. The geometry of sources and receivers employed is displayed in Fig. 3.8: the active source $\mathbf{s}$ (yellow star) is a 5.8 magnitude earthquake which occurred in Mexico on 27/04/2009, and was recorded by the array of backbone receivers $\mathbf{x}$ (blue circles) and by most of the target sensors $\mathbf{r}$ (red triangles). Our aim is to use SRI to redatum the earthquake recordings from the backbone array onto the target sensors, hence creating a set of interferometric Green's functions which can in most cases be compared with the true earthquake recordings. In the case where the target sensors did not originally record the earthquake, the results of SRI provide new information on the earthquake's properties. Compared to the synthetic and small-scale experiments in the previous sections, the boundary S' of sources used here is not composed of active seismic sources but rather of uncorrelated sources of seismic ambient noise. In Fig. 3.8 these noise sources are schematically represented by black stars located along the coast of the nearby oceans, but note that their origin may be located elsewhere.

For all of the backbone seismometers in Fig. 3.8, instrument response files and up to 2 years (January 2009 to December 2010) of vertical-component, daily ambient-noise records, sampled at 4 Hz, were downloaded from the IRIS database. Records of the target earthquake at the backbone seismometers and at the available target receivers were also downloaded, with each trace starting at the time of the event and being 8000 seconds long. The processing of the ambient-noise data broadly followed the guidelines of Bensen et al. (2007), and a detailed description of the processing workflow for a UK ambient-noise dataset can be found in Chapter 5.

After removing instrument response, mean and trend from each day file, the data was bandpass filtered between 0.01 and 1 Hz and normalised first in the time domain (using one-bit normalisation) and then in the frequency domain (whitening). Inter-receiver interferometry between each target sensor $\mathbf{r}$ and each of the backbone receivers $\mathbf{x}$ was performed by first cross-correlating the processed daily noise files and then stacking all available cross-correlations over the total recording period (equation (3.2)). We then stacked the causal and the time-reversed acausal part of each stack of cross-correlations to produce a one-sided Green's function $G(\mathbf{x},\mathbf{r})$ for each target sensor and backbone seismometer pair. As in the previous synthetic and small-scale examples, these Green's functions correspond to the signals that would have been recorded by the backbone seismometers at $\mathbf{x}$ if earthquakes had occurred at the location of the target receivers $\mathbf{r}$. All

[3]This section is a summary of Section 4.3 in Entwistle et al. (2015), of which I am a co-author. My contribution to this section consisted of creating the Fortran90 code for the 2D Voronoi tessellation using subroutines originally by Malcolm Sambridge (Australian National University). With the exception of the Voronoi tessellation code, all work presented in this section was carried out by Elizabeth Entwistle.

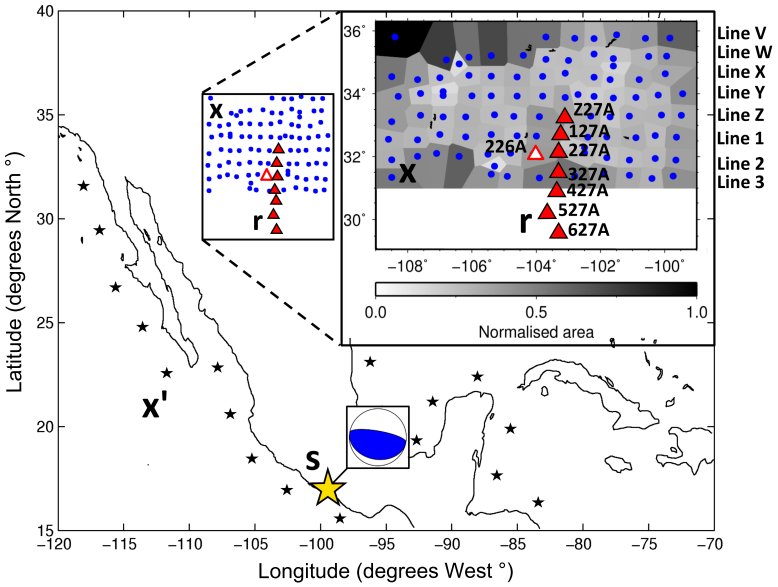

Figure 3.8. Acquisition geometry used to construct virtual seismograms of the 27/04/2009 M 5.8 Mexico earthquake (large yellow star with source mechanism) using correlation-correlation SRI. The boundary of sources $\mathbf{x}'$ is represented by uncorrelated ambient noise sources (black stars positioned schematically in oceans). Ambient noise from these sources is recorded by the backbone receiver array $\mathbf{x}$ (blue circles) and by 8 target sensors $\mathbf{r}$ (filled and unfilled red triangles) located within New Mexico. The backbone array consists of 8 approximately parallel lines of seismometers (from Line V in the north of the array to Line 3 in the south, with the letters taken from station notation employed in naming the USArray Transportable Array). For each target sensor, 2 backbone array lines are used to perform SRI as indicated in Fig. 3.9. A tessellation of Voronoi cells, each having one of the backbone seismometers at its nucleus, is used to weigh the contribution of each inter-receiver Green's function during summation over the boundary receivers in the second stage of SRI.

interferometric Green's functions were cut at 8000 seconds, making them of the same length as the earthquake records.

In order to restrict the frequency content of interferometric Green's functions and earthquake records to the same high-energy frequency band, a second bandpass filter with corners at 0.02 and 0.1 Hz was applied to the interferometric and earthquake traces before the inter-source interferometry step. Hence, inter-source interferometry was applied by cross-correlating each earthquake record $R(\mathbf{x},\mathbf{s})$ with each interferometric Green's function $G(\mathbf{x},\mathbf{r})$, and integrating over boundary receivers $\mathbf{x}$. According to Curtis et al. (2012) and to equation (3.4), this gives the acausal part of the signal that would have been recorded at location $\mathbf{r}$ from source $\mathbf{s}$ if a sensor had been installed at $\mathbf{r}$ at the time of the event. As already discussed in the previous chapter, for practical applications the integral in equation (3.4) is normally discretised as a sum over receivers on boundary S (see equations (2.15)–(2.16) for the inter-receiver interferometry equivalent). However, we found that giving an equal weight to each cross-correlation when irregularities in the backbone array are present substantially degraded the quality of the SRI results. Hence, we employed a Voronoi tessellation of the area covered by the

backbone array (inset in the top-right corner of Fig. 3.8) to weigh the contribution of each inter-source cross-correlation to the final stack. Each Voronoi cell i is identified by the position of a nucleus at which one of the backbone receivers $\mathbf{x}_i$ is located, so that each point within each Voronoi cell is closer to its nucleus (backbone receiver) than to the nucleus of any other cell. The edges of the Voronoi-tessellated area are also down-weighted or tapered by a half-sinusoidally shaped taper to prevent edge effects. For each backbone sensor $\mathbf{x}_i$, the tapered, normalised area of its corresponding Voronoi cell is then used to as a weighting factor for the contribution of its cross-correlation to the total cross-correlation stack. Hence, backbone sensors located in an area of high seismometer density or near the edges of the backbone array contribute less to the final Green's function than those located in areas where backbone seismometers are sparse or are near the centre of the backbone array.

Finally, the earthquake and SRI records were bandpass filtered within a common frequency band of highest energy, which in this case was found to be 0.04–0.06 Hz. This ensured that a proper comparison could be made between the true and interferometric traces. Also, similarly to the small-scale experiment where backbone sensors were only present on one side of the target source and receiver, for each target sensor the results of SRI only displayed energy in the acausal component, which was therefore time-reversed to produce the causal Green's function between $\mathbf{s}$ and $\mathbf{r}$.

The results of SRI for 8 target sensors and the true earthquake recordings at 7 target sensors are shown in Fig. 3.9(a): traces are plotted as a function of epicentral distance from $\mathbf{s}$, and the inter-source step of SRI was performed using the backbone array lines indicated above each trace on the left. All seismograms are normalised to their maximum amplitude and the quality of the match between the true and SRI seismograms is measured in terms of the correlation coefficient, indicated above each trace on the right. As in the previous small-scale example, the moveout of the surface-wave arrival is clearly visible as the epicentral distance from the source increases. In most cases, the SRI traces are in good agreement with the true earthquake records, reaching up to a correlation coefficient of 0.93 at sensor 227A. The grey ellipse on trace Z27A highlights a series of non-physical arrivals on the SRI trace, which are responsible for the relatively low correlation coefficient. These spurious arrivals disappear when SRI is performed using a combination of cross-correlation and convolution (not shown here but discussed in detail in Entwistle et al. (2015)). Sensor 226A (unfilled triangle in Fig. 3.8) was not active when the earthquake occurred, hence the SRI trace in this case constitutes an entirely new record of the earthquake. This also proves that reliable virtual earthquake seismograms may be produced on sensors which were installed either before or after the earthquake occurred, provided that the properties of the medium have not changed significantly between the time of the deployment and the occurrence of the event. Fig. 3.9(b) shows the results of SRI when the summation of inter-source cross-correlations is performed over the entire backbone array without Voronoi tessellation, rather than using only two lines per target sensor and the Voronoi tessellation

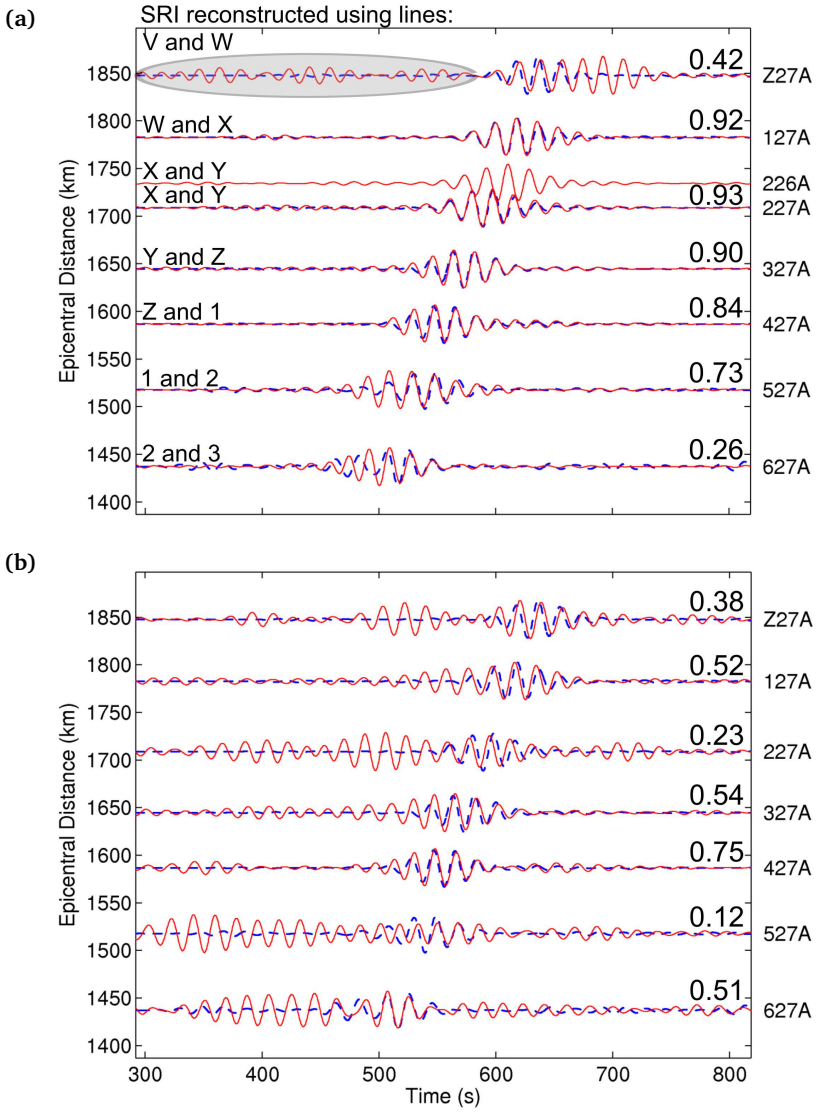

Figure 3.9. Comparison of seismograms for the M 5.8 Mexico earthquake constructed using correlation-correlation SRI (red solid traces) with real recordings (blue dashed traces) at target sensors denoted by red triangles in Fig. 3.8. No real earthquake recording is available at sensor 226A. The quality of the match between the real and SRI seismograms is quantified by the correlation coefficient, stated above each trace on the right. (a) SRI seismograms are constructed by integrating over 2-line combinations of seismometers and using the tapered, normalised area of each Voronoi cell (see inset in the top-right corner of Fig. 3.8) as a weighting factor during stacking. (b) Integration over boundary S is performed by summing over all backbone seismometers, rather than as an interpolated sum over Voronoi cells. The grey shaded ellipse in panel (a) highlights the spurious, non-physical arrivals that occur prior to the main surface wave arrivals constructed at target sensor Z27A.

shown in Fig. 3.8. In this case, the quality of the match is significantly degraded, as also indicated by the low correlation coefficients. Thus our Voronoi weighting scheme is shown to be effective.

3.5 Concluding remarks

In this chapter I have shown how source-receiver interferometry can successfully be applied to real datasets at different length scales to construct a virtual seismogram between an active source **s** and one or more target receivers **r**. When no real seismogram was originally recorded from **s** to **r**, the results of SRI provide entirely new information on the properties of the medium which would have otherwise been lost.

Starting from a synthetic example which uses data generated with the Foldy modelling code (Chapter 2), I presented the results of SRI when an ideal acquisition geometry and exact, noiseless data are available. Then, I extended the application of SRI to a small-scale, real-data example in which partial source and receiver boundaries are used. In this case, boundary sources and receivers were located in the stationary phase regions on either side of the target source and receiver, providing a strictly one-sided illumination onto the target source and receivers in both steps of SRI. Nevertheless, the results of SRI showed an excellent match to the true seismograms, demonstrating the reliability of the method in a controlled real-data experiment with an ideal acquisition geometry. Finally, I presented the results of SRI in a large-scale experiment which used earthquake and ambient-noise data from a selection of USArray seismometers to construct virtual earthquake seismograms using correlation-correlation SRI. In this case, the excellent match between the true and SRI seismograms was quantified by correlation coefficients, which peaked at 0.93. In addition, the use of spatial tapering and Voronoi cells to weigh the contribution of each inter-source cross-correlation to the final Green's function proved to be a better alternative to simply stacking all cross-correlations over the entire backbone array as performed in previous studies. In fact, this weighted integration method ensured that the largest contribution to the SRI Green's functions was made by backbone receivers located in the region of stationary phase. Additional experiments by Entwistle et al. (2015) showed that, when even larger scale experiments are performed, more robust results from SRI can indeed be obtained when the backbone array is restricted to those seismometers whose locations better approximate the stationary phase points of the receiver boundary. Similar results were previously obtained in a field experiment by Duguid (2010), who found that the results of SRI substantially degraded when full boundaries were used. In that case, even at small distances, Green's functions estimated from SRI appeared to contain significant non-physical energy when fully enclosing boundaries were used, while the number of spurious arrivals was greatly reduced when only the sources and receivers located in the stationary phase regions were employed.

Within this chapter, all experiments were performed using correlation-correlation SRI, which assumes the medium to be non-attenuative and requires source and receiver boundaries to surround the target source and receiver. However, an alternative form of SRI which uses a combination of cross-correlation and convolution may be a better option when the medium is attenuative and a suitable acquisition geometry (e.g., Fig. 1.22(a) and (c)) is available. Further experiments by Entwistle et al. (2015) showed that this was indeed the case, as the use of convolution in the second stage of SRI greatly reduced the amount of non-physical energy in the final SRI traces.

Finally, although all virtual source seismograms presented here were constructed within relatively narrow frequency bands (8–15.5 Hz in the small-scale experiment, and 0.04–0.06 Hz in the large-scale experiment), these multi-scale applications of SRI show that this new type of *retrospective* seismology is indeed possible in both earthquake and exploration settings, allowing seismologists to create new recordings of seismic events where no sensors were originally installed.

CHAPTER 4

Discussion

In Part I of this thesis I provided a comprehensive introduction to the field of seismic interferometry and a number of published examples of its application. Using an exact waveform modelling method that produces almost error-free results, I then quantified the effect of the various approximations present in the simplified interferometric formulae. Finally, I presented synthetic and real-data examples of the application of source-receiver interferometry within the context of retrospective seismology, which allows one to produce previously unrecorded signals by redatuming seismic energy in space and time onto new sensor locations.

In this chapter, I discuss the issues and challenges that have emerged from the studies in Part I of this thesis, particularly focusing on the current uses and various aspects of the Foldy modelling method, and on practical elements of retrospective seismology at various scales.

4.1 Current status and future of the Foldy modelling code

To date, the Foldy modelling code presented in Chapter 2 has been used in a range of studies within the Edinburgh Interferometry Project (EIP) research group to test and investigate existing and new theory in wavefield interferometry and scattering. Since it produces theoretically exact results, it is ideal to test new theory and algorithms in scattering acoustic media, as modelling errors can be discounted. However, the code also presents certain limitations which cannot be overcome and may require the use of alternative grid-based modelling methods (i.e., finite-differences). In this section I provide examples of the use of the Foldy modelling code in a number of published papers,

discuss its beneficial contribution to these studies, and examine theoretical aspects and practical limitations of the method.

4.1.1 Uses and benefits

Within interferometry, Meles et al. (2013) and Meles & Curtis (2013c) initially used the Foldy modelling code to analyse the scattering problem in inter-receiver interferometry (IRI) and source-receiver interferometry (SRI), particularly focusing on the distribution of points of stationary phase. They concluded that the latter may out-perform the former if used to reconstruct singly-scattered wave energy when complete boundaries are not available. More precisely they showed that, for the single diffractor problem, the combination of cross-correlation and convolution in SRI shifts non-physical energy resulting from the first inter-receiver step, into physical, stationary energy in the inter-source step. In addition, while IRI requires access to specific, a priori unknown source locations to retrieve the scattered Green's function, in SRI any scattered event provides the correct scattering kinematics, and any source and receiver boundary location may effectively be considered a stationary point. Meles & Curtis (2013b) and Meles & Curtis (2014a) used the Foldy modelling method to extend this analysis to the multiple-diffractor problem, showing that in SRI any boundary source-receiver pair produces kinematically correct physical arrivals for singly- as well as multiply-scattered waves. In addition, since non-physical artefacts are also produced when more than one scatterer is present, they developed an algorithm which allows the traveltimes of physical, scattered waves of any order to be predicted and subsequently used to discriminate physical and non-physical events in the SRI results.

Löer et al. (2013) and Löer et al. (2014) used the Foldy modelling code to conduct a thorough analysis of the contribution of each term in the SRI formula (e.g., equation (1.28)) when the Green's functions in the integrand are separated into their direct and scattered component. They found that when source and receiver boundaries are incomplete, coarsely sampled or one-sided, non-physical energy is introduced into the results of SRI. Out of the eight terms that constitute the sum within the double SRI integral, four produce purely non-physical, non-stationary energy, and two can be combined and used to produce robust estimates of the scattered wavefields. One of these two terms is also associated with standard imaging (migration) methods.

An additional application of the Foldy method was carried out by Meles & Curtis (2013a) and Meles & Curtis (2014b), who used the Foldy modelling code to develop and test the method of diffractor 'finger-printing'. This method allows one to identify individual scatterers inside an acoustic medium using the move-outs of wave energy emitted and recorded by arrays of sources and receivers, respectively. For any recording of diffracted energy between any array source and any array receiver, it also allows each multiply-scattered arrival to be decomposed into its single-scattering components, and

hence its ordered diffraction path to be reconstructed. Löer et al. (2015) later automated the method using the cross-correlation of receiver gathers for different common sources (or source gathers for different common receivers) to identify the move-out associated with each scatterer and hence its 'finger-print', testing the method on data produced with the Foldy code.

In all of the above examples, the use of the Foldy modelling code, as opposed to alternative grid-based modelling methods such as finite-differences, provided a number of advantages. First, since Green's functions are calculated analytically in the frequency domain, the code does not require a modelling grid to compute the wavefield as it propagates through the medium. Hence modelling-related computations are rapid, allowing a large number of experiments to be performed for different geometries of sources, receivers and scatterers in a relatively short time. In addition, since direct and scattered events can easily be separated in the Foldy method and code, by choosing the direct and scattered part of the wavefield to be independent outputs, it is easy to perform operations which combine the two parts or analyse them individually without the need to perform direct/scattered wavefield separation on the modelled traces themselves (as is the case with finite-differences, for example). Also, within interferometry (see Chapter 2), the contribution of Green's function derivatives to the interferometric equations are easy to analyse, and the effects of approximating the interferometric formulae may be quantified on numerically exact results (e.g., Fig. 2.5). If wavefields were modelled using a grid-based modelling scheme with numerical dispersion or grid-related geometrical approximations, or a non-exact analytical method such as the Born approximation (see Section 4.1.2), it would not be possible to determine whether imperfections in the interferometric traces are a result of approximations in the interferometric formula or of the non-exact modelling method. Finally, the expertise and knowledge obtained while performing simple tests with the exact Foldy code may be carried forward to later experiments on complex models that require alternative grid-based modelling methods.

4.1.2 Foldy versus Lippmann-Schwinger formulations

Consider the case where a source and a receiver are located at positions $\mathbf{x}_S$ and $\mathbf{x}_R$ within a medium of smooth background velocity $v_0(\mathbf{x})$ containing an arbitrary distribution of scatterers of finite size. Let the total slowness field $s(\mathbf{x}) = 1/v(\mathbf{x})$ be represented by $s(\mathbf{x}) = s_0(\mathbf{x}) + \delta s(\mathbf{x})$, where $s_0(\mathbf{x}) = 1/v_0(\mathbf{x})$ is the background slowness field and $\delta s(\mathbf{x})$ is a small perturbation to the background slowness (Schuster, 2009). The Lippmann-Schwinger equation (Stolt & Benson, 1986) provides a full representation of the total wavefield between $\mathbf{x}_S$ and $\mathbf{x}_R$ as a sum of direct and scattered Green's functions, and in the frequency domain is given by

$$G_T(\mathbf{x}_R, \mathbf{x}_S) = G_0(\mathbf{x}_R, \mathbf{x}_S) + 2\omega^2 \int_V G_T(\mathbf{x}, \mathbf{x}_S) s_0(\mathbf{x}) \delta s(\mathbf{x}) G_0(\mathbf{x}_R, \mathbf{x}) \mathrm{d}V \,, \tag{4.1}$$

where ω denotes angular frequency, G_0 denotes the *direct* Green's function between two locations (which may be calculated using equations such as (B.2)–(B.5)), G_T denotes the *total* Green's function between two locations (which includes all inter-scatterer interactions and intra-scatterer effects such as reflections, refractions and diffractions occurring within the scatterer – see Wapenaar et al. (2010b)), and integration is performed over each infinitesimal element $\mathbf{x}$ of volume V. From equation (4.1), the scattered field between $\mathbf{x}_S$ and $\mathbf{x}_R$ may be obtained by subtracting the direct field from the total field, giving

$$\begin{aligned}\delta G(\mathbf{x}_R,\mathbf{x}_S) &= G_T(\mathbf{x}_R,\mathbf{x}_S) - G_0(\mathbf{x}_R,\mathbf{x}_S) \\ &= 2\omega^2 \int_V G_T(\mathbf{x},\mathbf{x}_S) s_0(\mathbf{x}) \delta s(\mathbf{x}) G_0(\mathbf{x}_R,\mathbf{x}) \mathrm{d}V \ .\end{aligned} \tag{4.2}$$

Equation (4.1) may be analysed with respect to the expression for the total field between $\mathbf{x}_S$ and $\mathbf{x}_R$ in the case of point scatterers (i.e., Foldy's formulation) given in equation (2.1), which is here repeated using the same Green's function notation as in equation (4.1) in order to ease this comparison:

$$G_T(\mathbf{x}_R,\mathbf{x}_S) = G_0(\mathbf{x}_R,\mathbf{x}_S) + \sum_{i=1}^{N} \widetilde{G}_T(\mathbf{x}^{(i)},\mathbf{x}_S) A^{(i)} G_0(\mathbf{x}_R,\mathbf{x}^{(i)}) \ . \tag{4.3}$$

Here $G_0(\mathbf{x}_R,\mathbf{x}_S)$ denotes the direct wavefield from $\mathbf{x}_S$ to $\mathbf{x}_R$, $\widetilde{G}_T(\mathbf{x}^{(i)},\mathbf{x}_S)$ denotes the total wavefield (direct and scattered) reaching scatterer (i) located at $\mathbf{x}^{(i)}$, $A^{(i)}$ is the complex scattering amplitude of scatterer (i), and $G_0(\mathbf{x}_R,\mathbf{x}^{(i)})$ is the direct Green's function between scatterer (i) and receiver $\mathbf{x}_R$, which may be computed from equations (B.2)–(B.5).

By comparing equations (4.1) and (4.3), a number of similarities may be noticed. First, in both cases the total wavefield is given as a sum of direct and scattered fields, and direct Green's functions may be evaluated using the analytical formulae in equations (B.2)–(B.5). Second, in both equations the scattered wavefield (second term on the right-hand side) is expressed as a sum involving direct and scattered fields. This sum is denoted by the numerical summation over scatterers in equation (4.3), while it corresponds to an integral over all infinitesimal elements $\mathbf{x}$ of volume V in equation (4.1).

Despite these similarities the two equations also present some substantial differences. In equation (4.1), the total wavefield $G_T(\mathbf{x},\mathbf{x}_S)$ includes not only all inter-scatterer interactions, but also the effect of all non-linear processes that occur inside each scatterer as this is excited by the passing wavefield (e.g., internal reflections, refractions and diffractions), ensuring that energy is conserved as the wavefield propagates. Hence, the scattered wavefield is non-linear in terms of the incident field (Wapenaar et al., 2010b). Also, the quantity $s_0(\mathbf{x})\delta s(\mathbf{x})$ in equation (4.1) is a *real* number which accounts for the perturbation in the velocity field that causes energy to diffract, and contributions to the scattered field $\delta G(\mathbf{x}_R,\mathbf{x}_S)$ are only made by those elements $\mathbf{x}$ of V at which $\delta s(\mathbf{x}) > 0$.

On the other hand, since diffractors have infinitely small size in the Foldy formulation, the total wavefield $\widetilde{G}_T(\mathbf{x}^{(i)}, \mathbf{x}_S)$ in equation (4.3) includes direct Green's functions and inter-scatterer interactions only, while all non-linear intra-scatterer effects are accounted for by the *complex* scattering amplitude $A^{(i)}$. In fact, for energy to be conserved, the multiple scattering process which results from intra-scatterer effects needs to be taken into account even for the idealised concept of a single point-scatterer, and the use of the complex scattering amplitude $A^{(i)}$ to express intra-scatterer non-linearity makes the scattered field in equation (4.3) non-linear in terms of the parameter contrast but linear in terms of the incident field (Wapenaar et al., 2010b). In order to solve the forward problem of scattered wavefields, the Foldy formulation therefore expresses the wavefield incident on each scatterer $\widetilde{G}_T(\mathbf{x}^{(i)}, \mathbf{x}_S)$ in equation (4.3) as the sum of a direct and scattered component (see equation (2.3)), which reduces the non-linear multiple-scattering forward problem to a linear system of equations that can be solved by matrix inversion (equations (2.4)–(2.6)). The multiple scattering process is represented by the scattering matrix ($\mathbf{M}$ in equations (2.4)–(2.6)) which only contains direct, analytical inter-scatterer Green's functions and scattering amplitude terms.

In contrast, the fact that term $G_T(\mathbf{x}, \mathbf{x}_S)$ in the Lippmann-Schwinger formulation contains the contribution of all non-linear processes occurring inside the scatterers, does not allow the same simplification to be made in equation (4.1). If scattering is weak, the total incident field $G_T(\mathbf{x}, \mathbf{x}_S)$ is often approximated by the direct field $G_0(\mathbf{x}, \mathbf{x}_S)$ to give the Born (linearised) forward modelling equation for scattered wavefields:

$$\delta G(\mathbf{x}_R, \mathbf{x}_S) \approx 2\omega^2 \int_V G_0(\mathbf{x}, \mathbf{x}_S) s_0(\mathbf{x}) \delta s(\mathbf{x}) G_0(\mathbf{x}_R, \mathbf{x}) \mathrm{d}V \, . \tag{4.4}$$

When only a single scatterer is present in the medium, equation (4.4) provides a good (but not exact) representation of the scattered field. However, the Born approximation fails to represent second and higher order scattering, hence is not valid when multiple scatterers are present in the medium. In addition, Wapenaar et al. (2010b) find that non-physical arrivals are introduced into interferometric Green's function estimates when scattered wavefields are modelled according to equation (4.4). This is due to the fact that the Born approximation does not conserve energy (Rodberg & Thaler, 1967; Born & Wolf, 1999), hence it is applicable to first-order scattering processes only. When wavefields are decomposed into a sum of direct and scattered components and cross-correlated as in interferometry, the cross-correlation of the scattered parts produces a term which is proportional to second-order scattering, which is not consistent with the requirements for the Born approximation and hence produces non-physical artefacts.

In contrast, the Foldy modelling method provides a full representation of the multiple-scattering process which includes all forms of non-linearity. However, the representation of the scattered field given in equation (4.3) is only valid in the far-field, i.e., when sources and receivers are far from the scattering domain and scatterers are far

from each other (Groenenboom & Snieder, 1995; Wapenaar et al., 2010b; Douma et al., 2011). In physical terms, the region of far-field may be identified by the distance at which $k|\mathbf{r}| \gg 1$, where k denotes the wavenumber and $|\mathbf{r}|$ denotes the distance between each pair of scatterers or from each scatterer to either a source or a receiver. Hence, while in the far field a scatterer of finite size can mathematically be treated as a point-scatterer whose location coincides with the central location of the physical scatterer (Mishchenko, 2006), in the near-field (where $k|\mathbf{r}| \ll 1$) equation (4.3) fails to correctly represent the diffracted wavefield. The Foldy representation of the scattered field is therefore equivalent to the Lippmann-Schwinger equation for a uniform background medium with embedded scatterers only when sources and receivers are located in the far-field zone. This detail was omitted in the work by Foldy (1945) which we used as a basis to develop our Foldy modelling code, explaining why errors are introduced into the results when scatterers are located in the near-field as discussed in the next section.

4.1.3 Effects of the far-field approximation

As discussed in the previous section, the Foldy method of waveform modelling is based on the far-field assumption, hence errors are introduced into the modelled waveforms when the Foldy code is applied to cases where scatterers are located in the near-field region. This effect can be observed in the simple experiment shown in Figs 4.1–4.2: here, a source is located at [0 0] m, point-scatterers are located at [10.501 0.5] and [0.5 10.501] m, and receivers are located in a grid pattern every meter in the x and y direction from -50.5 to $+50.5$ m. Hence, receivers at [10.5 0.5] and [0.5 10.5] m are assumed to be located in the near-field since each lies only 1 mm away from one of the two scatterers. The medium has uniform velocity 200 m s^{-1} and density 1000 kg m^{-3}. Green's functions in the range 0.39–100 Hz were calculated using the 2D formula (equation (B.3)) in Fig. 4.1 and the 3D formula (equation (B.5)) in Fig. 4.2, and applying a Ricker wavelet centred on 20 Hz to the analytical results. The snapshots of wavefield propagation in Figs 4.1–4.2 were obtained by plotting the amplitude of the Green's functions at all receivers at different times, using a constant (clipped) colour scale in the left column and a colour scale normalised to the amplitudes of the snapshot in the right column. At 0 s (top rows), just before the source fires, the amplitude of the field is zero everywhere except near the location of the two scatterers, which can clearly be identified as the two points of largest amplitude. The same occurs after the main direct and scattered wavefronts have propagated beyond the medium boundaries and only a low-amplitude, multiply-scattered wavefield is diffusing through the medium (bottom two rows). At intermediate times, the scatterers are more or less visible as two points of large amplitude.

The fact that these non-zero amplitudes are observed by receivers located in the near-field region around the two scatterers is clearly an error introduced by the modelling code. This error results from the fact that the equations that are used to calculate the

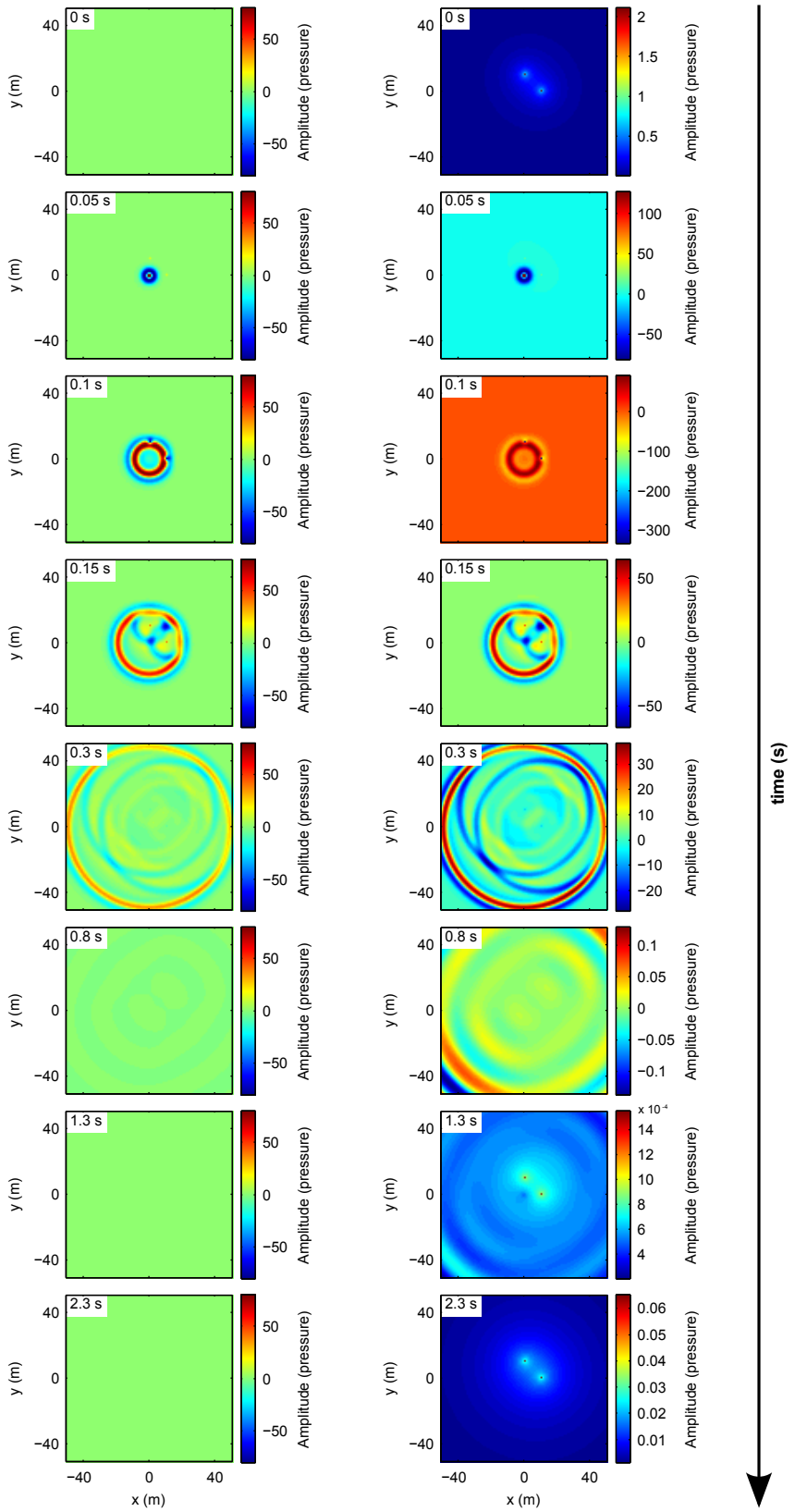

Figure 4.1. Snapshots of wavefield propagation in 2D for a source located at [0 0] m and two point-scatterers located at [10.501 0.5] and [0.5 10.501] m. Each row displays the wavefield at the same point in time, with a constant (clipped) colour bar on the left and a colour bar scaled to the amplitudes of the corresponding snapshot on the right. Note that the time axis is not uniform.

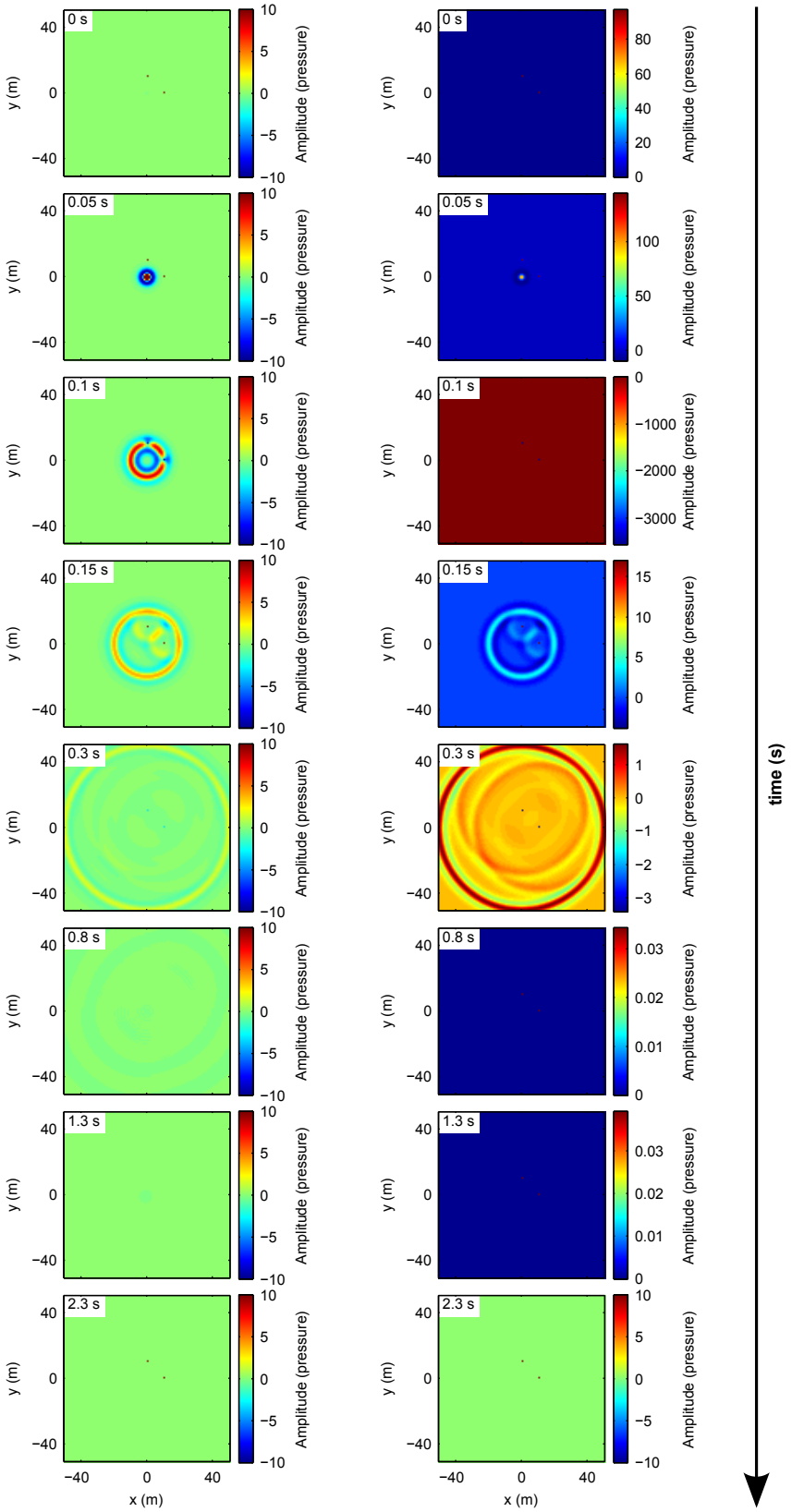

Figure 4.2. Snapshots of wavefield propagation in 3D for a source located at [0 0] m and two point-scatterers located at [10.501 0.5] and [0.5 10.501] m. Each row displays the wavefield at the same point in time, with a constant (clipped) colour bar on the left and a colour bar scaled to the amplitudes of the corresponding snapshot on the right. Note that the time axis is not uniform.

scattered field in the Foldy formulation (e.g., equation (4.3) above) are only applicable in the far-field zone (Groenenboom & Snieder, 1995; Wapenaar et al., 2010b; Douma et al., 2011). The Foldy code should therefore not be used in cases where sources and receivers are located particularly close to the scattering domain, or in applications such as imaging where sources and receivers may be co-located with scatterers. However note that, unlike grid-based modelling schemes which use a leapfrog approach (in which the wavefield computed at time t_i depends directly on the state of the wavefield at the previous time-step t_{i-1}), the Foldy method models wavefields by solving different linear systems of equations for different receiver points. The validity of the solution in the far field is therefore not affected by the erroneous results produced in the near field, where the formalism of equation (4.3) is not correct. Although this might seem counter-intuitive, it explains why non-zero amplitudes in the near-field zone are observed *before* the origin time of the source, and why artefacts present at a certain point in time are not propagated through the model as the wavefield diffuses through the medium, but are restricted to the region of near-field. As can be observed in Figs 4.1–4.2, the results obtained in the far field can in fact be considered correct.

The definition of far-field and near-field zone is intimately related to the range of modelled wavelengths with respect to the scatterer's size (Mishchenko, 2006), and from what can be observed in Figs 4.1–4.2 it also appears to depend on the formula that is used to evaluate the Green's function. In fact, the near-field region appears to be relatively wide in the 2D case (Fig. 4.1), where it encloses a number of receivers located around the scatterers, while it is limited to the two receivers located closest to the scatterers in the 3D case (Fig. 4.2). Although the reasons behind this behaviour are not entirely clear, this effect might partly be due to the shape of the Green's function in the two cases: while in 3D the Green's function is impulsive and non-zero only at the wavefront (Fig. 2.2(e)), the impulse response in 2D is not impulsive, but has infinite duration and is non-zero everywhere within the wavefront (Fig. 2.2(e)). Hence, an impulsive input in 2D leads to a sound response of infinite duration (Snieder, 2009), which might explain the wider size of the near-field region in 2D.

4.1.4 Current limitations and outlook

Despite the several advantages that the exact Foldy modelling method presents, the Foldy code should not be regarded as a substitute of grid-based modelling schemes, but rather as a complementary solution when simple geometries are considered. In fact, in its present state the code can only be applied to simple non-attenuating media of uniform velocity which may contain one or more isotropic point-scatterers, hence the effects of attenuation, non-isotropic scattering, and smooth velocity variations may not currently be investigated. However, the main drawback of the Foldy method is the fact that, as explained in the

previous section, it is based on the far-field assumption, hence artefacts are introduced into the results when sources and receivers are located particularly close to the scatterers.

Nevertheless, its successful use in a number of published studies (references in Section 4.1.1) demonstrates the potential of the method when testing existing and new theory in interferometry and scattering. Provided that the far-field assumption is satisfied, the code generates effectively exact waveform data which can be used to test new algorithms, and any discrepancy from the expected results may safely be attributed to errors in the theory behind the algorithm. As discussed in Section 4.1.2, the Foldy modelling method is also a much safer choice compared to the Born approximation in simple scattering acoustic media, since it includes all forms of non-linearity in the multiple-scattering process. As proved by Wapenaar et al. (2010b), the choice of a non-linear modelling method as opposed to Born is also beneficial in the case of a single scatterer.

In terms of evolution of the code, possible areas of future development may include the following:

- adding the option of attenuation. This may be achieved by introducing an attenuation factor to scale the amplitude of each direct Green's function computed by the code (i.e., source-to-scatterer, inter-scatterer, and scatterer-to-receiver). The amount of attenuation may depend on the distance between the points at which the Green's function is evaluated, and different forms of dependence may be implemented (e.g., linear, exponential, etc.).
- extension to non-isotropic scattering. This could be achieved by introducing, for instance, direction-dependent attenuation of the wavefield at each scatterer in such a way that the scattering matrix is consistent with the optical theorem for anisotropic scatterers (Wapenaar et al., 2010b).
- extension to the elastic domain. In its current state the Foldy modelling code models waveforms in the acoustic domain, but an equivalent version of the code could be implemented where Green's functions are evaluated in the elastic domain. Such implementation may also include conversions between P- and S-wave modes as the wavefield interacts with the scatterers.

4.2 Restrospective seismology with SRI

In Chapter 3 I presented a number of applications of source-receiver interferometry to synthetic and real datasets. These experiments highlighted the potential of SRI in constructing signals between an active source and a target receiver, which need not be installed at the time of the event, using only energy produced and recorded by surrounding boundaries of sources and receivers, respectively. Within this section, I

analyse practical aspects and discuss possible scenarios for future applications of SRI in earthquake seismology.

4.2.1 Effect of approximations in the interferometric formulae

The synthetic experiment performed using data generated with the exact, error-free Foldy modelling method (Section 3.2) provided a good starting point to describe the different steps of SRI and its practical application. By using a canonical geometry of sources and receivers and the approximate interferometric formulae in equations (3.2) and (3.4), the recording between a source and a receiver was constructed using the principles of SRI, and the SRI trace closely matched the true trace (Fig. 3.4(b)).

Since we can be confident that no errors were introduced into the data by the modelling method itself, any discrepancy between the SRI and the true trace can safely be attributed to the application of interferometry. For instance, the small-amplitude arrival near 0.09 s on the SRI trace in Fig. 3.4 can be interpreted as a non-physical artefact since no energy should reach the receiver before the large-amplitude direct arrival. This non-physical arrival is the result of cross-correlation of scattered monopole wavefields to $\mathbf{s}$ and $\mathbf{r}$, and its amplitude is proportional to the energy diffracted by the scatterer that produced it. Non-physical events of similar origin were also observed in the monopole inter-receiver interferometry example presented in Chapter 2 (Fig. 2.5), and using equation (2.17) they were related to the paths of scattered energy that produced them. By applying equation (2.17) to the geometry of this experiment (Fig. 3.2), we obtain an arrival time for this non-physical event of ~ 0.09 s, which matches what is observed on the SRI trace in Fig. 3.4(b). Given that both enclosing boundaries are full, that care was taken in setting the spacing between boundary sources and receivers to less than half the Nyquist wavelength, and that sufficient sources and receivers are therefore located in all possible stationary-phase regions, the origin of this spurious event might be attributed to the lack of dipole Green's functions in the approximate interferometric formulae. Indeed, when the same experiment is conducted using the exact interferometric formulae in SRI (i.e., equations (3.1) and (3.3)) which include dipole Green's functions, this non-physical event does not appear, and the two traces match perfectly (Fig. 4.3).

One of the assumptions made when the interferometric formulae are approximated is that the surrounding boundaries of sources and receivers are large. Hence, the amplitude of this non-physical event might decrease if the size of the enclosing boundaries is increased to a larger radius than in this example. However, this also means that many more sources and receivers would need to be placed on the boundaries in order to maintain the same sub-Nyquist source and receiver spacing. Because this requires a much larger memory capacity, it was not attempted within this project given the limited memory available, but might provide an interesting point to test the impact of one of the assumptions made when approximating the exact interferometric equations. In addition, the results of this

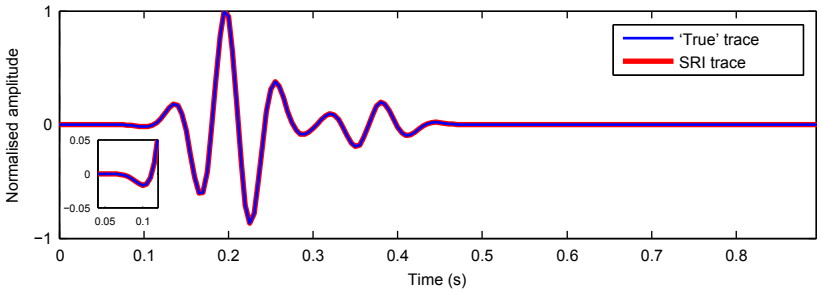

Figure 4.3. Comparison of Green's function constructed using SRI (thick red trace) with the true Green's function (thin blue trace) from source **s** to receiver **r** as shown in Fig. 3.2. The exact interferometric formulae in equations (3.2) and (3.4) are used in SRI. The 'true' Green's function is obtained by convolving the true Green's function in Fig. 3.4(a) with the square of the complex conjugate of the source wavelet. The magnified panel highlights the part of the SRI trace where a non-physical arrival was present when the approximate interferometric formulae were used in SRI (Fig. 3.4(b)).

synthetic experiment, performed using an ideal geometry of sources and receivers on error-free data, constitute a good point of reference to which the results of SRI on real data can be compared.

4.2.2 Correlation-correlation versus correlation-convolution approach

The large-scale example discussed in Section 3.4 extends the application of SRI to earthquake seismology scales where acquisition conditions are far from ideal scenarios. In this example, and in all of the other large-scale examples presented in Entwistle et al. (2015), boundary sources are constituted by ambient-noise sources whose location is generally unknown, boundary receivers may be inactive during some of the recording period or entirely missing, and the medium is most likely scattering and attenuative. Nevertheless, the SRI results in Fig. 3.9 display a relatively good match with the true traces recorded at the target sensors.

In some cases, spurious arrivals such as the one highlighted by the grey ellipse in Fig. 3.9(a) are present, and may be associated with non-physical energy which arises from the cross-correlation of direct wavefields with scattered wavefields. As noticed in initial experiments by Halliday & Curtis (2009a) and more recently by Meles & Curtis (2014a) and Löer et al. (2014), these events should cancel upon integration over the receiver boundary, but this does not occur when the integration boundaries are incomplete or when the medium is strongly scattering or attenuative. In the latter case, energy is lost during the propagation of the wavefield from the boundary sources to the receivers, hence wavefields may not be time-reversed without also re-injecting the attenuated energy (Snieder, 2007). Since the operation of cross-correlation involves the time-reversal (i.e., complex conjugation in the frequency domain) of one of the two waveforms and the Earth's crust in this area is likely to be attenuative, non-physical events are therefore introduced when ambient-noise records are cross-correlated to create

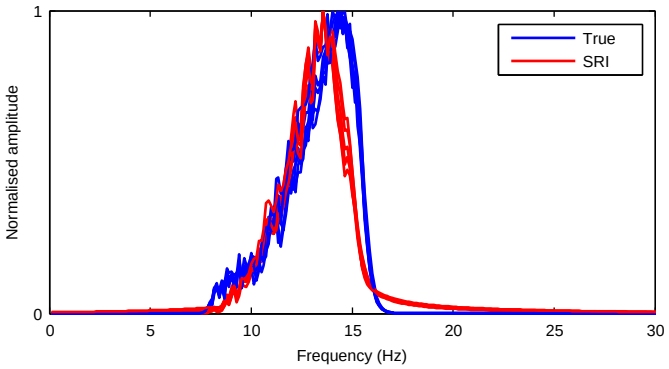

Figure 4.4. Frequency spectra for the true (blue) and SRI (red) traces in Fig. 3.7, representing the wavefield from source $\mathbf{s}$ to target sensors $\mathbf{r}_i$ in Fig. 3.5. Note that the true recordings have a slightly higher frequency content compared to the SRI results despite being band-pass filtered within the same frequency band of 8–15.5 Hz.

the set of target sensor to backbone array Green's functions. Non-physical events may also be generated by scatterers located outside bounding surfaces S and S' which can diffract energy back into the boundaries, contradicting one of the basic assumptions made by the approximate interferometric formulae (equations (3.2) and (3.4)) that no energy may re-enter a boundary once it has left (Wapenaar & Fokkema, 2006). All of these spurious arrivals created during the first, inter-receiver step of SRI are propagated to the second inter-source step, giving rise to the artefacts that we can observe in Fig. 3.9.

Halliday & Curtis (2009a) propose that the operation of convolution may be a better choice than cross-correlation when the medium is strongly attenuative, since the former does not involve time-reversal. In fact, in an example which uses the same earthquake and array of target receivers but a different backbone array located between the target source and receiver, more accurate Green's function estimates were produced by Entwistle et al. (2015) when cross-correlation was replaced with convolution in the inter-source step of SRI. In this case, any non-physical arrival resulting from the first inter-receiver step was suppressed during the inter-source step of SRI thanks to the process of convolution.

In the engineering scale experiment described in Section 3.3, such non-physical arrivals are not observed when SRI is performed using a correlation-correlation approach. However, although band-pass filters were applied before each step of SRI to ensure coherency between the waveforms in the frequency domain, we found that the true recordings always appeared to contain slightly higher frequencies compared to the SRI traces constructed between source $\mathbf{s}$ and target sensors $\mathbf{r}_i$ (Fig. 4.4). This is likely to be due to attenuation of high frequencies as energy produced by boundary sources $\mathbf{x}'$ travels towards the backbone receivers $\mathbf{x}$. Since this propagation path is tens of meters long and high frequencies are normally more easily attenuated than lower frequencies, it is likely that a relatively large amount of energy is lost at high frequencies, while less energy is lost at low frequencies. This in turn causes the results of inter-receiver and then

inter-source interferometry to have a lower high-frequency content than the true recordings from $\mathbf{s}$ to $\mathbf{r}_i$. Since the dataset for this small-scale experiment also includes records from a boundary of sources located between the target and backbone receivers, the results of SRI could therefore be improved by using convolution rather than cross-correlation in the first inter-receiver step. In hindsight, previous work by Duguid (2010) on the same dataset also showed that convolution in (inter-source) interferometry performs better than interferometry by cross-correlation in this acquisition area. Hence, as shown in the large-scale experiment discussed above, an SRI approach combining convolution and cross-correlation might provide a fruitful alternative to purely correlational SRI, and produce more robust Green's function estimates in attenuative and strongly scattering media.

4.2.3 Effect of spatial irregularities on enclosing boundaries

Coarse sampling and irregularities on source and receiver boundaries have been shown to substantially reduce the quality of the Green's functions estimated with SRI (Löer et al., 2014). Within the earthquake-scale SRI example presented in Section 3.4, an attempt was made to compensate for irregularities in the array of backbone receivers by discretising the integral over boundary S in equation (3.4) using Voronoi cells. As shown in the top-right corner of Fig. 3.8, the relatively irregular distribution of seismic stations, together with the fact that stations at desired locations were sometimes missing, caused a relatively large variability in the shape and size of the different Voronoi cells. By weighting the contribution of the inter-source cross-correlation computed at each backbone seismometer by the (tapered) normalised area of its corresponding Voronoi cell, SRI Green's function estimates which closely matched the true recordings were obtained (Fig. 3.9(a)). In contrast, the quality of the interferometric Green's functions considerably decreased when a simple unweighted summation was performed over the backbone receivers (Fig. 3.9(b)). Compared to the Voronoi-weighted results in Fig. 3.9(a), most of the SRI Green's functions obtained with direct, unweighted stacking in Fig. 3.9(b) present large-amplitude non-physical energy before the main surface-wave arrival, and the correlation coefficients between the true and interferometric traces are generally lower than those calculated when Voronoi interpolation is performed. Hence, the use of Voronoi interpolation appears to considerably enhance the results obtained when evaluating the inter-source interferometric integral. Due to source-receiver reciprocity, we would therefore expect similar benefits to be obtained in inter-receiver interferometry if a similar approach was adopted in acquisition scenarios where the location of boundary sources is known.

The absence of seismic stations at locations assumed to correspond to the points of stationary phase appears to be a further factor which causes the quality of SRI results to degrade. For instance, consider the Green's functions constructed at stations Z27A and

627A in Fig. 3.9(a), which were computed using backbone receiver lines V–W and 2–3, respectively. As can be seen in Fig. 3.8, lines V and 3 are the most spatially irregular, and the results of SRI at the corresponding target receivers present the lowest correlation coefficients in Fig. 3.9(a). These poor reconstructions are likely to be due to unfilled boundary positions on lines V and 3, which breaks the requirement of a sufficient number of receivers to be located in the regions of stationary phase. In addition, further examples in Entwistle et al. (2015) showed that the quality of Green's function estimates also appears to be affected by the lateral extent of the backbone array with respect to its distance from the target sensors. Insight on possible causes of this behaviour is given in the next section.

4.2.4 Sampling of stationary-phase regions – synthetic examples

The study of the regions of stationary phase is still a relatively unexplored area of seismic interferometry. Nevertheless, a number of studies including the recent earthquake-scale work by Entwistle et al. (2015) discussed above, and previous work by Duguid (2010) on a small-scale dataset, showed that reducing the integration boundaries in inter-receiver, inter-source and source-receiver interferometry to the regions of stationary phase can substantially improve interferometric Green's function estimates. Moreover, the sampling of integration boundaries appears to play an important role on the quality of interferometric Green's functions, particularly in connection with the distance between the boundary and the locations at which Green's functions are to be constructed. In this section, I provide a number of synthetic examples that highlight how different amounts of non-physical energy are introduced into the results of interferometry depending on the sampling of the surrounding boundaries, and particularly of the regions of stationary-phase. These examples should not be regarded as a completed piece of work, but rather as the starting point for further studies on this subject. In addition, while all of the following examples examine the case of inter-receiver interferometry, due to source-receiver reciprocity similar effects are likely to be observed in inter-source and source-receiver interferometry scenarios.

Consider the case illustrated in Figs 4.5–4.7: here, inter-receiver interferometry is used to construct the Green's function between two pairs of receivers located in the centre (blue triangles at $\mathbf{x}_A$ and $\mathbf{x}_B$) and near the edge (green triangles at $\mathbf{x}_C$ and $\mathbf{x}_D$) of the boundary of sources. Waveform data is generated using the exact Foldy method to model 2048 frequencies between ~ 0.05 and 100 Hz in a medium of velocity 1000 m s^{-1}, and a Ricker wavelet centred on 20 Hz is applied to the analytical Green's functions. Interferometry is performed using the exact interferometric formulae for positive volume injection sources (Appendix A.2.2), hence no approximations are made in interferometric theory.

When the spacing between the boundary sources is set to half the Nyquist wavelength (5 m) as in Fig. 4.5(a), and cross-correlations between source pairs $\mathbf{x}_A$–$\mathbf{x}_B$ and $\mathbf{x}_C$–$\mathbf{x}_D$ are computed for each boundary source, the cross-correlation gathers in Figs 4.5(b)–(c) are

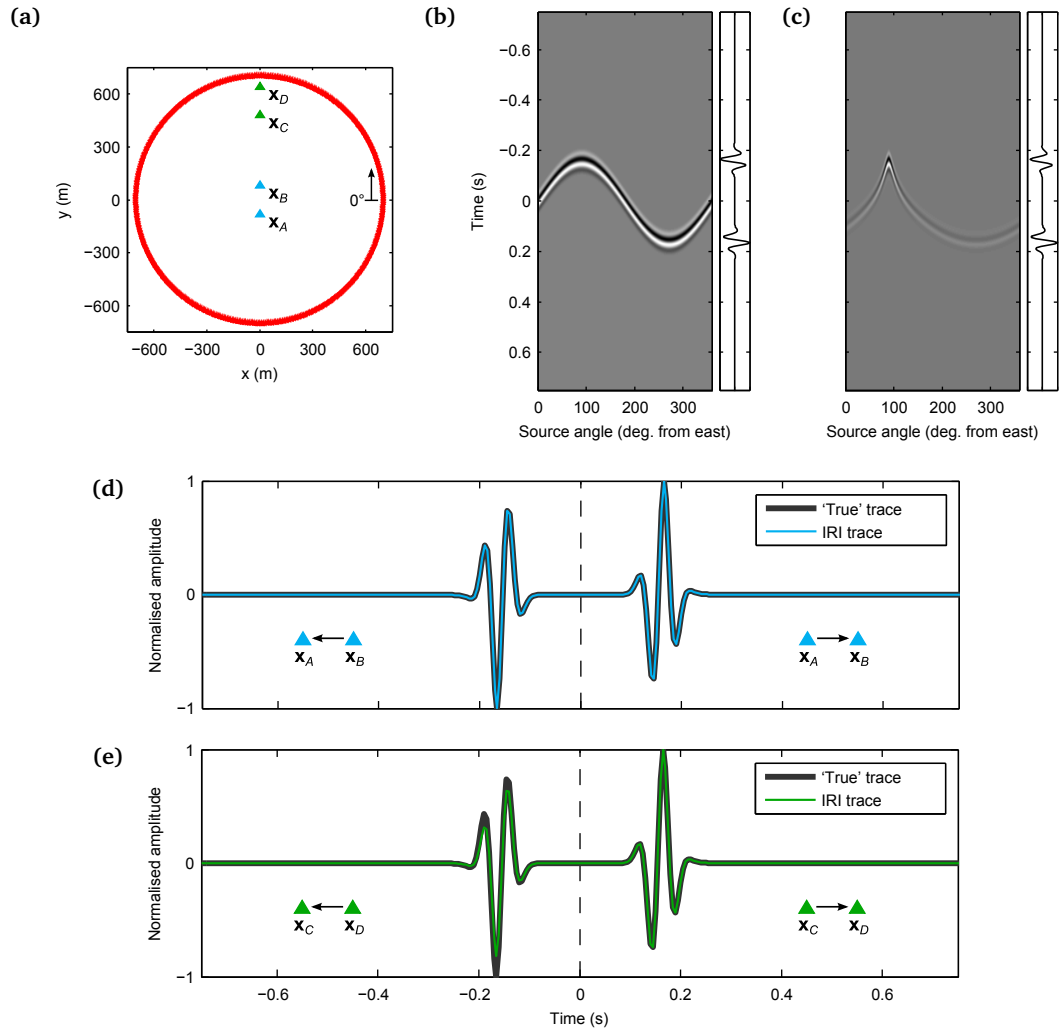

Figure 4.5. Synthetic inter-receiver interferometry (IRI) example in which a spacing of 5 m (half of the Nyquist wavelength) between boundary sources is used. The data was generated using the Foldy code to model 2048 frequencies between $\sim$ 0.05 and 100 Hz in a medium of velocity 1000 m s^{-1}, and applying a Ricker wavelet centred on 20 Hz. Positive volume injection sources were used to generate the wavefields, and interferometry was performed using the exact formulae in Appendix A.2.2. (a) Geometry: 880 sources (red stars) surround two pairs of receivers ($\mathbf{x}_A$–$\mathbf{x}_B$ and $\mathbf{x}_C$–$\mathbf{x}_D$) between which the Green's function is constructed. (b) Cross-correlation gather for $\mathbf{x}_A$–$\mathbf{x}_B$ (left) and sum of all of the cross-correlations (right) giving the causal and acausal Green's function between $\mathbf{x}_A$ and $\mathbf{x}_B$. (c) Cross-correlation gather for $\mathbf{x}_C$–$\mathbf{x}_D$ (left) and sum of all of the cross-correlations (right) giving the causal and acausal Green's function between $\mathbf{x}_C$ and $\mathbf{x}_D$. (d) Comparison of Green's function from IRI (thin blue trace) and 'true' Green's function (thick dark grey trace) for receiver pair $\mathbf{x}_A$–$\mathbf{x}_B$. (e) Comparison of Green's function from IRI (thin green trace) and 'true' Green's function (thick dark grey trace) for receiver pair $\mathbf{x}_C$–$\mathbf{x}_D$. Note that, for a proper comparison with the IRI results (see equation (A.48)), the 'true' Green's functions are created by convolving the true analytical Green's functions with the complex conjugate of the source wavelet and stacking this signal with its inverted time-reverse. In panels (d) and (e) the causal parts represent energy travelling in directions $\mathbf{x}_A \rightarrow \mathbf{x}_B$ and $\mathbf{x}_C \rightarrow \mathbf{x}_D$; the acausal parts represent energy travelling in directions $\mathbf{x}_B \rightarrow \mathbf{x}_A$ and $\mathbf{x}_D \rightarrow \mathbf{x}_C$. The source angle in panels (b) and (c) is measured anti-clockwise from [700 0] m as indicated by the arrow in panel (a).

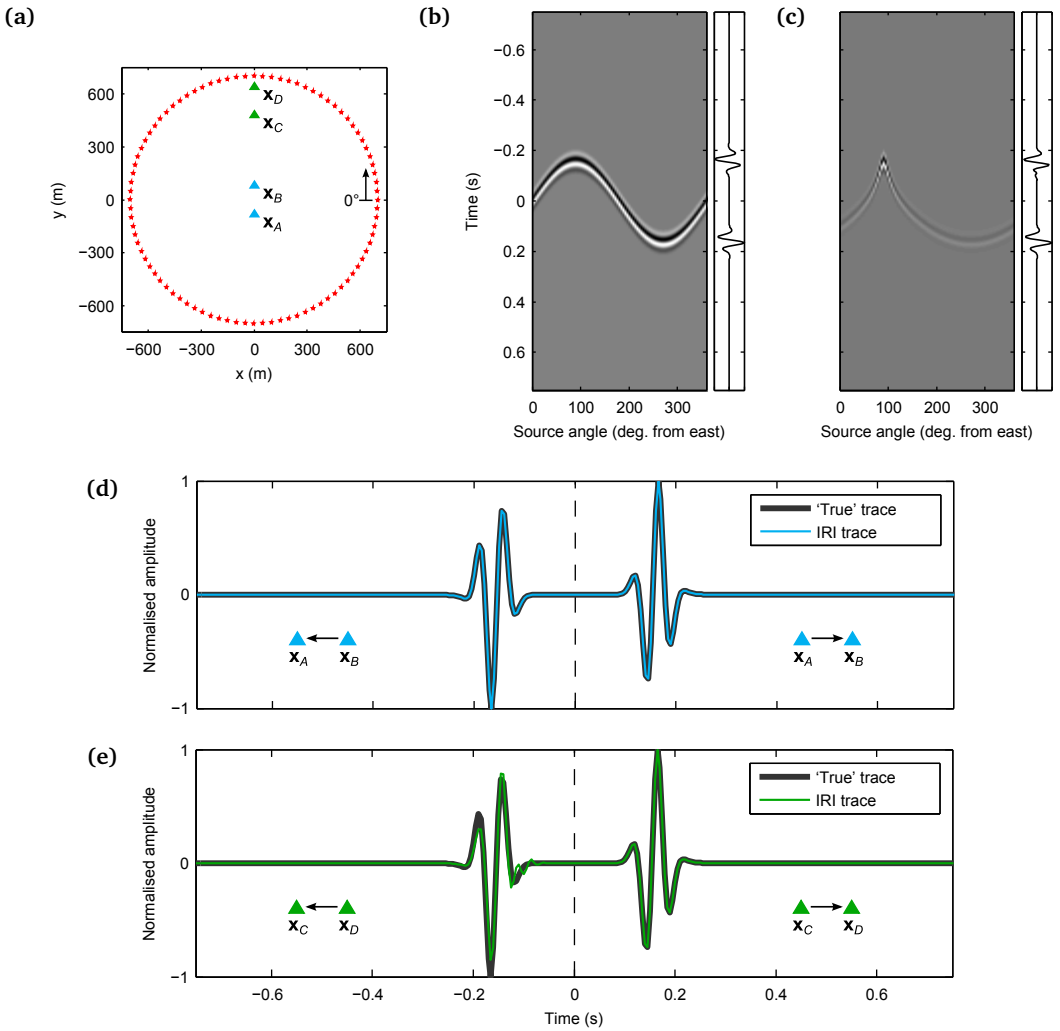

Figure 4.6. Synthetic inter-receiver interferometry (IRI) example in which a spacing of 50 m (ten times that used in the example in Fig. 4.5) between boundary sources is used. The data was generated using the Foldy code to model 2048 frequencies between ~ 0.05 and 100 Hz in a medium of velocity 1000 m s^{-1}, and applying a Ricker wavelet centred on 20 Hz. Positive volume injection sources were used to generate the wavefields, and interferometry was performed using the exact formulae in Appendix A.2.2. (a) Geometry: 88 sources (red stars) surround two pairs of receivers ($\mathbf{x}_A$–$\mathbf{x}_B$ and $\mathbf{x}_C$–$\mathbf{x}_D$) between which the Green's function is constructed. (b) Cross-correlation gather for $\mathbf{x}_A$–$\mathbf{x}_B$ (left) and sum of all of the cross-correlations (right) giving the causal and acausal Green's function between $\mathbf{x}_A$ and $\mathbf{x}_B$. (c) Cross-correlation gather for $\mathbf{x}_C$–$\mathbf{x}_D$ (left) and sum of all of the cross-correlations (right) giving the causal and acausal Green's function between $\mathbf{x}_C$ and $\mathbf{x}_D$. (d) Comparison of Green's function from IRI (thin blue trace) and 'true' Green's function (thick dark grey trace) for receiver pair $\mathbf{x}_A$–$\mathbf{x}_B$. (e) Comparison of Green's function from IRI (thin green trace) and 'true' Green's function (thick dark grey trace) for receiver pair $\mathbf{x}_C$–$\mathbf{x}_D$. Note that, for a proper comparison with the IRI results (see equation (A.48)), the 'true' Green's functions are created by convolving the true analytical Green's functions with the complex conjugate of the source wavelet and stacking this signal with its inverted time-reverse. In panels (d) and (e) the causal parts represent energy travelling in directions $\mathbf{x}_A \rightarrow \mathbf{x}_B$ and $\mathbf{x}_C \rightarrow \mathbf{x}_D$; the acausal parts represent energy travelling in directions $\mathbf{x}_B \rightarrow \mathbf{x}_A$ and $\mathbf{x}_D \rightarrow \mathbf{x}_C$. The source angle in panels (b) and (c) is measured anti-clockwise from [700 0] m as indicated by the arrow in panel (a).

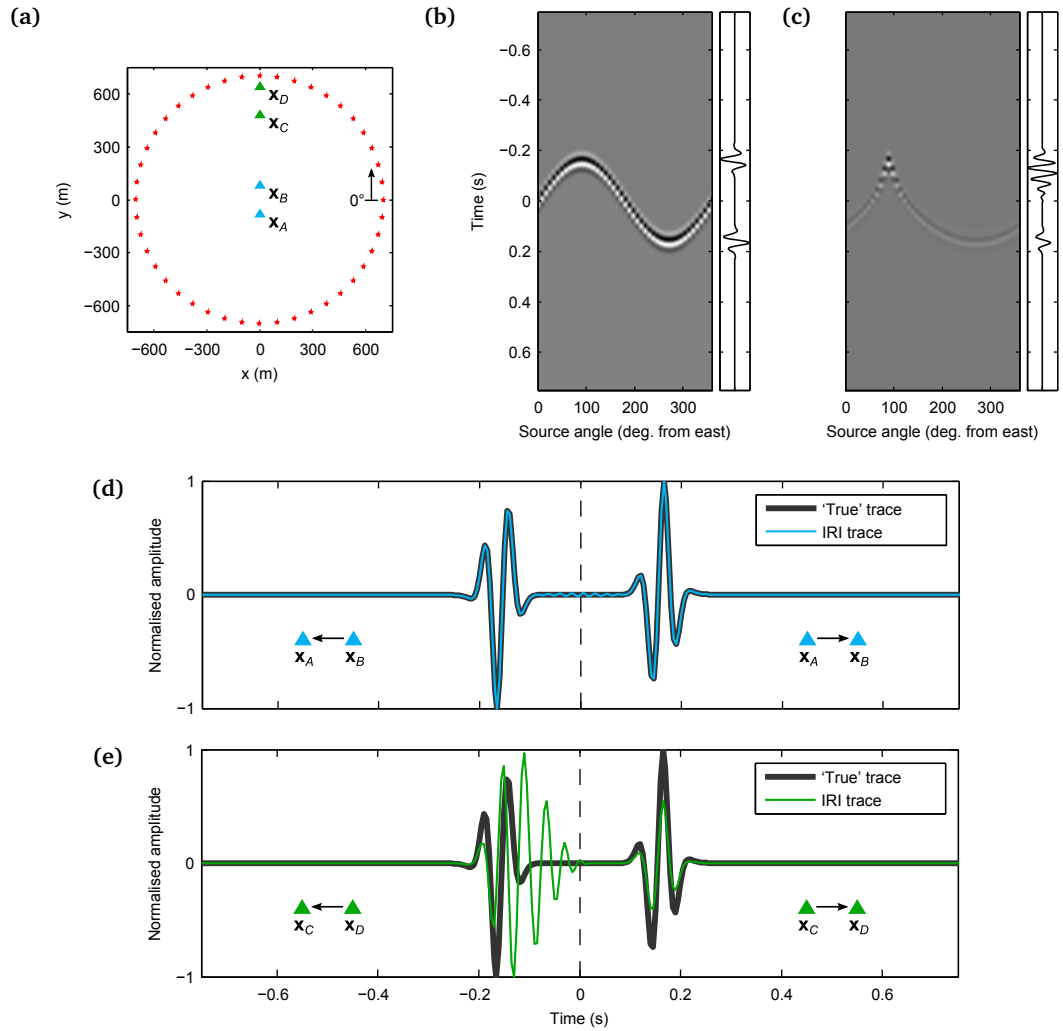

Figure 4.7. Synthetic inter-receiver interferometry (IRI) example in which a spacing of 100 m (twenty times that used in the example in Fig. 4.5) between boundary sources is used. The data was generated using the Foldy code to model 2048 frequencies between ∼ 0.05 and 100 Hz in a medium of velocity 1000 m s^{-1}, and applying a Ricker wavelet centred on 20 Hz. Positive volume injection sources were used to generate the wavefields, and interferometry was performed using the exact formulae in Appendix A.2.2. (a) Geometry: 44 sources (red stars) surround two pairs of receivers ($\mathbf{x}_A$–$\mathbf{x}_B$ and $\mathbf{x}_C$–$\mathbf{x}_D$) between which the Green's function is constructed. (b) Cross-correlation gather for $\mathbf{x}_A$–$\mathbf{x}_B$ (left) and sum of all of the cross-correlations (right) giving the causal and acausal Green's function between $\mathbf{x}_A$ and $\mathbf{x}_B$. (c) Cross-correlation gather for $\mathbf{x}_C$–$\mathbf{x}_D$ (left) and sum of all of the cross-correlations (right) giving the causal and acausal Green's function between $\mathbf{x}_C$ and $\mathbf{x}_D$. (d) Comparison of Green's function from IRI (thin blue trace) and 'true' Green's function (thick dark grey trace) for receiver pair $\mathbf{x}_A$–$\mathbf{x}_B$. (e) Comparison of Green's function from IRI (thin green trace) and 'true' Green's function (thick dark grey trace) for receiver pair $\mathbf{x}_C$–$\mathbf{x}_D$. Note that, for a proper comparison with the IRI results (see equation (A.48)), the 'true' Green's functions are created by convolving the true analytical Green's functions with the complex conjugate of the source wavelet and stacking this signal with its inverted time-reverse. In panels (d) and (e) the causal parts represent energy travelling in directions $\mathbf{x}_A \rightarrow \mathbf{x}_B$ and $\mathbf{x}_C \rightarrow \mathbf{x}_D$; the acausal parts represent energy travelling in directions $\mathbf{x}_B \rightarrow \mathbf{x}_A$ and $\mathbf{x}_D \rightarrow \mathbf{x}_C$. The source angle in panels (b) and (c) is measured anti-clockwise from [700 0] m as indicated by the arrow in panel (a).

obtained. As expected, while the move-out for the central receiver pair follows a relatively regular, sinusoid-like curve, the move-out obtained for the receiver pair located near the edge of the boundary has a more irregular shape, with a narrower peak in the acausal part (due to energy travelling from $\mathbf{x}_D$ to $\mathbf{x}_C$) and a wider peak in the causal part (due to energy travelling from $\mathbf{x}_C$ to $\mathbf{x}_D$). As these two gathers are stacked, the interferometric Green's functions in Figs 4.5(d)–(e) are obtained as a result of constructive and destructive interference between neighbouring traces. Since the source spacing is small and a sufficiently large number of sources are present on the boundary, both interferometric Green's functions yield a good match to the true signals at positive and negative times.

When boundary sources are decimated by a factor of ten, increasing the source spacing to 50 m (Fig. 4.6(a)), the interferometric traces in Figs 4.6(d)–(e) are obtained. In this case, the interferometric Green's function obtained for the central receiver pair (Fig. 4.6(d)) still matches the true signal relatively well, while spurious arrivals are introduced into the Green's function constructed for the receiver pair located near the boundary. However, these non-physical events only seem to appear in the acausal part of the signal, representing energy travelling from $\mathbf{x}_D$ to $\mathbf{x}_C$, while no spurious arrivals are visible in the causal part which represents energy travelling in the opposite direction.

Looking at the acausal part of the cross-correlation gather in Fig. 4.6(c), we see that these spurious arrivals correspond to the narrow peak in the move-out at negative times, and are likely to be caused by incomplete cancellation of energy upon stacking over the coarsely-sampled boundary. However, the same coarse spacing does not seem to influence the interferometric results at positive times, where the move-out in the cross-correlograms is much wider and smoother due to the larger distance between the stationary-phase sources and the receivers in question.

Similar results are obtained when the boundary sources are decimated by a factor of twenty relative to those in Fig. 4.5, increasing the source spacing to 100 m (Fig. 4.7). In this case, small-amplitude non-physical events are introduced before the main arrival in the Green's function constructed between the central pair of receivers (Fig. 4.7(d)). However, the largest amount of non-physical energy is found in the acausal part of the Green's function in Fig. 4.7(e), representing energy travelling from $\mathbf{x}_D$ to $\mathbf{x}_C$. In contrast, despite a mismatch in amplitude, the Green's function constructed in the opposite direction still matches the true signal relatively well.

Hence, the sampling interval of the integration boundary appears to more or less affect the quality of the results depending on the distance between the stationary-phase sources and the location of the receivers in question. Although this was here only demonstrated in the case of inter-receiver interferometry, due to source-receiver reciprocity we also expect this to be the case in inter-source interferometry. Moreover, the results shown in Figs 4.5–4.7 are intuitively correct, since they simply demonstrate that denser information is needed to produce accurate results at short length scales, while

coarser sampling might still produce acceptable results at larger distances. With respect to the cross-correlation gathers in panel (c) of Figs 4.5–4.7, this means that the narrow move-out at negative times requires fine sampling in order to yield accurate Green's function estimates, while the wider move-out at positive times may still provide acceptable results when sampled coarsely. Although the examples in Figs 4.5–4.7 simply serve to briefly illustrate this concept, a detailed study of this relationship might constitute an interesting point for further research and provide useful guidelines for future applications of interferometry using partial boundaries.

4.2.5 Future applications of retrospective seismology

In the small- and large-scale examples presented in Chapter 3, SRI successfully allowed Green's functions to be constructed between a source and a set of target receivers, some of which were not installed at the time of occurrence of the source. Despite being currently limited to narrow ranges of frequencies, these results are encouraging and pave the way for a new type of 'retrospective' seismology in which the energy from a seismic source may be redatumed in space and time onto new sensor locations, even long after this energy has dissipated.

Within earthquake seismology, dense seismometer networks which include both permanent and temporary seismic stations, such as the USArray, provide ideal acquisition conditions for this form of retrospective seismology to be applied. Ideally, a large permanent array of seismometers could be used as a backbone array to obtain both earthquake and continuous ambient-noise records. A smaller temporary array (i.e., the target sensors) could then be deployed to record ambient noise, and moved to different locations within the permanent array at regular intervals of $\sim$ 6 months (i.e., long enough to produce reliable Green's functions from ambient-noise interferometry). A database of inter-station Green's functions could then be constructed between permanent and temporary stations by simply cross-correlating ambient noise recorded during the overlapping recording times of the two networks. Thus, any earthquake occurring near the designated location of a temporary seismometer before or after its deployment, could quickly be redatumed onto the target seismometer by using the inter-station Green's functions in the database and the earthquake records from the permanent array as described in Chapter 3.

Finally, Curtis et al. (2012) show that it is possible to obtain the phase of the source time function T by deconvolving the acausal part ($A = T^*G^*$) of the SRI Green's function from its causal component ($C = T^*G$), without the use of inverse theory. However, this requires backbone arrays to be located on either side of the target source and receivers, which was not the case in either of the real-data examples presented in Chapter 3.

Part II

Non-linear tomography

CHAPTER 5

Non-linear transdimensional tomography: theory and method

In Earth science, a number of inverse problems aim at answering the following question: "Given a set of available data, what can we infer about the Earth's properties?". Within seismology, tomography (from Greek τομή, meaning slice) is a type of inverse problem which uses recorded seismic wave energy to obtain images (2D slices) of the Earth's interior. Although it is now a widely used method in geophysics, the origins of tomography lie in the medical field, where it is common practice to produce images of the interior of the body using X-rays. Just as X-rays are attenuated differently by the different tissues that constitute the human body, the propagation of seismic waves is affected by the different lithologies that make up the subsurface of the Earth. Typically, a set of source-to-receiver traveltimes can be inverted to obtain a map of seismic velocities within the Earth, and since relationships exist between seismic velocity and rock composition such maps can be used to identify and locate different geological formations.

In this chapter I describe various steps that were taken within this project to produce group-velocity maps of the British Isles from ambient noise interferometry. I begin by describing the station networks for which ambient noise recordings were obtained and provide an overview of the data processing techniques employed. I then describe how ambient noise cross-correlations were used to obtain inter-station traveltimes along a number of paths, and finally how these traveltimes were used to produce Love-wave group velocity maps of the British Isles using a fully non-linear version of the reversible-jump Markov chain Monte Carlo algorithm.

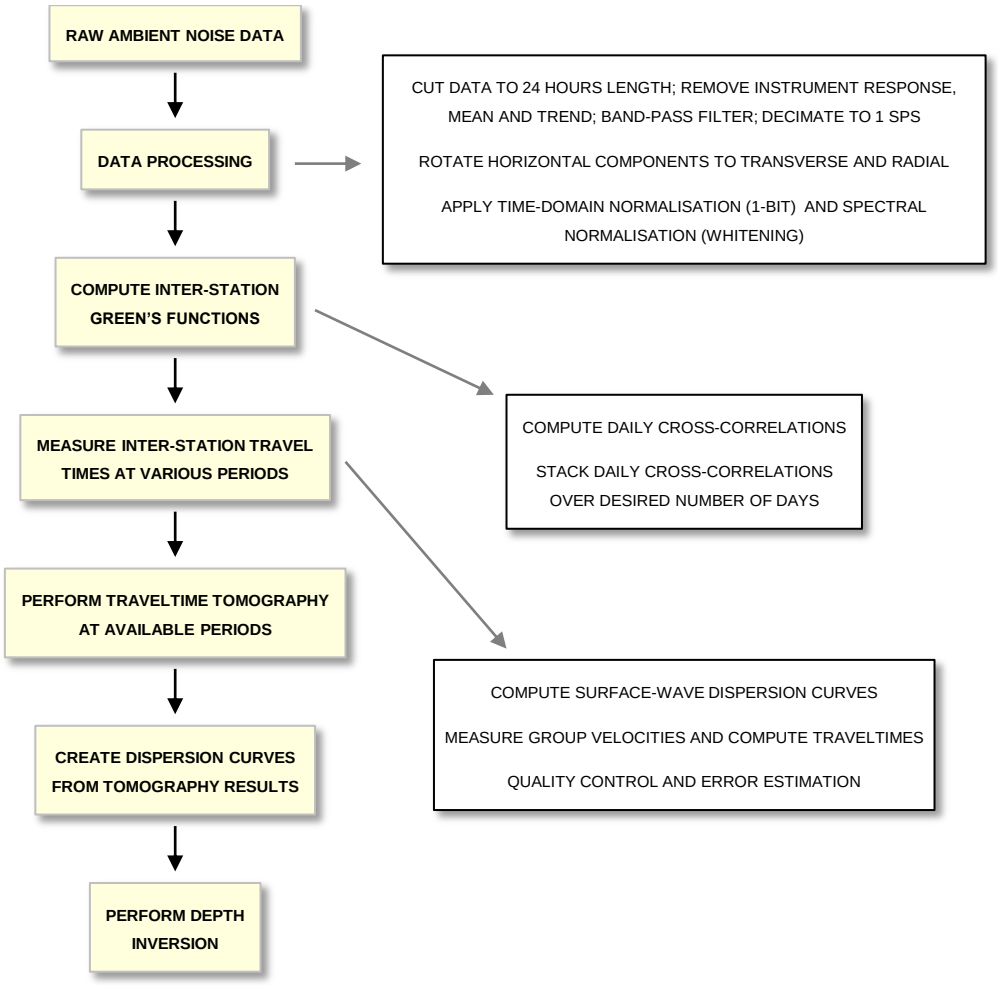

Figure 5.1. Schematic summary of data processing and inversion workflow.

5.1 From ambient noise to seismic velocity maps: the workflow

We followed the workflow displayed in Fig. 5.1 to produce seismic velocity maps of the British Isles from seismic ambient noise. Continuous ambient noise records were obtained from several stations belonging to a number of different networks across the region. Raw noise records were pre-processed following the guidelines of Bensen et al. (2007) and then cross-correlated to produce a dataset of inter-station Green's functions. We then applied the frequency-time analysis method of Herrmann & Ammon (2002) to calculate dispersion curves and obtain a series of inter-station seismic traveltimes in various frequency bands. These traveltimes constituted the datasets that were used to perform Love-wave traveltime tomography at different periods. Finally, we created a set of dispersion curves from the results of tomography, and used a surface-wave dispersion inversion method to estimate the shear-velocity structure beneath the Irish Sea. The latter stage of this study is described separately in Section 7.6.

5.2 Stations and data processing

Raw ambient noise records were obtained and pre-processed by Heather Nicolson (a former PhD student) and Brian Baptie (head of Seismology at the British Geological Survey). In this section, I therefore provide a concise summary of the station networks and processing techniques employed, and refer the reader to Heather Nicolson's PhD thesis (Nicolson, 2011) for more details.

5.2.1 Stations

Although well known for being a seismically quiescent region, the British Isles are characterised by the presence of a relatively large number of seismic stations, most of which have been recording continuously for the last decade. The continuous ambient noise records used within this project were obtained from a number of seismic stations belonging to different networks across the region (Fig. 5.2–5.3):

- 23 stations from the Reflections Under the Scottish Highlands (RUSH-II) array in Scotland, a temporary network of broadband seismometers which were deployed in the early 2000s with the aim of identifying mantle reflectors beneath the Scottish Highlands (Asencio et al., 2003; Bastow et al., 2007). The array was arranged along three approximately linear profiles, and recorded seismic noise continuously for two years from August 2001 (except for a gap of approximately six months in 2002).
- 29 stations from the British Geological Survey (BGS) network in Scotland and England. The BGS network includes broadband and short-period instruments, many of which have been recording data continuously since the early 2000s.
- 3 stations from the Atomic Weapons Establishment (AWE) Blacknest array in England. The AWE Blacknest array was created as part of the UK's pioneering efforts to record teleseismic earthquakes, and is currently part of an international system for monitoring nuclear explosions.
- 5 stations from the British Isles Seismic Experiment (BISE) network in England, which was deployed with the aim of constructing seismic receiver functions across southern Britain.
- 1 station from the Observatories and and Research Facilities for European Seismology (ORFEUS) network in Ireland.

All stations recorded the vertical (Z) and horizontal (east – E, and north – N) components of seismic ambient noise. Continuous noise measurements were available for BGS, AWE Blacknest and ORFEUS stations for most of 2010. Since the majority of inter-station raypaths from these three networks were oriented in the north-south direction, the

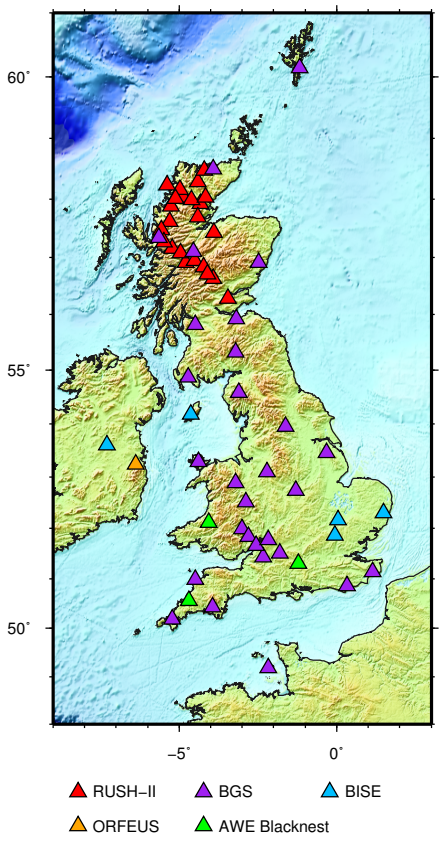

Figure 5.2. Station location map.

decision to include BISE stations in the dataset was made in an attempt to improve the resolution in the east-west direction. Ambient noise data from BISE stations was available for 2006-2007, and cross-correlation with BGS, AWE Blacknest and ORFEUS stations were only possible if the latter were active at the recording time of BISE. From here onwards, the combination of BGS, AWE Blacknest, BISE and ORFEUS stations will be referred to as the "UK-wide" array. Since no cross-correlations were produced between RUSH-II stations and the UK-wide array, the traveltime datasets resulting from the two arrays may be considered as completely independent.

5.2.2 Data processing

In order to obtain high quality Green's functions for use in traveltime tomography, a series of pre-processing steps must be applied to raw ambient noise records prior to cross-correlation. The aim of these steps is to accentuate the coherent noise signal by removing unwanted events (e.g., earthquakes) and instrument irregularities. As some of the pre-processing operations introduce non-linear changes to the waveforms, it is important for these steps to be applied in the correct order. Following this pre-processing stage, noise cross-correlations may be computed between the available stations.

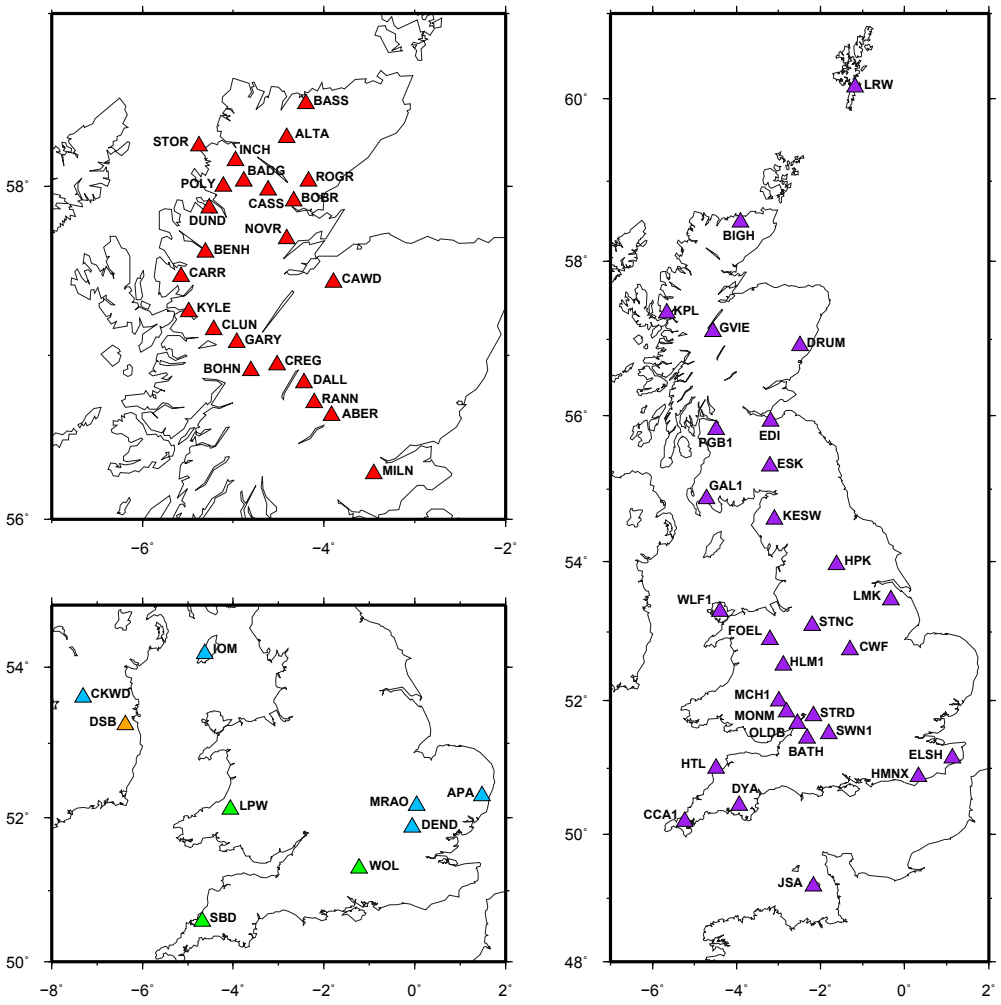

Figure 5.3. Location map of RUSH-II (red triangles), BGS (purple triangles), AWE Blacknest (green triangles), BISE (blue triangles) and ORFEUS (orange triangles) stations.

Within this study, the pre-processing and cross-correlation of noise data was carried out by Heather Nicolson and Brian Baptie, who broadly followed the guidelines of Bensen et al. (2007). Here I provide an outline of the methods that they applied to produce a set of transverse-component Green's functions from ambient noise cross-correlations. These Green's functions constituted the dataset which I subsequently processed to obtain a set of inter-station traveltimes for tomography.

Single station data pre-processing

Raw single-station ambient noise files were pre-processed using the Seismic Analysis Code (SAC) and automated routines. Noise records from all stations were first converted to SAC format (if not in this format already) and then cut to 24-hour-long files, from midnight to midnight. The mean was removed from each day file to ensure that the amplitude axis was centred on zero. Linear trends in the data were also removed by fitting a straight line

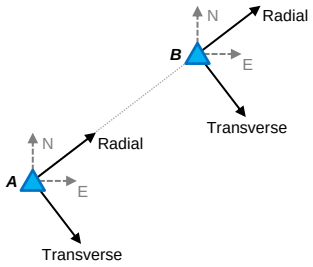

Figure 5.4. Definition of radial and transverse components of ground motion with respect to the recorded north (N) and east (E) components.

through each day-file and then subtracting it from the data, ensuring the removal of the effect of any instrument-related trends from the signals.

Since the different networks included different types of seismic instruments, the instrument response associated to each seismometer was removed by deconvolving it from each day-file using the *transfer* function in SAC. All waveforms were then transformed to recordings of ground velocity, and the data was finally band-pass filtered by applying a 5–50 seconds band-pass filter to the RUSH-II dataset and a high-pass filter at 100 seconds to the UK-wide data. In order to reduce both the storage space and computational power required for processing, the data was decimated to a sampling rate of one sample per second. Although this imposed a limit on the lowest period that could be recovered, it did not affect the period range we were interested in analysing.

In order to compute Love-wave Green's functions, the east and north components of noise were rotated into the radial and transverse components using the *rotate* command in SAC. Taking the pair of stations in Fig. 5.4 as an example, this was done by temporarily changing the SAC headers to set the event location to station A and the receiver location to station B. The north component was rotated into the radial direction, lying along the great circle arc which joins the two stations and pointing from station A to station B. The east component was then rotated into the transverse direction, ninety degrees with respect to the radial direction.

Next, the transverse components for each station were normalised in both the time and frequency domain. The aim of time domain normalisation is the removal of non-stationary noise sources from the data, such as large amplitude events (e.g., earthquakes) and instrument abnormalities. Bensen et al. (2007) describe a variety of temporal normalisation methods and favour the use of either running-absolute-mean or water-level normalisation. However, both methods are computationally expensive and are generally prescribed for data recorded in areas of high seismicity. Since the British Isles are known to be a seismically quiet region, the noise data for this study was normalised in the time domain using the less expensive one-bit normalisation, which divides each time-sample by its absolute value retaining only the sign of the original signal (i.e., all positive amplitudes are replaced by a $+1$ and all negative amplitudes by a -1).

Normalisation in the frequency domain aims at broadening the frequency spectrum of the noise by reducing the high-amplitude effects of the primary (around 15 s period) and secondary (around 7.5 s period) microseisms, and the Earth's hum (above 50 s period). Spectral normalisation was performed in SAC using the *whiten* command, which flattens the frequency spectrum of the input time series by adding white noise.

Cross-correlation and stacking

The cross-correlation of two functions $f(t)$ and $g(t)$ yields a measure of the similarity between them. Say $f(t)$ and $g(t)$ are time series (such as ambient noise records) which are shifted by some time lag τ_0. The cross-correlation between $f(t)$ and $g(t)$ is a function of τ and is given by

$$C_{fg}(\tau) = \int_{-\infty}^{+\infty} f(t)g(t+\tau)\mathrm{d}t \; . \tag{5.1}$$

Performing cross-correlation of two very long time series enhances the Green's function signal, but may also impose a large unnecessary computational burden if the cross-correlation function is evaluated for time lags far greater than required. In fact, both traces need to be simultaneously stored in memory and a number of computationally expensive operations (e.g., Fourier transforms) must be executed on each trace. However, since cross-correlation is a linear process, stacking several cross-correlations computed over shorter time windows produces the same result as running a single cross-correlation over a longer time window for those time lags in common between the two windows. In order to increase the signal-to-noise ratio and reduce the computational cost, we therefore cross-correlated transverse day-files between all possible station pairs and then stacked all daily cross-correlations over the available recording period.

The result of cross-correlation is a two-sided waveform which is twice the length of the original ones, with a *causal* (at positive times) and an *acausal* (at negative times) part representing energy travelling in opposite directions. If noise sources were uniformly distributed around the receivers, the causal and acausal components would have equal amplitude and the cross-correlation function would be symmetric around zero lag-time. However, in most cases noise sources are not distributed uniformly in space, causing energy to propagate mainly in one of the two directions between the receivers. This is a typical case observed in the British Isles, where most seismic energy travels from west to east due to the majority of noise sources being located in the Atlantic Ocean. An example of cross-correlations performed between pairs of stations in the RUSH-II array is shown in Fig. 5.5: while noise cross-correlations between stations CLUN and BASS produce a symmetric signal, noise cross-correlations between stations STOR and CAWD and stations MILN and KYLE produce asymmetric Green's functions with a larger causal and acausal component, respectively.

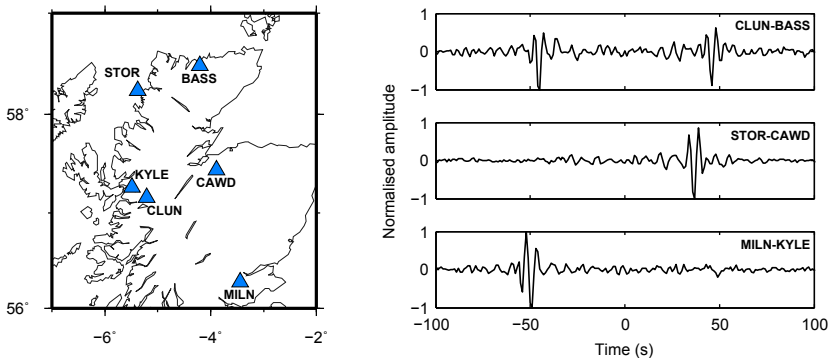

Figure 5.5. Typical results of ambient noise cross-correlation across the Scottish Highlands computed between the pairs of stations shown in the map (blue triangles). While the CLUN–BASS cross-correlation is symmetric around zero lag-time, noise cross-correlations between station pairs STOR–CAWD and MILN–KYLE yield asymmetric results with a larger causal and acausal component, respectively.

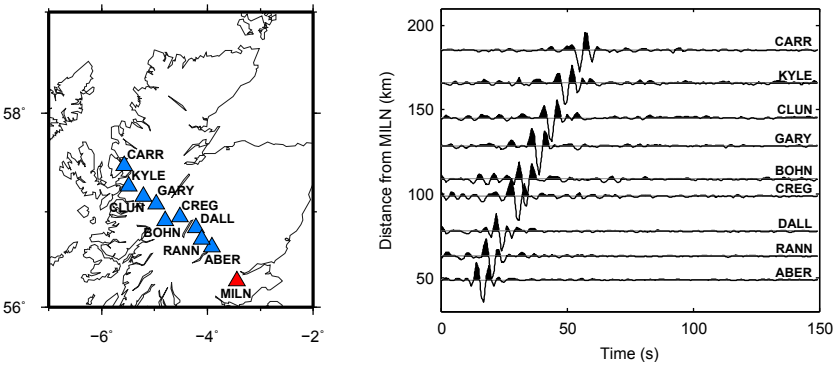

Figure 5.6. Example of Green's function emergence along an array of stations in the Scottish Highlands. Station MILN (red triangle) acts as a virtual source whose signal is recorded by the array of stations indicated by the blue triangles.

Since the computed cross-correlations were prevalently asymmetric and it was not always possible to establish whether the causal or acausal components were more reliable, we assumed both components to be equally valid and constructed the final, one-sided Green's functions by stacking the causal and time-reversed acausal parts. Although so doing allowed the data processing stage to be automated, we are aware that it may have added the potential for some information to be lost along some paths. An example of the resulting one-sided Green's functions is shown in Fig. 5.6, where station MILN (red triangle) acts as a virtual source whose signal is recorded at a number of other stations (blue triangles). The surface wave move-out is clearly visible as the distance from MILN increases.

In order to test the validity of the interferometric Green's function computed between a pair of seismic stations, we can compare the results of interferometry with true earthquake recordings provided an earthquake occurred near the location of one of the

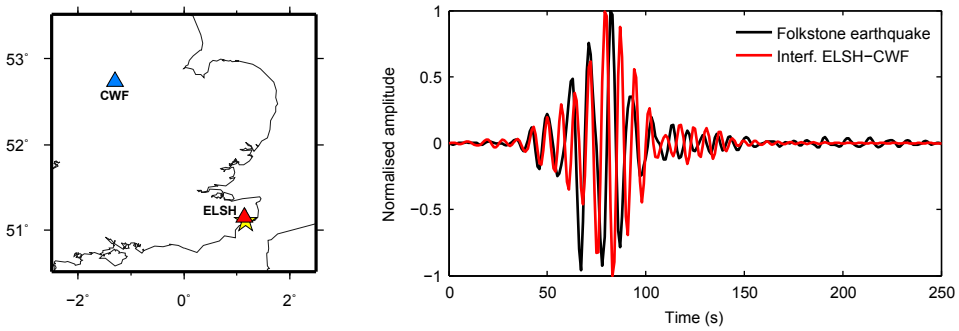

Figure 5.7. Comparison of the true recording of the Folkstone earthquake at station CWD (black solid line) and the interferometric trace constructed by cross-correlating ambient noise data recorded at stations ELSH and CWD (red solid line). Each trace is normalised to its maximum amplitude. The earthquake epicentre is denoted by a yellow star in the map on the left.

stations. Figure 5.7 shows such comparison for the Folkstone earthquake, a 4.2-magnitude earthquake which occurred on 28 April 2007 at 07:18 UTC and was recorded by a number of seismic stations in the south of England. Although differences between the true and interferometric result are expected, the true trace (black solid line in Fig. 5.7) looks remarkably similar to the interferometric result obtained from ambient-noise interferometry between stations ELSH and CWF (red solid line in Fig. 5.7). The differences between the two traces can be explained by the presence of different effective source time-functions in the earthquake and noise records, and to the earthquake epicentre and station ELSH not being exactly co-located.

Surface-wave dispersion measurement

Surface Rayleigh and Love waves are dispersive: within a surface-wave packet, longer-period waves penetrate deeper within the Earth due to their longer wavelength, while shorter-period waves mainly propagate in shallower layers. Because seismic velocity generally increases with depth, longer-period waves tend to travel faster than shorter-period ones, hence surface-wave arrivals of increasing period can be observed on a seismogram at earlier times (Fig. 5.8). Analysis of surface-wave traveltimes at different periods hence provides information on the Earth's structure at different depths. Similarly, the different types of particle motion that characterise surface Rayleigh and Love waves account for the different sensitivity of the two surface-wave types, with Love waves having higher sensitivity in shallower layers than Rayleigh waves (Aki & Richards, 2002). Hence, while Rayleigh-wave tomography may show geological structures down to the lower crust and upper mantle, Love-wave group velocity maps are expected to be more representative of shallow sedimentary and quaternary layers, depending on surface geology and period.

We used the frequency-time analysis (FTAN) method of Herrmann & Ammon (2002) to obtain inter-station Love-wave traveltimes in different frequency bands. In the time

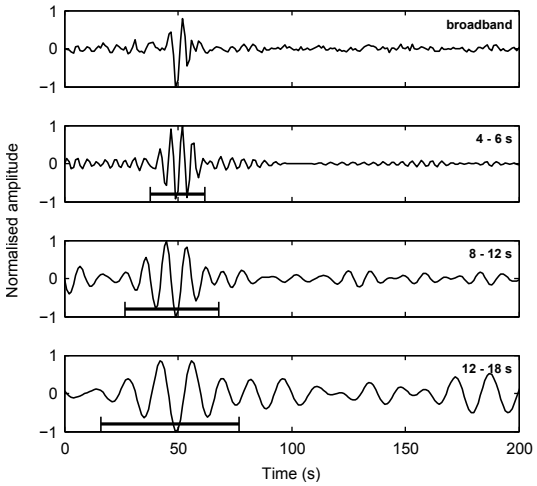

Figure 5.8. Interferometric Green's functions computed between stations MILN and KYLE. The raw, broadband seismogram is shown at the top and band-pass filtered seismograms at progressively increasing periods are given below. The horizontal bars indicate the approximate position of the dominant Love-wave energy. Note that the arrival time of surface wave energy decreases with increasing period.

domain, a dispersed single-mode surface-wave signal can be expressed as:

$$s(t) = \frac{1}{2\pi} \int_{-\infty}^{+\infty} A(\omega) \mathrm{e}^{\iota(\omega t - kx + \phi)} \mathrm{d}\omega \,, \tag{5.2}$$

where $A(\omega)$ denotes the signal amplitude, ϕ is the phase, and ω and k are angular frequency and wave number, respectively. We can define a Gaussian filter $H(\omega)$ centred on frequency ω_0 as

$$H(\omega) = \mathrm{e}^{-\alpha(\omega-\omega_0)^2/\omega_0^2} \,, \tag{5.3}$$

where α is a distance-dependent constant which defines the filter width. By applying filter $H(\omega)$ to signal $s(t)$ we obtain the filtered signal $g(t)$:

$$g(t) = \frac{1}{2\pi} \int_{-\infty}^{+\infty} A(\omega) H(\omega) \mathrm{e}^{\iota(\omega t - kx + \phi)} \mathrm{d}\omega \,. \tag{5.4}$$

Here, the signal amplitude in the neighbourhood of ω_0 is given by

$$A(\omega) = A_0 \mathrm{e}^{-\gamma(\omega-\Omega)^2/\omega_0^2} \mathrm{e}^{\gamma(\omega-\Omega)^2/\omega_0^2} \,, \tag{5.5}$$

where $A_0 = A(\omega_0)$, $A(\omega)$ peaks at $\omega = \Omega$, and γ controls the width of the signal spectrum. The group velocity of the filtered signal can be computed from the peak arrival time of the envelope function by using the length of the great circle arc connecting the two stations as an estimate of their distance. The procedure can be repeated iteratively to determine

the group velocity at different central frequencies ω_0. A dispersion curve may then be produced by plotting the measured group velocities versus central frequencies or periods.

Within this project, FTAN was performed using the *do_mft* program, which is part of the *Computer Programs in Seismology* package by Herrmann & Ammon (2002). The program is run through an interactive graphic interface and allows group velocities to be picked manually and matched to either the fundamental or higher modes. Within this study we only analysed the fundamental mode, which can easily be identified on a dispersion plot since it normally lies along the contour of maximum energy. As an example, the Love-wave dispersion curve obtained by applying FTAN to the interferometric Green's function between stations MILN and KYLE is shown in Fig. 5.9(a), where the left-hand plot shows points on the amplitude spectrum of the waveform which is displayed on the right-hand side of the figure, and the central panel is the group velocity versus period dispersion plot. The black symbols represent the group velocities of various modes (squares for the fundamental mode), and the colours in the central plot correspond to amplitude contours, with red indicating large amplitude and blue indicating low amplitude. Figure 5.9(b) shows the dispersion curve in Fig. 5.9(a) after the fundamental mode has been picked (white dots).

In case of particularly noisy data, a phase-matched filter (i.e., a linear filter whose Fourier phase is equal to that of the signal (Herrin & Goforth, 1977)) may be applied iteratively around the picked dispersion curve to further isolate the fundamental mode, ensuring that any other energy is removed from the data. As an example, when a phase-matched filter is applied to the dispersion curve in Fig. 5.9(a)–(b), the filtered dispersion curve in Fig. 5.9(c) is obtained.

Once group dispersion measurements have been obtained at all available periods and inter-station paths, these can be turned back into traveltime measurements and fed into a tomographic inversion program. Note that, while the output of *do_mft* is given in terms of periods and group velocities, what the program actually measures is the arrival time of the wave packet at each period. Since errors might be present in the measured traveltimes (due, for instance, to instrument errors or time-shifts introduced during the automated processing), it is important to identify and reject bad quality data and perform an accurate estimation of traveltime uncertainties. I describe how this was done for both the RUSH-II and UK-wide datasets in the next section.

Within this project, group velocity picking for RUSH-II data was performed by myself and Heather Nicolson, while the picking of group velocities for the UK-wide array was performed by David Jenkins as part of his 4^{th} year undergraduate project, which I supervised.

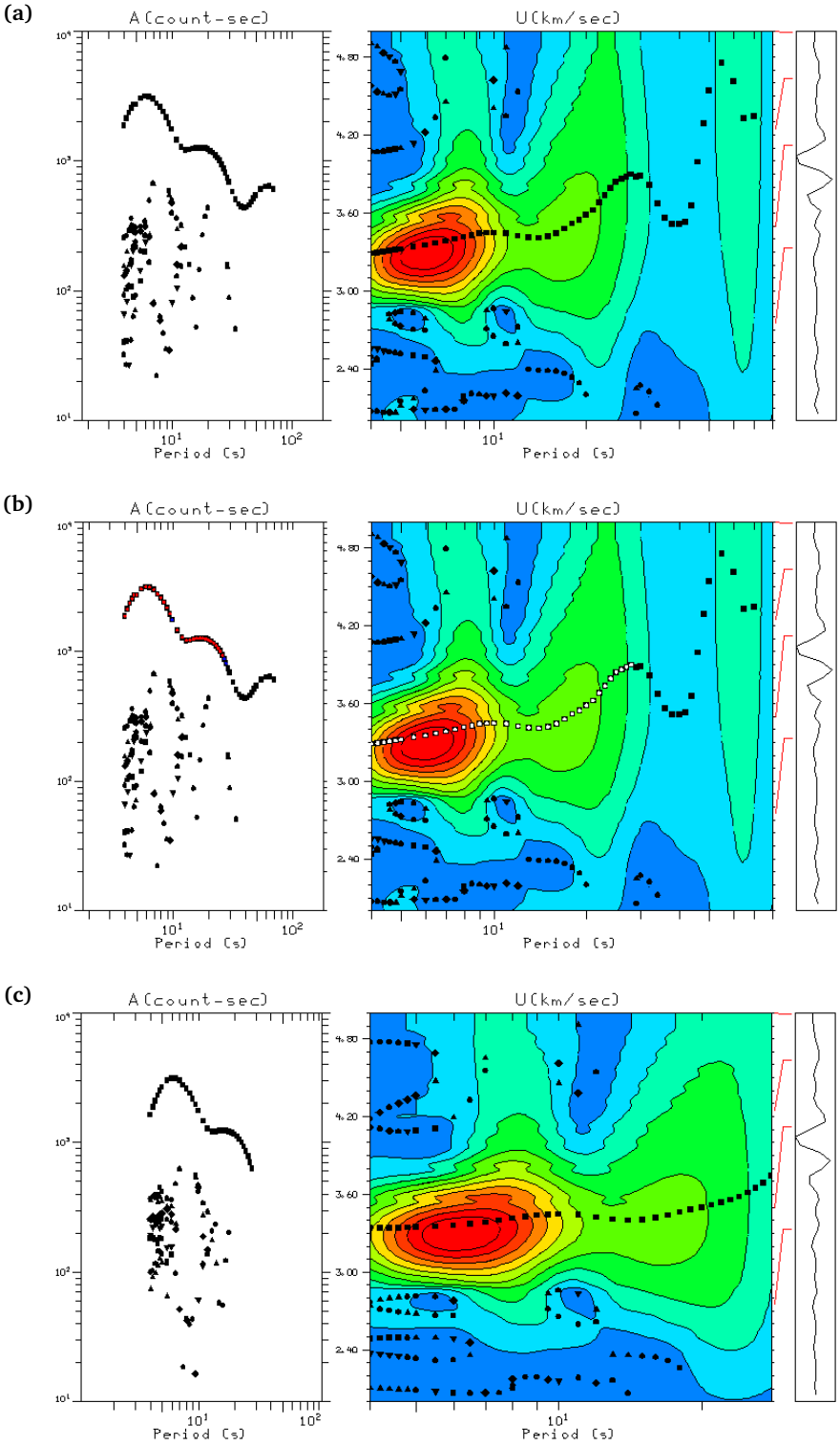

Figure 5.9. Example of FTAN on the interferometric Green's function between stations MILN and KYLE. (a) Love-wave group-velocity dispersion plot. (b) The fundamental mode is picked interactively. (c) Phase-matched filtered dispersion curve.

Quality control and error estimation

Due to the large volume of data involved in an ambient-noise cross-correlation study, most of the data processing procedure must be automated in order to require only minimal human interaction. So doing creates the potential for errors to be introduced into the dataset, hence quality control measures must be employed in order to identify and reject erroneous measurements. By following the guidelines of Bensen et al. (2007), we first rejected dispersion measurements obtained along paths with an inter-station distance of less than 3 wavelengths. In a second data selection stage, we then estimated the uncertainty associated with each dispersion measurement and used this quantity to reject measurements with too large uncertainty. This step is described below.

Compared to the analysis of real-earthquake data, estimating traveltime uncertainties from interferometric Green's functions presents the advantage of repeatability. Previous studies (Bensen et al., 2007; Lin et al., 2007; Yang et al., 2007) showed that the ambient-noise field may exhibit seasonal dependence, hence an estimate of the seasonal variability of the dispersion measurements can be made from overlapping 3-month stacks of cross-correlations. Since a measurement should be repeatable in order to be considered valid, outliers may easily be identified and removed from the dataset. For the tomographic inversion, traveltime measurements can be obtained from the 12-month cross-correlation stacks, and the standard deviation of the dispersion measurements over the 3-month stacks may be used as a conservative measure of uncertainty.

Analysing the seasonal variability of the interferometric Green's functions is ideal when all stations record simultaneously for long periods of time. However, as is the case for this study, gaps in the recording time might be present, making an accurate estimation of seasonal variability unfeasible. Within this study, we first constructed a reference Green's function estimated for each available inter-station path by stacking cross-correlations over all available days. We then constructed additional sets of inter-station Green's function estimates (four for the RUSH-II dataset and five for the UK-wide dataset) by stacking an equal number of randomly-chosen daily cross-correlations, with each daily cross-correlation appearing in only one random stack. This allowed us to obtain completely independent group-velocity estimates at all possible periods from each random stack, and to estimate the inter-station traveltime uncertainty at each period by calculating the standard deviation of the traveltimes measured in each random stack. As an example, the reference Green's function and dispersion curve obtained by stacking all available daily cross-correlations for path MILN–KYLE is shown in Fig. 5.10 (black lines). The Green's functions and dispersion curves resulting from the four random cross-correlation stacks are marked by red lines.

Traveltime uncertainties may be used during tomography to inversely weight the importance of the corresponding traveltimes, so that traveltimes with large uncertainty have less influence on the results than those with small uncertainty. However, our initial

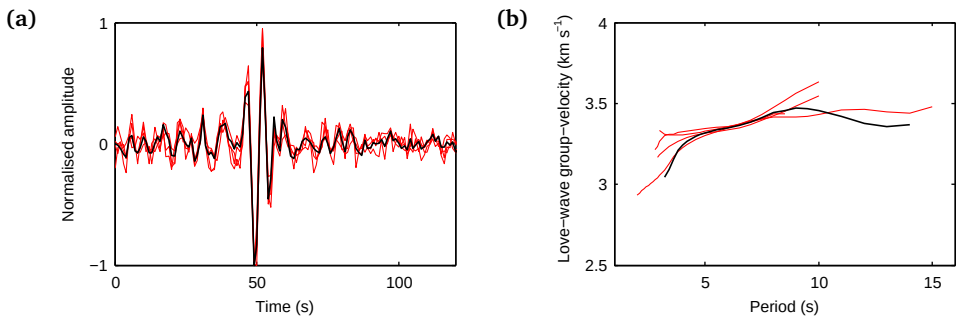

Figure 5.10. Example of uncertainty estimation from multiple random stacks of cross-correlations for inter-station path MILN–KYLE. (a) Broadband waveforms of the reference Green's function (black line) and four random stacks (red lines). (b) Dispersion curves obtained by applying FTAN to the waveforms shown in panel (a).

experiments (see Section 7.3) and previous studies (Nicolson et al., 2012, 2014) showed that the magnitude of the traveltime uncertainties measured with the method described above is too low. We therefore performed tomography by estimating traveltime uncertainties during inversion as described in Section 5.3.1. Nevertheless, the traveltime uncertainties from the randomly-stacked cross-correlations were used as a means for quality control in terms of measurement repeatability, as all paths with uncertainty greater than 5% of the total traveltime were excluded from the inversion dataset.

5.3 Seismic traveltime tomography

In seismic tomography, recordings of seismic waves are used to infer the velocity structure of the Earth's subsurface. Assuming the physics of wave propagation is adequately understood, we can relate a seismic dataset $\mathbf{d}$ to a subsurface model $\mathbf{m}$ using the expression

$$\mathbf{d} = \mathbf{g}(\mathbf{m}) \,, \tag{5.6}$$

where $\mathbf{g}$ is a forward function that relates $\mathbf{m}$ to $\mathbf{d}$. In surface-wave traveltime tomography, $\mathbf{d}$ is often a vector representing first-arriving source-to-receiver traveltimes, and $\mathbf{m}$ a vector of seismic slownesses of different cells in a fixed spatial grid.

In traveltime tomography, a set of source-to-receiver traveltimes is measured from recorded waveforms and constitutes the vector of observations $\mathbf{d}^{obs}$. The *forward problem* consists of finding a set of traveltimes $\mathbf{d}^{pred}$ through velocity model $\mathbf{m}$. The *inverse problem* consists of finding a certain model $\mathbf{m}$ such that $\mathbf{d}^{pred}$ matches the observed traveltimes $\mathbf{d}^{obs}$ as closely as possible. The agreement between observed and predicted traveltimes may be quantified by a misfit function such as the weighted least-squares

misfit:

$$\psi(\mathbf{m}) = \sum_{i=1}^{n} \left(\frac{d_i^{obs} - d_i^{pred}}{\sigma_i} \right)^2 , \tag{5.7}$$

where d_i^{pred} is the i^{th} traveltime predicted from model $\mathbf{m}$ and σ_i is the uncertainty associated with traveltime d_i^{obs}.

Solving an inverse problem in geophysics poses a number of challenges which go beyond merely finding a solution that mathematically fits the observed data. A typical issue when seeking a solution $\mathbf{m}$ to equation (5.6) is that more than one model may adequately fit the data. In an optimisation framework, the combination of parameters that provides the best fit (i.e., the least misfit) to the observations is generally regarded as the model solution. In contrast, stochastic inversion schemes do not limit the solution to a single model but can produce a large ensemble of valid models, so that each model parameter is represented by a *posterior* distribution rather than a single value. Obviously, regardless of the inversion scheme employed, the solution to a geophysical inverse problem must also make sense physically.

Data noise, which may be defined as the part of the data that cannot be explained by the model, also plays a fundamental role in inverse problems as it determines how accurately the model should fit the observations. The sources of uncertainty in a dataset are multiple and normally include measurement and modelling errors. In the context of seismic tomography, measurement errors might be caused by our inability to pick exact traveltimes on a waveform, while modelling errors may be due to approximations in the physics of the forward problem such as the use of the wrong raypath geometry or model parametrisation.

Within this project, we used a fully non-linear version of the reversible-jump Markov chain Monte Carlo (rj-McMC) algorithm (Bodin & Sambridge, 2009) to solve the tomographic inverse problem in a Bayesian framework and obtain an ensemble of solutions which are distributed according to the posterior distribution. The forward problem was solved using the Fast Marching Method (Sethian & Popovici, 1999; Rawlinson & Sambridge, 2004), which computes first-arriving source-to-receiver raypaths by solving the eikonal equation. Both methods are described in detail in the following sections.

5.3.1 The non-linear rj-McMC algorithm in tomography

Since its emergence in the 1970s, the field of seismic tomography has developed greatly thanks to the efforts of early pioneers and to substantial increases in computational power (Nolet, 2008). Nowadays, a wide variety of tomographic algorithms and inversion methods are available to produce velocity maps of the Earth's subsurface from first-arrival

traveltimes (Rawlinson & Sambridge, 2003; Nolet, 2008; Rawlinson et al., 2010). In most cases, these methods parametrise the Earth using fixed cells or grids of points whose shapes and sizes are chosen in advance (Bodin & Sambridge, 2009). The choice of cell (or grid) size is normally a compromise between model resolution and model uncertainty: when large cells (or coarse grids) are used, resolution is low and velocities are averaged over relatively large areas, hence the uncertainties on the estimated velocities are small; in contrast, a decrease in cell (or grid) size increases model resolution but also causes data noise to map as large uncertainties onto the model space, leading to solution non-uniqueness. In addition, since the information recovered by tomographic inversion strongly depends on the distribution of seismic rays across the area of interest, irregularities in the distribution of sources and receivers may lead to uneven spatial sampling of the model space, with some parts of the model being resolved better than others. Regularisation parameters such as damping and smoothing are normally applied in such cases in order to reduce the influence of data noise and deal with the ill-constrained parts of the model. However, since regularisation is normally applied uniformly to the entire model, this might cause loss or bias of information in the well-constrained areas (Bodin & Sambridge, 2009).

Moreover, as the path taken by a seismic ray depends on the velocity structure of the medium itself, the tomographic problem is inherently non-linear. Traditional inversion methods normally linearise the problem by fixing the raypaths, and only account for non-linearity by performing several iterations of inverting for the best-fit model, updating the ray geometry and repeating the linearised inversion. Although so doing partially takes care of the non-linear nature of the problem, the use of an approximate raypath geometry might introduce biases and artefacts into the final solution.

Within this section I describe a method for seismic traveltime inversion which takes into account both irregularities in the distribution of information and the non-linear character of the tomographic problem. This method is based on the tomographic reversible-jump Markov chain Monte Carlo (rj-McMC) algorithm of Bodin & Sambridge (2009), who use a variable Voronoi-cell tessellation of the 2D geographical space to parametrise the model and let the number and position of the model parameters vary freely during inversion. So doing allows the model parametrisation to vary spatially according to the distribution of information and subsurface structure, ensuring that the method is entirely data-driven. In its original formulation, the algorithm was partially linearised as raypaths were kept fixed within successive portions of the Markov chain. Since raypaths are directly influenced by the structure of the medium, so doing introduced the potential for raypath-related artefacts to be present in the solution. Using the original code as a basis, we therefore produced a new inversion code which calculates raypaths at each step of the Markov chain, making our tomographic method entirely non-linear.

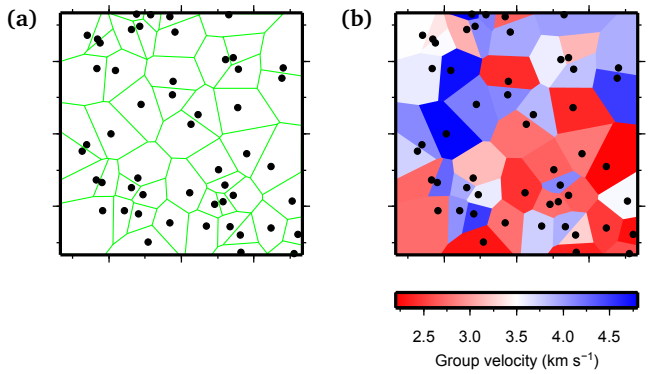

Figure 5.11. Example of Voronoi tessellation of a 2D plane. (a) Each Voronoi cell is identified by the location of its nucleus (black dots), and cell boundaries are defined by the perpendicular bisectors of pairs of neighbouring nuclei (green lines). (b) The Voronoi tessellation is turned into a velocity model by assigning a value of group velocity to each cell.

Model parametrisation with Voronoi cells

The implementation of the rj-McMC algorithm in seismic traveltime tomography (Bodin & Sambridge, 2009) uses Voronoi cells to parametrise the velocity model. A Voronoi tessellation of the geographical 2D space is achieved by defining a set of n nuclei (the black dots in Fig. 5.11) which are identified by their geographical coordinates and a value of seismic group or phase velocity. The 2D plane is then divided into n non-overlapping regions of different seismic velocity such that each region contains the portion of plane which is closest to its nucleus. Note that Voronoi nuclei are not necessarily located at the centre of their corresponding cells, but rather cell boundaries are defined by the perpendicular bisectors of pairs of neighbouring nuclei. A velocity model can therefore be defined as $\mathbf{m} = [n, \mathbf{c}, \mathbf{v}]$, where $\mathbf{c}$ and $\mathbf{v}$ are arrays of nuclei coordinates and velocity values, respectively. As velocity is kept constant within each Voronoi cell, the dimension of model $\mathbf{m}$ is $3n$.

During the inversion, the location and number of Voronoi nuclei in the model is allowed to vary, making the number of Voronoi cells in the model one of the inversion parameters. Since Voronoi cells change shape and size throughout the Markov chain, this allows the model parametrisation to dynamically adapt to the spatial distribution of both information and subsurface structure.

Data noise parametrisation

Within a transdimensional inversion framework, the magnitude of data uncertainties determines the level of complexity of the final solution. Bodin et al. (2012b) propose a method for uncertainty parametrisation which allows data noise to be determined during the inversion. Since the use of accurate uncertainties prevents data over- or under-fitting, so doing allows the traveltimes to be fit up to the appropriate uncertainty level, and makes the rj-McMC method almost entirely data-driven.

If traveltime uncertainties are available, the *a priori* uncertainties σ_{prior} may be up- or down-scaled by a factor λ which can be determined during inversion. Hence, for a certain raypath k with *a priori* uncertainty σ^k_{prior}, the *a posteriori* uncertainty σ^k_{post} is given by

$$\sigma^k_{post} = \lambda \times \sigma^k_{prior} \, . \tag{5.8}$$

Since λ is an additional parameter to be determined during the inversion, this makes the dimension of the model equal to $3n+1$. If multiple datasets with different data noise levels are combined, and a λ value is determined for each dataset, the model dimension becomes $3n + 1 \times n_{ds}$, where n_{ds} is the number of independent datasets to be combined.

If no information is available on data uncertainties, data noise may be parametrised as a linear function of path length. In this case, the *a posteriori* uncertainty on the traveltime corresponding to raypath k is given by

$$\sigma^k_{post} = a \times d_k + b \, , \tag{5.9}$$

where d_k is the source-to-receiver length of raypath k (here defined as the *actual* length of raypath k as traced through each model considered), and a and b are hyperparameters to be estimated during the inversion. This type of data noise parametrisation makes the model dimension equal to $3n + 2$ if a single a and b are estimated for the entire dataset, and $3n+2\times n_{ds}$ if n_{ds} datasets with different distance-dependence for noise are combined.

When data noise is parametrised and estimated during the inversion, the model is defined by the combined set $\mathbf{m} = [n, \mathbf{c}, \mathbf{v}, \mathbf{h}]$, where $\mathbf{h}$ is the array of vector hyperparameters ($\mathbf{h} = [\lambda_1, \lambda_2, ...]$ or $\mathbf{h} = [a_1, b_1, a_2, b_2, ...]$), and n, $\mathbf{c}$ and $\mathbf{v}$ were defined in the previous section.

Bayes' theorem

Within a Bayesian framework, information is represented by probability density functions. Bayesian inference makes use of Bayes' theorem (Bayes & Price, 1763) to estimate the *a posteriori* probability distribution (also known as 'posterior distribution') $p(\mathbf{m}|\mathbf{d}^{obs})$, which can be defined as the probability density of model $\mathbf{m}$ given data $\mathbf{d}^{obs}$. Bayes' theorem states that $p(\mathbf{m}|\mathbf{d}^{obs})$ can be estimated by combining observations with *a priori* information on the model according to

$$p(\mathbf{m}|\mathbf{d}^{obs}) \propto p(\mathbf{d}^{obs}|\mathbf{m})p(\mathbf{m}) \, . \tag{5.10}$$

Here, $p(\mathbf{d}^{obs}|\mathbf{m})$ is the likelihood function, which expresses the probability of observing dataset $\mathbf{d}^{obs}$ given model $\mathbf{m}$, and prior information on model $\mathbf{m}$ (i.e., everything we know about the model before performing the inversion) is represented by the *a priori* probability density $p(\mathbf{m})$. Equation (5.10) therefore represents how prior information on the model is updated by the data to give the posterior distribution.

The likelihood

The likelihood function $p(\mathbf{d}^{obs}|\mathbf{m})$ can be thought of as a measure of misfit between observed and predicted data. For a simple least-squares misfit such as that in equation (5.7), the likelihood function is Gaussian:

$$p(\mathbf{d}^{obs}|\mathbf{m}) \propto \mathrm{e}^{-\psi(\mathbf{m})/2} \,. \tag{5.11}$$

The prior

Since all inferences on the posterior are relative to the prior distribution, priors have great importance in Bayesian inversion schemes as the final result may be heavily influenced by the choice of an incorrect prior. In order to prevent any prior-related biases from being introduced into the solution, we chose uniform prior distributions with wide bounds for all model parameters. As all parameters are independent and have different dimensions, the model prior can be split into the product of four terms:

$$p(\mathbf{m}) = p(n)p(\mathbf{c}|n)p(\mathbf{v}|n)p(\mathbf{h}) \,, \tag{5.12}$$

where n is the number of Voronoi nuclei, $p(n)$ is the prior on the number of Voronoi nuclei/cells, $p(\mathbf{c}|n)$ is the prior on Voronoi nuclei location, $p(\mathbf{v}|n)$ is the prior on cell velocity, and $p(\mathbf{h})$ is the prior on noise hyperparameters.

The prior on the number of Voronoi cells is a uniform distribution over interval $I = \{n \in N | n_{min} \leq n \leq n_{max}\}$ such that

$$p(n) = \begin{cases} \frac{1}{\Delta n} & \text{if } n \in I \\ 0 & \text{otherwise,} \end{cases} \tag{5.13}$$

where $\Delta n = (n_{max} - n_{min})$.

Assuming that Voronoi nuclei can only be positioned on a finite grid of N points (where $N = n_x \times n_y$) with equal probability, the prior on Voronoi nuclei location is given by

$$p(\mathbf{c}|n) = \left[\frac{N!}{n!(N-n)!} \right]^{-1} . \tag{5.14}$$

The prior on cell velocity is a uniform distribution over interval $J = \{v_i \in \Re | v_{min} \leq v_i \leq v_{max}\}$ such that for each cell i

$$p(v_i|n) = \begin{cases} \frac{1}{\Delta v} & \text{if } v_i \in J \\ 0 & \text{otherwise,} \end{cases} \tag{5.15}$$

where $\Delta v = (v_{max} - v_{min})$. Since the velocity of each cell is independent from the others, the prior on velocity for all cells is

$$p(\mathbf{v}|n) = \prod_{i=1}^{n} p(v_i|n)\,. \tag{5.16}$$

The prior on the set of noise hyperparameters $\mathbf{h}$ can be obtained by considering each hyperparameter as independent. The prior on each hyperparameter h_j is a uniform distribution over interval $H_j = \{h_j \in \Re | h^j_{min} \leq h_j \leq h^j_{max}\}$ such that

$$p(h_j) = \begin{cases} \frac{1}{\Delta^j h} & \text{if } h_j \in H_j \\ 0 & \text{otherwise,} \end{cases} \tag{5.17}$$

where $\Delta^j h = (h^j_{max} - h^j_{min})$. Since each hyperparameter is independent from the others, the prior on all hyperparameters is

$$p(\mathbf{h}) = \prod_{j=1}^{m} p(h_j)\,, \tag{5.18}$$

where m is the total number of hyperparameters.

By combining equations (5.13), (5.14), (5.16), (5.18) as in (5.12), the full prior probability density function can be expressed as

$$p(\mathbf{m}) = \frac{n!(N-n)!}{N!(\Delta v)^n \Delta n(\prod_{j=1}^{m} \Delta^j h)}\,, \tag{5.19}$$

provided that all parameters fall within the boundaries of their respective priors. If one of the parameters falls outside the range of its prior, the full prior in equation (5.19) becomes zero.

A Bayesian approach to tomography

Markov-chain Monte Carlo (McMC) is an iterative stochastic approach which uses Bayes' theorem to generate samples from a posterior probability density. Samples are generated in sequence along a chain, with each sample being a perturbation of the one that precedes it. The initial model of the chain is selected randomly from prior distributions, and a randomly-selected model parameter is perturbed at each step of the chain. Compared to traditional McMC, the rj-McMC algorithm by Bodin & Sambridge (2009) does not fix the model parametrisation, hence 'jumps' in model dimension can also be made by adding or deleting model parameters (i.e., Voronoi cells).

Overall, five types of perturbations can be performed on model $\mathbf{m}$: a *birth* step adds a Voronoi cell to the current model; a *death* step removes a randomly-selected Voronoi cell; a *move* step changes the position of a randomly-selected Voronoi nucleus; a *velocity* step perturbs the velocity of a randomly-selected cell; a *noise* step perturbs a randomly-selected noise hyperparameter. In order to create a new model $\mathbf{m}'$ from the current model $\mathbf{m}$, the i^{th} component of $\mathbf{m}$ may be perturbed according to a so-called proposal distribution as

$$\mathbf{m}' = \mathbf{m} + u\sigma_i \mathbf{e}_i \,, \tag{5.20}$$

where u is a random deviate from a Gaussian distribution $N(0,1)$, σ_i is the standard deviation of the proposal, and $\mathbf{e}_i$ is the unit vector in the i^{th} direction. For instance, if the velocity of cell i is to be perturbed, a new velocity value v_i' for the cell can be obtained from

$$v_i' = v_i + u \times \sigma_v \,, \tag{5.21}$$

where v_i is the current velocity of cell i and σ_v is the standard deviation of the velocity proposal. Similarly, if a new cell is added at location $\mathbf{c}_{n+1}'$, the velocity of the new cell is obtained from

$$v_{n+1}' = v_i + u \times \sigma_{bd} \,, \tag{5.22}$$

where v_i is the current velocity at location $\mathbf{c}_{n+1}'$ and σ_{bd} is the standard deviation of the velocity proposal in the case of *birth* and *death* moves.

Compared to the original algorithm by Bodin & Sambridge (2009), we update the raypath geometry at each step of the Markov chain, hence our approach to transdimensional tomography is fully non-linear. Our algorithm consists of the following steps (Fig. 5.12):

1. An initial velocity model $\mathbf{m}$ is drawn from a uniform distribution of Voronoi-tessellated models and data noise parameters.
2. All raypaths and traveltimes are calculated through $\mathbf{m}$.
3. A new model $\mathbf{m}'$ is proposed by randomly perturbing the current model $\mathbf{m}$ using one of the types of perturbation described above.
4. All raypaths and traveltimes are calculated through $\mathbf{m}'$.
5. The acceptance ratio $\alpha(\mathbf{m}'|\mathbf{m})$ is calculated according to the following equation (Bodin & Sambridge, 2009):

$$\alpha(\mathbf{m}'|\mathbf{m}) = \min\left[1, \frac{p(\mathbf{m}')}{p(\mathbf{m})} \times \frac{p(\mathbf{d}^{obs}|\mathbf{m}')}{p(\mathbf{d}^{obs}|\mathbf{m})} \times \frac{q(\mathbf{m}|\mathbf{m}')}{q(\mathbf{m}'|\mathbf{m})} \times |\mathbf{J}|\right] . \tag{5.23}$$

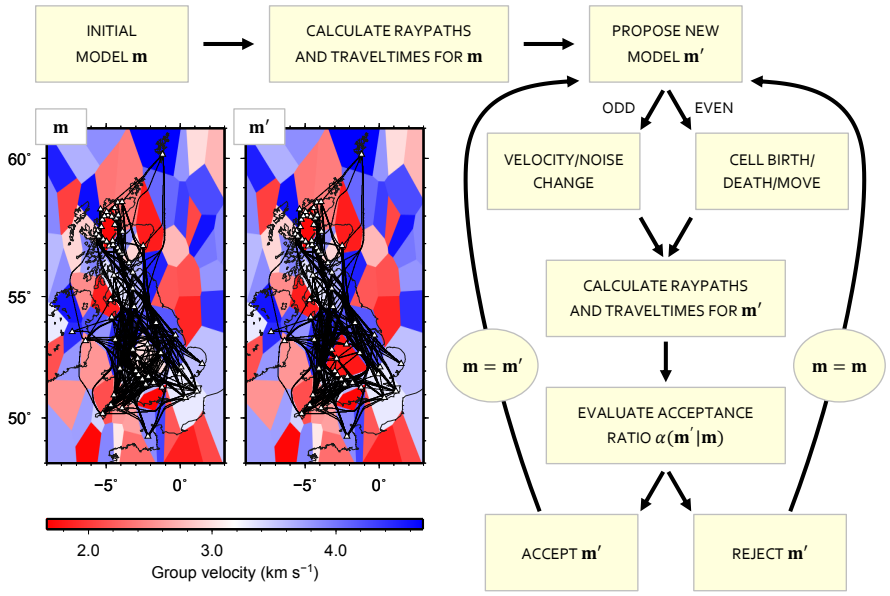

Figure 5.12. Workflow of the transdimensional rj-McMC algorithm. This samples the model space by producing an ensemble of Voronoi tessellated models distributed according to the Bayesian posterior probability distribution. For each proposed model, the correct raypaths and traveltimes are calculated and used in the calculation of the likelihood by updating the entire ray geometry. Note how the ray geometry may change dramatically from $\mathbf{m}$ to $\mathbf{m}'$ if one of the model parameters (in this case the velocity value of the cell centred near −2.5°E, 52.5°N) is changed.

where the second term in the square bracket involves the product of the prior, likelihood and proposal ratios and the Jacobian of the transformation from $\mathbf{m}$ to $\mathbf{m}'$ (see the next section for a description of the terms in equation (5.23)).

6. Depending on the value of $\alpha(\mathbf{m}'|\mathbf{m})$, the chain goes back to step 3 after either accepting or rejecting the proposed model $\mathbf{m}'$. If $\alpha \geq r$ (where r is a random deviate from a uniform distribution $N(0,1)$), the change is accepted, and $\mathbf{m}'$ replaces $\mathbf{m}$ as the new current model. If $\alpha < r$, the change is rejected and $\mathbf{m}'$ is simply discarded.

The use of $\alpha(\mathbf{m}'|\mathbf{m})$ as an acceptance parameter ensures that all models that improve the data fit are accepted, while those that do not are randomly accepted or rejected depending on their likelihood. Also, thanks to the natural parsimony of Bayesian inference, overly complicated models are naturally avoided (Bodin & Sambridge, 2009).

At the end of the chain, an ensemble of representative samples is obtained by discarding the first few hundred thousand iterations from the Markov chain as 'burn-in' and only retaining every few hundredth model to ensure that the samples in the ensemble are approximately uncorrelated. Useful statistical moments can then be calculated from the ensemble. These may include low-order statistics such as an average model and an estimate of its uncertainty in terms of standard deviation across the ensemble, and higher-order statistical moments such as skewness and kurtosis (Bodin et al., 2012a). In

addition, multiple chains which are independent of one another are normally run in parallel, ensuring that a large portion of the model space is explored by starting the chains from different initial conditions.

The acceptance ratio α

The expression for the acceptance ratio $\alpha(\mathbf{m}'|\mathbf{m})$ (equation (5.23)) involves the product of prior, likelihood and proposal ratios and the Jacobian of the transformation from $\mathbf{m}$ to $\mathbf{m}'$. Since the complete derivation of all of these terms is relatively lengthy and beyond the scope of this chapter, in this section I simply provide a description of each term and its contribution to $\alpha(\mathbf{m}'|\mathbf{m})$, and refer the reader to Bodin & Sambridge (2009) for further details.

The calculation of the prior ratio involves the evaluation of the prior for $\mathbf{m}$ and $\mathbf{m}'$ using equation (5.19). In the case of perturbation types which do not involve a change in dimension (i.e., *velocity*, *move* and *noise* steps), $p(\mathbf{m}) = p(\mathbf{m}')$, hence the prior ratio is unity. For perturbation types which involve a jump in dimension, the prior ratio is

$$\left[\frac{p(\mathbf{m}')}{p(\mathbf{m})}\right]_{birth} = \begin{cases} \frac{n+1}{(N-n)\Delta v} & \text{if } (n+1) \in I \text{ and } v'_{n+1} \in J \\ 0 & \text{otherwise} \end{cases} \tag{5.24}$$

for a *birth* step, and

$$\left[\frac{p(\mathbf{m}')}{p(\mathbf{m})}\right]_{death} = \begin{cases} \frac{(N-n+1)\Delta v}{n} & \text{if } (n-1) \in I \\ 0 & \text{otherwise} \end{cases} \tag{5.25}$$

for a *death* step.

The evaluation of the likelihood ratio involves the computation of raypaths through the Voronoi tessellation of $\mathbf{m}$ and $\mathbf{m}'$ (except if a *noise* move is performed) and the calculation of source-receiver traveltimes. For a Voronoi velocity model with n cells, the traveltime of raypath k is given by

$$t_k = \sum_{i=1}^{n} \frac{L_{ik}}{v_i} , \tag{5.26}$$

where L_{ik} is the length of ray k in cell i and v_i is the velocity of cell i. If raypath k does not pass though cell i, L_{ik} is equal to zero. Once traveltimes have been calculated, the likelihood function may be evaluated using equation (5.11).

The proposal probability $q(\mathbf{m}'|\mathbf{m})$ expresses the probability to go from $\mathbf{m}$ to $\mathbf{m}'$. Similarly, $q(\mathbf{m}|\mathbf{m}')$ expresses the probability for the reverse move, from $\mathbf{m}'$ to $\mathbf{m}$. In the case of perturbation types which do not involve a change in dimension, $q(\mathbf{m}'|\mathbf{m})$ and

$q(\mathbf{m}|\mathbf{m}')$ are symmetrical distributions, hence their ratio is unity. For perturbation types which involve a jump in dimension, we obtain different proposal ratios depending on the type of perturbation. For a *birth* step which creates a new cell at location $\mathbf{c}'_{n+1}$ we get

$$\left[\frac{q(\mathbf{m}')}{q(\mathbf{m})}\right]_{birth} = \frac{\sqrt{2\pi}(N-n)}{n+1}\sigma_{bd}\mathrm{e}^{\left\{\frac{(v'_{n+1}-v_i)^2}{2\sigma^2_{bd}}\right\}}, \tag{5.27}$$

where v'_{n+1} is the velocity of the added cell and v_i is the current velocity at location $\mathbf{c}'_{n+1}$. For a *death* step which involves the deletion of cell i we get

$$\left[\frac{q(\mathbf{m}')}{q(\mathbf{m})}\right]_{death} = \frac{n}{\sigma_{bd}\sqrt{2\pi}(N-n+1)}\mathrm{e}^{\left\{-\frac{(v'_j-v_i)^2}{2\sigma^2_{bd}}\right\}}, \tag{5.28}$$

where v'_j is the velocity at $\mathbf{c}_i$ in the new tessellation (i.e., after the deletion of cell i).

The Jacobian term $|\mathbf{J}|$ accounts for scale changes occurring in the case of transdimensional perturbations by normalising the difference in volume between the two model spaces of different dimension. Besides being equal to one in the case of model perturbations which do not involve a change in dimension, Bodin & Sambridge (2009) show that $|\mathbf{J}|$ is unity even for *birth* and *death* steps, hence can be ignored.

By substituting the expressions for the Jacobian and for the prior, likelihood and proposal ratio into equation (5.23), an expression for $\alpha(\mathbf{m}'|\mathbf{m})$ can be obtained for each type of model perturbation. For model perturbations which do not involve a change in dimension we get

$$\alpha(\mathbf{m}'|\mathbf{m}) = \begin{cases} \min\left[1, \frac{p(\mathbf{d}^{obs}|\mathbf{m}')}{p(\mathbf{d}^{obs}|\mathbf{m})}\right] & \text{if } \forall i \in [1,n],\ v_i \in J \\ 0 & \text{otherwise.} \end{cases} \tag{5.29}$$

For model perturbations involving a change in dimension we get

$$\alpha(\mathbf{m}'|\mathbf{m}) = \begin{cases} \min\left[1, \frac{\sigma_{bd}\sqrt{2\pi}}{\Delta v}\mathrm{e}^{\left\{\frac{(v'_{n+1}-v_i)^2}{2\sigma^2_{bd}} - \frac{\psi(\mathbf{m}')-\psi(\mathbf{m})}{2}\right\}}\right] & \text{if } (n+1)\in I \text{ and } v'_{n+1}\in J \\ 0 & \text{otherwise} \end{cases} \tag{5.30}$$

in case of a *birth* step, and

$$\alpha(\mathbf{m}'|\mathbf{m}) = \begin{cases} \min\left[1, \frac{\Delta v}{\sigma_{bd}\sqrt{2\pi}}\mathrm{e}^{\left\{-\frac{(v'_j-v_i)^2}{2\sigma^2_{bd}} - \frac{\psi(\mathbf{m}')-\psi(\mathbf{m})}{2}\right\}}\right] & \text{if } (n-1)\in I \\ 0 & \text{otherwise} \end{cases} \tag{5.31}$$

in case of a *death* step.

5.3.2 Raytracing with the Fast Marching Method

We used the Fast Marching Method (FMM) (Sethian, 1996; Sethian & Popovici, 1999; Rawlinson & Sambridge, 2004) to calculate forward traveltimes through the Voronoi-tessellated 2D space. The FMM is a fast and unconditionally-stable scheme that allows the eikonal equation to be solved using finite differences. According to the eikonal equation, the magnitude of the traveltime gradient at any point along a wavefront equals the slowness (i.e., the inverse of the velocity) at that point:

$$|\nabla_{\mathbf{x}} T| = s(\mathbf{x}) \,, \tag{5.32}$$

where $\nabla_{\mathbf{x}}$ is the gradient operator, T is the traveltime of the wavefront and $s(\mathbf{x}) = \frac{1}{v(\mathbf{x})}$ is the slowness at position $\mathbf{x}$. Contrary to many eikonal grid-based methods, which might fail to solve the eikonal equation in the presence of gradient discontinuities that may cause for instance the first-arrival wavefront to cross itself, the FMM tracks the evolution of a wavefront by applying an upwind entropy condition, such that if a point has been passed by the wavefront it cannot be passed again. Sethian & Popovici (1999) explain this concept by comparing the wavefront to the boundary of a propagating flame which separates a burning region from an unburnt region. In this scenario, the entropy condition may be stated as "once a point burns, it stays burnt". With respect to the schematic geometry for the FMM in Fig. 5.13, the burnt region corresponds to the 'upwind' points, the unburnt region corresponds to the 'downwind' points, and the wavefront may be denoted by the region of points called 'narrow band', moving upwind to downwind.

The entropy-satisfying upwind scheme employed by the FMM in 3D may be expressed as:

$$\begin{bmatrix} \max\left(D_a^{-x}T, -D_b^{+x}T, 0\right)^2 \\ +\max\left(D_c^{-y}T, -D_d^{+y}T, 0\right)^2 \\ +\max\left(D_e^{-z}T, -D_f^{+z}T, 0\right)^2 \end{bmatrix}_{ijk}^{1/2} = s_{i,j,k} \,, \tag{5.33}$$

where T is traveltime, (i,j,k) are grid increment variables in Cartesian coordinates (x,y,z), and integer variables a, b, c, d, e, f denote the order of the upwind finite-difference operator used in each case. For instance, for grid spacing δx in direction $-x$, the upwind operators of order 1, 2, 3 for $D^{-x}T_i$ are (Rawlinson & Sambridge, 2004):

$$\begin{aligned} D_1^{-x}T_i &= \frac{T_i - T_{i-1}}{\delta x} \\ D_2^{-x}T_i &= \frac{3T_i - 4T_{i-1} + T_{i-2}}{2\delta x} \\ D_3^{-x}T_i &= \frac{11T_i - 18T_{i-1} + 9T_{i-2} - 2T_{i-3}}{6\delta x} \end{aligned} \tag{5.34}$$

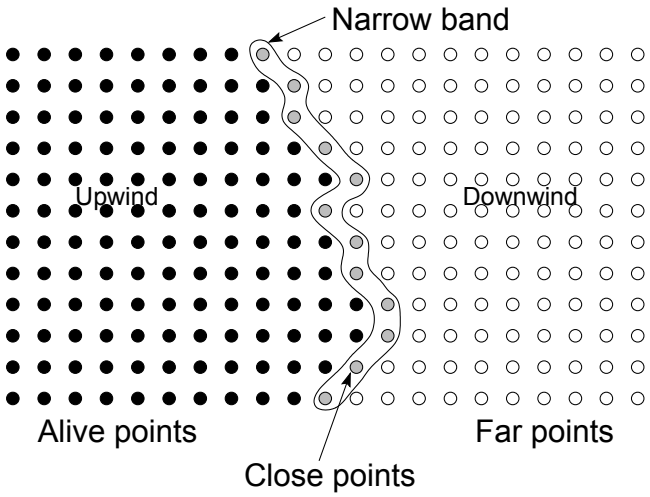

Figure 5.13. Schematic diagram illustrating the principle of the narrow-band method. *Alive* points (black dots) have been passed by the narrow band (i.e. wavefront) and their traveltimes are correctly calculated. *Close* points (grey dots) lie within the narrow band and are given trial traveltimes. *Far* points (white dots) lie downwind and have no associated traveltime. From Rawlinson & Sambridge (2004).

The use of upwind entropy-satisfying finite-difference approximations of the gradient term ensures unconditional stability of the FMM as gradient discontinuities in the wavefront are correctly addressed, meanwhile allowing the order of accuracy to be controlled by using the operator of maximum order allowed.

The FMM traces raypaths by tracking the evolution of the first-arrival wavefront across a grid of closely-spaced points (a 'propagation grid' or 'modelling grid') using a *narrow-band* approach (Fig. 5.13). Traveltimes at each grid point are calculated by solving equation (5.33) for T in the direction of flow of information, i.e. 'upwind' to 'downwind' from smaller to larger traveltimes. Depending on their position relative to the wavefront, grid points can be classified as either *alive*, *close* or *far*, as shown in Fig. 5.13: *alive* points lie upwind and have their traveltime correctly calculated (black dots); *close* points lie within the narrow band and have trial traveltime values (grey dots); *far* points lie downwind and have no associated traveltime values (white dots). The narrow band can essentially be regarded as an approximation of the first-arrival wavefront as it propagates through the medium until all points become *alive*.

An example of the evolution of a wavefront using the narrow-band approach is illustrated in Fig. 5.14. The FMM starts by identifying the source point, which is tagged as *alive* (left panel). Traveltimes to its neighbouring points, which become the narrow band, are calculated, and the point with the smallest traveltime is chosen as the next *alive* point (centre panel). If they are not yet part of the narrow band (i.e. they are *far* - white dots), the points in the neighbourhood of this new *alive* point become *close* and are added to the narrow band (grey points), and their traveltimes are calculated; if they were *close* points already, their traveltimes are recalculated (right panel). Of the new set of *close* points, the

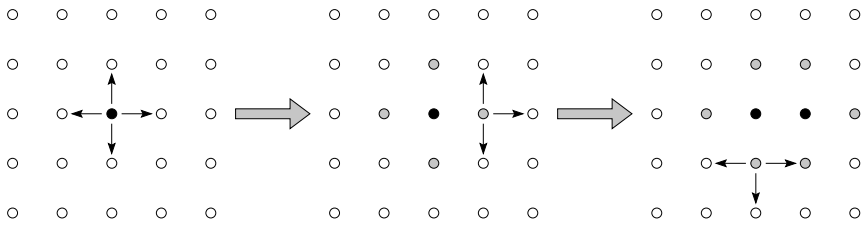

Figure 5.14. Evolution of the narrow band using the FMM. The source point is labelled as *alive* (black dot) and traveltimes to its four neighbouring points are calculated. These points become *close* and form the narrow band (grey dots). The *close* point which has the shortest traveltime becomes the next *alive* point. Its neighbouring *far* points are added to the narrow band and their traveltimes are calculated, while its neighbouring points that are already *close* have their traveltimes updated. The point in the narrow band with the smallest traveltime becomes the next *alive* point, and the scheme is repeated until all points in the grid become *alive*. From Rawlinson & Sambridge (2004).

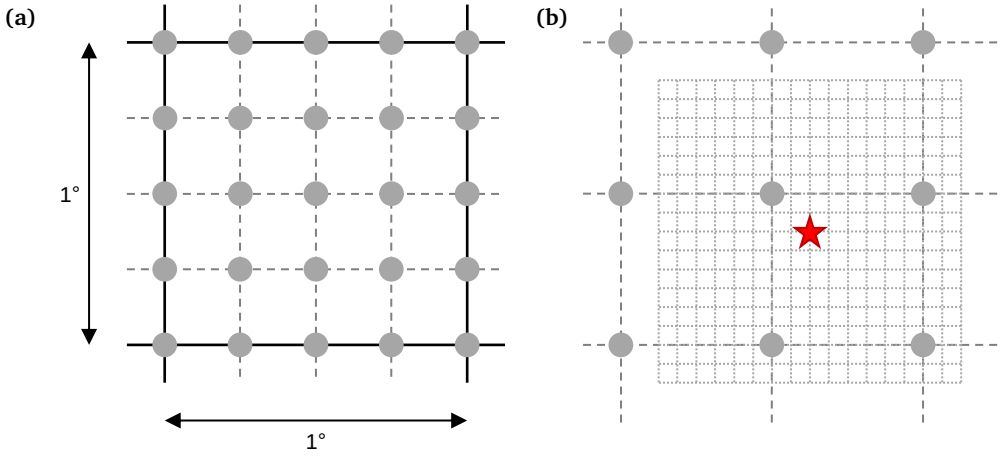

Figure 5.15. Definition of raypath modelling grids. (a) A 'propagation' grid is defined by dividing a $1^\circ \times 1^\circ$ sector into 4×4 cells. (b) A refined grid is defined near the source by dividing each propagation cell into 8×8 sub-cells up to a distance of one propagation cell from the source.

one with shortest traveltime is then tagged as *alive* and the procedure is iteratively repeated until all points in the grid become *alive* as the narrow band travels downwind.

Within this thesis, raypath modelling grids were defined by dividing each $1^\circ \times 1^\circ$ sector into a number of 'propagation' cells. In order to properly account for the high curvature of the wavefront near the source, a refined grid, defined by dividing each of these propagation cells into a number of sub-cells, was also applied close to the sources. An example of how a modelling grid is obtained is shown in Fig. 5.15. In this case, a propagation grid is defined by dividing each $1^\circ \times 1^\circ$ sector into 4×4 cells (Fig. 5.15(a)). In the magnified view in plot (b), grid refinement is applied near a source by dividing each propagation grid cell into 8×8 sub-cells up to a distance of one propagation cell from the source.

Figure 5.16 shows an example of raypaths computed through a Voronoi-tessellated 2D velocity model (panel (a)) using the FMM. In this case, the traveltime field in Fig. 5.16(b)

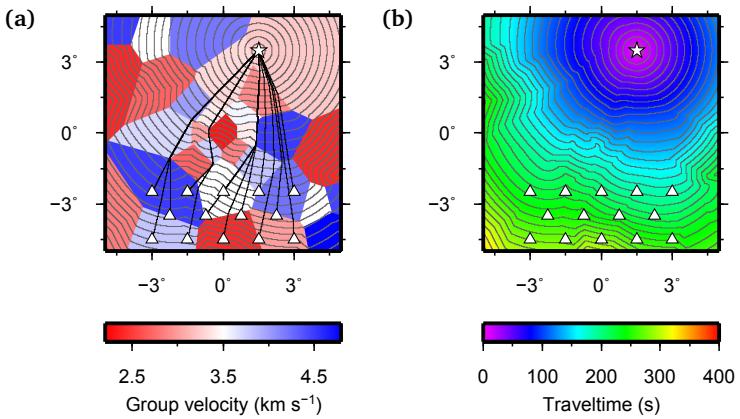

Figure 5.16. Example of the FMM in a Voronoi-tessellated 2D space. (a) Velocity field, raypaths (black lines) and wavefront at 10 s intervals (grey lines). (b) Traveltime field and wavefront at 10 s intervals (grey lines).

was first calculated using a very thin grid of points with a spacing of $1/100^{\text{th}}$ of a degree (and a thinner spacing of $1/1000^{\text{th}}$ of a degree up to 1° from the source). Raypaths were then computed by following the direction of steepest descent along the traveltime field, from the receiver to the source. The thin grey lines in both plots approximate the wavefront at intervals of 10 s as contours of the traveltime field; raypaths are always perpendicular to the wavefronts. Note how the FMM appears to be a particularly robust scheme even when large velocity variations and gradient discontinuities on the wavefront are present.

Since the FMM requires the calculation of the entire traveltime field across the model in order to compute the raypaths, the computation time of the FMM forward modeller increases as a function of the size of the propagation grid (see Section 8.3.1 for a detailed comparison of computational cost versus grid size). Because the rj-McMC inversion method requires a large number of models to be generated (of the order of 10^6 models per Markov chain), within this project it was necessary to define an inversion grid size which could provide a good compromise between raypath accuracy and computation time. After several experiments with different grid sizes, we defined a raypath modelling grid by dividing each $1° \times 1°$ area into 16×16 propagation cells, and each propagation cell into 4×4 sub-cells within a distance of 0.5° from the source. This raypath modelling grid was used to perform all of the inversions presented in Chapters 6 and 7. Although computing the ray geometry at each step of the Markov chain dramatically increased the computation time compared to using a fixed ray geometry as in Bodin & Sambridge (2009), so doing ensured that the physics of ray propagation was never approximated, and that the correct traveltimes were used in the estimation of the likelihood function. This in turn prevented raypath- and parametrisation-related biases from being introduced into the final solutions, as shown in Chapter 6.

CHAPTER 6

Uncertainty loops in traveltime tomography from non-linear wave physics[1]

Estimating image uncertainty is fundamental to guiding the interpretation of geoscientific tomographic maps. We reveal novel uncertainty topologies (loops) which indicate that while the speeds of both low- and high-velocity anomalies may be well constrained, their locations tend to remain uncertain. The effect is widespread: loops dominate around a third of UK Love wave tomographic uncertainties, changing the nature of interpretation of the observed anomalies. Loops exist due to 2nd and higher order aspects of wave physics; hence, although such structures must exist in many tomographic studies in the physical sciences and medicine, they are unobservable using standard linearised methods. Higher order methods might fruitfully be adopted.

6.1 Introduction

Tomographic imaging of the interior of solid and fluid media has revolutionised science and technology in fields as diverse as medicine (Kevles, 1996; Wang et al., 2008; Herman, 2009), materials science (Midgley & Dunin-Borkowski, 2009; Kwon & Zewail, 2010), chemistry (Kim et al., 2010), physics (D'Ariano et al., 2003; Paris & Řeháček, 2004), biology (Wang & Hu, 2012; Fridman et al., 2012; Milne & Subramaniam, 2009), oceanography (Spindel & Worcester, 1990) and geology (Nolet, 2008; Rawlinson et al., 2010; Tanimoto & Lay, 2000). Practitioners derive insight into medium properties by

[1]This chapter has been published as Galetti et al. (2015b).

interpreting tomographically-derived images (models); analysing their uncertainties is key to ensuring that such interpretations are robust (Sambridge et al., 2006; Beaumont & Rannala, 2004; Vasco et al., 2003; Song et al., 2006). A recent paradigm shift in assessing uncertainty is to consider solving for *all* tomographic models that fit recorded data, rather than estimating only a single model or image (Beaumont & Rannala, 2004; Gallagher et al., 2009; Bodin & Sambridge, 2009). This requires that both algorithmic and parametrisation-based constraints on models are reduced to a minimum, as are theoretical simplifications in the physics used to interrogate the medium. In this study we remove most standard simplifications by allowing both model parametrisations and data uncertainties to vary within the inversion, and by removing all linearisation of ray propagation physics in Markov chain Monte Carlo tomography. For this reason we refer to the physics employed by our inversion method as non-linear. This reveals novel structures that dominate tomographic uncertainty estimates and change interpretations. These structures are shown to derive from the use of variable model parametrisation and non-linear (2^{nd} order and above) physics in ray tracing, and are enhanced when both ray paths and model parametrisation vary freely during inversion.

6.2 Love-wave tomography of the British Isles

Within the Earth sciences, tomographic imaging of the Earth's crust and uppermost mantle has been revolutionised in recent years by the advent of ambient-noise interferometry (Campillo & Paul, 2003). Cross-correlations of pairs of recordings of ambient seismic waves that reverberate within the Earth, produce estimates of band-limited Green's functions between locations of the recording seismometers. Since noise sources are mainly confined to the Earth's near surface, these estimates are usually dominated by surface waves that would have propagated between the two seismometer locations if one had been occupied by a source (Wapenaar & Fokkema, 2006). The latter is referred to as a *virtual* (imagined) seismic source. Surface-wave traveltimes between pairs of seismometer locations can thus be measured and used to image the Earth's seismic velocity structure tomographically (Shapiro et al., 2005).

We cross-correlated the horizontal components of all pairs of simultaneously recording seismometers across the UK in 2001–2003, 2006–2007 and 2010 (years that provided a useful spread of seismometer locations). Virtual sources were thus constructed from each seismometer, providing an estimate of the Love-wave components of inter-seismometer Green's functions. Seismometer locations and possible inter-seismometer ray paths are illustrated in Fig. 5.12, showing a high density of stations and hence rays in the north and south-west, with lower density in the central and eastern UK. We applied frequency-time analysis to the resulting Green's function estimates to measure the time taken by fundamental-mode Love waves to travel between each pair of seismometers around periods

within the main noise band of 6 s to 12 s period (Nicolson et al., 2014). Those traveltimes are then used for traveltime tomography.

We modified the stochastic (reversible-jump Markov chain Monte Carlo - rj-McMC) tomographic method of Bodin & Sambridge (2009) to avoid any linearisation of the physics of ray propagation. This method allows the Voronoi cell-based model parametrisation to vary within the inversion and produces a large family of model samples, the distribution of which is consistent with the Bayesian posterior probability distribution of the model given the data (traveltimes) and *a priori* information. The relationship between traveltimes and velocity is non-linear in that the traveltime integrand is a non-linear function of velocity because ray trajectories depend on the velocity structure of the medium itself. Previous studies linearised the physics by fixing the rays at locations consistent with their best estimate of the mean model at successive stages of the tomographic inversion (Bodin & Sambridge, 2009). We trace new rays through every model considered, hence never linearise the overall inverse problem. A large number of model samples (3 million from 16 parallel Markov chains) are generated, out of which 160000 are selected to be analysed.

Figure 6.1 shows the maps of the mean velocity of 10 s period Love waves (a), and the standard deviation of that velocity at each point across the UK (b), both derived from the 160000 velocity model samples. Consistent with other studies (Nicolson et al., 2012, 2014) and geological expectations, high mean seismic velocities are observed in the metamorphic and igneous complexes of Scotland in the north, Southern Uplands ($\sim 55^{\circ}$N), and Cornwall (south-west); low velocities are observed in sediments of the Midland valley ($\sim 56^{\circ}$N), Irish Sea (magnified panel), and basins around London in the south.

Off-shore uncertainties are equal to their *a priori* values since few rays visit marine areas. Within the region interrogated by the data, uncertainties are generally lower in the north and south-west of the UK where there is a relatively high density of seismometers; uncertainties are higher where the seismometer density is lower. This is also as expected.

The high-uncertainty loop-like features such as the one highlighted are not expected. Looking carefully at uncertainty map (b), similar loop-like topologies of various shapes and sizes are observed to span much of the UK mainland (e.g., around low-velocity anomalies at -3°E, 50.5°N; -1.5°E, 51.5°N; -5.5°E, 51.5°N; and around the high-velocity anomaly at -1°E, 53°N). Indeed the loops themselves define all of the highest uncertainties observed on land, and conducting synthetic tomography tests across various known velocity structures we find that loops *always* seem to contain the highest uncertainties.

Figure 6.1(c) shows the uncertainty estimated from the same data using standard linearised (1^{st} order) methods here using Fast-Marching Surface Tomography (FMST, Rawlinson & Sambridge (2005)): ray paths begin at a priori estimates of their positions (traced through the prior model, here homogeneous). After iteratively inverting for the best-fit model, re-tracing rays through that model, and repeating the linearised inversion

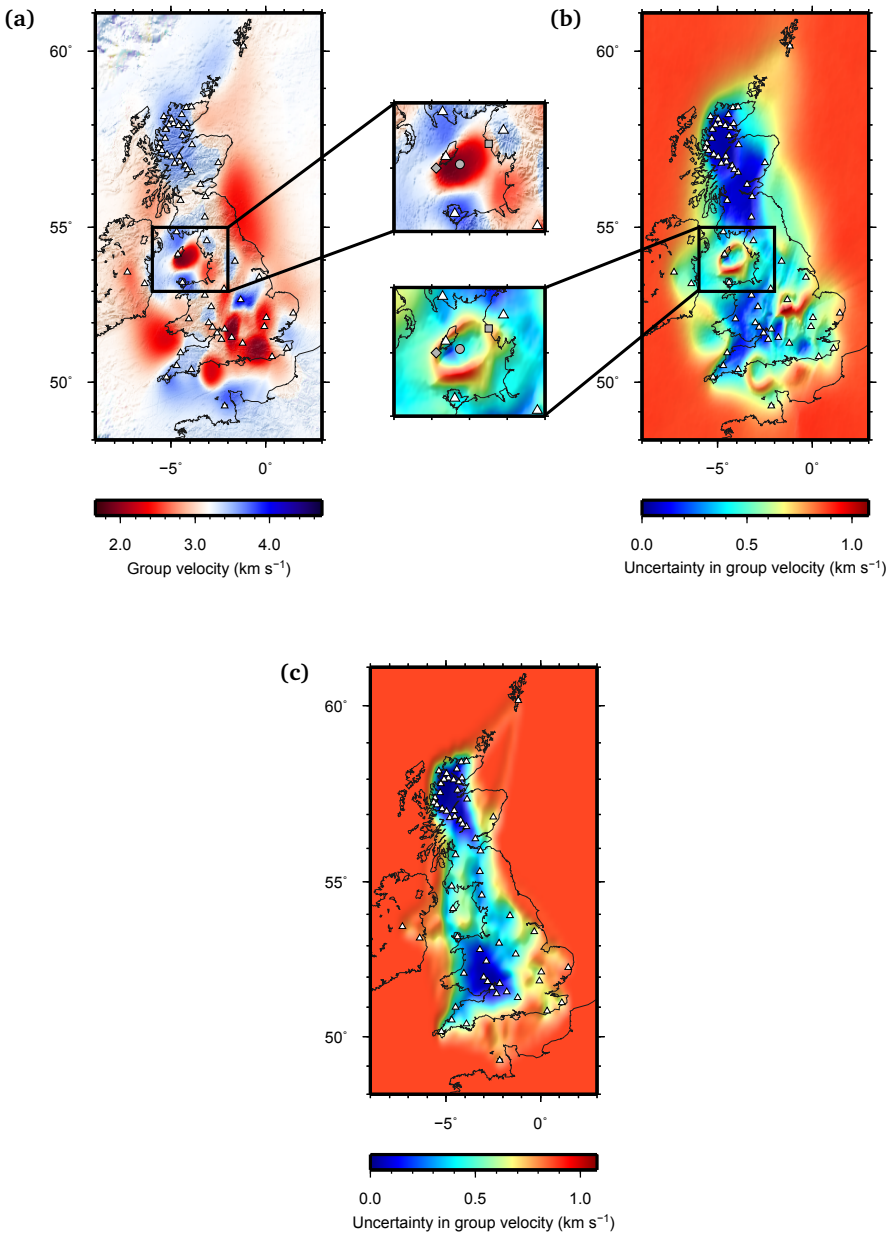

Figure 6.1. Ambient-noise Love-wave tomography of the British Isles at 10 s period. (a) Average velocity model, (b) standard deviation map, obtained from an ensemble of 160000 models, with two details highlighted in magnified plots. (c) Standard deviation map for the same data inverted using linearised tomography.

with rays fixed at their new positions (similar to Nicolson et al. (2014)), uncertainties are estimated from linearised covariances calculated using the final set of rays. No loops are observed, showing that loop structures are not produced when we include only 1st order physics and fix the model parametrisation.

In retrospect, similar loop-like uncertainty structures are observable in other studies which use transdimensional tomography with fixed ray geometries. These studies linearise the physics of wave propagation but remain non-linear in the model

parametrisation (e.g., Fig. 9(a) of Bodin & Sambridge (2009); Fig. 7 of Young et al. (2013b)). To assess the effect of fixed and variable parametrisation and ray paths, we performed synthetic tests first using a linearised subspace inversion scheme (FMST, Rawlinson & Sambridge (2005)), and then using McMC tomography with either fixed or variable (transdimensional) Voronoi-cell parametrisation, and either fixed or variable rays. We found that loops may emerge when either ray paths or model parametrisation are allowed to vary freely during inversion (either creates non-linearity in the model-data relationship). However, when rays are fixed, the uncertainty structure is strictly dictated by the ray geometry regardless of the inversion scheme and type of model parametrisation employed, and loops are observed only in extremely fortuitous cases. Also, only a combination of variable ray paths and parametrisation were observed to ensure a fully non-linear estimation of velocity structures and uncertainty without introducing clear raypath- or parametrisation-related biases. Tomographic uncertainties are therefore particularly dominated by loop structures only when both parametrisation and rays vary freely, explaining why they have not previously been recognised as important features of uncertainty.

6.3 Discussion

To explain the origin of such loops, Fig. 6.2 shows rays between a single source and receiver through an otherwise homogeneous medium that contains a low velocity anomaly. Although this example simplifies the typical geophysical scenario above, related geometries occur in other fields such as medical tomography and non-destructive testing in materials science.

Since rays are by definition minimum-traveltime paths, Fig. 6.2(a) illustrates that first-arriving energy does not pass through very low velocity anomalies, but rather refracts around their edges with traveltime t_1. This occurs unless the anomaly's velocity becomes sufficiently high that it is equally quick to go around or through the anomaly (third from left plot). The first arriving energy passes through the anomaly if its velocity is higher than this threshold; in that case the traveltime is sensitive to the velocity inside the anomaly, and hence changes. Traveltime measurement t_1 therefore only provides an upper bound on velocities of anomalies of fixed shape and size.

Row (b) shows similar phenomena when varying both the anomaly's size and velocity simultaneously. Traveltime t_1 is obtained for a larger anomaly with higher velocity (left), or a smaller anomaly with lower velocity (center plots), in each case resulting from energy passing through the anomaly. This occurs down to the same size and velocity threshold as in the top row (third from left plot), beyond which the earliest arriving energy refracts around the anomaly's edge.

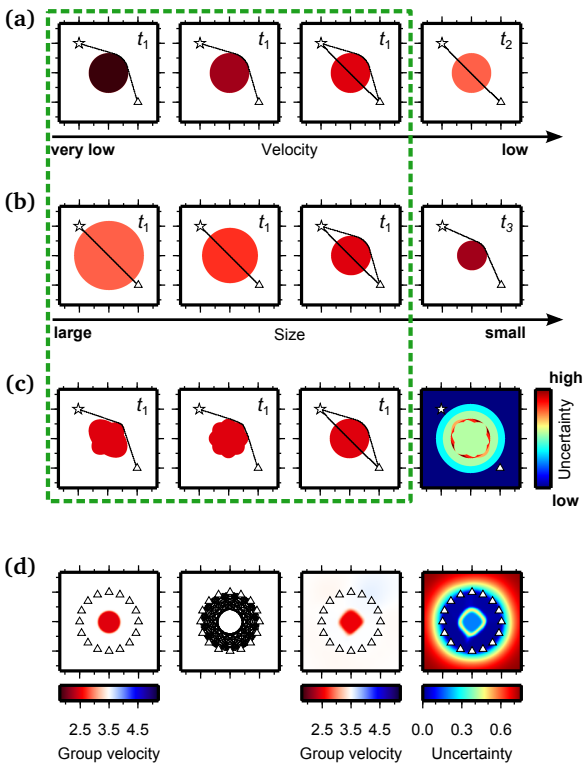

Figure 6.2. Effect of a low velocity anomaly (dark to light red) on synthetic rays and traveltimes. (a) The velocity of the circular anomaly increases from left to right. (b) Both size and velocity of the anomaly decrease from left to right. (c) Three anomalies with similar velocity and size but different shape. The green dashed box encloses velocity models that are all compatible with a given traveltime t_1; models on the right produce different traveltimes t_2 and t_3. The standard deviation across all models within the box is shown in the fourth plot of row (c). (d) Synthetic tomography of the low-velocity anomaly located at the center of an array of receivers: true velocity field and ray paths are shown in the first two plots; ensemble average and uncertainty map from fully non-linear rj-McMC tomography are in the right two plots.

The first two plots in row (c) of Fig. 6.2 show the effect of a variation in the shape of the circular anomaly at which the ray path switch takes place (third plot). Although the three anomalies have different shapes, the ray path is similar and the same traveltime t_1 is obtained. Shapes of all other circular anomalies within the dashed box can vary similarly without affecting the traveltime. The fourth plot in row (c) shows the uncertainty map obtained by calculating the standard deviation across all models within the dashed box. The largest uncertainties occur in a loop spanning the edges of the anomalies in row (c), resembling the uncertainty loops observed in UK tomography.

Now consider the inverse (tomography) problem: all anomalies within the box result in traveltime t_1, and for any measured traveltime a similar set of plots exist (scaled appropriately). Hence, any traveltime only constrains the maximum velocity of a circumnavigable low velocity anomaly (top row of plots), and only constrains the anomaly's boundary to lie within some geometrical bounds (examples in the second and third rows). The anomaly can be further constrained by other sources and receivers, but

each individual traveltime measurement results in uncertainty that can be characterised schematically similarly to the range of models in Fig. 6.2. We thus expect an upper-bounded velocity on the interior of low velocity anomalies, and a high velocity uncertainty at any point within some geometrical annulus spanning the edge of each anomaly (the high-uncertainty annulus in the fourth plot of Fig. 6.2(c)) since that point may lie either inside or outside of the anomaly, hence its velocity may range from low to high values. The combined effect of both types of uncertainty should thus produce the observed loops of high uncertainty in the locations of anomaly edges, as confirmed by marginal probability histograms in Fig. 6.3 calculated at three points in Fig. 6.1.

To check this intuition, row (d) of Fig. 6.2 shows an application of the fully non-linear transdimensional algorithm to the synthetic problem above. The first plot in row (d) shows a circular velocity anomaly of velocity 2.5 km s^{-1} within a circular array of receivers and background velocity of 3.5 km s^{-1}. To emulate typical ambient-noise tomography scenarios, traveltimes were calculated along inter-receiver paths (true rays are shown in the second plot). The ensemble average and uncertainty map from tomography are shown in the two right plots. The ensemble average approximates the true velocity model and the uncertainty map illustrates that, while the amplitude of the anomaly is reasonably constrained, velocities on its boundaries have far larger uncertainties, producing a loop-like structure. Similar experiments showed that loops are thinner and have lower uncertainties around high-velocity anomalies.

In Fig. 6.1, uncertainty loops appear to exhibit finer spatial detail than the velocity anomalies themselves. Loops define uncertainty in the anomaly boundaries: the loop's thickness therefore depends on the geometry of available seismometer arrays, and generally becomes narrower for denser arrays. Thus uncertainty loops provide a new way to interpret tomographic images: they surround isolated anomalies, and define uncertainty in anomaly shapes. For example, within the magnified Irish Sea, the uncertainty loop shows that the anomaly may extend south-east and be part of another low-velocity anomaly. Also, note that if a discontinuity in the velocity field occurred along a linear boundary, a 'line' of high uncertainty (in the location of that boundary) may be observed, rather than a closed loop.

The main difference in character between the models that lie within the dashed box in Fig. 6.2 and those in the right hand column is a switch of ray trajectories. Uncertainty loops therefore exist in part because ray paths move. This seems odd since Fermat's theorem states that traveltime changes only to second and higher orders with perturbations in ray path caused by velocity changes in the medium. However, that statement concerns the *forward* problem of predicting traveltimes given a velocity structure. The *inverse* problem consists of attributing observed raypath-averaged traveltimes to specific anomalies within the medium. Estimating ray path geometries is critical to locating these anomalies correctly, hence such second and higher order effects are central elements of tomography and uncertainty analysis. The latter holds true for

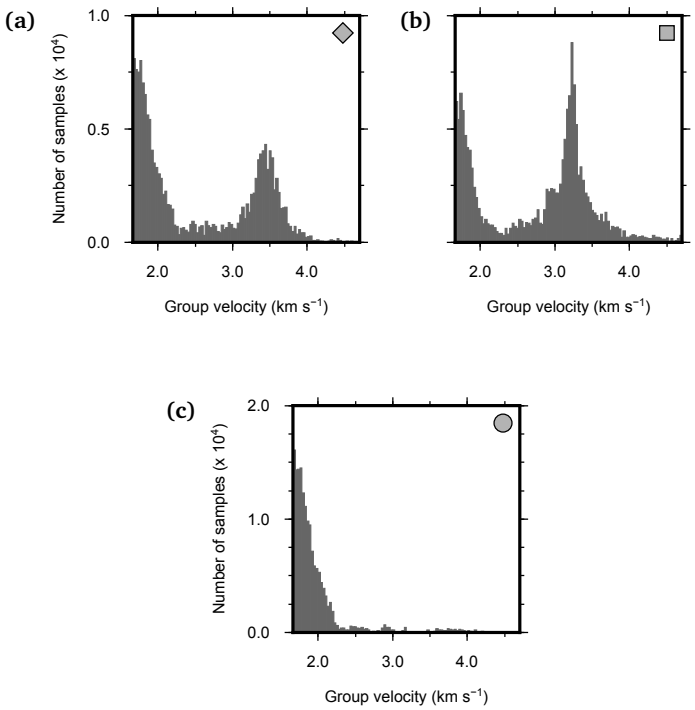

Figure 6.3. Posterior probability densities for velocities at different geographical points in the UK. Histograms are calculated at positions marked by the grey (a) diamond (−4.875°E, 54°N), (b) square (−3.5°E, 54.375°N), (c) circle (−4.25°E, 54.0625°N) in magnified plots in Fig. 6.1. Points (a) and (b) may be either inside or outside of the anomaly, hence each has probability maxima at two velocities and a large range. Point (c) is inside the anomaly and bounded above.

both low and high velocity anomalies as both cause ray path deviations (e.g., the high velocity anomaly at −1°E, 53°N also has a corresponding loop). This explains why uncertainty loops have not been observed to dominate uncertainties previously: they only dominate when both model parametrisation and ray paths are allowed to vary freely within the uncertainty analysis, which has almost never been the case in previous (usually linearised) tomography studies.

CHAPTER 7

Transdimensional Love-wave tomography of the British Isles[1]

One of the aims of this PhD thesis is to apply ambient-noise interferometry and the fully non-linear transdimensional inversion method described in Chapter 5 to compute Love-wave group-velocity maps of the British Isles at various periods. Within this chapter, I first introduce the geological setting of the British Isles and describe the sources of active and passive seismicity in the region. I also provide an outline of the method of ambient-noise tomography, explain why it is ideal for a tomographic study of this region, and justify our choice of the rj-McMC algorithm as the inversion method. I then describe a number of experimental inversions which we performed on a 10-second-period traveltime dataset in order to assess the impact of different types of data noise parametrisation on the inversion results. I explain how I interpreted these results in order to choose the most appropriate form of data noise parametrisation to be used for the inversion of all other available traveltime datasets. Finally I present Love-wave group-velocity maps of the British Isles for a number periods and discuss their significance in terms of previous geophysical and geological studies of the area. I conclude the chapter by outlining some preliminary work involving the inversion of Love-wave group-velocities obtained from the tomography maps in order to produce a 3D shear-velocity model of the crust below the British Isles.

[1]The work in this chapter is currently being prepared for submission as Galetti et al. (2015a).

7.1 Geological setting and seismicity of the British Isles

The British Isles are an intra-plate archipelago located in the north-west of the European shelf at the north-east margin of the Atlantic Ocean. The current geology of the British Isles is the result of a complex structural and tectonic history combining several deformation events with under-plate and isostatic uplift.

The basement of the British Isles is composed of a complex amalgamation of discrete terranes (i.e., "fault-bounded blocks with a distinct geological history", Woodcock & Strachan (2012)) of Precambrian and Lower Palaeozoic age (Fig. 7.1). Plate motion reconstructions show that in the early Phanerozoic the northern part of the British Isles (Scotland and north-west Ireland) was located on the passive margin of Laurentia, while the southern part (England, Wales, south-east Ireland) was located on the subducting margin of the Avalonian micro-continent. The terranes were joined together during the Caledonian orogeny, which occurred across the Ordovician, Silurian and Devonian periods (∼510–380 Ma) and caused the closure of the Iapetus Ocean as Laurentia and Avalonia collided. The closure of the Iapetus Ocean is currently marked by the Iapetus Suture, which runs from north-east England (almost along the current border between Scotland and England), across the Irish Sea and towards south-west Ireland.

Prior to the Caledonian orogeny, the Laurentian and Avalonian blocks underwent very different geological histories which resulted in the formation of very distinct lithological bodies in the two regions. The Laurentian part is characterised by the presence of high-grade metamorphic (Lewisian gneisses) and meta-sedimentary (Moine and Dalradian supergroups) complexes north of the Highland Boundary Fault, island-arc volcanics and aeolian sediments in the Midland Valley, and sandstones and mudstones in the Southern Uplands. The Avalonian part includes island-arc volcanics, resulting from its location next to the passive destructive margin of Gondwana in the Neoproterozoic, and granitic plutons and deformed volcanic-sedimentary sequences from the Cadomian orogeny in the late Neoproterozoic (650–550 Ma). However, most of the pre-Caledonian evidence of Avalonia is now covered by the products of the Varisican orogeny (Devonian and Carboniferous periods), which occurred as the Armorican micro-continent collided with Avalonia as the plate motion that had previously caused the Caledonian orogeny continued. Evidence of the Varisican orogeny can be found in the Varisicides in the south of England, bound to the north by the Varisican Front which separates them from the more weakly deformed rocks to the north. A large granitic batholith was emplaced in Devon and Cornwall towards the end of the Varisican orogeny, and the Rheic Ocean eventually closed as the continent collided with Gondwana, forming the supercontinent Pangaea and bringing the components of the British Isles to their approximately present position by the early Permian.

In terms of seismicity, the British Isles is a relatively quiescent area, as earthquakes tend to be infrequent and of relatively small magnitude. Figure 7.1 shows instrumental

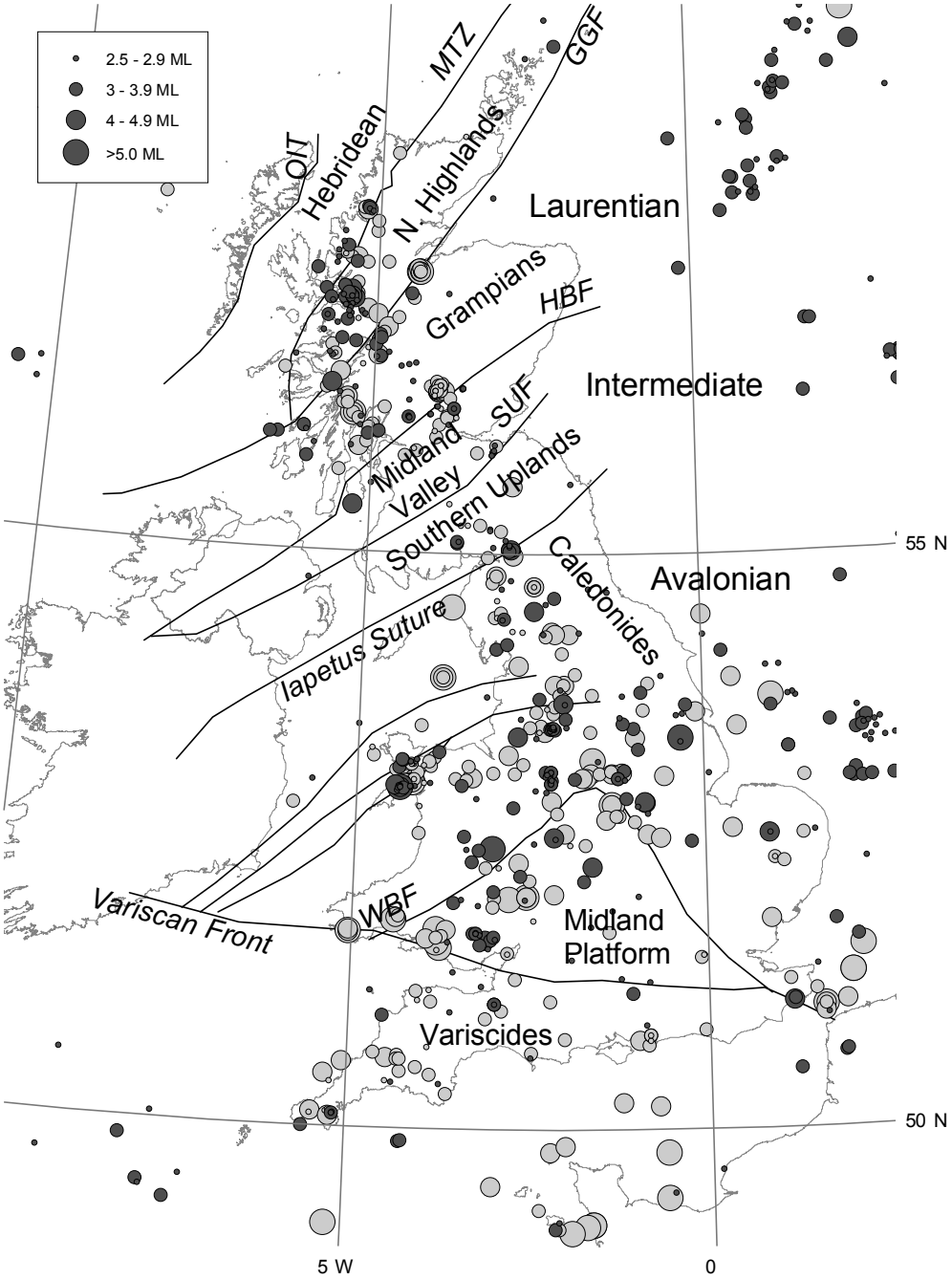

Figure 7.1. Seismicity and terrane boundaries in the British Isles. The circles indicate the location of earthquakes from instrumental (1970–present, dark grey) and historical (pre-1970, light grey) records in the British Geological Survey catalogue, which includes events with $M_L > 4.0$ up to 1700, events with $M_L > 3.0$ from 1700 to 1970, and events with $M_L > 2.0$ thereafter (Musson, 1996). The size of the circles denotes earthquake magnitude. The boundaries between the different geological terranes are after Bluck et al. (1992) and are abbreviated as follows: Outer Isles Thrust (OIT); Moine Thrust (MTZ); Great Glen Fault (GGF); Highland Boundary Fault (HBF); Southern Uplands Fault (SUF); Welsh Borderland Fault System (WBF). From Baptie (2010).

(1970–present) and historical (pre-1970) seismicity in the British Isles for earthquakes with $M_L > 2.0$ and $M_L > 3.0$, respectively (Baptie, 2010). The distribution of earthquake epicentres in the British Isles is relatively irregular, with almost no seismic activity in the north-east of mainland Britain, Ireland and the north-west Atlantic margin. Most earthquakes are located along a north-south band which mainly spans the western flank of mainland Britain. This band is relatively narrow in Scotland and increases in width towards the south.

The biased distribution of earthquakes, the absence of large-magnitude events, and the fact that the historical earthquakes in Fig. 7.1 were not recorded on digital seismometers, impose a limit on our ability to image the region tomographically using local active sources. Seismic tomography using teleseismic earthquakes also presents a number of challenges due to large attenuation at low periods and to the fact that information in their seismograms is not limited to the British Isles geographical area (i.e., it is confounded with information about Earth properties along the rest of the teleseismic paths of energy propagation). In fact, only a limited number of studies have so far attempted to image the crust and upper mantle beneath the British Isles using traditional earthquake tomography methods (Arrowsmith et al., 2005; Luckett & Baptie, 2015). However, being an archipelago bounded by the Atlantic Ocean to the west, the North Sea to the east and the Norwegian Sea to the north, the British Isles are naturally surrounded by sources of seismic ambient noise, including the primary (12–14 seconds period) and secondary (6–8 seconds period) oceanic microseisms, waves, wind and ocean currents. Since these sources are relatively constant and repeatable, the British Isles are therefore an ideal region for a tomographic study which uses ambient-noise interferometry.

7.2 Ambient-noise tomography with the rj-McMC algorithm

Over the last ten years, seismic interferometry has been revolutionising the way seismologists study the Earth by providing novel ways of obtaining information on the Earth's interior from naturally-occurring seismic ambient noise. Rather than removing it to improve data quality, seismologists can now extract useful information from seismic noise by cross-correlating noise traces recorded at pairs of seismic receivers. So doing yields the Green's function between the two receiver locations (see Chapter 1). Since most ambient-noise sources are located near the surface of the Earth, Green's functions constructed from noise cross-correlations typically contain the surface-wave component of the wavefield that would have propagated between the two receivers if one of them had been a source. Because interferometric traces can be treated just like real earthquake seismograms, seismic interferometry obviates the need for earthquakes to be recorded, allowing virtual seismic sources to be placed anywhere on Earth where there is a seismometer, and at any desired time. Using a combination of ambient-noise and

source-receiver interferometry, seismologists can even reconstruct unrecorded earthquake seismograms at seismic stations that were not installed at the time that the earthquake occurred (Curtis et al., 2012; Entwistle et al., 2015).

Within the context of seismic tomography and imaging, seismic interferometry has significantly increased our ability to image the Earth's interior. Particularly, since the natural distribution of earthquakes is strongly irregular and mainly localised to plate margins (Fig. 1.4), interferometry provides a powerful tool for earthquake and crustal seismologists by allowing virtual earthquakes or sources to be placed even in seismically quiescent regions. Hence, traditional imaging methods may now be applied to areas of the Earth that could not previously be investigated due to a lack of active seismic energy sources. The method of *ambient-noise tomography* (ANT) has recently emerged as a novel imaging technique which makes use of information retrieved from ambient-noise cross-correlations, rather than earthquake records, to invert for subsurface structure. First applied to real data by Shapiro et al. (2005), ANT is now commonly used to image both seismically active and quiescent areas, and it is ideal when the area of interest is characterised by little seismic activity such as the interior of a continent or the bottom of the ocean. To date, ANT has been used at regional and continental scales to produce group-velocity maps using mainly Rayleigh-wave motion, but a number of studies have also used Love-wave cross-correlations to image Europe (Li et al., 2010a), Asia (Cho et al., 2007; Li et al., 2010b) and North America (Bensen et al., 2008; Lin et al., 2008; Roux, 2009). In addition, ANT has been successfully used to produce images of smaller-scale structures such as volcanic edifices (Masterlark et al., 2010; Jay et al., 2012; Nagaoka et al., 2012) and inhomogeneities in oil and gas fields (Haney & Douma, 2010, 2012), as well as of local structures at engineering seismology scales (Picozzi et al., 2009; Pilz et al., 2012) and on the seabed (Mordret et al., 2013a,b; de Ridder & Dellinger, 2011; de Ridder et al., 2014).

However, just as the natural distribution of earthquakes is strongly irregular and localised to plate margins, the distribution of seismic stations over the Earth's surface is also far from uniform, with many areas (e.g., central Africa, Russia, northern Canada) having very little coverage. On the other hand, certain regions such as the US are well covered by dense receiver networks, and others (e.g., Australia, south America) have variable coverage with higher station density in areas of higher seismic activity or population. Due to irregularities in the distribution of seismic receivers, resolution when performing ANT may therefore vary to a great extent across regions which are unevenly sampled, being higher in the parts of the model that are well covered by receivers and decreasing where station density is scarce. The choice of an appropriate inversion method to perform ANT that can correctly compensate for regions of variable station coverage, is therefore particularly critical.

A variety of tomography methods that take non-uniform sampling into account have been developed using irregular model parametrisations, and an extensive overview of

these methods can be found in Rawlinson et al. (2010). Recently, an implementation of model parametrisation that uses Voronoi cells was proposed by Bodin & Sambridge (2009), who used Bayes' theorem, Markov-Chain Monte Carlo (McMC) and the reversible-jump algorithm to invert traveltime data over a large number of velocity models and obtain an ensemble of solutions which are distributed according to the posterior probability distribution (Section 5.3.1). This method is referred to as 'transdimensional', in the sense that the number of parameters is itself one of the quantities which are determined during inversion. Hence, the method can be largely data driven as it requires only the minimum amount of assumptions to be made by the user who simply defines prior probability distributions on the various parameters. When little information on the model is available before the inversion, prior distributions may be set to uninformative uniform distributions with wide bounds, ensuring that the final models are not biased by the choice of the prior. Compared to more traditional inversion methods that keep the model parametrisation fixed, this method is particularly flexible as it dynamically adapts to non-uniform data coverage without requiring the use of any arbitrary regularisation (e.g., damping and smoothing), and was used successfully by Bodin & Sambridge (2009) to obtain Rayleigh-wave velocity models of Australia from ambient-noise interferometry.

Within this study, the resolution of seismic tomography across the British Isles is bound to be strongly variable due to irregularities in the distribution of the seismic stations used (Fig. 5.2). Figure 7.2 shows all valid raypaths (i.e., raypaths that satisfy the quality control conditions described in Section 5.2.2) at each of the analysed periods assuming a uniform background velocity. As can be seen in Fig. 7.2, the number of valid raypaths is not constant but varies with period, generally decreasing as period increases with the exception of the paths at 4 seconds period. This variation is likely to be due to the quality checks applied to the traveltime dataset at each period (see Section 5.2.2), and also to the fact that it was not always possible to pick group-velocities at all periods on each path. As expected, ray density is highest in Scotland within the dense RUSH-II array and decreases in northern England where station density is scarce. Good raypath coverage is also found in the south of England, where most stations from the UK-wide array are located, and is low along the coast, in marine areas and in Ireland since most stations are located on mainland Britain. In a previous study, Nicolson et al. (2014) attempted to partially even out the station distribution by resampling the RUSH-II array so that it covered as large an area as possible with relatively uniform station separation. This allowed them to use a uniform grid for inversion and to choose the appropriate grid size from chequerboard resolution tests. However, as noted in Section 5.3.1, the use of traditional inversion methods, which combine regular grids with the application of regularisation parameters, may introduce biases and artefacts into the solution when the data distribution is spatially uneven. In such cases, the choice of a dynamically-adaptive method such as the rj-McMC algorithm is particularly favourable. Within this study, we therefore used the rj-McMC tomography

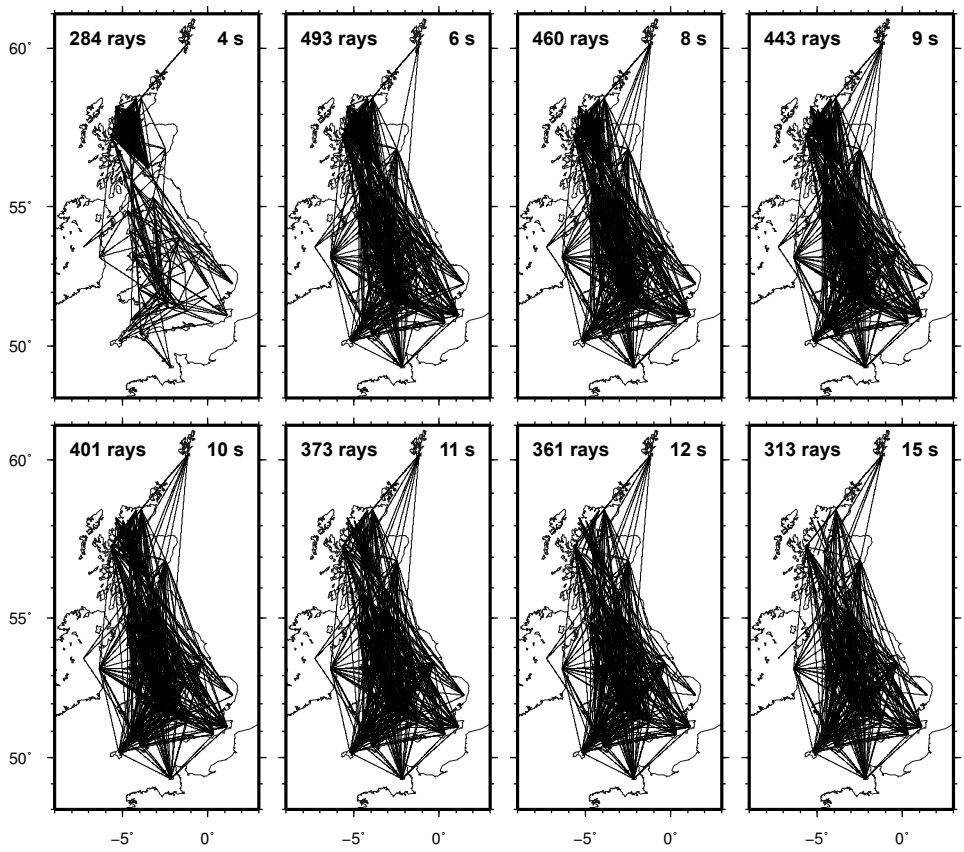

Figure 7.2. Raypaths used for tomography at all of the analysed periods. Note how the density of active raypaths is particularly uneven across the imaged area.

method to remove any *a priori* constraints on grid size and avert the use of regularisation parameters during inversion. In addition, by allowing rays to be re-computed at each step of the Markov chain, we prevented any raypath-related biases from being introduced into the final solution.

7.3 Traveltime uncertainty parametrisation

Traveltime uncertainties are a fundamental part of seismic traveltime datasets as they define how accurately the observed traveltimes should be fit during inversion. Within a transdimensional framework, the use of correct uncertainty measurements is particularly critical as their magnitude directly influences the number of model parameters, hence the complexity of the solution. One of the advantages of ambient-noise tomography compared to more traditional earthquake tomography methods is the ability to estimate traveltime uncertainties from the variability of the interferometric Green's functions in time. As an example, Lin et al. (2007) and Yang et al. (2007) used 3-month stacks of cross-correlations to analyse the repeatability of interferometric Green's functions and estimate uncertainty in the dispersion measurements. However, more recent studies by

Nicolson et al. (2012); Nicolson et al. (2014) showed that the same approach on a Rayleigh-wave dataset from the British Isles yielded traveltime uncertainties that were lower than expected. Hence, although a number of tomography studies have successfully been conducted using Green's functions from ambient noise and their associated uncertainties, it is still unclear how exactly uncertainties in ambient-noise datasets should be quantified, and research on this topic is ongoing.

Within this section, I describe a number of experiments that we conducted while testing the fully non-linear rj-McMC algorithm described in Chapter 5 with different types of data noise parametrisation. The results of these experiments highlight the impact of data uncertainties on the final solution, and may provide guidelines for future studies. In all of the following experiments, we inverted the same 10 second period traveltime dataset by running 16 parallel Markov chains for 3 million iterations each, discarding the first 500000 samples as burn-in and only retaining every 500$^{\text{th}}$ sample in the solution ensemble. We gave uniform priors to cell velocities (Table 7.1), number of cells (10–300) and noise hyperparameters (when present).

We performed an initial inversion using the traveltime uncertainties obtained from independent random stacks of daily cross-correlations as described in Section 5.2.2. The average 10 second group-velocity map and the posterior distribution on the number of cells obtained in this case are shown in Figs 7.3(a) and 7.4(a), respectively. Although the velocity map shows realistic features which correlate with the known geology, the number of parameters needed to constrain the velocity model is very high, with the majority of samples having a number of Voronoi cells that falls at the higher end of the prior distribution. We also found that similar posterior distributions were obtained for priors with even higher upper bounds, hence this is unlikely to be due to our particular choice of prior being too narrow. In transdimensional tomography, the number of Voronoi cells needed to constrain the data is directly affected by the level of data noise (Bodin et al., 2012b): since the data is fitted up to the noise level, large traveltime uncertainties produce simpler models with fewer Voronoi cells, while small uncertainty values cause more cells to be added into the model, increasing its complexity. The effect observed in Fig. 7.4(a) can therefore be explained as a consequence of the measured traveltime uncertainties being too small and the data being over-fitted.

In a non-transdimensional case, a similar behaviour was observed by Nicolson et al. (2012); Nicolson et al. (2014), who used a linearised inversion method to produce a set of of tomographic maps of the British Isles at various periods using different combinations of damping and smoothing. They then calculated the weighted root-mean-square of the data residuals (RMS_W) for each map, a dimensionless quantity which provides a measure of the normalised misfit of the post-inversion modelled data:

$$RMS_W = \sqrt{\frac{1}{N}\sum_{i=1}^{N}\frac{x_i^2}{\sigma_i^2}}\,, \tag{7.1}$$

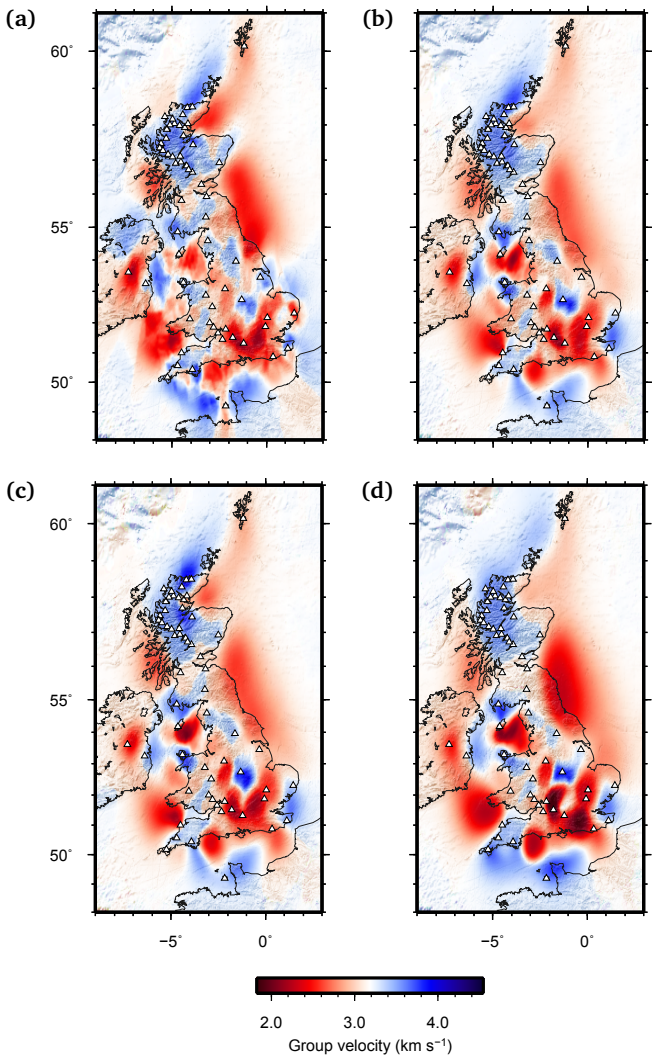

Figure 7.3. Average Love-wave group-velocity maps obtained from transdimensional tomography with different types of data noise parametrisation at 10 seconds period. (a) Traveltime uncertainties are estimated from random stacks of noise cross-correlations. (b) Traveltime uncertainties are estimated by multiplying those obtained from random cross-correlations stacks by scaling factor λ, which is estimated during inversion. (c) Traveltime uncertainties are estimated by multiplying those obtained from random cross-correlations stacks by scaling factors λ_1 (for RUSH-II stations) and λ_2 (for the UK-wide array), which are estimated during inversion. (d) Traveltime uncertainties are assumed to vary with source-to-receiver distance, and are parametrised according to equation (5.9).

where N is the number of raypaths, and x_i and σ_i are the traveltime residual and uncertainty associated with raypath i, respectively. As the RMS_W includes a ratio of traveltime residuals to uncertainties, values which are greater than 1 denote solutions that are mostly affected by the regularisation parameters (and that should therefore be discarded), while an RMS_W which is less than 1 indicates that the observed traveltimes fit the solution to within data uncertainties. Nicolson et al. (2012); Nicolson et al. (2014) obtained RMS_W values greater than 1 even when no regularisation was applied during

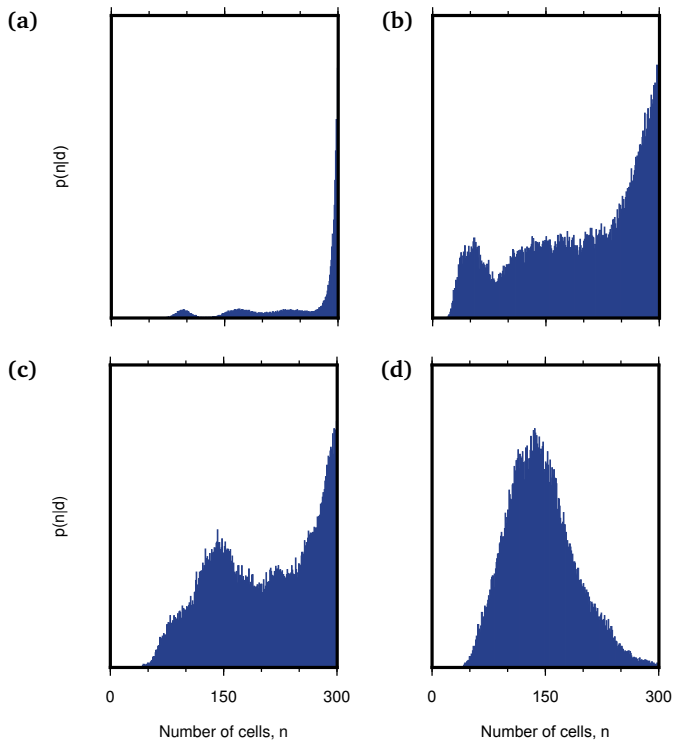

Figure 7.4. Posterior distributions on number of cells associated with the Love-wave group-velocity maps shown in Fig. 7.3. (a) Posterior on number of cells associated with the average map in Fig. 7.3(a). (b) Posterior on number of cells associated with the average map in Fig. 7.3(b). (c) Posterior on number of cells associated with the average map in Fig. 7.3(c). (d) Posterior on number of cells associated with the average map in Fig. 7.3(d).

inversion, indicating that the level of data noise estimated with this method was not sufficiently large.

We therefore tried inverting the same traveltime dataset by multiplying the measured uncertainties by scaling factor λ (as in equation (5.8)), whose value was estimated as one of the inversion parameters. A uniform prior between 0.2 and 8 was chosen for λ, and to evaluate the effect of the combination of the two datasets (RUSH-II and UK-wide) inversions were performed first for a single λ for both datasets and then for two separate values of λ, one for each dataset. Average velocity maps and posteriors on the number of cells are shown in Figs 7.3(b) and 7.4(b) for a single λ, and in Figs 7.3(c) and 7.4(c) for two separate λ values. Although the velocity maps in Figs 7.3(b) and 7.3(c) show similar structures to those observed in the previous case (Fig. 7.3(a)), the posteriors on the number of cells show a significant reduction in the number of parameters needed to constrain the structure, as some of the data is no longer over fitted. In both cases, the posteriors on λ (Figs 7.5(a) and 7.5(b)) peak at values which are greater than one, confirming that the uncertainties measured from the independent cross-correlation stacks should be scaled up to larger values. In particular, Fig. 7.5(b) shows that the magnitude of scaling factor λ is expected to be around 1 for the RUSH-II dataset (dark blue), while

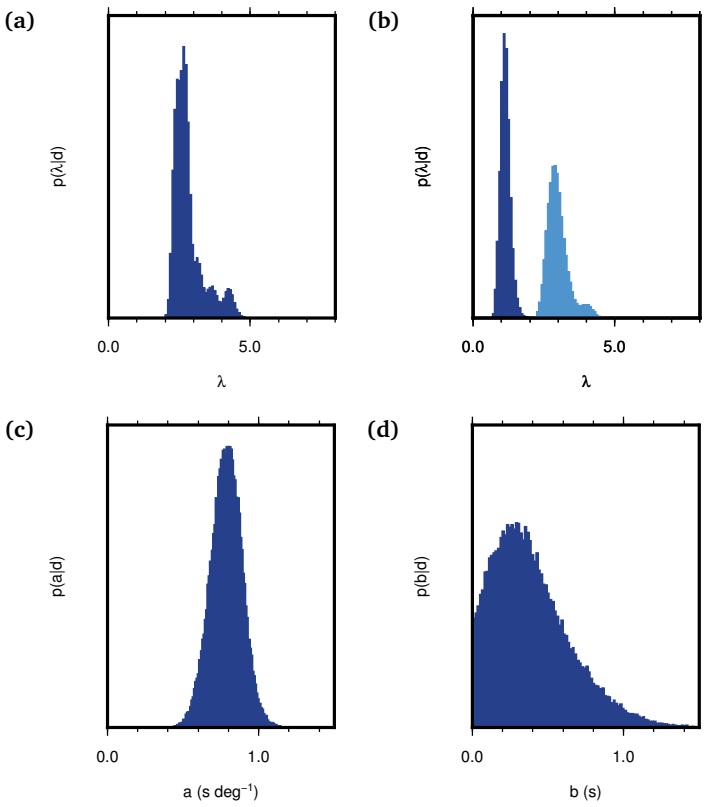

Figure 7.5. Posterior probability distributions on noise hyperparameters (a) λ for RUSH-II and UK-wide arrays combined, (b) λ for separate RUSH-II (dark blue) and UK-wide (light blue) arrays, (c) a and (d) b.

it peaks around 3 for the UK-wide array (light blue), suggesting that the magnitude of the measured uncertainties is significantly different in the two datasets. This is consistent with the findings of Nicolson et al. (2012); Nicolson et al. (2014), who showed that the uncertainty estimation method described in Section 5.2.2 seemed to work relatively well for a study across the Scottish Highlands which used Rayleigh-wave data from the RUSH-II newtork (Nicolson et al., 2012), while it appeared to have flaws when applied over the whole of the British Isles using a similar array of stations to the UK-wide deployment from this study (Nicolson et al., 2014). Nevertheless, Figs 7.4(b)–7.4(c) show that the majority of models are still characterised by a very large number of Voronoi cells that tends to the upper bound of the prior, suggesting that the scaled uncertainties are still not large enough to be considered reliable.

Finally we performed the inversion by assuming data noise proportional to source-to-receiver distance as in equation (5.9): uniform priors were chosen for a (0.3–1.2 deg s^{-1}) and b (0.0–1.5 s) in that equation. The average velocity map and the posterior distribution on the number of cells are shown in Figs 7.3(d) and 7.4(d), respectively. The posteriors on noise hyperparameters a and b are shown in Figs 7.5(c) and 7.5(d), respectively. Although the overall velocity structures are comparable to those observed in the previous cases, the posterior on the number of cells shows that traveltimes are correctly fitted up to the

estimated uncertainty values. For this reason, we chose this data noise parametrisation to invert seismic traveltimes at all of the other analysed periods.

Overall, the four velocity maps in Fig. 7.3 display similar high- and low-velocity features which agree with one another and with the known geology of the area (see Section 7.4). However, the magnitude of these structures appears to be strongly influenced by the data noise parametrisation employed during inversion. In particular, the magnitude of the velocity structures observed in Fig. 7.3(a) appears to be lower than in the other cases (compare for instance the Irish sea low-velocity anomaly near −4°E, 54°N, and the high-velocity anomaly near −1°E, 52.5°N), and the large number of Voronoi cells in the posterior causes the boundaries between low- and high-velocity structures to look 'staggered', as some of the sharp Voronoi cell boundaries are still visible. This does not seem to happen in the average map of Fig. 7.3(d), which looks smoother and does not reveal the presence of Voronoi cells in the ensemble models. In general, an increase in the smoothness of the average map can be observed from panel (a) to (d) in Fig. 7.3, even though on average fewer cells are used in (d) than in (a), (b) or (c); this can be related to an improvement in the estimation of the number of parameters needed, which in turn is connected to a better estimation of traveltime uncertainties.

Plots showing the variation of the number of cells throughout the Markov chain can also provide useful information on convergence, which can be assumed to have been reached when the number of Voronoi cells becomes relatively stationary around the region of highest probability. Figure 7.6, which displays the number of Voronoi cells versus sample number for all Markov chains run in the four cases discussed above, shows that convergence is not reached by the end of the Markov chains in the first three cases (Figs 7.6(a)–(c)), while it is reached within a few hundred thousand iterations when data noise is parametrised according to equation (5.9) (Fig. 7.6(d)). A similar behaviour is observed on plots of noise parameters versus iteration number (not shown).

7.4 Love-wave group-velocity maps

Within this study, we performed traveltime tomography at 4, 6, 8, 9, 10, 11, 12 and 15 seconds period. We chose uniform priors for the number of Voronoi cells (10–400), cell velocity and location, and hyperparameters a (0.3–3.0 deg s^{-1}) and b (0.0–2.0 s). The cell velocity prior was chosen by measuring the average velocity (v_{avg}) across all active paths at each period and providing upper and lower velocity bounds defined by half-width θ_v around v_{avg}, which was chosen depending on the range of observed velocities (Table 7.1). Note that average velocity v_{avg} generally increases with increasing period.

For each period, 16 Markov chains were run in parallel for 3 million iterations each, and every 500th sample after a burn-in period of 500000 iterations was included in the ensemble. As a means of quality control, we analysed plots similar to those in Fig. 7.6 to

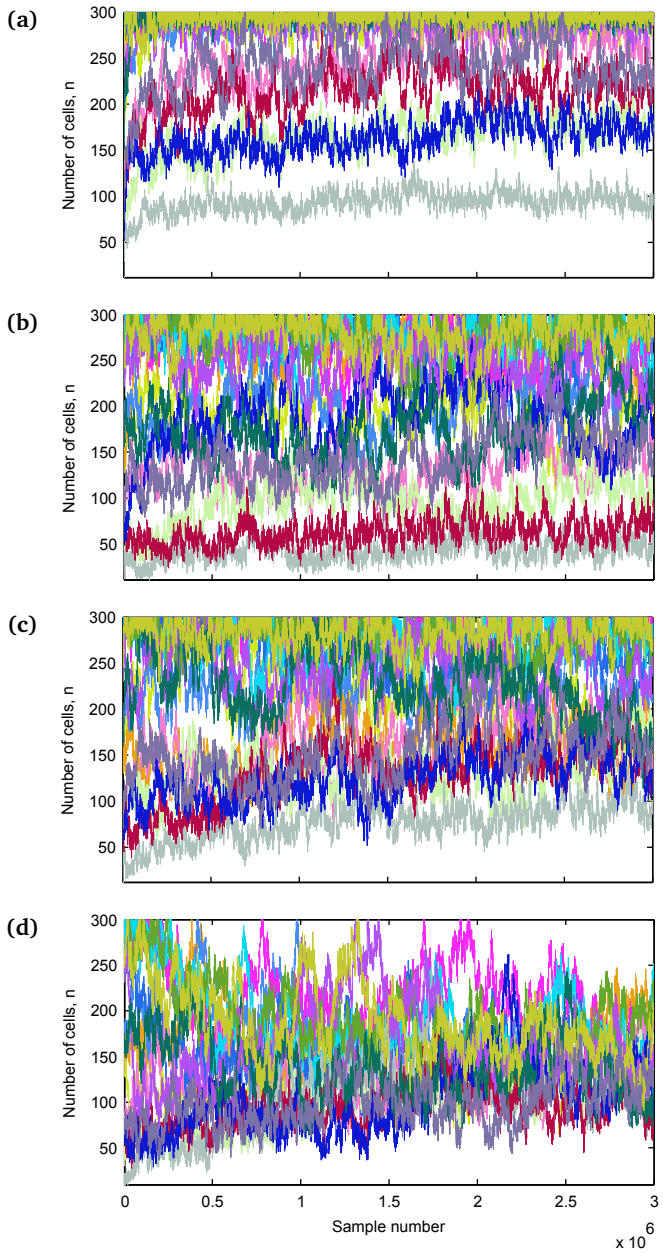

Figure 7.6. Number of Voronoi cells versus iteration number on each of the 16 Markov chains ran for the four experiments in Figs 7.3–7.4. (a) Traveltime uncertainties are estimated from independent random stacks of noise cross-correlations. (b) Traveltime uncertainties are estimated by multiplying those obtained from random cross-correlations stacks by scaling factor λ, which is estimated during inversion. (c) Traveltime uncertainties are estimated by multiplying those obtained from random cross-correlations stacks by scaling factors λ_1 (for RUSH-II stations) and λ_2 (for the UK-wide array), which are estimated during inversion. (d) Traveltime uncertainties are assumed to vary with source-to-receiver distance and are parametrised according to equation (5.9).

Period (s)	v_{avg} (km s^{-1})	θ_v (km s^{-1})
4	3.1720	1.7224
6	3.0464	1.5707
8	3.0701	1.5093
9	3.1218	1.5652
10	3.1847	1.6211
11	3.2292	1.3436
12	3.2482	1.2045
15	3.3239	1.1965

Table 7.1. Average velocity (v_{avg}) and upper and lower velocity bounds (θ_v) used to define the velocity prior at each of the analysed periods. At each period, the bounds of the uniform velocity prior is given by $v_{avg} \pm \theta_v$.

identify Markov chains which displayed an anomalous behaviour compared to the others and remove them from the analysed ensemble. Average velocity models and maps of standard deviation were calculated from the model ensemble, together with posterior distributions on number of cells, noise hyperparameters a and b, velocity at each point, and density of Voronoi nuclei across the ensemble.

The results of non-linear rj-McMC tomography at all of the analysed periods are shown in Figs 7.7–7.14. In order to ease the comparison of velocity structures and uncertainties between the various periods, all average and standard deviation maps are also plotted in Figs 7.15–7.16 using the same colour scale.

7.5 Comments and interpretation

The group-velocity maps in Fig. 7.15 and in panel (a) of Figs 7.7–7.14 display the average group-velocity at each geographical point across the ensemble of Voronoi velocity models. Despite the ensemble models being parametrised by Voronoi cells, the average maps are smooth and do not show any trace of the Voronoi cell geometry. In general, an increase in group velocity is observed with increasing period, reflecting the general tendency of seismic velocity to increase with depth. The only exception to this trend is given by the 4 second average map, whose average background velocity is larger than those observed at both 6 and 9 seconds period. This is likely due to the fact that most raypaths at 4 seconds are located in the Scottish Highlands (as can be seen in Fig. 7.2), which are well known for being a region of high velocity due to their metamorphic origin. In general, the velocity structures that can be observed in the average maps seem to correlate well with the geology of the area (see below).

The standard deviation maps in Fig. 7.16 and in panel (b) of Figs 7.7–7.14 display the standard deviation of group-velocity across the ensemble of Voronoi velocity models, and provide an indication of how well the velocities in the average maps are constrained. From these plots, it is evident that the magnitude of the uncertainties depends on both raypath coverage and underlying velocity structure. Off-shore uncertainties are large due

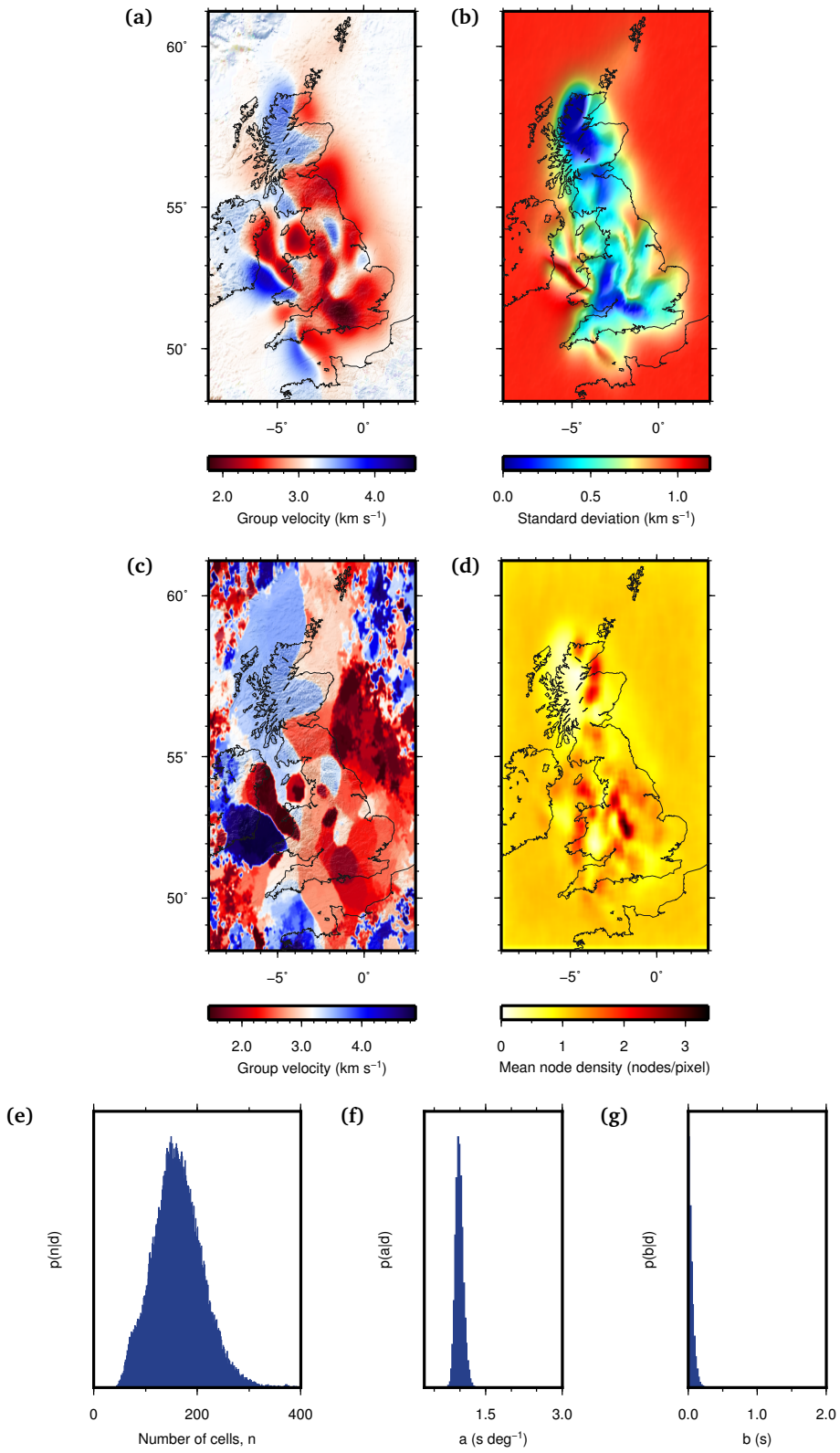

Figure 7.7. Results of non-linear rj-McMC tomography at 4 seconds period. (a) Average Love-wave group-velocity map. (b) Standard deviation map. (c) Map of maximum-probability group-velocity. (d) Map of Voronoi node density across the ensemble (average number of nuclei per $0.5° \times 0.5°$ pixel). (e) Posterior on number of Voronoi cells. (f) Posterior on noise hyperparameter a. (g) Posterior on noise hyperparameter b. At this period 284 traveltime data were included.

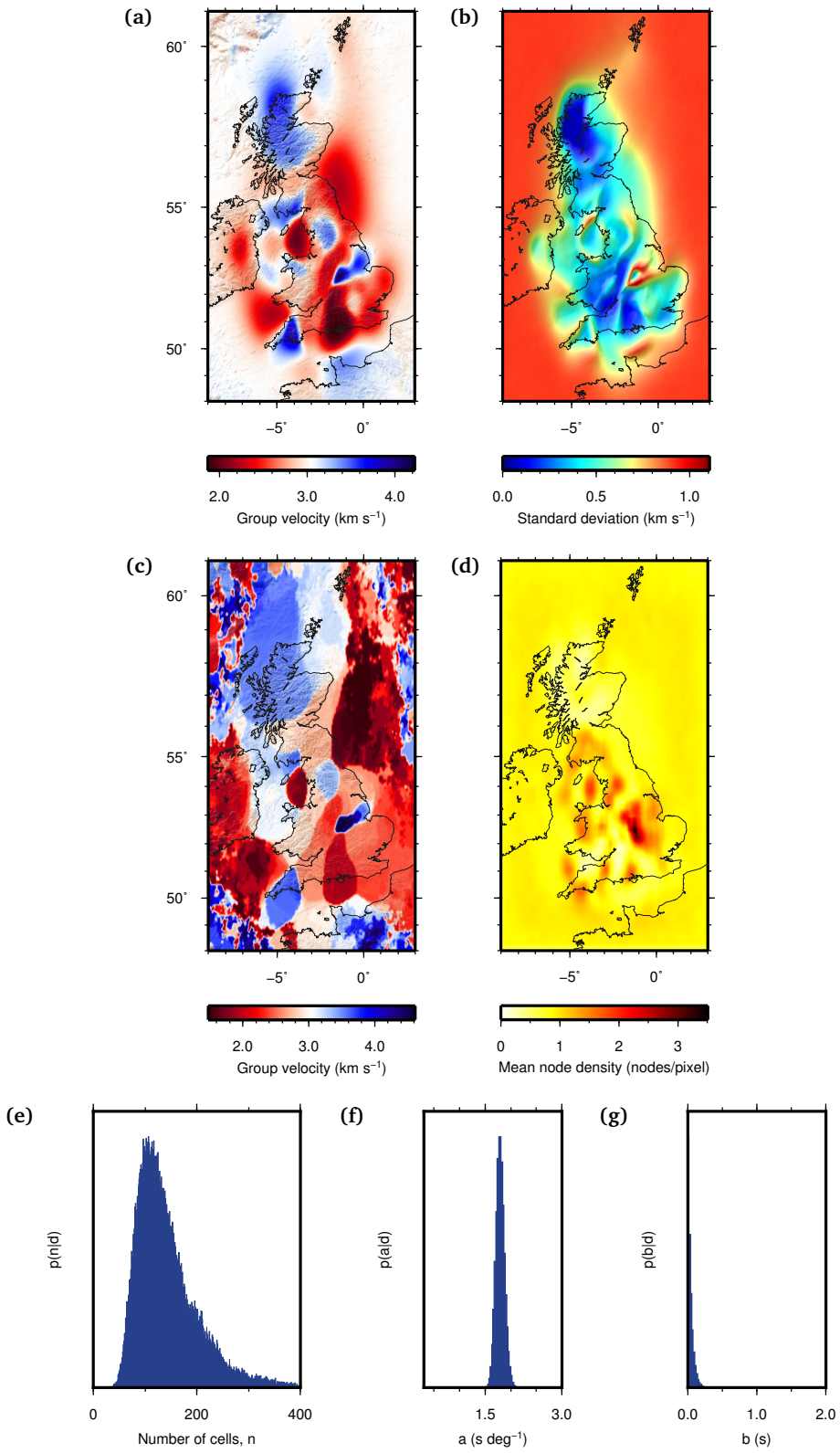

Figure 7.8. Results of non-linear rj-McMC tomography at 6 seconds period. (a) Average Love-wave group-velocity map. (b) Standard deviation map. (c) Map of maximum-probability group-velocity. (d) Map of Voronoi node density across the ensemble (average number of nuclei per $0.5° \times 0.5°$ pixel). (e) Posterior on number of Voronoi cells. (f) Posterior on noise hyperparameter a. (g) Posterior on noise hyperparameter b. At this period 493 traveltime data were included.

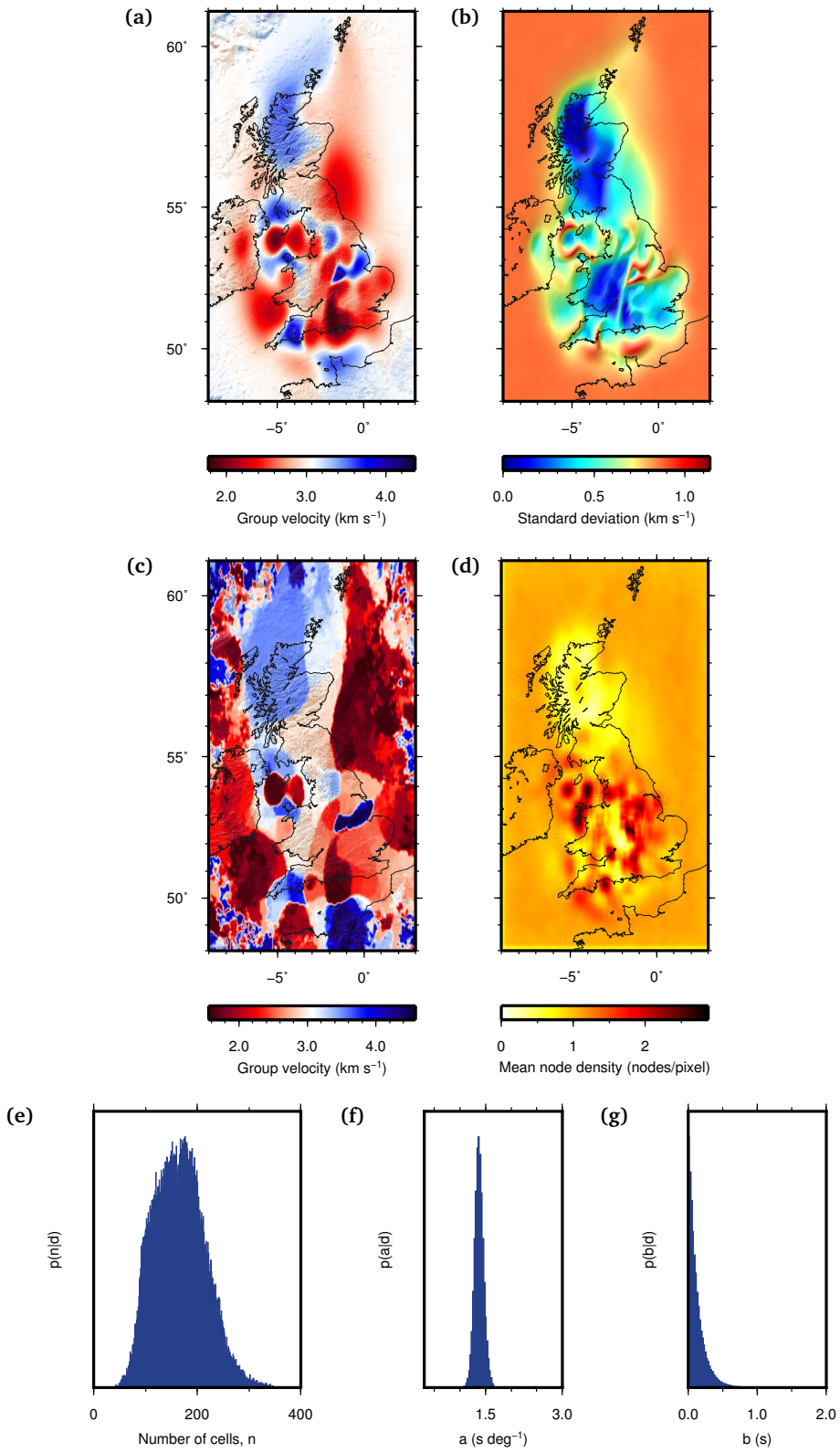

Figure 7.9. Results of non-linear rj-McMC tomography at 8 seconds period. (a) Average Love-wave group-velocity map. (b) Standard deviation map. (c) Map of maximum-probability group-velocity. (d) Map of Voronoi node density across the ensemble (average number of nuclei per $0.5° \times 0.5°$ pixel). (e) Posterior on number of Voronoi cells. (f) Posterior on noise hyperparameter a. (g) Posterior on noise hyperparameter b. At this period 460 traveltime data were included.

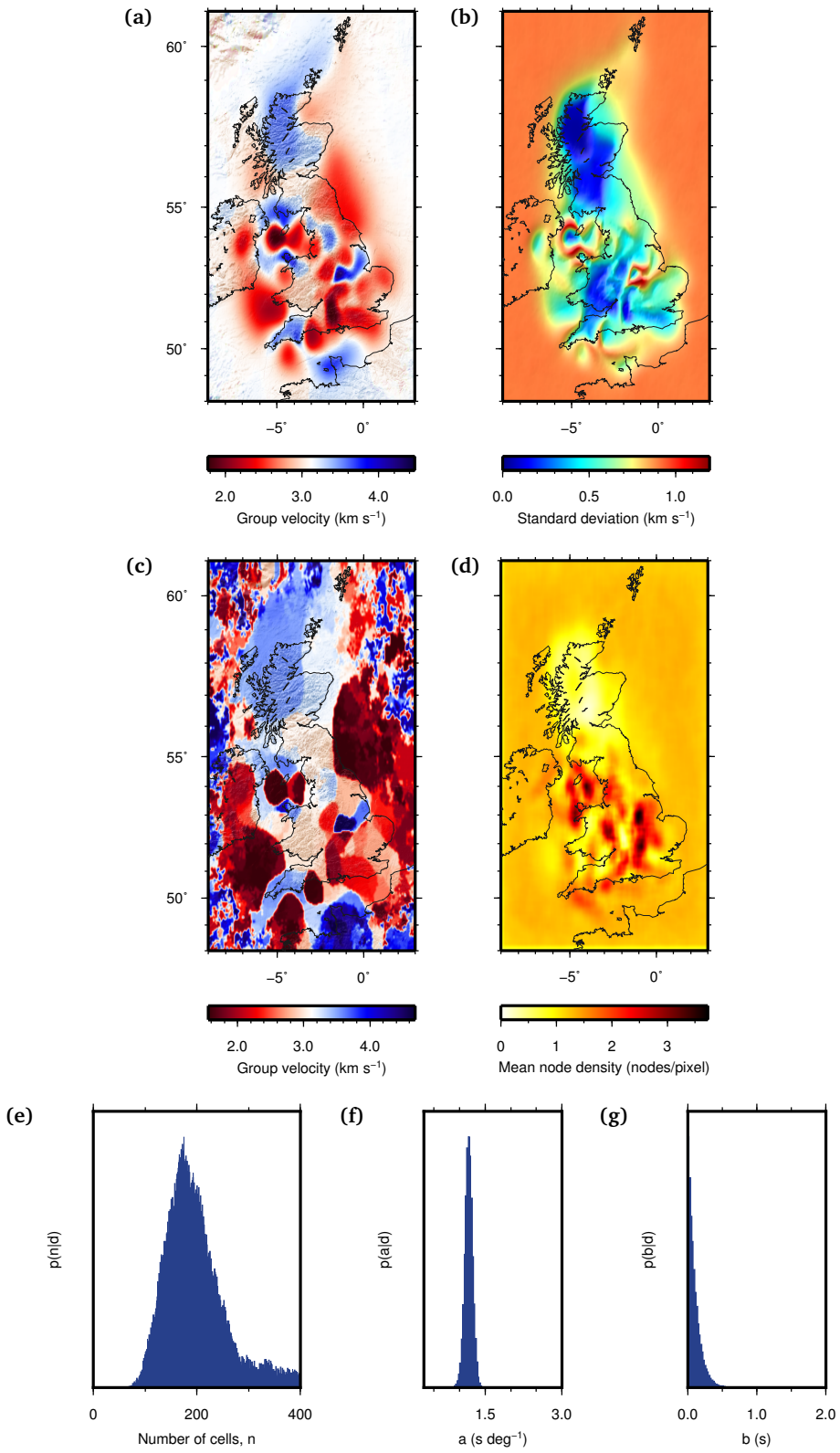

Figure 7.10. Results of non-linear rj-McMC tomography at 9 seconds period. (a) Average Love-wave group-velocity map. (b) Standard deviation map. (c) Map of maximum-probability group-velocity. (d) Map of Voronoi node density across the ensemble (average number of nuclei per $0.5° \times 0.5°$ pixel). (e) Posterior on number of Voronoi cells. (f) Posterior on noise hyperparameter a. (g) Posterior on noise hyperparameter b. At this period 443 traveltime data were included.

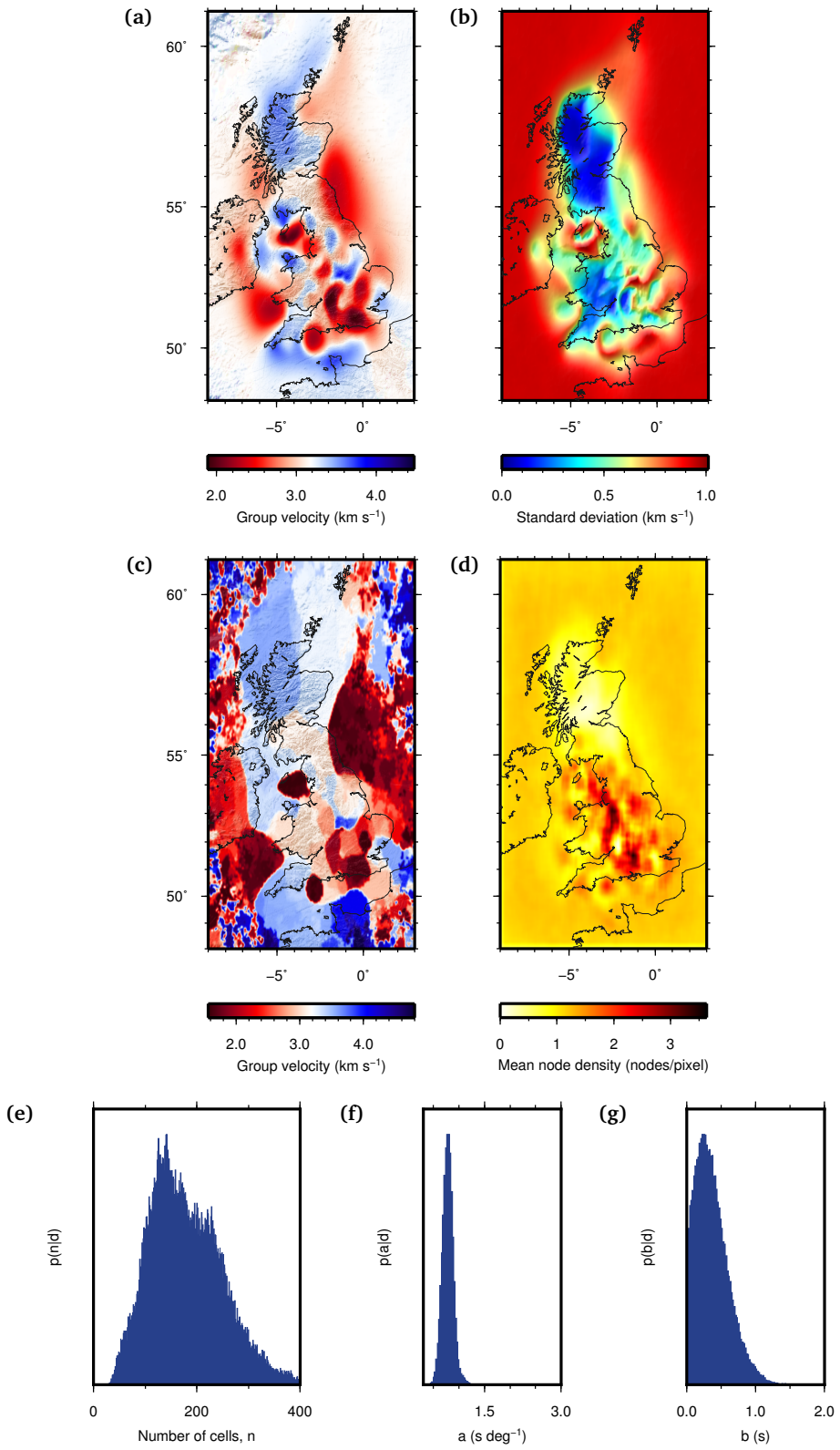

Figure 7.11. Results of non-linear rj-McMC tomography at 10 seconds period. (a) Average Love-wave group-velocity map. (b) Standard deviation map. (c) Map of maximum-probability group-velocity. (d) Map of Voronoi node density across the ensemble (average number of nuclei per $0.5° \times 0.5°$ pixel). (e) Posterior on number of Voronoi cells. (f) Posterior on noise hyperparameter a. (g) Posterior on noise hyperparameter b. At this period 401 traveltime data were included.

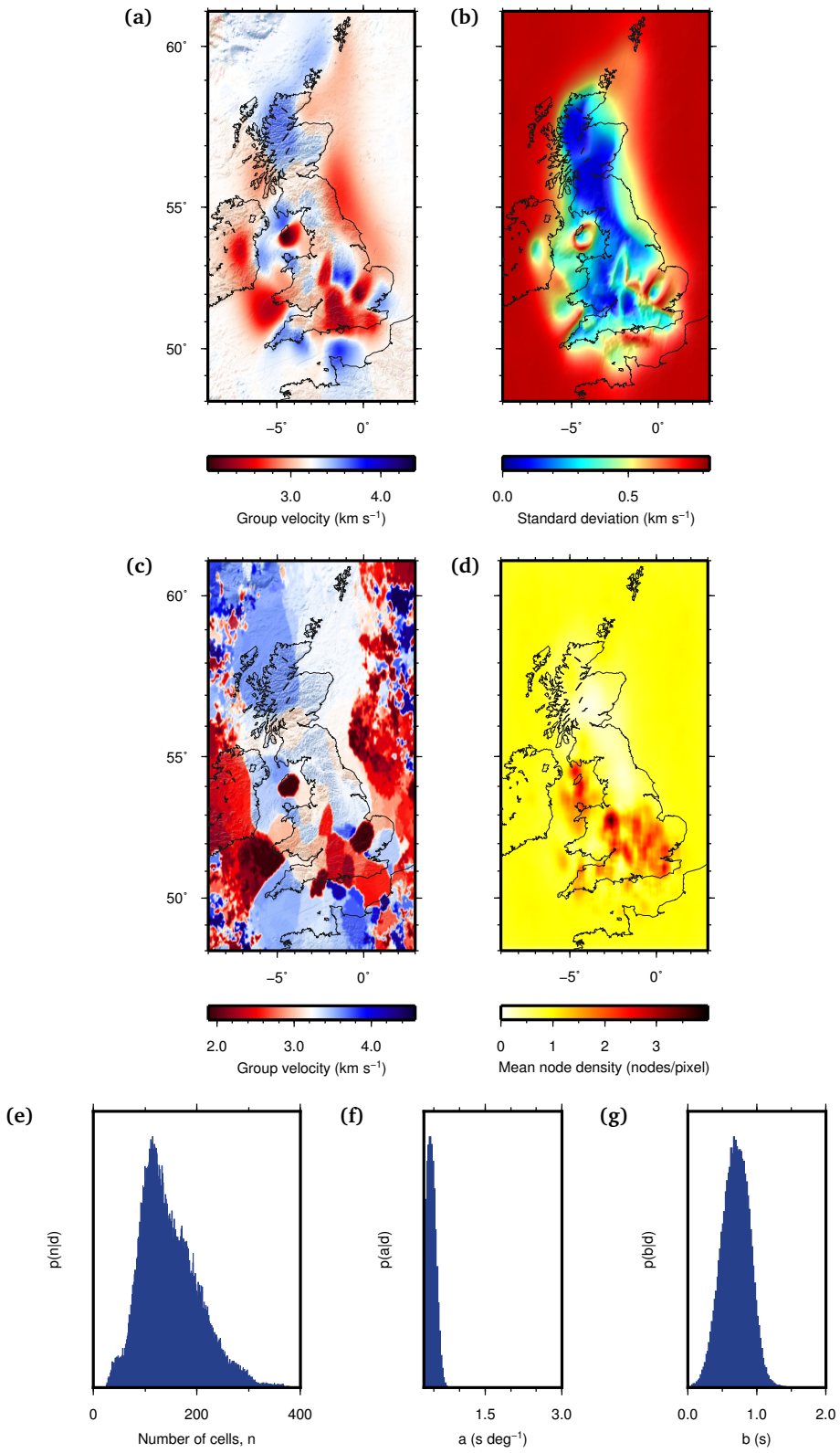

Figure 7.12. Results of non-linear rj-McMC tomography at 11 seconds period. (a) Average Love-wave group-velocity map. (b) Standard deviation map. (c) Map of maximum-probability group-velocity. (d) Map of Voronoi node density across the ensemble (average number of nuclei per $0.5° \times 0.5°$ pixel). (e) Posterior on number of Voronoi cells. (f) Posterior on noise hyperparameter a. (g) Posterior on noise hyperparameter b. At this period 373 traveltime data were included.

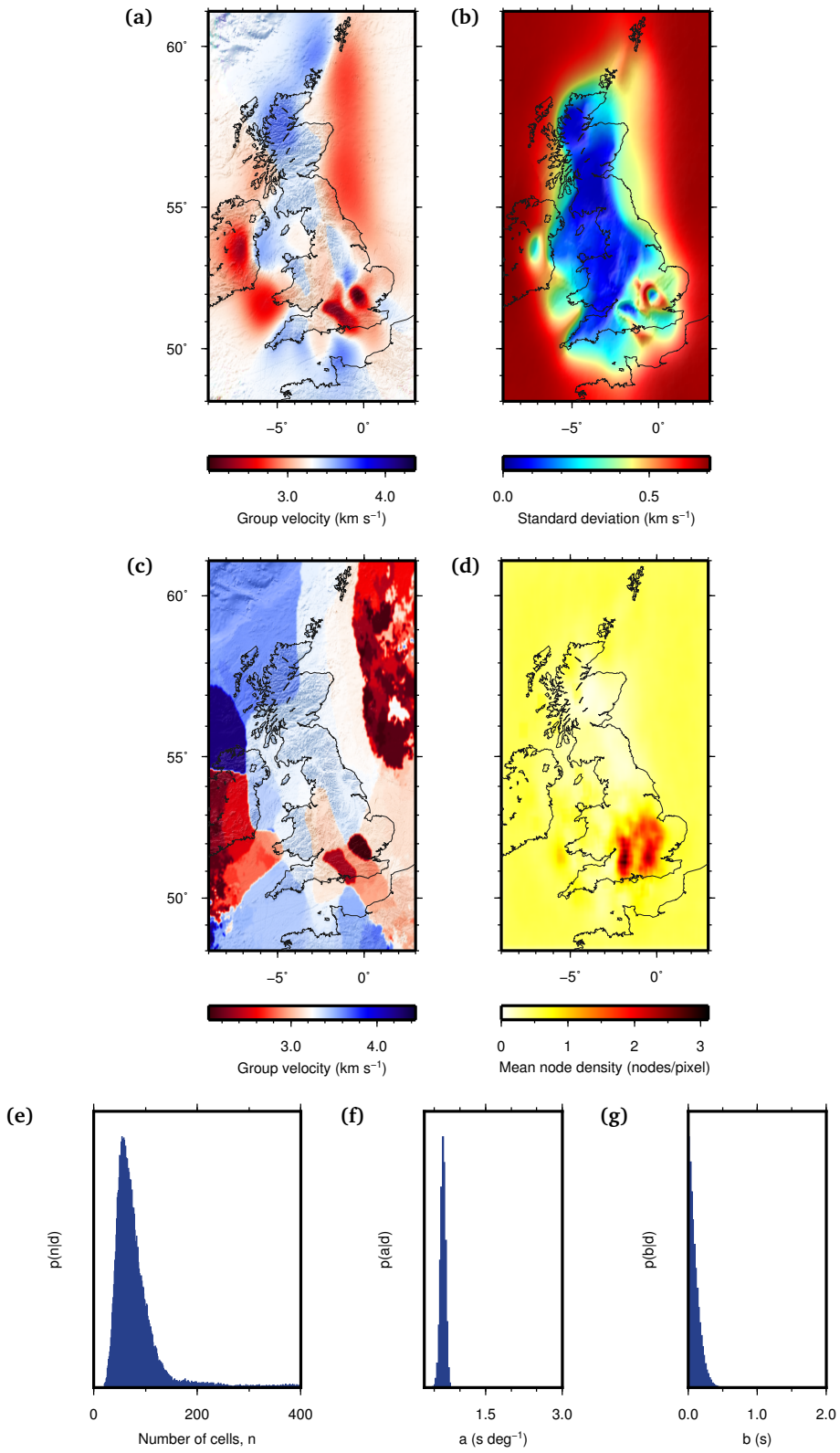

Figure 7.13. Results of non-linear rj-McMC tomography at 12 seconds period. (a) Average Love-wave group-velocity map. (b) Standard deviation map. (c) Map of maximum-probability group-velocity. (d) Map of Voronoi node density across the ensemble (average number of nuclei per $0.5° \times 0.5°$ pixel). (e) Posterior on number of Voronoi cells. (f) Posterior on noise hyperparameter a. (g) Posterior on noise hyperparameter b. At this period 361 traveltime data were included.

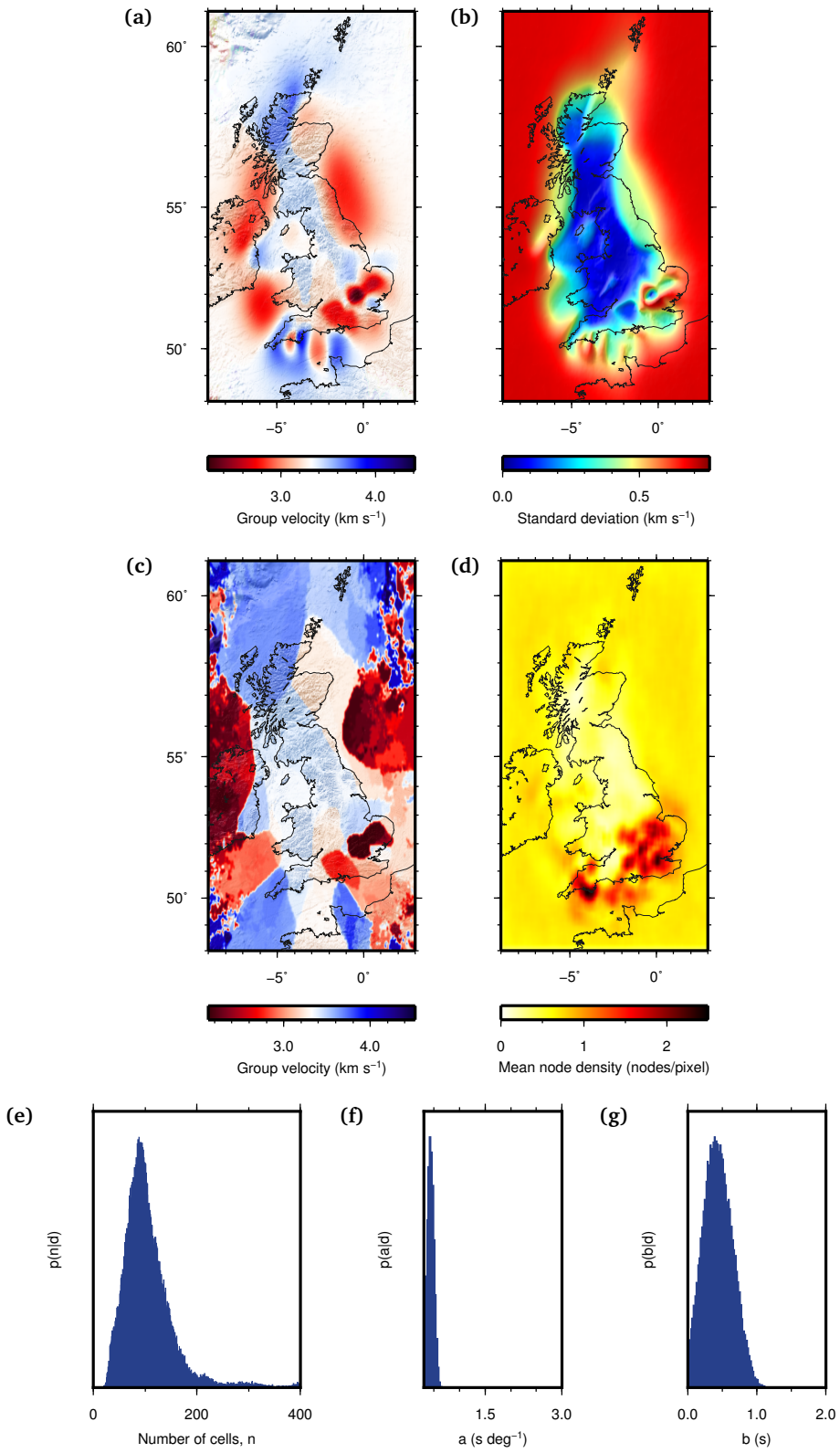

Figure 7.14. Results of non-linear rj-McMC tomography at 15 seconds period. (a) Average Love-wave group-velocity map. (b) Standard deviation map. (c) Map of maximum-probability group-velocity. (d) Map of Voronoi node density across the ensemble (average number of nuclei per $0.5° \times 0.5°$ pixel). (e) Posterior on number of Voronoi cells. (f) Posterior on noise hyperparameter a. (g) Posterior on noise hyperparameter b. At this period 313 traveltime data were included.

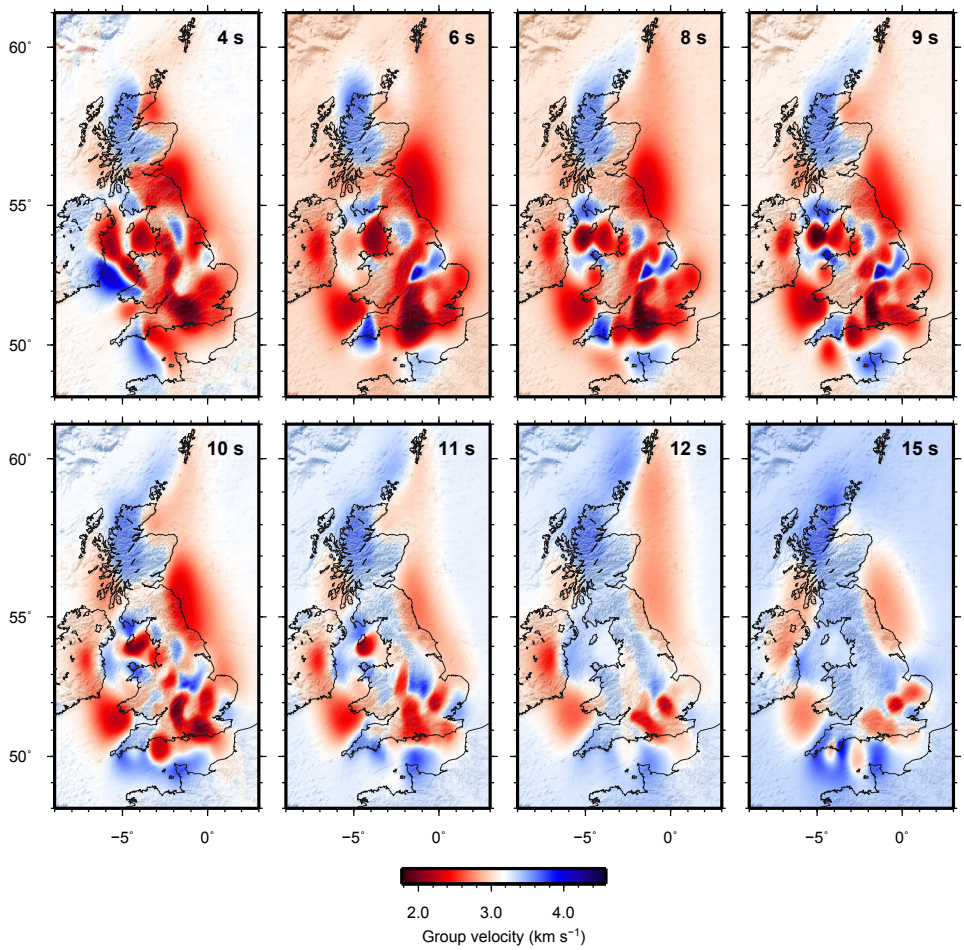

Figure 7.15. Average Love-wave group-velocity maps from non-linear rj-McMC tomography at all of the analysed periods and displayed using the same colour scale.

to the lack of raypaths in marine areas and in most cases are equal to their a priori value. Within the regions interrogated by raypaths, the magnitude of uncertainties presents large variations across the range of analysed periods. Between 4 and 10 seconds, uncertainties are lower in Scotland and south-west England due to the denser ray coverage, while they are higher in the north of England and along the west coast of mainland Britain where raypath density is lower. In addition, loop structures of high uncertainty such as those discussed in Chapter 6 can be observed surrounding the low-velocity anomaly in the Irish Sea (near −4°E, 54°N), various low-velocity anomalies in the south of England (near −3°E, 50.5°N; 0°E, 52°N; −5.5°E, 51.5°N), and a high-velocity anomaly near −1°E, 54°N. At 11 seconds period, uncertainties decrease in magnitude and are relatively uniform across mainland Britain, with the exception of the high-uncertainty loops near −4°E, 54°N; −2°E, 52.5°N; and 0°E, 52°N. At 12 and 15 seconds period, uncertainties are relatively low and uniform across the investigated area, with the exception of the high-uncertainty loop surrounding the low-velocity anomaly near 0°E, 52°N.

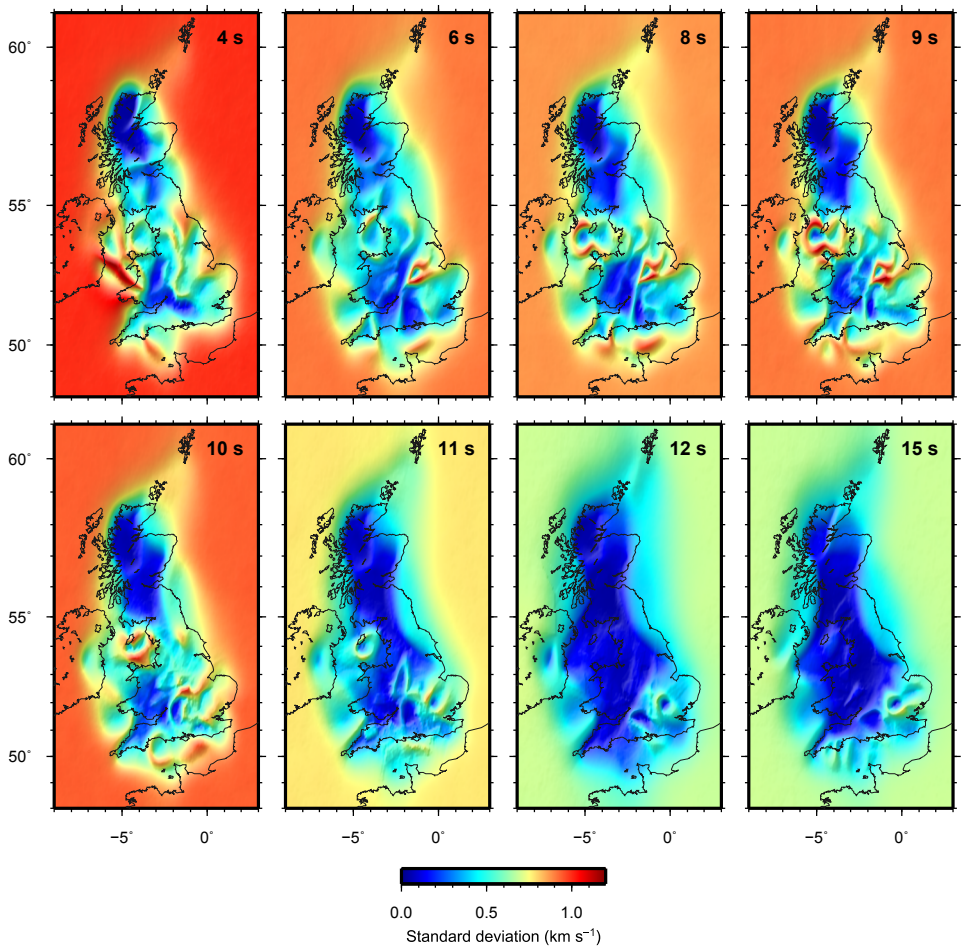

Figure 7.16. Standard deviation maps associated with the results shown in Fig. 7.15, again displayed on the same colour scale.

Figure 7.17 shows posterior probability distributions for velocity at four different points at 10 seconds period. As expected, the histograms show a sharp peak in group-velocity in well-sampled areas of low uncertainty (inverted triangle and square), while no clear peak is visible in areas that are not investigated by the raypaths (diamond). In these cases, since no new information is added by the observations, the velocity posterior corresponds to the uniform prior. In intermediate cases where few raypaths are present (i.e., at the location identified by the circle), a peak in the velocity distribution might be visible within a larger spread of velocities, causing uncertainties to be relatively large.

The maps of maximum-probability group-velocity in panel (c) of Figs 7.7–7.14 were obtained by plotting the group-velocity with largest probability at each geographical point. As expected, off-shore areas with little or no ray coverage present large spatial variability in group-velocity, which is likely to be due to the absence of a clear peak in the velocity distribution (as is the case for the point marked by a diamond in Fig. 7.17). On the other hand, regions which are investigated by raypaths present group-velocity values which are close to the average, as can also be observed in the top-row histograms in Fig. 7.17.

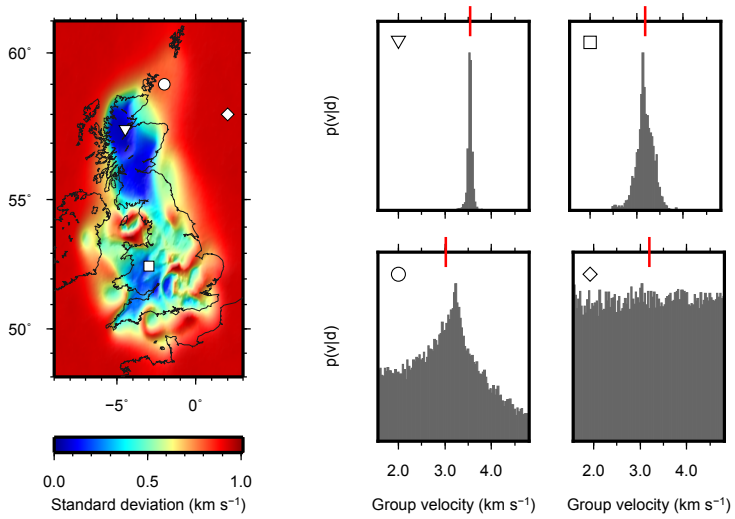

Figure 7.17. Posterior probability densities for velocity at different locations in the British Isles at 10 seconds period. Histograms are calculated at positions marked by different symbols in the standard deviation map on the left: inverted triangle at −4.5°E, 57.5°N; square at −3°E, 52.5°N; circle at −2°E, 59°N; diamond at 2°E, 58°N. The red segments mark the average velocity at each location as can be observed in Fig. 7.11(a).

However, compared to the average group-velocity maps, the boundaries between low- and high-velocity zones in the maximum-probability maps appear sharper. This effect is most likely due to the fact that only the peak velocity at each point is considered in the maximum-probability maps, while the whole range of posterior velocities contributes to the velocity observed at each point in the average maps. In addition, in some cases (e.g., the Irish Sea low-velocity anomaly at 8–11 seconds period) the maximum-probability group-velocity appears to hit the prior velocity boundaries, suggesting that the velocity priors in Table 7.1 might be too narrow in such cases. However, additional inversions which were carried out with a wider prior were slow at converging over the same number of iterations, and the trace of Voronoi cells was still visible in the resulting maps. Hence longer Markov chains should have been run to reach convergence when using wider priors than those in Table 7.1. Given the practical limitations in computing time on the ECDF cluster and that the inversion at each period took about one month of computation time per Markov chain, running even longer Markov chains would have been unfeasible for us. For these reasons, the priors in Table 7.1 were considered appropriate for inversion at each of the analysed periods since their biasing effect on the final results was only limited to certain geographical areas of low velocity.

Since the rj-McMC algorithm uses variable parametrisation, maps of Voronoi node density (panel (d) of Figs 7.7–7.14) can provide information on the spatial distribution of the model parameters (Voronoi cells). We created such maps by discretising the model space in a series of partially-overlapping square sectors (i.e., pixels) of 0.5° × 0.5° area, and calculated the average density of Voronoi nodes in each pixel over the ensemble of

Voronoi models. High node density indicates the presence of small-scale velocity structures that are resolved by the data, while low node density is found in regions which are relatively uniform or where the seismic velocity is poorly resolved. As expected, the density of Voronoi nuclei is relatively uniform in off-shore regions where raypaths are not present, while it appears to be strongly dependent on the underlying velocity structure in the resolved areas. In particular, despite generally having the highest raypath coverage, the Scottish Highlands present a relatively low number of Voronoi cells across the range of analysed periods, which is likely due to their relatively uniform composition at the length scales resolvable by this dataset. In contrast, high node density is generally found in England and in the Irish Sea where low-velocity anomalies are present. This is particularly evident at 12 and 15 seconds period, where the largest node density corresponds to the uncertainty loop structures in the south-west of England.

The posterior distributions on number of Voronoi cells n and on noise hyperparameters a and b are shown in panels (e)–(g) of Figs 7.7–7.14. The number of Voronoi cells reflects the level of detail which can be seen in the average and maximum-probability maps, and does not appear to be strongly related to the number of raypaths used. The posteriors on noise hyperparameters a and b indicate how the noise level is expected to vary depending on the length of the raypaths: for instance, at 10 seconds period, the posterior on a suggests that traveltime uncertainties are expected to increase by ~ 0.85 seconds for each 1° increase in ray length, while according to the posterior on b a noise level of ~ 0.25 seconds is expected when source and receiver are co-located (although this value is merely extrapolated as no station pairs closer than 3 wavelengths are used in this study). In general, with the exception of the 4 seconds period maps, hyperparameter a appears to decrease with increasing period, while hyperparameter b does not seem to have any dependence on period. In particular, apart from 10, 11 and 15 seconds period, the posterior for b always peaks at 0 seconds.

In terms of geology, the average and maximum-probability maps can be used to identify various geological features at relatively shallow depths in the British Isles. In general, rocks of sedimentary origin are shown as low-velocity regions, while igneous and metamorphic complexes are displayed as high velocities. Figure 7.15 shows a general increase in the average group-velocity with increasing period together with a decrease in the number of visible features.

Between 4 and 10 seconds period, the Lewisian and Dalradian complexes in the Scottish Highlands are clearly visible as regions of high seismic velocity, which is consistent with their crystalline metamorphic origin. High velocities in northern Britain also mark the accretionary complex of the Southern Uplands, following a SW-NE trend in the south of Scotland. The same trend is followed by the Midland Valley, which can be identified as the low-velocity zone bounded by the Highland Boundary Fault to the north and the Southern Uplands Fault to the south. Low seismic velocities can also be observed in off-shore sedimentary basins such as the Firth of Forth and the Moray Firth. In

northern England, the limestones of the Pennines can be identified by a high-velocity region following an approximately north-south trend. Similarly, the Lake District corresponds to an area of higher than average velocity, and the granitic intrusions in Cornwall and north-west Wales are also marked by high seismic velocities. The Midland Platform has been found to be an area of high crustal thickness by a number of authors (Chadwick & Pharaoh, 1998; Tomlinson et al., 2006) and can be observed as a region of lower than average velocity in the south of England. Low velocities are also found in a number of sedimentary basins such as the Irish Sea, the London Basin at the south-east corner of the Midland Platform, the Anglian Basin east of the Midland Platform, the Wessex-Weald basin south of the Varisican Front, and the Welsh, Cheshire and Worcester Basins west of the Midland Platform.

The high-velocity feature in the East Midlands was previously observed in Rayleigh-wave tomography studies of the area by Nicolson (2011) and Nicolson et al. (2014), who related it to the northern limit of the Anglo-Brabant Massif. This feature also emerged when experimental inversions at 6 seconds period were performed by removing either station CWF (located in the middle of the anomaly at most periods) or station LMK (located on the north-eastern edge of the anomaly) from the dataset, hence it is robust and cannot be due to the quality of the data recorded at these two stations. Surface geology around station CWF includes ancient volcanic breccias, and evidence from gravity and magnetic data suggests that granitic batholiths and dykes underlie an area to the east of CWF (B. Baptie, personal communication, 16/02/2015), which may explain the origin of this high-velocity feature. Alternatively, the anomaly may be interpreted as evidence of Proterozoic basement in an area of thin sedimentary cover. However, more detailed studies are currently needed in order to understand the exact origin of this feature.

Between 11 and 15 seconds period the various sedimentary basins progressively disappear as the depth to which these periods are sensitive increases. The low-velocity anomaly associated with the Irish Sea basin decreases in size between 4 and 11 seconds period and is no longer visible at 12 seconds period. Similarly, the low velocities found in the Midland Valley become less pronounced as period increases, and the formation becomes essentially undistinguishable from the neighbouring high-velocity complexes at 12 seconds period. Since the thickness of the Midland Valley sediments is suggested to be between 4 and 8 km (Dentith & Hall, 1989, 1990), the 12 and 15 seconds maps are therefore likely to be representative of the basement rocks below this depth rather than the overlying sediments. In contrast, the sedimentary basins in the south of England decrease in size but are still visible between 11 and 15 seconds period.

7.6 One step further: Love-wave group-velocity inversion

Although it is well known that group-velocity maps at increasing periods are representative of increasingly larger depths within the Earth, such maps do not contain any indication on the depth of the observed structures in that they only yield average velocities over a range of depths. Hence, a further step must be taken after the tomographic inversion in order to relate velocity structures to actual depths in the Earth's subsurface. A common way to achieve this involves producing a set of group-velocity dispersion curves by sampling the 2D average group-velocity and standard deviation maps at all of the analysed periods over a regular grid of geographical points. A dispersion curve can then be constructed at each geographical point by taking group-velocity measurements from the 2D average maps and uncertainty values from the 2D standard deviation maps at the available periods. Each dispersion curve may then be inverted independently for a 1D shear-velocity (v_S) profile, and by repeating the inversion for each available dispersion curve (i.e., each available geographical point) a 3D v_S model of the crust may be obtained. Within this section, I provide an insight on preliminary results which I recently obtained from inversion of Love-wave group-velocity dispersion data from the Irish Sea basin. Although this piece of work is not yet mature, it nevertheless provides a natural extension to the tomography results presented in Section 7.4, hence can be regarded as the starting point for more detailed future studies.

We discretised the average group-velocity and standard deviation maps presented in the previous section over a regular grid of geographical points with a spacing of $1/16^{\text{th}}$ of a degree. As a means of quality control, we used the standard deviation maps from tomography to remove dispersion measurements with excessively large uncertainty from the dispersion dataset. At each of the analysed periods, the a priori standard deviation σ_{prior} on velocity can be expressed as

$$\sigma_{prior} = \sqrt{\frac{(v_{max} - v_{min})^2}{12}}\,, \tag{7.2}$$

where v_{min} and v_{max} are the lower and upper bounds on the velocity prior, respectively (see Table 7.1). Since a posterior standard deviation value near σ_{prior} indicates that no additional information was obtained on group velocities from tomography, we constructed dispersion curves using only those points having a posterior standard deviation less than 75% of σ_{prior}. This means that different dispersion curves (at different geographical points at which a dispersion curve was constructed) had different numbers of data points, with a minimum of 2 considered as a candidate for subsequent analysis (Fig. 7.18). As expected, no dispersion curves were constructed in off-shore areas where resolution is low, and dispersion curves with the largest number of data points were constructed on mainland Britain where the density of raypaths is largest. In total,

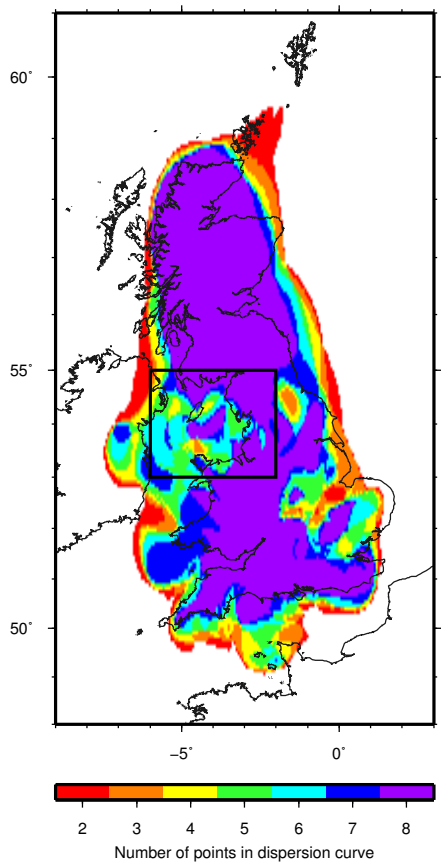

Figure 7.18. Number of dispersion data points at each geographical location in the British Isles. The box denotes the extent of the area around the Irish Sea basin for which Love-wave group-velocity inversion was performed.

14665 dispersion curves were produced over the imaged area, and a subset of 2145 curves was used for the inversion in the Irish Sea basin (denoted by the box in Fig. 7.18).

Similarly to tomography, we used the rj-McMC algorithm to solve the inverse problem. In fact, the concept of transdimensionality is not limited to traveltime tomography but can be adapted to a number of different inverse problems including regression (Gallagher et al., 2011), inversion of controlled source electromagnetic data (Ray et al., 2014), inversion of surface-wave dispersion (Young et al., 2013a), and joint inversion of surface-wave dispersion and receiver function data (Bodin et al., 2012c). In all of these cases, rather than obtaining a single 'best-fit' model which might be heavily influenced by the choice of model parametrisation, the solution is represented by an ensemble of millions of samples, all of which fit the recorded data to within uncertainties, and the parametrisation itself is inferred from the data during the inversion.

The workflow of the rj-McMC algorithm for group-velocity inversion resembles that of tomography described in Section 5.3.1, and is illustrated in Fig. 7.19. The layered model is described by a series of 'Voronoi nuclei' (the black dots in Fig. 7.19) which are assigned a depth and a v_S value. The vertical position of the collection of Voronoi nuclei determines

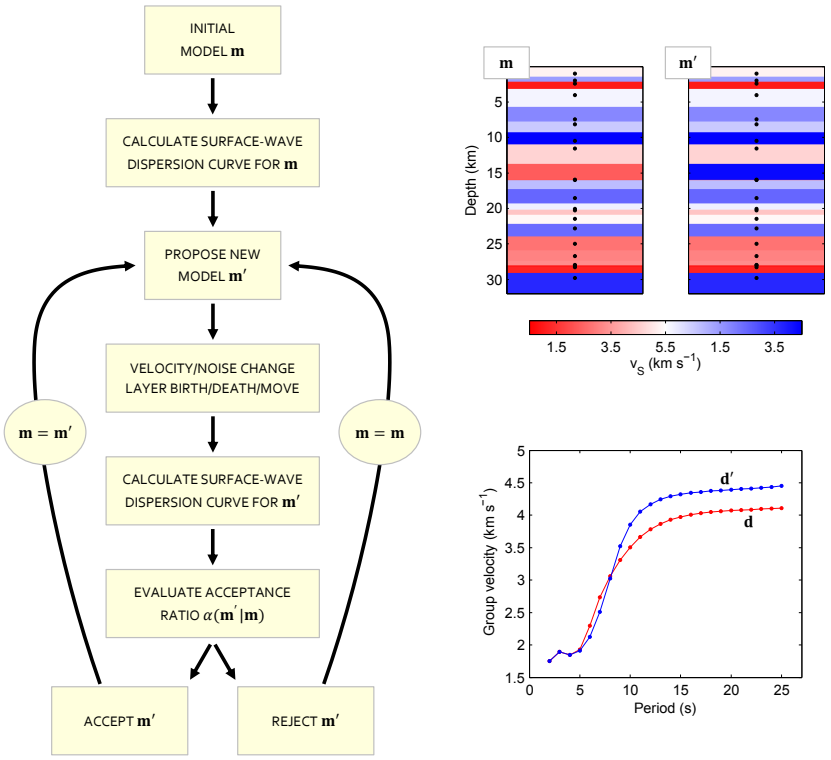

Figure 7.19. Workflow of the transdimensional rj-McMC algorithm in surface-wave dispersion inversion. This samples the model space by producing an ensemble of layered models distributed according to the Bayesian posterior probability distribution. For each proposed model, a group- or phase-velocity dispersion curve is calculated and used in the calculation of the likelihood.

the thickness and depth of the uniform horizontal layers. Note that each Voronoi nucleus is not necessarily located at the centre of its corresponding layer, but rather each layer boundary is equidistant to its two adjacent nuclei. Similarly to its traveltime tomography equivalent, this method uses Bayes' theorem (equation (5.10)) and Markov chain Monte Carlo to produce an ensemble of layered models $\mathbf{m}$ which are distributed according to the posterior distribution. Prior distributions are given on the depth of Voronoi nuclei, number of layers and layer velocity. Data noise may also be parametrised by defining a hyperparameter λ which serves as a scaling factor for the a priori uncertainties (similar to equation (5.8)) and which can be estimated during the inversion. As in the case of traveltime tomography with variable data noise, this ensures that the final solution is not overly affected by the absolute value of the noise level.

The initial model $\mathbf{m}$ is generated randomly, and subsequent models $\mathbf{m}'$ are proposed by randomly perturbing one of the parameters of $\mathbf{m}$ (i.e., adding/deleting/moving a layer, changing a layer's velocity, or changing the data noise hyperparameter λ). The proposed model $\mathbf{m}'$ is either accepted or rejected depending on its likelihood (see equation (5.23)): if it improves the data fit, it is accepted; if it worsens the data fit, it is randomly accepted or rejected. When the proposed model is accepted, it replaces $\mathbf{m}$ as the current model, and the chain continues. At the end of the Markov chain, the first few hundred thousand

samples are discarded as 'burn-in', and only every few hundredth model is retained in the analysed ensemble to ensure that the samples are uncorrelated. The results of the 1D inversion can then be visualised as 2D posteriors of v_S probability versus depth, or as 1D average or maximum-probability profiles of v_S. In addition, a posterior on the location of discontinuities may be obtained.

In group-velocity inversion, the forward problem consists of calculating Rayleigh- or Love-wave group-velocities for a given layered velocity model. We solved the forward problem using the DISPER80 subroutines by Saito (1988), which require values for compressional velocity v_P, shear velocity v_S and density ρ to be defined for each layer in order to compute group velocities. In this study, we only allowed v_S to vary during inversion, keeping the v_P/v_S ratio fixed to a typical crustal value of 1.76, and density was assumed to be dependent on v_P as in Kurita (1973):

$$\rho = 2.35 + 0.036 \times (v_P - 3.0)^2 \,. \tag{7.3}$$

Although the DISPER80 forward modelling subroutines are fast and therefore ideal for use in a Monte Carlo scheme, they may produce incorrect dispersion curves when relatively unusual models are proposed. For instance, we found that the code produced unreliable results when a particularly low-velocity layer was present at very large depths or when the half-space had lower velocity than the layers above, as might happen when models are generated randomly. In these cases, we found that a very small ($\sim 1\%$) change in v_S in one of the layers created much larger ($\gg 1\%$), unrealistic changes in group velocity at all periods (see Section 8.4 for more details). In order to prevent this from happening, after a number of trials we imposed an 80% limit on the velocity drop between any two consecutive layers of increasing depth (i.e., at every step of the Markov chain, the shear-velocity of layer i must be at least 80% of the shear-velocity of layer $i-1$ above it). This type of parametrisation ensured that the models in the Markov chain produced reliable dispersion curves, while still allowing velocity to decrease with depth if needed. However, we are aware that this also implies that the prior on velocity was not uniform at all depths, and that more detailed studies are needed in order to understand the exact origin of this issue.

We performed transdimensional Love-wave group-velocity inversion at all possible geographical points in the Irish Sea basin (black box in Fig. 7.18) by running 16 parallel Markov chains for 2 million iterations, discarding the first 500000 samples on each chain as burn-in, and only retaining every 200$^{\text{th}}$ sample for analysis. In order to prevent the prior from biasing the final results, we used wide priors and set their ranges to 500–8500 km s^{-1} for v_S, 0–60 km for the depth of Voronoi nuclei, 2–30 for the number of layers, and 0.01–10.01 for λ.

Figures 7.20–7.21 show the results of Love-wave group-velocity inversion at -4°E, 54°N. The 2D posterior on v_S in Fig. 7.20(a) shows the presence of a clear peak in

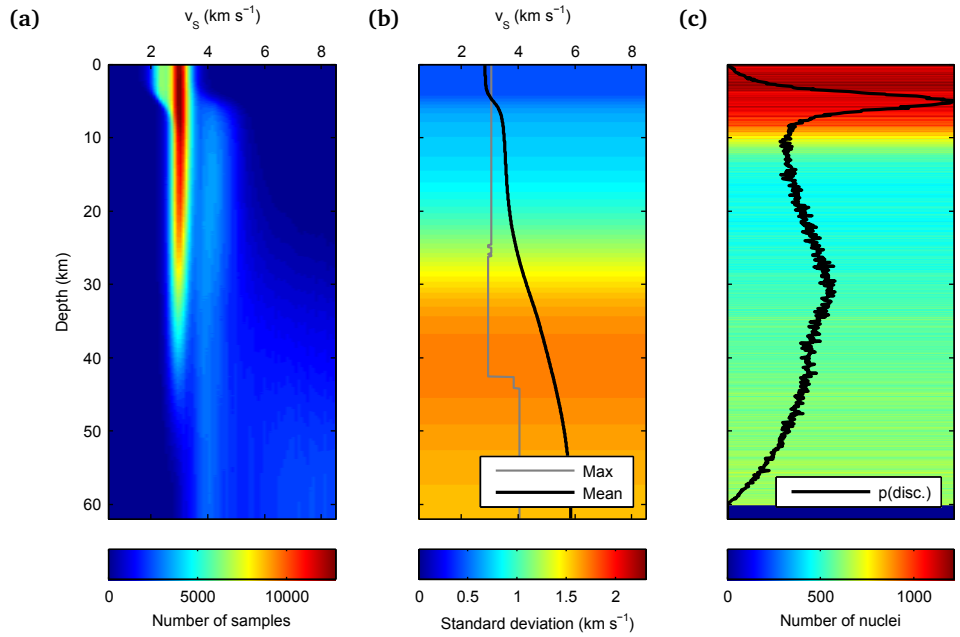

Figure 7.20. Results of Love-wave group-velocity inversion at −4°E, 54°N. (a) Posterior probability distribution on v_S as a function of depth. (b) Average v_S (black solid line), maximum-probability v_S (grey solid line), and standard deviation of v_S (background image). (c) Posterior probability distribution on the depth of discontinuities (black solid line) and location of Voronoi nuclei (background image).

the shear-velocity distribution, corresponding to the profile of maximum-probability v_S in panel (b), down to ∼ 40 km. The average v_S profile in Fig. 7.20(b) displays a relatively sharp increase in velocity at 4–5 km depth, which is also marked by a peak in the posterior on discontinuities in Fig. 7.20(c) and is likely to correspond to the depth of the sedimentary basin at this geographical location. As expected, the standard deviation profile in Fig. 7.20(b) shows an increase in uncertainty with depth, indicating that the limit of significant resolution is located around depths of up to ∼ 25 km. The posterior on the number layers in Fig. 7.21(a) peaks at 2, indicating that simpler models are favoured during inversion. Finally, figure 7.22 shows the inverted data and the best-fitting dispersion curves on each of the 16 Markov chains. As expected, the spread in the modelled curves depends on the size of the uncertainties, being the lowest where uncertainties are smallest (i.e., 12 and 15 seconds period). However, the posterior distribution on noise hyperparameter λ (Fig. 7.21(b)) presents a peak near 2, indicating that the uncertainties obtained from tomography might be too low and should be scaled up by a factor of ∼ 2.

The average v_S and standard deviation maps in Figs 7.23–7.22 were obtained by performing transdimensional Love-wave group-velocity inversion at all of the 2145 geographical points within the black box in Fig. 7.18, merging all 1D profiles into a 3D model, and taking horizontal slices of average shear-velocity and standard deviation at various constant depths. The evolution of the sedimentary basin with depth can clearly be

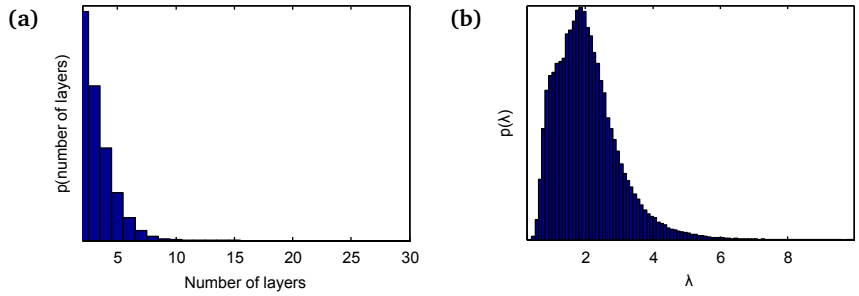

Figure 7.21. Results of Love-wave group-velocity inversion at −4°E, 54°N. (a) Posterior probability distribution on number of layers. (b) Posterior probability distribution on noise hyperparameter λ.

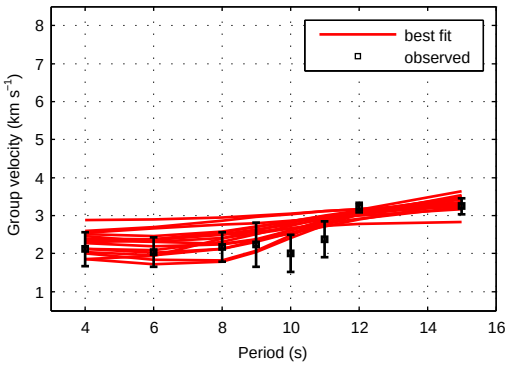

Figure 7.22. Observed and modelled data for Love-wave group-velocity inversion at −4°E, 54°N. The small black squares denote the dispersion data points obtained from the average group-velocity maps in Figs 7.7–7.14, with uncertainties marked by error bars. The red solid lines denote the data obtained from the best-fitting model for each of the 16 Markov chains run for the inversion.

seen in the average v_S maps: the shear-velocity in the basin increases from the surface to 4 km depth, and little trace of the sedimentary basin remains below 5 km. In addition, the area of the basin which is characterised by the lowest velocity down to 4 km (near −3.6°E, 53.8°N) is replaced by high-velocities below 5 km. However, since this is associated with an increase in uncertainty, the increase in shear-velocity with depth may not be as sharp as indicated by the average maps.

Overall, the combination of rj-McMC tomography and Love-wave group-velocity inversion proved to be a practical two-step method to investigate the variation of shear-velocity with depth in the crust. Thanks to the Bayesian nature of both inversion schemes, ensembles of hundreds of thousands of models, rather than single models, were produced at each inversion stage. Love-wave group-velocity maps provided a first insight into the crustal structure of the British Isles, and in the second inversion stage a set of dispersion curves was produced over a regular grid of geographical points and independently inverted for v_S. Most of the resulting shear-velocity models are relatively simple and best described by two to three layers, probably due to the relatively limited spread of periods available. From the ensemble of models at each geographical point, an

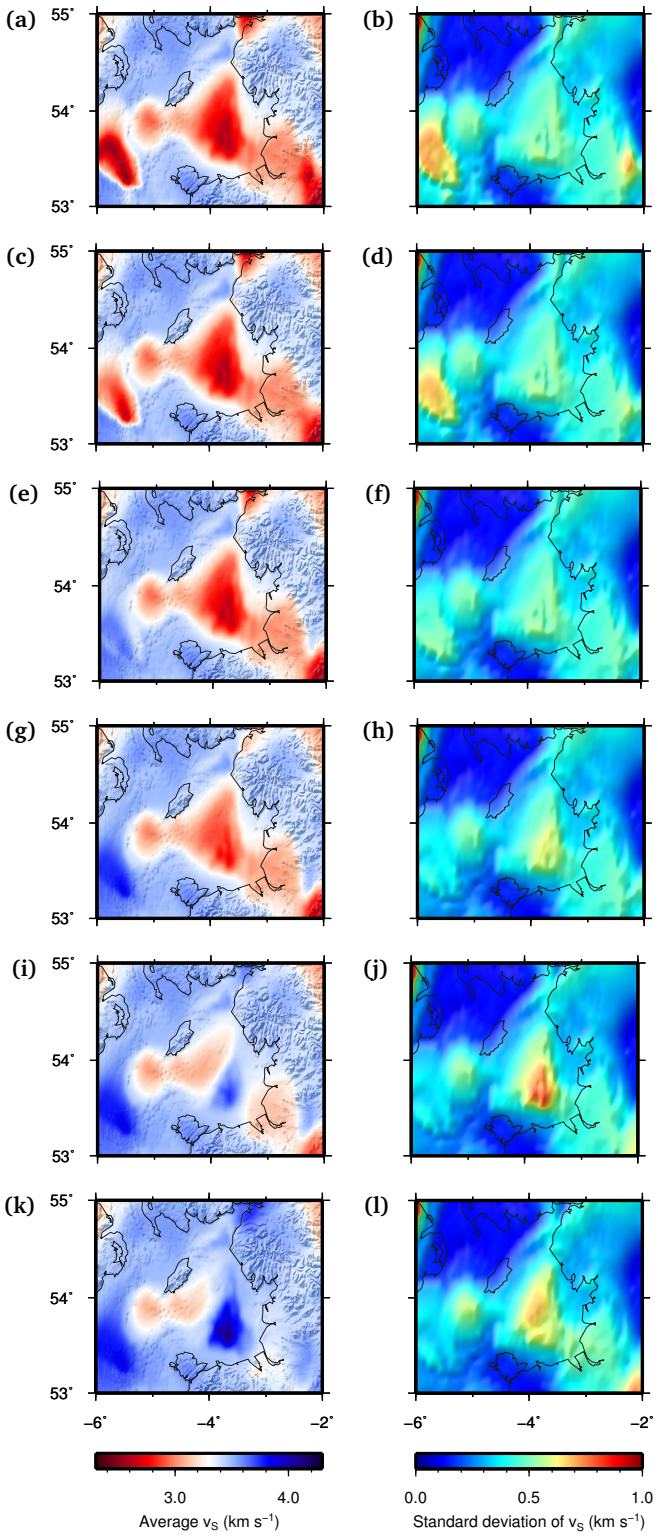

Figure 7.23. Results of Love-wave group-velocity inversion of 2145 dispersion curves in the Irish Sea. Average (left) and standard deviation (right) maps of v_S around a depth of (a)–(b) 1 km, (c)–(d) 2 km, (e)–(f) 3 km, (g)–(h) 4 km, (i)–(j) 5 km, (k)–(l) 6 km.

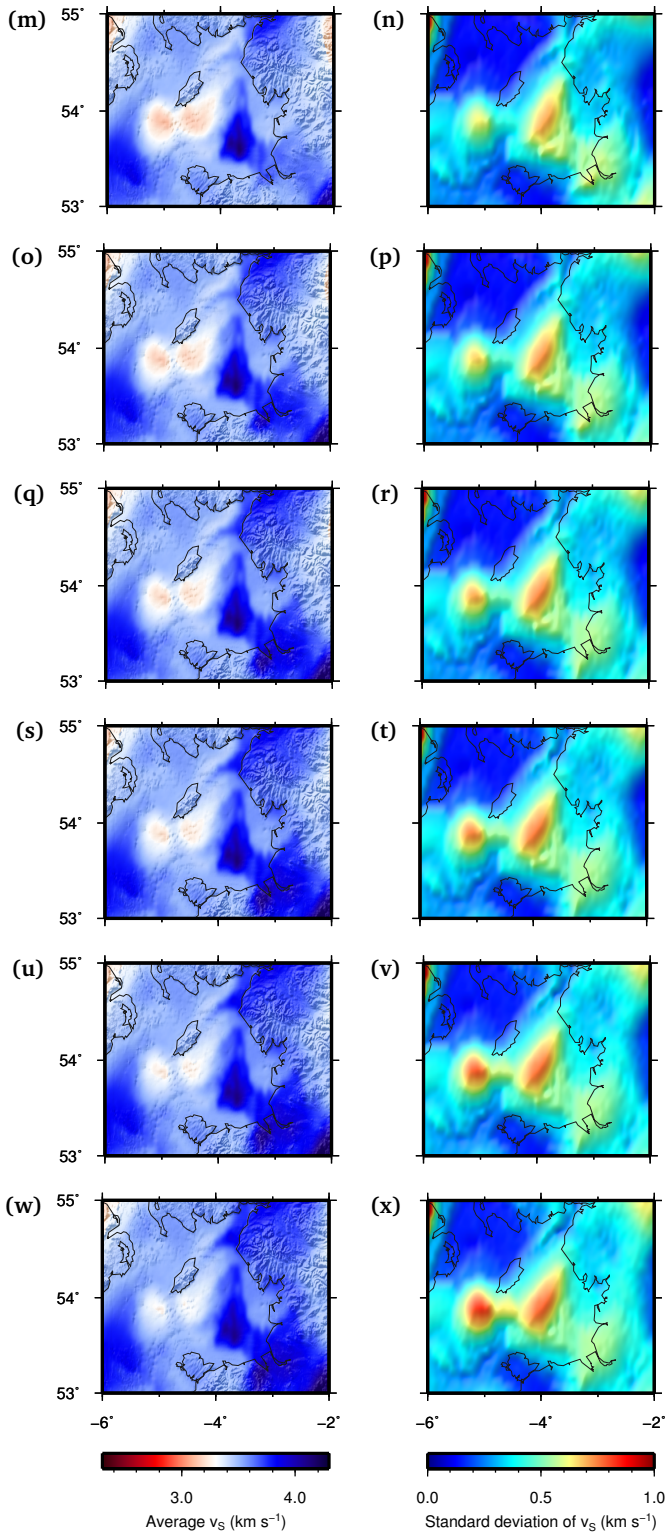

Figure 7.22. Results of Love-wave group-velocity inversion of 2145 dispersion curves in the Irish Sea. Average (left) and standard deviation (right) maps of v_S around a depth of (m)–(n) 7 km, (o)–(p) 8 km, (q)–(r) 9 km, (s)–(t) 10 km, (u)–(v) 11 km, (w)–(x) 12 km.

average v_S and standard deviation profile were calculated and merged to create a full 3D model of the crust. However, due to the relatively large computational cost of the inversion (10–15 minutes per dispersion curve), this second step of the inversion was only performed in a relatively small sector around the Irish Sea sedimentary basin. Future work may therefore include extending the tomographic inversion to further periods and performing Love-wave group-velocity inversion at all possible geographical points to obtain a detailed full 3D model of the crust beneath the British Isles.

CHAPTER 8

Discussion

In Part II of this thesis I showed how seismic interferometry can be used to produce Love-wave Green's functions across the British Isles from seismic ambient noise. I then presented a fully non-linear tomography method which uses the rj-McMC algorithm to invert seismic traveltimes. This method was implemented in a Fortran code by combining the original rj-McMC method by Bodin & Sambridge (2009) with an eikonal raypath modeller (Rawlinson & Sambridge, 2004). The use of variable raypath geometries with Voronoi cell parametrisation allowed new uncertainty topologies to arise, changing the interpretation of tomographic maps. Finally, I presented the results of Love-wave ambient-noise tomography in the British Isles, discussed their significance with respect to the known geology of the area, and provided an overview of preliminary results from group-velocity inversion in the Irish Sea basin.

In this chapter, I discuss the issues, limitations and challenges that have emerged from this study, particularly focusing on the computational cost that a fully non-linear Monte Carlo inversion involves. I then provide guidelines on possible developments and improvements that can be made to the non-linear tomography code. Finally, I provide insight on the issues and challenges that emerged when performing Love-wave group-velocity inversion across the Irish Sea.

8.1 Linearised versus fully non-linear approach

Monte Carlo methods are not habitually used in tomographic imaging due to the large computational cost that they involve. If the model dimension is large (i.e., if the velocity model is defined by a large number of Voronoi cells, the prior on velocity is very wide, etc.)

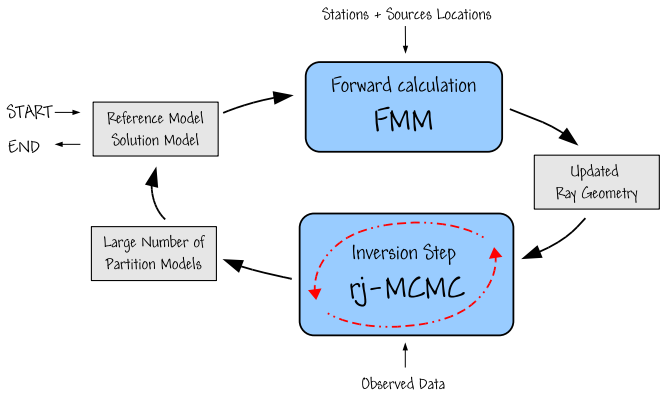

Figure 8.1. Workflow of the original rj-McMC algorithm by Bodin & Sambridge (2009). The algorithm consists of two loops: in the inner loop (red dashed arrows), the transdimensional McMC sampler is used to produce an ensemble of models which satisfies the observed data; in the outer loop (black solid arrows), the Fast Marching Method (FMM) is used to compute raypath geometries using either a uniform background medium (first iteration) or the spatial average of the models generated in the outer loop (subsequent iterations). From Bodin & Sambridge (2009).

then a huge number of samples need to be generated in order to explore the whole model space. As the predicted data has to be computed each time a new model is proposed, the computational cost of MC methods may become prohibitive.

Bodin & Sambridge (2009) overcome this issue partly by using a compact representation or parametrisation of the velocity structure using Voronoi cells, and partly by linearising the inverse problem: to achieve the latter, the raypath geometry is kept fixed across the Markov chain, thereby avoiding the computation of raypaths for each proposed model and saving computation time (see Fig. 8.1 for a description of the algorithm). As shown for a simple synthetic tomography experiment in Fig. 8.2(a)–(c), the inversion routine is started by defining a uniform velocity model for which the raypath geometry is calculated (left plot in panel (a)). These straight raypaths are used to perform the first run of rj-McMC tomography. At the end of that Markov chain, an ensemble average seismic velocity model is calculated and used to update the raypath geometry, which is in turn used to run the rj-McMC inversion a second time (Fig. 8.2(b)). Similarly, raypaths are recomputed for the ensemble average velocity model obtained from the second run, and a third iteration is performed using the new raypath geometry (Fig. 8.2(c)). The procedure can be repeated iteratively as many times as desired.

In addition, as the raypath geometry is independent of the Voronoi-tessellated velocity models proposed at each iteration, Bodin & Sambridge (2009) further speed up the calculations by recomputing only a subset of the traveltime data at each step of the Markov chain. In fact, since the position of the rays is fixed, only the traveltimes that correspond to raypaths passing through the area that is affected by the change need to be updated, while all of the other rays are unaffected. For instance, Fig. 8.3 shows the change in the geometry for a *birth* move in which a Voronoi cell is added to the model

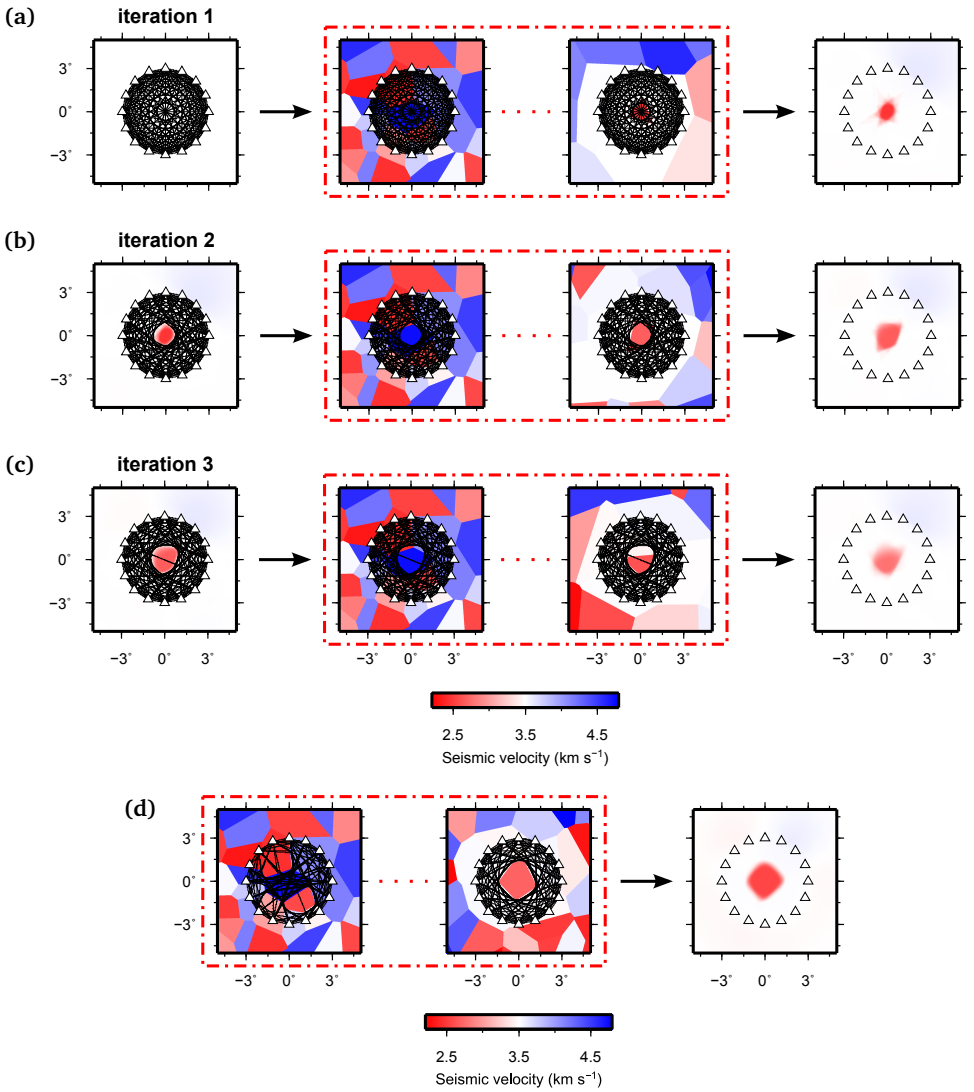

Figure 8.2. The rj-McMC algorithm in its (a)–(c) original and (d) modified version applied to a synthetic tomography experiment with a circular acquisition geometry of receivers (triangles) surrounding a low-velocity anomaly. (a) Straight raypaths (i.e., raypaths obtained using the uniform velocity model on the left) are used to perform the first rj-McMC inversion (middle plots) and obtain an ensemble average velocity model (right plot). (b) The average velocity model obtained from the first inversion is used to update the raypath geometry, and the rj-McMC inversion is repeated. (c) The average velocity model obtained from the second inversion is used to update the raypath geometry, and the rj-McMC inversion is repeated. (d) The modified rj-McMC algorithm, in which raypaths are calculated at each step of the Markov chain, consists of a single loop (red dashed box): each sample along the Markov chain is a Voronoi-tessellated velocity model, and raypaths are computed through each individual model in order to ensure a correct estimation of the likelihood; an average velocity model can be obtained from the ensemble of accepted models (right plot). In all panels, the black arrows correspond to the outer loop in Fig. 8.1, while the red dashed box identifies the inner loop in Fig. 8.1. Note that all of the inversions in this figure were run on a wider area (a sector of $20° \times 20°$ centred on 0°E, 0°N), but only the central magnified area (a sector of $10° \times 10°$) is shown for clarity.

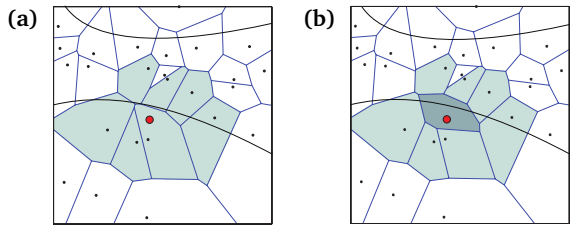

Figure 8.3. Example of *birth* ((a)→(b)) and *death* ((b)→(a)) of a Voronoi cell whose centre is denoted by the red dot. If the raypath geometry is kept fixed (as in Bodin & Sambridge (2009)), only the rays passing through the green cells are affected by the change in geometry. Hence, only the traveltimes corresponding to these rays need updating. From Bodin & Sambridge (2009).

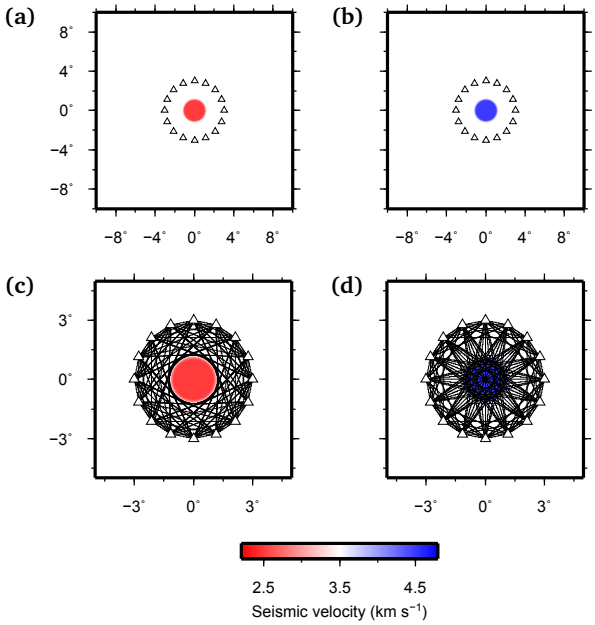

Figure 8.4. Synthetic velocity models showing a circular (a) low- and (b) high-velocity anomaly in the middle of a circular array of receivers (white triangles). The raypath geometries are shown in the magnified panels in (c) and (d).

(darker cell whose centre is denoted by the red dot in panel (b)): as the raypath geometry is kept fixed, only the ray passing through the green Voronoi cells is affected by the change, hence only the traveltime belonging to this ray needs to be updated when computing the acceptance ratio of the new model. On the other hand, the raypath passing near the top of the image is not affected by the change in geometry, hence its traveltime does not change. Together with keeping the raypath geometry fixed, this 'local' traveltime update contributes to a significant saving in computation time.

However, although this linearised approach may greatly reduce the computational cost of the rj-McMC method, it may also introduce artefacts into the solution as the wrong raypath geometry is used at *every* step of the Markov chain. In order to correctly account for non-linearity (i.e. for the effects of the underlying Voronoi-cell velocity structure on

raypaths), rays should instead be computed at each model proposed along the Markov chain (Fig. 8.2(d)), as described in Chapter 5. Although this increases the computation time, it ensures that non-linear effects are properly taken into account in the solution, as shown in the simple synthetic examples presented below.

Figure 8.4 shows a circular (a) low- and (b) high-velocity anomaly of radius 1° (with smooth edges increasing/decreasing to the background velocity up to 1.25° radius) located within a circular array of receivers and a regional velocity of 3.5 km s^{-1}. The low-velocity anomaly in (a) has a velocity of 2.5 km s^{-1}; the high-velocity anomaly in (b) has a velocity of 4.5 km s^{-1}. The true inter-receiver raypath geometries are shown in (c) and (d): as expected, first-arriving energy takes the quicker route *around* the low-velocity anomaly in Fig. 8.4(a), while it travels *through* the anomaly when this has a velocity that is higher than the background (Fig. 8.4(b)).

To emulate a typical ambient-noise tomography scenario where traveltimes are estimated between receiver locations, traveltimes were calculated along 120 inter-receiver rays. We added a small amount of random noise to the synthetic traveltimes by first calculating the length of each active raypath and then computing the noise standard deviation as in equation (5.9), using $a = 0.4$ and $b = 0.2$. The following priors were used for the various model parameters: [3 100] for number of Voronoi cells, [1.2 4.8] km s^{-1} for cell velocity, [0.1 1.0] for a, [0.0 0.8] for b. Transdimensional tomography using the rj-McMC algorithm was performed by running 16 parallel Markov chains for 3×10^6 iterations, and an ensemble of models was created by discarding the first 10^6 samples as burn-in and thinning the Markov chains to every 250^{th} model.

The results obtained using the linearised method of Bodin & Sambridge (2009) are shown in Figs 8.5–8.6 for the low-velocity case and in Figs 8.7–8.8 for the high-velocity case. In both cases, six iterations of the Markov chain were performed in order to obtain an ensemble-average velocity model and update the raypath geometry (outer loop in Fig. 8.1). Although the quality of the results generally improves as the number of iterations increases and the rays are updated, some of the features that are visible in both the average and the standard deviation map appear to be directly related to the raypath geometry. In particular, although the overall amplitude of the anomaly is well constrained in both cases, the size of the anomaly seems to be underestimated in the low-velocity case and overestimated in the high-velocity case. This effect is particularly visible at the first iteration, where straight raypaths (i.e., raypaths calculated assuming a uniform velocity model) were used. As shown in Fig. 8.9, samples taken from the ensemble of accepted models from the first iteration present a relatively small Voronoi cell in the middle of the circular receiver array in the case of a low-velocity anomaly (top row of Fig. 8.9), while the size of this central Voronoi cell is much larger in the case of a high-velocity anomaly (bottom row of Fig. 8.9).

The reason behind this effect can easily be understood by analysing the simple cartoon examples in Fig. 8.10. Consider the low-velocity case in Fig. 8.10(a), and suppose traveltime t_L was measured along the *true* raypath of first-arriving energy (green solid

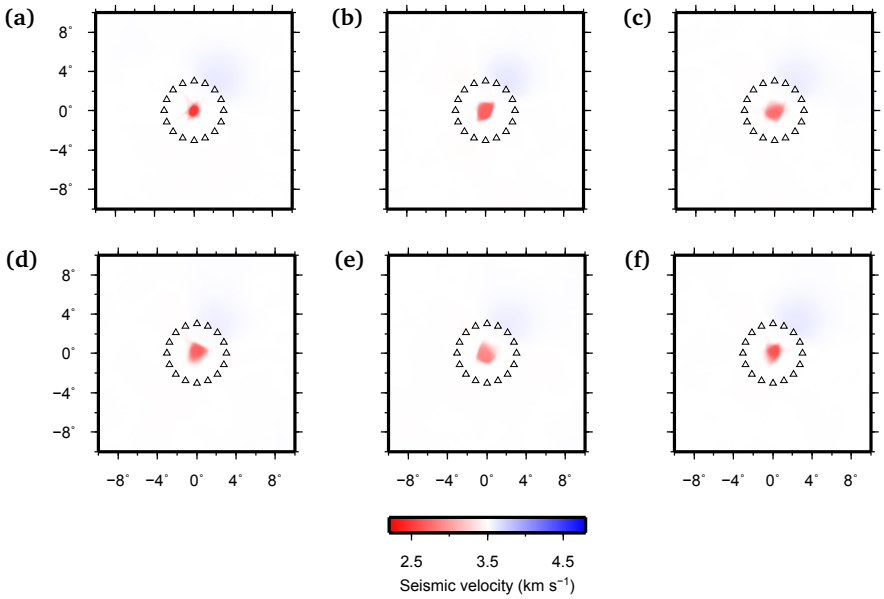

Figure 8.5. Results of rj-McMC tomography for the synthetic example in Fig. 8.4(a) using the original algorithm by Bodin & Sambridge (2009) (Figs 8.1–8.2). Average maps obtained after (a) 1, (b) 2, (c) 3, (d) 4, (e) 5, (f) 6 iterative inversions.

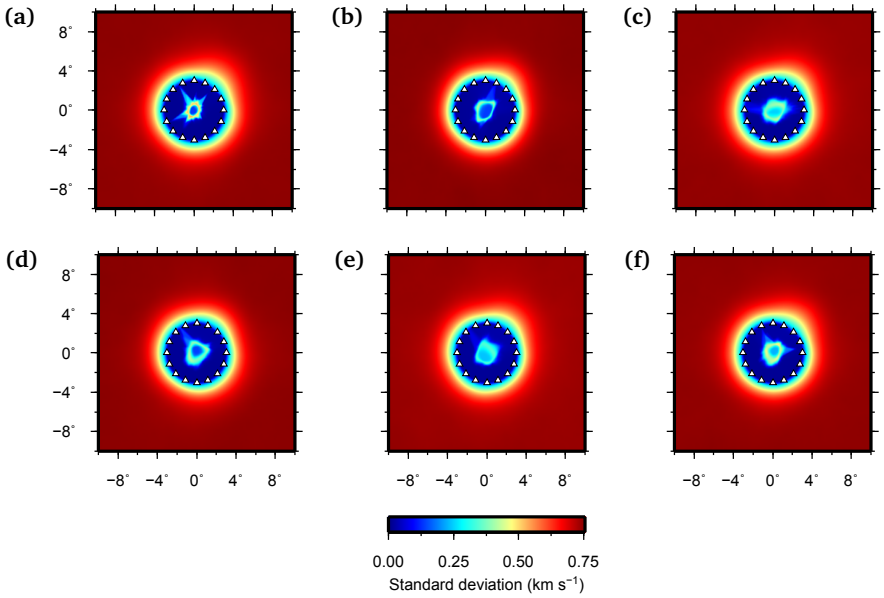

Figure 8.6. Results of rj-McMC tomography for the synthetic example in Fig. 8.4(a) using the original algorithm by Bodin & Sambridge (2009) (Figs 8.1–8.2). Standard deviation maps obtained after (a) 1, (b) 2, (c) 3, (d) 4, (e) 5, (f) 6 iterative inversions.

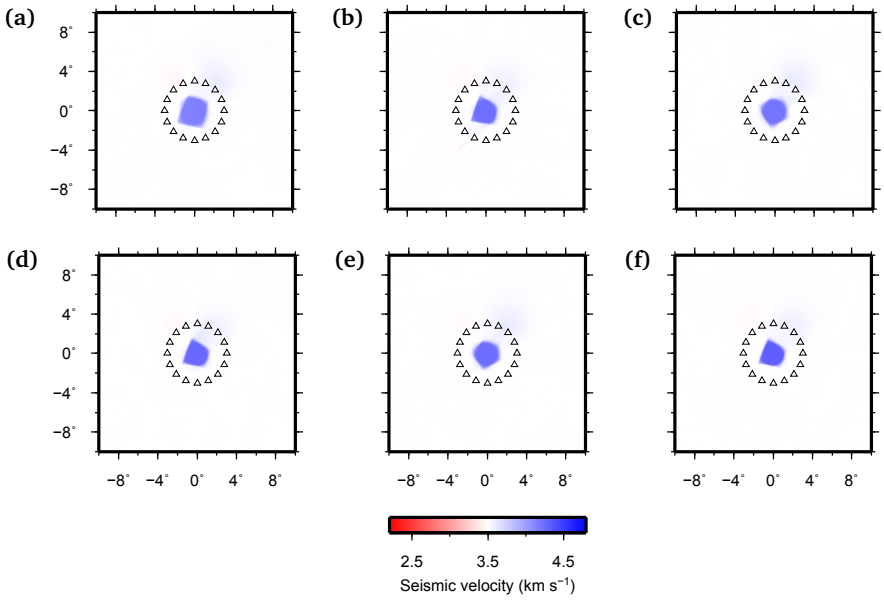

Figure 8.7. Results of rj-McMC tomography for the synthetic example in Fig. 8.4(b) using the original algorithm by Bodin & Sambridge (2009) (Figs 8.1–8.2). Average maps obtained after (a) 1, (b) 2, (c) 3, (d) 4, (e) 5, (f) 6 iterative inversions.

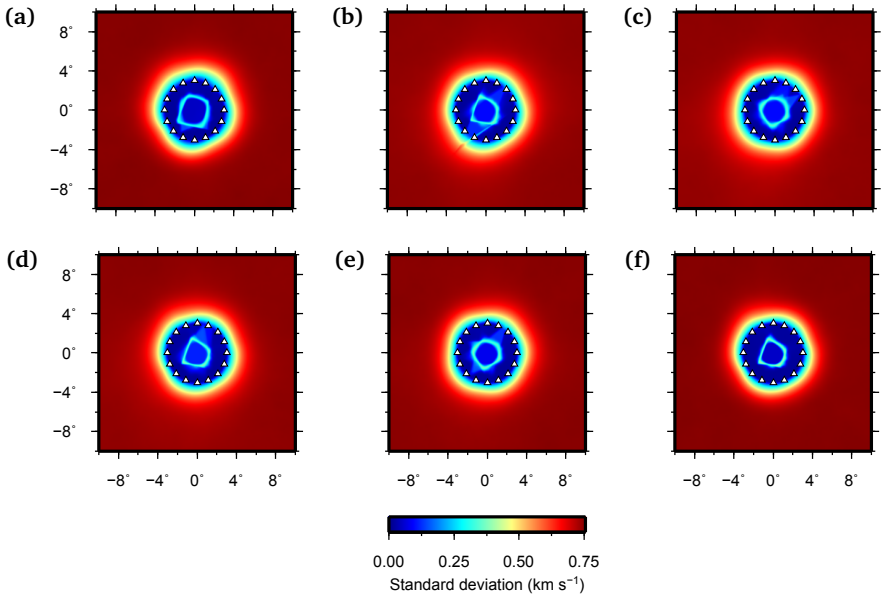

Figure 8.8. Results of rj-McMC tomography for the synthetic example in Fig. 8.4(b) using the original algorithm by Bodin & Sambridge (2009) (Figs 8.1–8.2). Standard deviation maps obtained after (a) 1, (b) 2, (c) 3, (d) 4, (e) 5, (f) 6 iterative inversions.

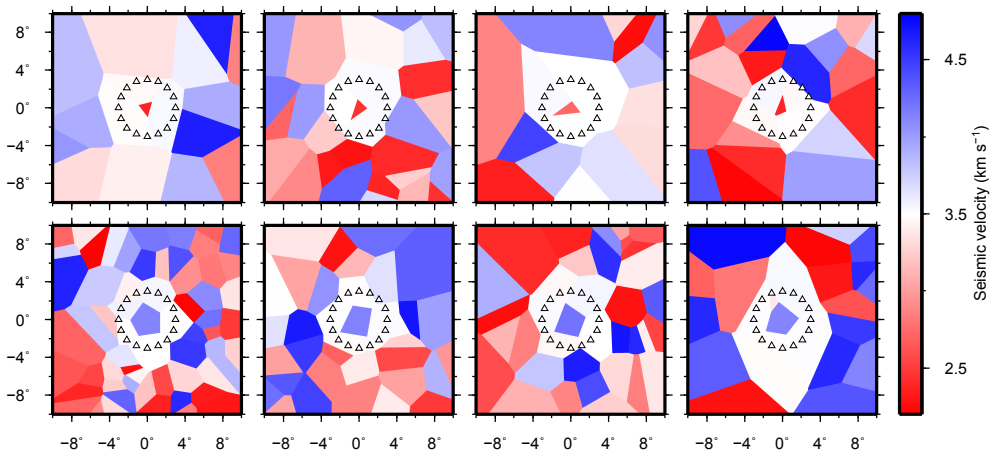

Figure 8.9. Samples from the ensemble of models obtained from the first iterative inversion of rj-McMC tomography for the synthetic examples in Fig. 8.5 (top row) and in Fig. 8.7 (bottom row). All models contain a Voronoi cell near the centre of the anomalies shown in the true models in Fig. 8.4. The size of this Vornoi cell is smaller than the true anomaly if it is low-velocity (top row), while it is larger than the true anomaly if it is high-velocity (bottom row).

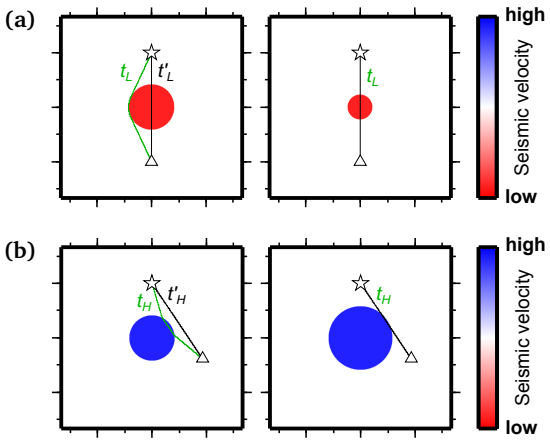

Figure 8.10. Cartoon example showing the effect of a fixed straight-raypath geometry on the size of a (a) low- and a (b) high-velocity anomaly.

line in left plot) which circles around the edge of the *true* anomaly. If an incorrect raypath is used (e.g., the straight raypath marked by the black solid line), the source-to-receiver traveltime is measured as $t'_L > t_L$. Hence, in order to fit the observed traveltime t_L for the same anomaly velocity, an anomaly of smaller size is needed (right panel). The opposite effect can be observed in the case of a high-velocity anomaly. Consider the high-velocity anomaly in the left plot of Fig. 8.10(b), and suppose traveltime t_H was observed along the *true* raypath of first-arriving energy (green solid line in left plot). Similarly to the previous example, if an incorrect raypath is used (e.g., the straight raypath marked by the black solid line), the source-to-receiver traveltime is measured as $t'_H > t_H$. In order to fit traveltime t_H for the same anomaly velocity, an anomaly of larger size is needed (right

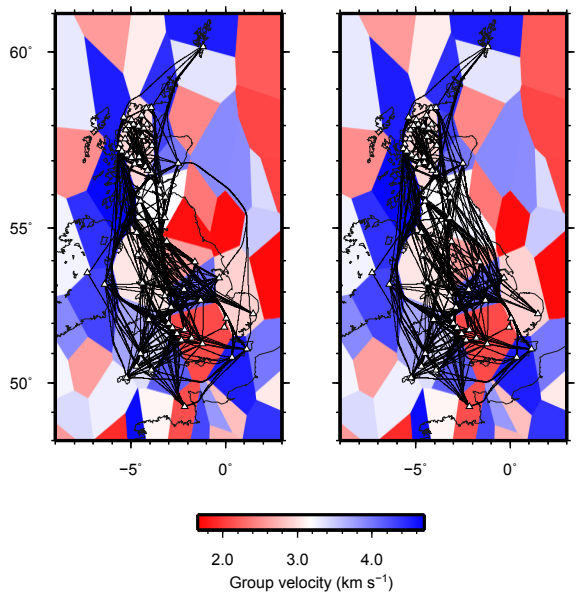

Figure 8.11. Example of Voronoi parametrisation of the British Isles and of a *velocity* step in the Markov chain. The velocity of the Voronoi cell centred near −2°E, 55°N is changed from the left to the right plot. Note how this perturbation influences raypaths which are relatively far from the affected cell.

panel). Although the examples in Fig. 8.10 only illustrate the case of a fixed raypath geometry with straight rays, similar effects are likely to occur when the wrong raypath geometry is used in the evaluation of source-to-receiver traveltimes, as these raypaths are unlikely to correspond to the true path taken by first-arriving energy. Hence, it is straightforward to note how allowing raypaths to move is of great importance when traveltime inversion is performed.

In addition, perturbations that affect a small part of the velocity model might have a strong influence on raypaths which are relatively far from the perturbed region. This can be observed in Fig. 8.11: here, the British Isles are parametrised using Voronoi cells (as in the inversions discussed in Chapter 6 and 7), the velocity of the Voronoi cell centred near −2°E, 55°N is changed from the left to the right plot, and raypaths are traced through both velocity models using the Fast Marching Method. While some of the raypaths head off-shore through the North Sea in the left plot, most rays trace through mainland Britain in the model on the right. Hence, different areas of the model space are interrogated in the two cases, highlighting the importance of a variable raypath geometry during the inversion.

The results obtained using our fully non-linear approach are shown in Fig. 8.12 for the low-velocity case and in Fig. 8.13 for the high-velocity case. In both cases, the approximate size and amplitude of the anomaly are correctly reconstructed, and the standard deviation map also shows loops of high uncertainty around the edges of the anomalies similar to those observed in UK tomography (Chapter 6). In constrast, such loops are only weakly

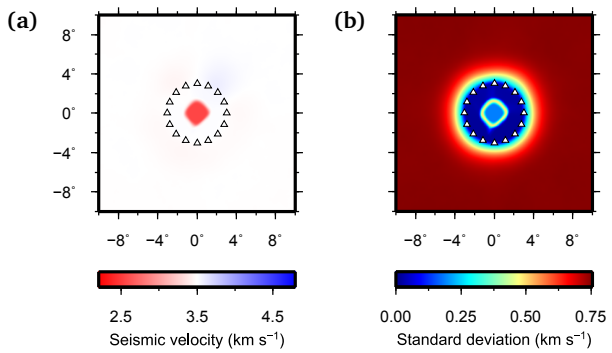

Figure 8.12. Results of rj-McMC tomography for the synthetic example in Fig. 8.4(a) using the modified rj-McMC algorithm which calculates the raypath geometry at each step of the Markov chain. (a) Average map. (b) Standard deviation map.

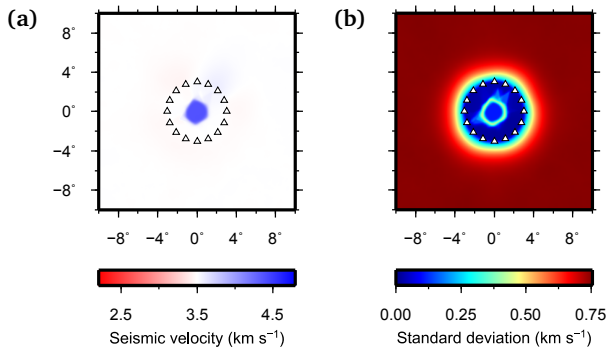

Figure 8.13. Results of rj-McMC tomography for the synthetic example in Fig. 8.4(b) using the modified rj-McMC algorithm which calculates the raypath geometry at each step of the Markov chain. (a) Average map. (b) Standard deviation map.

visible in the standard deviation maps obtained using the original linearised method by Bodin & Sambridge (2009).

8.2 Emergence of uncertainty loops

In Chapter 6 I discussed the emergence of high-uncertainty loops around the edges of low- and high-velocity anomalies. Loops indicate that, while the velocity of each anomaly may be fairly well reconstructed, its exact size and location tend to remain uncertain. Hence, these topologies effectively parametrise the uncertainty in the location of velocity anomalies, providing a fully non-linearised, Bayesian measure of spatial resolution. This is particularly important within the context of non-linear inverse problems, which normally require a more sophisticated approach than that offered by linearised methods (e.g., see below) in order to assess model resolution (e.g., Stark (2008)). However, when computational resources are available, model resolution may also be estimated by

sampling the posterior probability distribution (Maurer et al., 2010), which is essentially what the non-linearised rj-McMC algorithm achieves.

In Chapter 6 (and in the paper which resulted from it) it is stated that variability in both model parametrisation and raypaths plays a role in the emergence of these structures, and that loops may emerge when rays are kept fixed only in fortuitous cases. Within this section, I present the results of the synthetic tests which we performed in order to investigate how raypaths and parametrisation act in combination to create these novel uncertainty topologies. I first present results obtained using a standard linearised (1^{st} order) inversion method (Fast Marching Surface Tomography by Rawlinson & Sambridge (2005)), and then present those obtained from (rj-)McMC tomography using fixed and variable raypaths, and fixed and variable (Voronoi) parametrisation, in all possible combinations. The true velocity field and synthetic traveltimes are the same as those in the low-velocity anomaly example from the previous section (i.e., Fig. 8.4(a) and (c)).

8.2.1 Linearised FMST inversion

The Fast Marching Surface Tomography (FMST) method is an iterative linearised subspace inversion scheme which uses a fixed inversion grid and fixed raypaths over several iterations to solve the inverse problem. Hence, although each iteration assumes local linearity, this method partly accounts for the non-linear nature of the tomographic problem by updating the raypath geometry for each individual model considered (Fig. 8.14), similarly to the linearised version of the rj-McMC algorithm by Bodin & Sambridge (2009) described in Section 8.1.

At each iteration, the method seeks to minimise an objective function consisting of a weighted sum of data misfits and regularisation terms:

$$\begin{aligned} S(\mathbf{m}) =& (\mathbf{g}(\mathbf{m}) - \mathbf{d}^{obs})^{\mathrm{T}} \mathbf{C}_d^{-1} (\mathbf{g}(\mathbf{m}) - \mathbf{d}^{obs}) \\ &+ \epsilon (\mathbf{m} - \mathbf{m}_0)^{\mathrm{T}} \mathbf{C}_m^{-1} (\mathbf{m} - \mathbf{m}_0) + \eta \mathbf{m}^{\mathrm{T}} \mathbf{D}^{\mathrm{T}} \mathbf{D} \mathbf{m} \,, \end{aligned} \tag{8.1}$$

where $\mathbf{g}(\mathbf{m})$ and $\mathbf{d}^{obs}$ are the predicted and observed traveltimes, $\mathbf{m}$ is the vector of model parameters, $\mathbf{m}_0$ is the reference model, $\mathbf{C}_d$ and $\mathbf{C}_m$ are the a priori data and model covariance matrices respectively, $\mathbf{D}$ is a smoothing operator, and ϵ and η are the damping and smoothing factors, respectively.

Assuming the smoothing factor η is equal to zero, the standard deviation on each of the parameters of $\mathbf{m}$ can be calculated by taking the square root of the diagonal elements of the model covariance matrix, which is given by:

$$\tilde{\mathbf{C}}_m = \epsilon (\mathbf{G}^{\mathrm{T}} \mathbf{C}_d^{-1} \mathbf{G} + \epsilon \mathbf{C}_m^{-1})^{-1} \,, \tag{8.2}$$

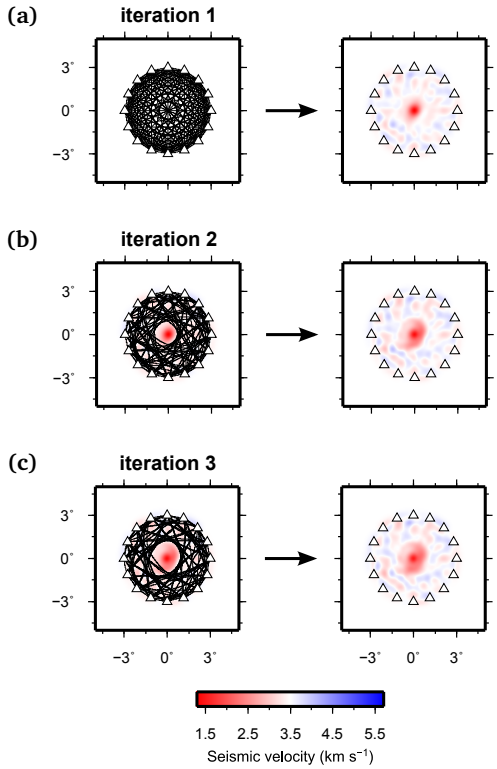

Figure 8.14. Schematic workflow of the FMST algorithm. (a) Straight raypaths (i.e., raypaths obtained using the uniform velocity model on the left) are used to perform the first FMST inversion and obtain a best-fit velocity model (right plot). (b) The velocity model obtained from the first iteration is used to update the raypath geometry, and the FMST inversion is repeated. (c) The velocity model obtained from the second iteration is used to update the raypath geometry, and the FMST inversion is repeated.

where $\mathbf{G} = \delta\mathbf{g}/\delta\mathbf{m}$ describes the rate of change of traveltimes with respect to model parameters and is normally referred to as the Fréchet matrix. In general, computing the model covariance matrix $\tilde{\mathbf{C}}_m$ is an expensive operation since it involves the inversion of a $n_m \times n_m$ matrix, where n_m is the number of model parameters.

Figure 8.15 shows the seismic velocity and standard deviation maps obtained by applying FMST inversion to the synthetic traveltimes described above using different raypath geometries. In panels (a)–(c), one iteration is performed using straight raypaths calculated assuming a uniform reference model. In panels (d)–(f), one iteration is performed using the true raypaths. Finally, in panels (g)–(i), ten iterations are performed as illustrated in Fig. 8.14. When straight rays are used, the standard deviation map shows a loop-like structure centred in the middle of the array, but its shape is completely dictated by the ray geometry rather than the true velocity field. In addition, since these uncertainty estimates do not depend on the traveltime values (only on their derivatives in the reference model - see equation (8.2)), the shape of the uncertainty structure does not change at all if the anomaly is moved or changes in amplitude. On the other hand, no loop-like uncertainty structures are visible when either the true raypaths are used in one

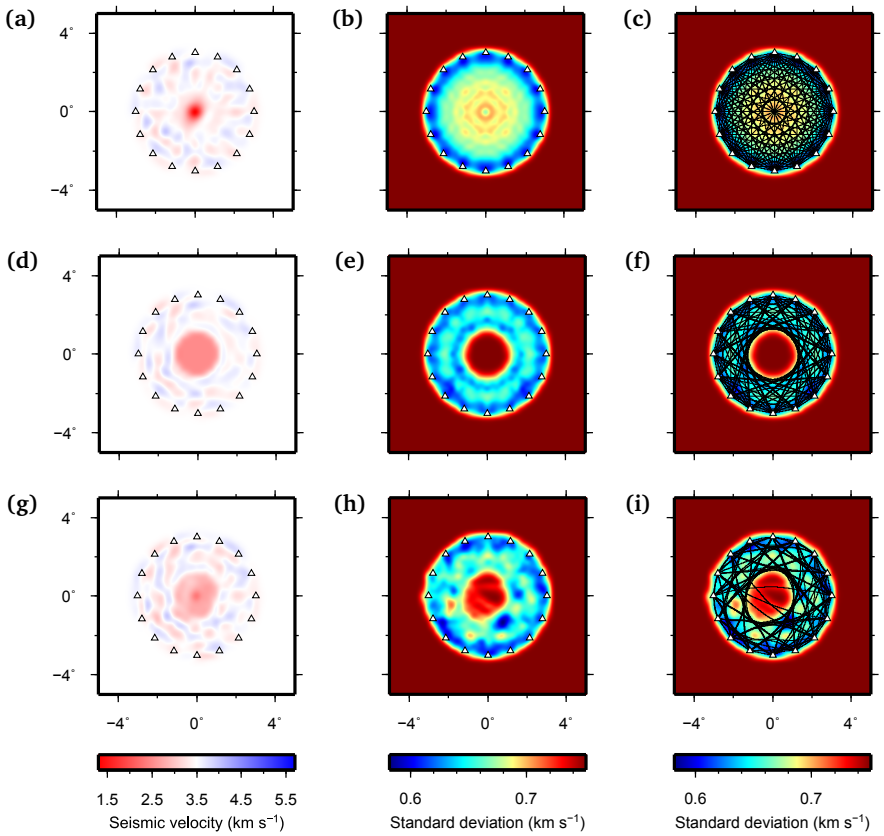

Figure 8.15. Average maps (left), standard deviation maps (centre) and standard deviation maps with overlaid ray geometry (right) obtained from FMST tomography performed with different raypaths and number of iterations. (a)–(c) One iteration using straight raypaths calculated assuming a uniform reference model. (d)–(f) One iteration using the true raypaths as in Fig. 8.4(c). (g)–(i) Ten iterations performed by updating raypaths at each iteration (as in Fig. 8.14), starting from the straight-ray case in panels (a)–(c). Only the raypaths used at the last iteration are shown in (i).

iteration or when raypaths are iteratively updated a number of times. The standard deviation map in Figs 8.15(h)–(i) particularly highlights the influence of the fixed ray geometry on the uncertainty structure, since standard deviation values are lower in areas of higher raypath density.

8.2.2 Monte Carlo inversion

In addition to the FMST experiments described in the previous section, we attempted to quantify the influence of raypaths and model parametrisation on the emergence of uncertainty loops in a (rj-)McMC inversion framework. We inverted the same synthetic traveltime dataset as above in a Monte Carlo setting using both fixed and variable parametrisation, and fixed and variable raypaths, in all possible combinations. The different experiments were conducted as follows:

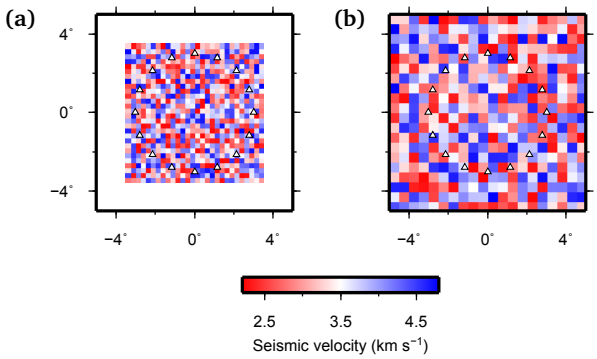

Figure 8.16. Example of model parametrisation using regular squares as Voronoi cells. (a) The Voronoi squares have area 0.25° × 0.25°. (b) The Voronoi squares have area 0.5° × 0.5°. Note that inversions using models such as the one in panel (a) were performed on a smaller area of 7° × 7° centred on 0°E, 0°N in order to reduce the computational cost.

- linear McMC tomography performed using fixed parametrisation and fixed raypaths. The model parametrisation was fixed by using small squares of 0.25° × 0.25° as Voronoi cells (Fig. 8.16(a)) and only allowing their velocity to change within the Markov chain (i.e., no *birth*/*death*/*move* changes were allowed, but only *velocity* and *noise* moves). The raypath geometry was fixed to either straight or true rays.

- linearised rj-McMC tomography performed with a geometry of either straight or true rays and variable Voronoi parametrisation as in Bodin & Sambridge (2009). The results of this experiment in the case of straight rays correspond to those shown in Figs 8.5(a) and 8.6(a).

- non-linear McMC tomography performed using fixed parametrisation and variable raypaths. The model parametrisation was fixed by using small squares of 0.5° × 0.5° as Voronoi cells (Fig. 8.16(b)) and only allowing their velocity to change as in the above case. Raypaths were re-computed at each step of the Markov chain.

- fully non-linear rj-McMC tomography performed by using variable Voronoi parametrisation and re-computing the raypaths at each step of the Markov chain. The results of this experiment correspond to those shown in Fig. 8.12.

The average maps, standard deviation maps and raypath geometries used for the inversions with fixed raypaths are shown in Fig. 8.17 for fixed model parametrisation, and in Fig. 8.18 for variable model parametrisation with Voronoi cells. In both cases, when the *incorrect* geometry of straight rays is used (Figs 8.17(a)–(c) and 8.18(a)–(c)), the average map shows the presence of a low-velocity anomaly at the centre of the circular receiver array, whose size is however underestimated probably as a result of the use of incorrect rays (as explained in the example in Fig. 8.10(a)). The standard deviation maps associated with these average models reveal loop-like structures of high uncertainty around the edges of the anomaly. However, when the true ray geometry is used during

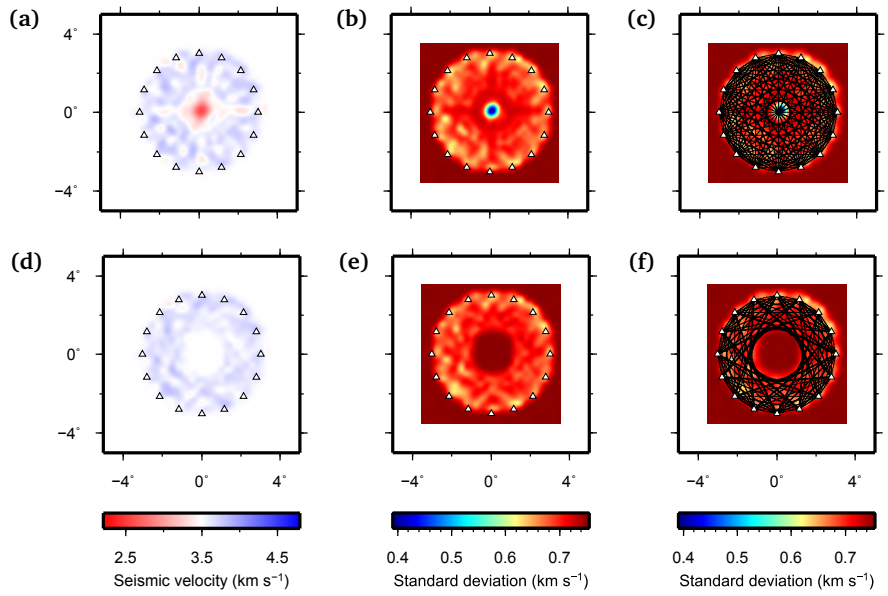

Figure 8.17. Average maps (left), standard deviation maps (centre) and standard deviation maps with overlaid ray geometry (right) obtained from linear McMC tomography using fixed raypaths and fixed parametrisation. (a)–(c) Inversion uses straight raypaths calculated assuming a uniform reference model. (d)–(f) Inversion uses the true raypaths as in Fig. 8.4(c). Note that, since fixed raypaths were used, both inversions were performed on a smaller area of 7°×7° centred on 0°E, 0°N in order to reduce the computational cost.

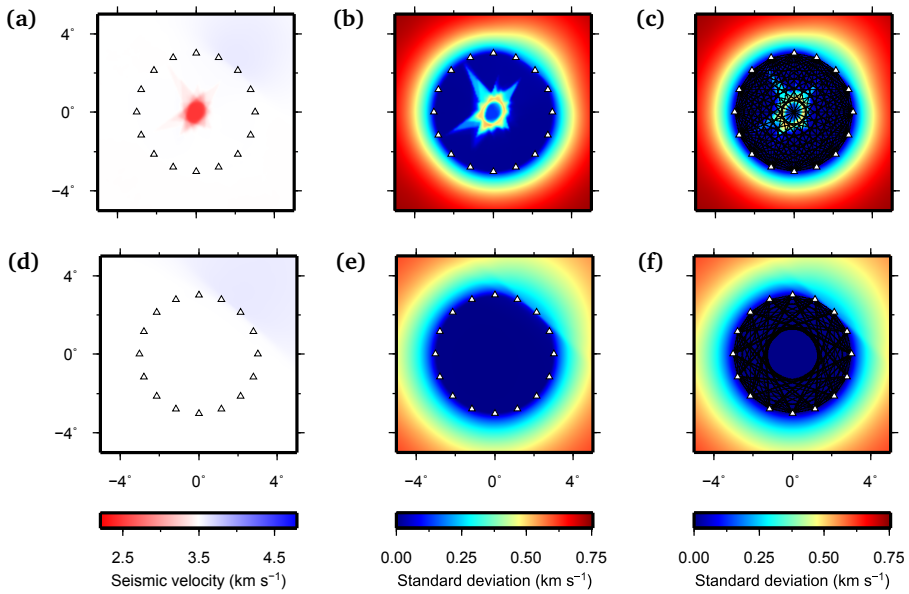

Figure 8.18. Average maps (left), standard deviation maps (centre) and standard deviation maps with overlaid ray geometry (right) obtained from linearised rj-McMC tomography using fixed raypaths and variable (Voronoi) parametrisation. (a)–(c) Inversion uses straight raypaths calculated assuming a uniform reference model. (d)–(f) Inversion uses the true raypaths as in Fig. 8.4(c). Note that both inversions were performed on a wider area of 20° × 20° centred on 0°E, 0°N to prevent edge effects from the Voronoi parametrisation.

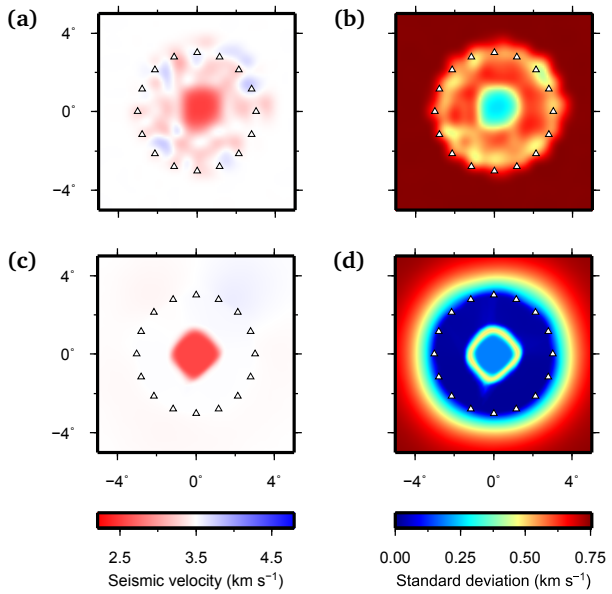

Figure 8.19. Average maps (left) and standard deviation maps (right) obtained from non-linear (rj-)McMC tomography using variable raypaths and either fixed or variable (Voronoi) parametrisation. (a)–(b) Inversion uses Voronoi squares to parametrise the model. (c)–(d) Inversion uses variable Voronoi cells to parametrise the model. Note that the inversion in panels (c)–(d) was performed on a wider area of 20° × 20° centred on 0°E, 0°N to prevent edge effects from the Voronoi parametrisation.

the inversion (Figs 8.17(d)–(f) and 8.18(d)–(f)), no low-velocity anomaly is constructed (since none of the rays traverses the anomaly) and no uncertainty loop is observed. Hence, the emergence of uncertainty loops is extremely fortuitous when raypaths are not allowed to vary freely during the inversion, and may only occur when an *incorrect* ray geometry is used regardless of the type of parametrisation employed. A similar effect can be observed in Figs 8.5–8.6, showing the results of inversion for the same synthetic dataset using variable Voronoi parametrisation and fixed raypaths over successive iterations.

On the other hand, uncertainty loops are present in the standard deviation maps when rays are allowed to move during the inversion, regardless of the type of model parametrisation used. This can be observed in Fig. 8.19, showing the results of non-linear (rj-)McMC tomography using fixed (panels (a)–(b)) and variable (panels (c)–(d)) model parametrisation. In both cases, the average map shows a low-velocity anomaly in the centre of the array whose size and amplitude approximate that of the true anomaly in Figs 8.4(a) and (c). In addition, the standard deviation maps associated with these average models reveal loop structures of high uncertainty around the edges of the anomaly. However, when the model parametrisation is fixed (Figs 8.19(a)–(b)), the loops are relatively thick and their edges are not as sharp as when the model is parametrised by variable Voronoi cells. This is likely to be due to the fact that the Voronoi parametrisation provides a much more efficient way to explore the model space, thus allows convergence

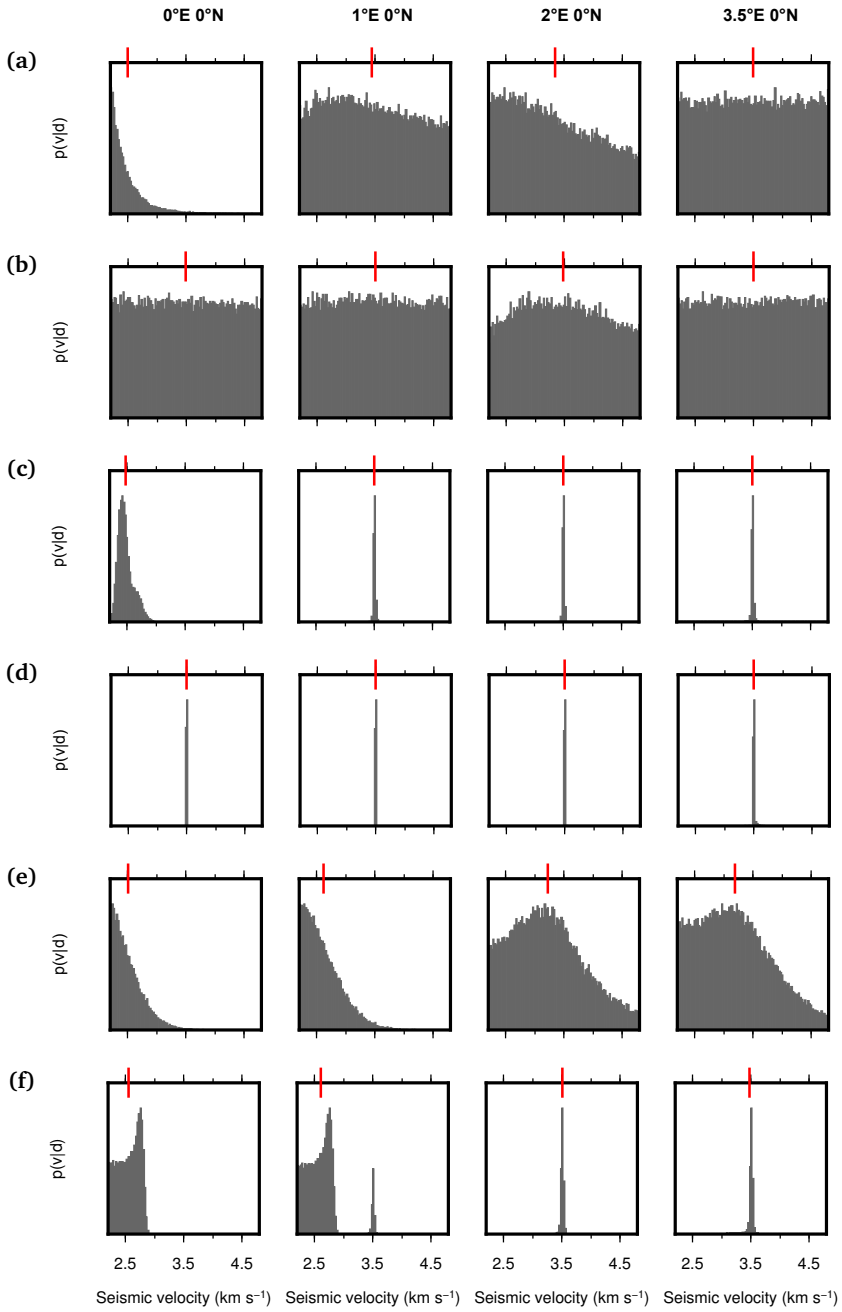

Figure 8.20. Posterior probability distributions for velocity at various points in the model obtained from (rj-)McMC tomography using either fixed or variable raypaths, and either fixed or variable (Voronoi) parametrisation: 0°E, 0°N (first column); 1°E, 0°N (second column); 2°E, 0°N (third column); 3.5°E, 0°N (fourth column). (a) Inversion uses fixed straight raypaths calculated assuming a uniform reference model, and fixed parametrisation (maps in Figs 8.17(a)–(c)). (b) Inversion uses fixed true raypaths as in Fig. 8.4(c), and fixed parametrisation (maps in Figs 8.17(d)–(f)). (c) Inversion uses fixed straight raypaths calculated assuming a uniform reference model, and variable Voronoi parametrisation (maps in Figs 8.18(a)–(c)). (d) Inversion uses fixed true raypaths as in Fig. 8.4(c), and variable Voronoi parametrisation (maps in Figs 8.18(d)–(f)). (e) Inversion uses variable raypaths and fixed parametrisation (maps in Figs 8.19(a)–(b)). (f) Inversion uses variable raypaths and variable Voronoi parametrisation (maps in Figs 8.19(c)–(d)). The red segments mark the average velocity at each location in each case.

to be reached more quickly. As an indication, the inversion in Figs 8.19(a)–(b) was performed using 6 million iterations on a grid of 20 × 20 (400 total) Voronoi squares, while the inversion in Figs 8.19(c)–(d) took only 3 million iterations with 30 Voronoi cells on average. Hence, the structure of the thick loop in Figs 8.19(a)–(b) may narrow and converge towards those in Figs 8.19(c)–((d)) after a (computationally infeasible) number of iterations.

Finally, Fig. 8.20 shows the posterior probability distribution on velocity for all of the cases analysed above at four different locations in the model: in the centre of the anomaly (0°E, 0°N, first column), near the edge of the anomaly (1°E, 0°N, second column), in the background medium outside the anomaly but within the circular array of receivers (2°E, 0°N, third column), and in the background medium outside the circular receiver array (3.5°E, 0°N, fourth column). When linear McMC tomography is performed using fixed raypaths and fixed parametrisation (Figs 8.20(a)–(b)), most of the posterior velocity distributions are either uniform or lack a clear peak, explaining the large values of standard deviation found at the corresponding locations in Fig. 8.17. The only exception to this trend is found in the top-left plot: in this case straight raypaths are used, hence low velocities are introduced in the centre of the model in order to fit the traveltimes corresponding to the rays passing through this location (similarly to the example in Fig. 8.10).

When linearised rj-McMC tomography is performed using fixed raypaths and variable Voronoi parametrisation (Figs 8.20(c)–(d)), the velocity posterior in the centre of the anomaly peaks near the true anomaly velocity if straight rays are used (for the same reasons as in the previous case), while all remaining distributions show a sharp peak at the velocity of the background medium. If the raypath geometry corresponds to the true rays, this effect can be explained by considering that first-arriving energy avoids the anomaly by travelling along its circular edge at the velocity of the background medium, hence all rays follow the correct path and are unable to detect the low-velocity region in the centre of the model. However, the fact that clear peaks, rather than uniform posteriors, are also found at the centre of the anomaly and outside the circular receiver array where no rays are present, is likely to be an effect of the relatively large size of the Voronoi cells, whose boundaries might extend beyond the limits of the interrogated region (as can be observed in Fig. 8.9). Indeed, when rays are fixed to the true geometry and the model is instead parametrised by fixed Voronoi squares, the posterior velocity distributions at locations where no rays are present correspond to the uniform prior (first and last plot in Fig. 8.20(b)).

When rays are allowed to move during the inversion (Figs 8.20(e)–(f)), the spread in posterior velocities is large if the parametrisation is kept fixed, explaining the large values of standard deviation in Fig. 8.19(b), while much clearer peaks are visible when the model is parametrised by Voronoi cells. However, for the same reasons discussed above,

the velocity posteriors in panel (e) might narrow and converge towards those in panel (e) after a much larger and computationally infeasible number of iterations.

When both raypaths and parametrisation are allowed to vary, an upper-bounded distribution is found in the centre of the anomaly since all possible anomaly velocities below a certain threshold produce similar traveltimes (as explained in the simple example in Fig. 6.2(a)). Near the edge of the anomaly at 1°E, 0°N, the velocity distribution presents a double peak which results from this point being located either inside or outside of the anomaly in the ensemble of models, explaining the large standard deviation values near this point and the emergence of the high uncertainty loop in Fig. 8.19(d).

8.3 Comments, guidelines and suggestions

Ray tracing within the fully non-linear rj-McMC program was implemented by turning the stand-alone code *fm2dss* by Nick Rawlinson into a Fortran subroutine that was included in the transdimensional tomography code. The *fm2dss* program uses the Fast Marching Method (FMM) to calculate first-arrival traveltimes through a 2D velocity medium using spherical-shell coordinates. It then traces raypaths from receivers to sources by following the direction of the traveltime gradient vector.

As the *fm2dss* code was not created for use in a Monte Carlo scheme, its implementation to compute raypaths at each iteration of the Markov chain may result in quite slow operation, increasing the computation time required for tomography. Within this section, I provide an indication of the computational cost of non-linear rj-McMC inversion and describe a number of attempts that have been and could be made in order to reduce this cost. I also provide a series of guidelines for future use of the code and for processing the results of rj-McMC inversion.

8.3.1 Computational cost

The major factor contributing to the computational cost of the fully non-linear rj-McMC method is the calculation of raypaths at each model proposed along the Markov chain. As an indication of computational cost, the inversion for the synthetic dataset created from the true model in Fig. 8.4(a),(c), performed by running 16 Markov chains of 3×10^6 models each in parallel on the ECDF cluster, took $\sim$ 18 hours for a fixed raypath geometry and 6 iterations (Figs 8.5-8.6), and $\sim$ 25 days when raypaths were updated at each model proposed along the chain (Fig. 8.12).

Since the FMM first calculates the traveltime from the source to each point of the grid, computation time is strongly dependent on the size of the propagation grid, increasing linearly with the number of grid points (i.e., for N propagation grid points, the computation complexity is $O(N)$). In terms of propagation cell size, this implies that decreasing the grid-point spacing by a factor k increases the computation time as $O(k^2)$.

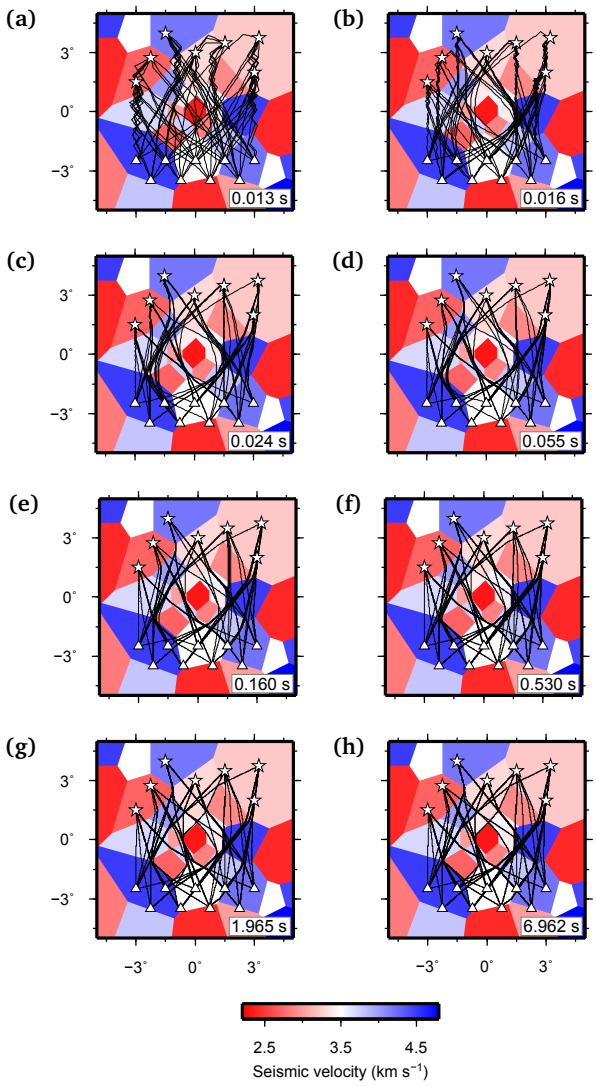

Figure 8.21. Effect of modelling grid size on raypaths in a Voronoi-tessellated 2D space. Modelling grids were obtained by dividing each 1° × 1° sector into (a) 1 × 1, (b) 2 × 2, (c) 4 × 4, (d) 8 × 8, (e) 16 × 16, (f) 32 × 32, (g) 64 × 64, (h) 128 × 128 cells, and no grid refinement was applied near the source. The time taken by program *fm2dss* to calculate raypath geometries in each case is indicated in the bottom-right corner of each plot.

Hence, while thinner grids ensure convergence to the true solution (Rawlinson & Sambridge, 2005), the time required for ray tracing substantially increases as the grid size decreases. In addition, as the traveltime field needs to be calculated separately for each source, computation time also rises with an increasing number of sources ($O(M \times N)$, where M and N are the number of sources and propagation grid points, respectively).

A comparison of the effects of different grid sizes on modelled raypaths in a Voronoi-tessellated 2D space is shown in Fig. 8.21. As expected, the raypath geometry converges to the true solution and fewer artefacts are present as the grid size decreases. However, the time taken for the computation is also strongly influenced by the grid size: for the

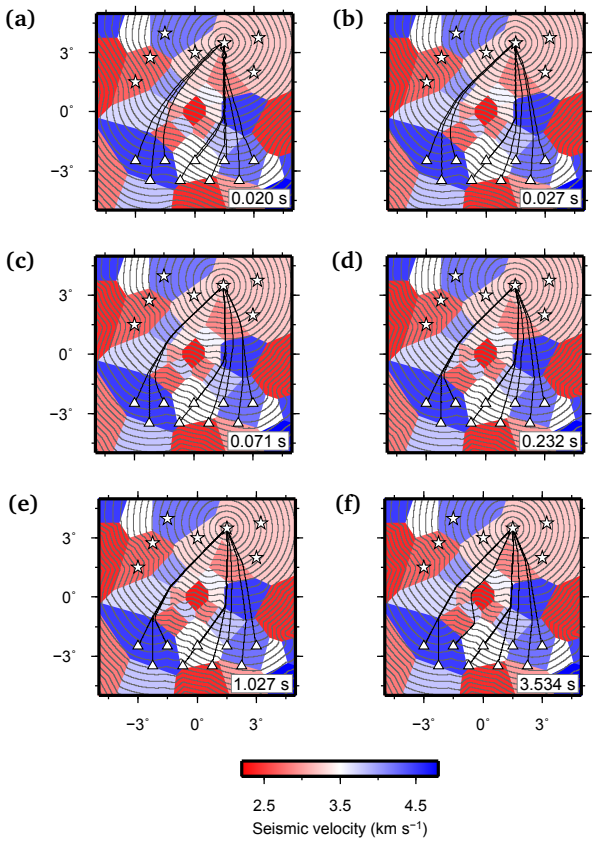

Figure 8.22. Effect of modelling grid size on raypaths in a Voronoi-tessellated 2D space with source grid refinement. Modelling grids were obtained by dividing each 1° × 1° sector into (a) 2 × 2, (b) 4 × 4, (c) 8 × 8, (d) 16 × 16, (e) 32 × 32, (f) 64 × 64 cells, and grid refinement (1°/64) was applied up to 0.5° from the source. The time taken by program *fm2dss* to calculate raypath geometries in each case is indicated in the bottom-right corner of each plot.

source-receiver geometry depicted in Fig. 8.21, computation time increases from 0.013 s for a grid with a 1° cell-size to 6.962 s for a grid with 1°/128 cell-size.

The wavefront at intervals of 10 s for one of these sources and the corresponding raypath geometry are shown in Fig. 8.22. In this case, grid refinement near the source location was applied in order to obtain a cell size of 1°/64 up to a distance of 0.5° from the source. The time required to compute raypath geometries from the source to all receivers is shown in the bottom-right corner of each plot. As in the previous figure, computation time increases dramatically with decreasing grid size, making the computation of raypaths in a fully non-linear rj-McMC setting prohibitive if particularly thin grids are used.

In the synthetic examples presented in this chapter and in all of the other rj-McMC tomography examples within this thesis, the choice of the modelling grid size was mainly dictated by a compromise between raypath accuracy and computation time. As explained in Section 5.3.2, raypath modelling grids were defined by dividing each 1° × 1° sector into 16 × 16 cells, and further dividing each propagation cell within a distance of 0.5° from the source into 4 × 4 sub-cells. From our experiments, this grid parametrisation

seemed to provide a good compromise between raypath accuracy and the time taken to perform the inversions. Although thinner grids would have allowed a grater precision in raypath computation, the increase in the time required for computation made their choice impractical.

In its current state, the ray-tracing subroutine, obtained from the standalone *fm2dss* code, computes the traveltime field and raypaths by looping over sources and tracing the raypath from each receiver back to the source by following the traveltime gradient vector. Hence, the time required to compute all raypaths at each proposed sample is a function of both the number of sources and the size of the grid (in terms of both propagation cell size and grid extent). As the *fm2dss* code was not originally meant for applications in a rj-McMC setting, a number of changes could be made to the ray-tracing subroutine in order to increase its speed and improve the efficiency and applicability of the tomography code. Such changes may include:

- parallelisation of the ray-tracer over sources. Since the traveltime field is calculated independently for each source, parallel processes could be used to compute raypaths from multiple sources simultaneously using the Message Passing Interface (MPI) or Open Multi-Processing (OpenMP). Experiments have shown that parallelising the raytracer over two processes with MPI roughly halves the running time for one Markov chain.
- updating raypaths locally. Since the investigated area may be large, a significant saving in computation time could be made by re-computing only those rays that pass near the area affected by the change from one model to the next in the Markov chain. However, experimental results have shown that care must be taken when only local raypath updates are performed (see Section 8.3.2).

Experimental results have also shown that a change in the size of the model may affect the computation time quite dramatically. For instance, the synthetic tests in Figs 8.12–8.13 were also performed on a geographically more limited inversion grid of $10^\circ \times 10^\circ$ centred on 0°E, 0°N (i.e., 4 times smaller). In that case the running time for the inversion was $\sim$ 9 days, almost a third of the time taken for the inversions in Figs 8.12–8.13. Hence, computation time may also be reduced by making the geographical boundaries of the model as narrow as possible around the area where sources and receivers are located. However, model boundaries should also be wide enough to avoid rays from tracing along the edges of the model and prevent edge effects from biasing the results.

8.3.2 Local raypath update

An attempt was made to increase the speed of the fully non-linear rj-McMC tomography code by re-computing the raypath geometry at each sample only partially, similarly to the partial traveltime update implemented by Bodin & Sambridge (2009) (Fig. 8.3). This was achieved by only retracing the rays passing through the Voronoi cell affected by the

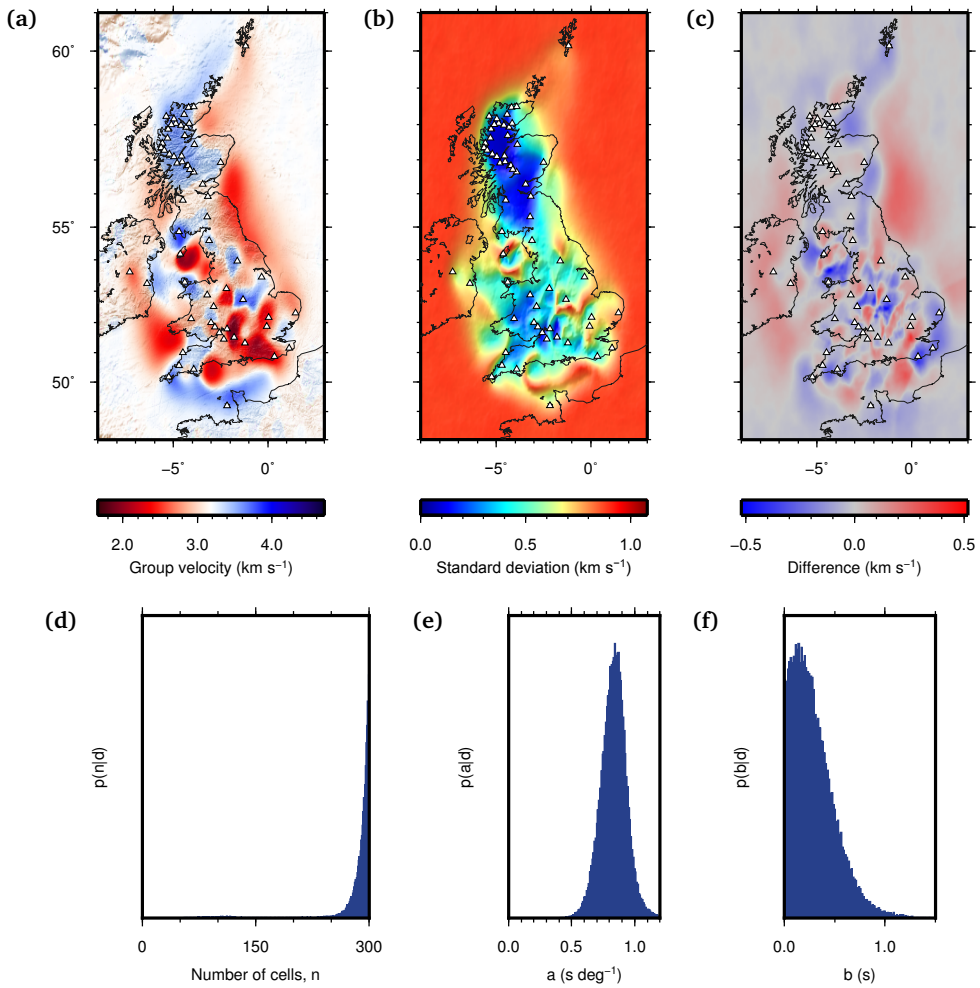

Figure 8.23. Results of Love-wave rj-McMC tomography at 10 seconds period performed by only updating raypaths locally. (a) Average group-velocity map. (b) Standard deviation map. (c) Difference between the map in (a) and that obtained by performing a full update of the raypath geometry at each step of the Markov chain (Fig. 6.1(a)). Posterior distributions on (d) number of Voronoi cells, (e) noise hyperparameter a, (f) noise hyperparameter b.

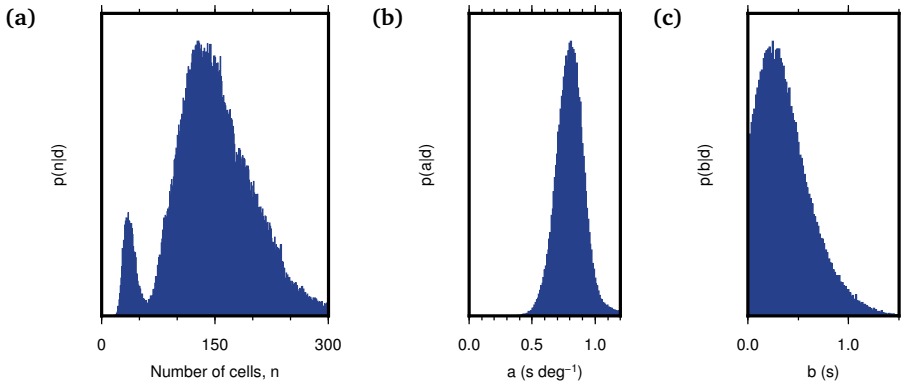

Figure 8.24. Posterior distributions on (a) number of Voronoi cells, (b) noise hyperparameter a, (c) noise hyperparameter b associated with the average and standard deviation maps in Figs 6.1(a)–(b). In this case all raypaths are updated at each step of the Markov chain.

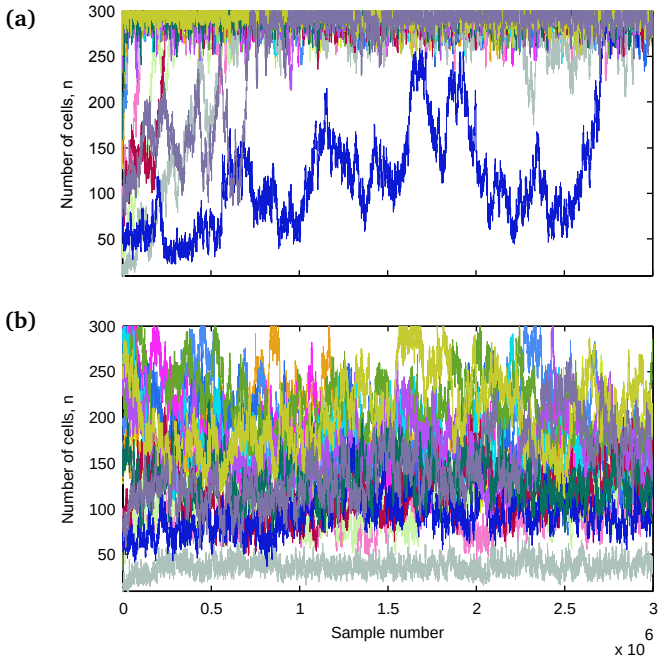

Figure 8.25. Number of Voronoi cells versus iteration number on each of the 16 Markov chains that were run for the experiments in this section and in Section 6.2. Tomography was performed by (a) updating the raypaths locally (results in Fig. 8.23) and (b) updating all raypaths (results in Figs 6.1(a)–(b) and 8.24) at each step of the chain.

change and its immediate neighbours. For instance, in Fig. 8.3 only the raypath passing through the grey Voronoi cells would need to be recomputed in a *birth* step ((a)→(b)) or a *death* step ((b)→(a)), while the ray near the upper edge of the plot would not need to be recomputed. Similarly, in a *velocity* step, only rays passing through the affected cell and its immediate neighbours would be updated, while in a *move* step raytracing would be performed on rays passing through the affected cell, in both its old and new position, and its immediate neighbours.

Although this approach seemed to succeed in speeding up the rj-McMC inversion, it also appeared to affect the number of Voronoi cells in the solution models. As an example, Fig. 8.23 shows the average map, standard deviation map and posterior distributions on the number of Voronoi cells and noise hyperparameters a and b for Love-wave tomography of the British Isles at 10 seconds period, using the same traveltime dataset and priors as the inversion discussed in Chapter 6. A map showing the difference between the UK velocity field in Chapter 6 (Fig. 6.1(a)) and that in Fig. 8.23(a) is also shown (Fig. 8.23(c)). Although the differences between the two maps are relatively small, the posterior distribution on the number of cells seems to favour models with a large number of Voronoi cells when only a local raypath update is performed (Fig. 8.23(d)). In contrast, inversion with a full raypath update (as presented in Chapter 6) yields convergence towards a number of cells which falls within the prior. This behaviour is also visible in Fig. 8.25, showing the number of cells at each iteration for

each of the 16 parallel Markov chains in the two cases. Note that the small isolated peak on the left of Fig. 8.24(a) is due to one of the chains not having converged (the grey line near the bottom edge of Fig. 8.25(b)).

Although the reason for this behaviour is not exactly understood, it is straighforward to notice that, as the raytracer here employed is eikonal and the path taken by a ray is derived from the traveltime field, a relatively small change in one area of the velocity model might affect the traveltime field quite dramatically. Hence, even rays that do not pass near the affected area might be influenced by the change in the model, as can be observed in the example provided in Figs 8.26–8.27. In Fig. 8.26, panels (a)–(b) show the *birth* of a new cell at the centre of a Voronoi-tessellated 2D space (the numbers in black identify the various cells), with the corresponding raypath geometry displayed in panels (c)–(d). The raypath geometry obtained when a *velocity* step is performed by changing the velocity of this new central cell is shown in Fig. 8.27, for both a low- and a high-velocity case. While the raypath geometry does not change in a low-velocity move (as first-arriving energy follows the path that avoids the low-velocity cell), some of the rays switch to a different path when a high-velocity move is performed, as passing through the high-velocity cell substantially decreases their traveltime. However, as can be seen in Table 8.1, neither of these rays originally passed through either the central Voronoi cell (cell 31) or its immediate neighbours (cells 1–6). Hence, following this example, if the raypath geometry was to be updated in a rj-McMC setting for a high *velocity* step (from the model in Fig. 8.26(d) to the model in Fig. 8.27(b)), none of the rays would be updated as they did not originally pass through the affected cell or its immediate neighbours. Hence, the wrong raypath geometry would be used in the computation of traveltimes and in the evaluation of the likelihood. In addition, this wrong ray geometry would be carried on along the Markov chain, affecting any subsequent change in the velocity model.

8.3.3 Convergence assessment

In a (rj-)McMC inversion scheme, it is important to collect a sufficient number of samples so that the ensemble of sampled models will be representative of the posterior probability distribution. If a Markov chain could be run for an infinite amount of time, it would explore the full model space and reach convergence in the region of highest probability. However, since computational limitations impose a practical limit on the running time of a Markov chain, convergence may not be reached by the end of the chain if this gets stuck in a local minimum. A practical solution to this problem is to run a series of Markov chains in parallel by starting from different initial conditions. This ensures that different regions of the model space can be explored simultaneously, and that anomalous Markov chains that are stuck in a local minimum can easily be identified (e.g., see Fig. 8.31(d)).

Although few tools are currently available for assessing convergence in a transdimensional framework (Bodin & Sambridge, 2009), information of Markov chain

Rec.	Fig. 8.26(c)	Fig. 8.26(d)	Fig. 8.27(a)	Fig. 8.27(b)
A	17 12 10 13 7 15	17 12 10 13 7 15	17 12 10 13 7 15	17 9 12 6 3 31 1 7 15
B	17 14 8 11 7 15	17 14 8 11 7 15	17 14 8 11 7 15	17 14 3 31 1 7 15
C	14 8 11 7 15	14 8 11 7 15	14 8 11 7 15	14 8 11 7 15
D	16 8 11 7 15	16 8 11 7 15	16 8 11 7 15	16 8 11 7 15
E	16 11 15	16 11 15	16 11 15	16 11 15
F	17 14 8 11 7 15	17 14 8 11 7 15	17 14 8 11 7 15	17 14 3 31 1 7 15
G	14 8 11 7 15	14 8 11 7 15	14 8 11 7 15	14 8 11 7 15
H	30 14 16 8 11 15	30 14 16 8 11 15	30 14 16 8 11 15	30 14 16 8 11 15
I	26 16 11 15	26 16 11 15	26 16 11 15	26 16 11 15

Table 8.1. Paths taken by rays in Figs 8.26(c)–(d) and 8.27 given as the number of each Voronoi cell crossed when tracing the rays from receiver to source. The Voronoi cell numbers correspond to those given in Figs 8.26(a)–(b). Note how the only changes in trajectory are observed for rays to receivers *A*, *B*, *F* when the velocity of central cell 31 is changed to a higher value. The underlined numbers denote cell 31 and its immediate neighbours.

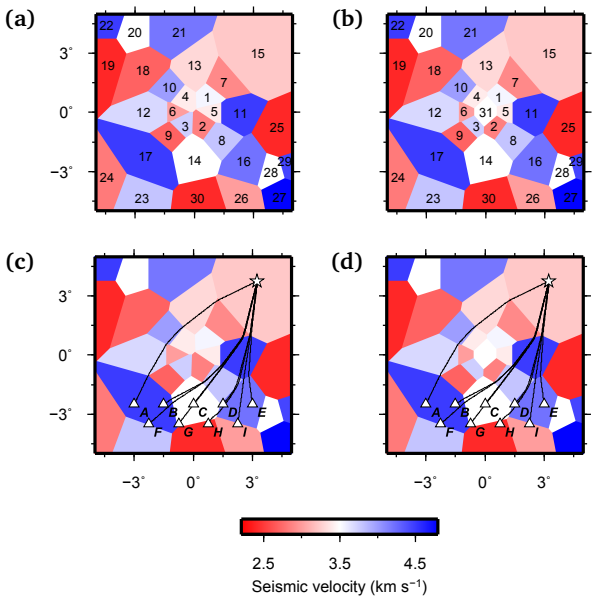

Figure 8.26. Example of cell *birth* in a Voronoi-tessellated 2D space. A new cell is added at the centre of the velocity model from (a) to (b). The raypath geometries corresponding to the models in (a) and (b) are shown in (c) and (d), respectively. Each Voronoi cell in the model is identified by a number which is shown in (a) and (b).

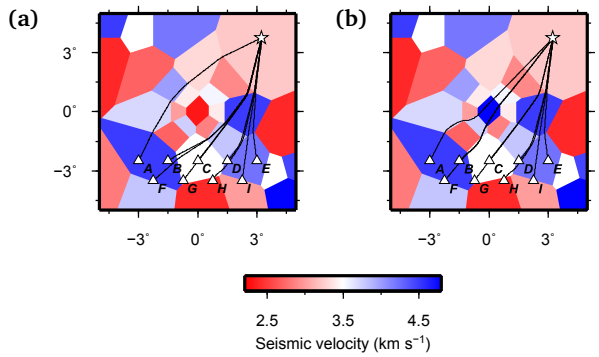

Figure 8.27. Example of a *velocity change* affecting the central Voronoi cell (cell 31) of the velocity model in Fig. 8.26(b). (a) The velocity of cell 31 is changed to a lower value. (b) The velocity of cell 31 is changed to a higher value.

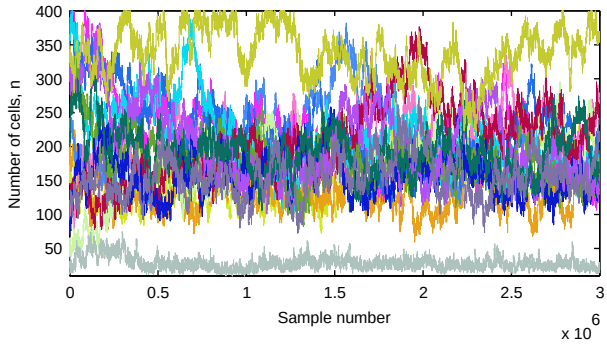

Figure 8.28. Number of Voronoi cells versus iteration number on each of the 16 Markov chains that were run for rj-McMC tomography at 9 seconds period.

convergence may be obtained by plotting the variation of a model parameter as a function of iteration. However, as opposed to traditional McMC methods where model parametrisation is fixed, in a rj-McMC tomography scheme the use of cell position and velocity parameters ($\mathbf{c}$, $\mathbf{v}$) to assess convergence is pointless since the geometry of the model may change at each step of the chain. Instead, useful convergence diagnostics may be obtained from plots of number of cells, noise hyperparameters, or velocity at a certain geographical location versus iteration. Convergence is said to be reached when the value of one of these parameters becomes stationary and no drifts are present as the parameter is plotted as a function of sample number.

As discussed in Chapter 7, we used plots of the number of Voronoi cells versus iteration number such as that in Fig. 8.28 to assess convergence and identify anomalous Markov chains. These were then removed from the ensemble of analysed models when performing Love-wave tomography of the British Isles at various periods (Chapter 7). Although most Markov chains appeared to converge during 3 million iterations, an anomalous Markov chain was identified while performing the inversion at 9 seconds period. Figure 8.28 shows the number of Voronoi cells versus sample number for each of the 16 Markov chains that

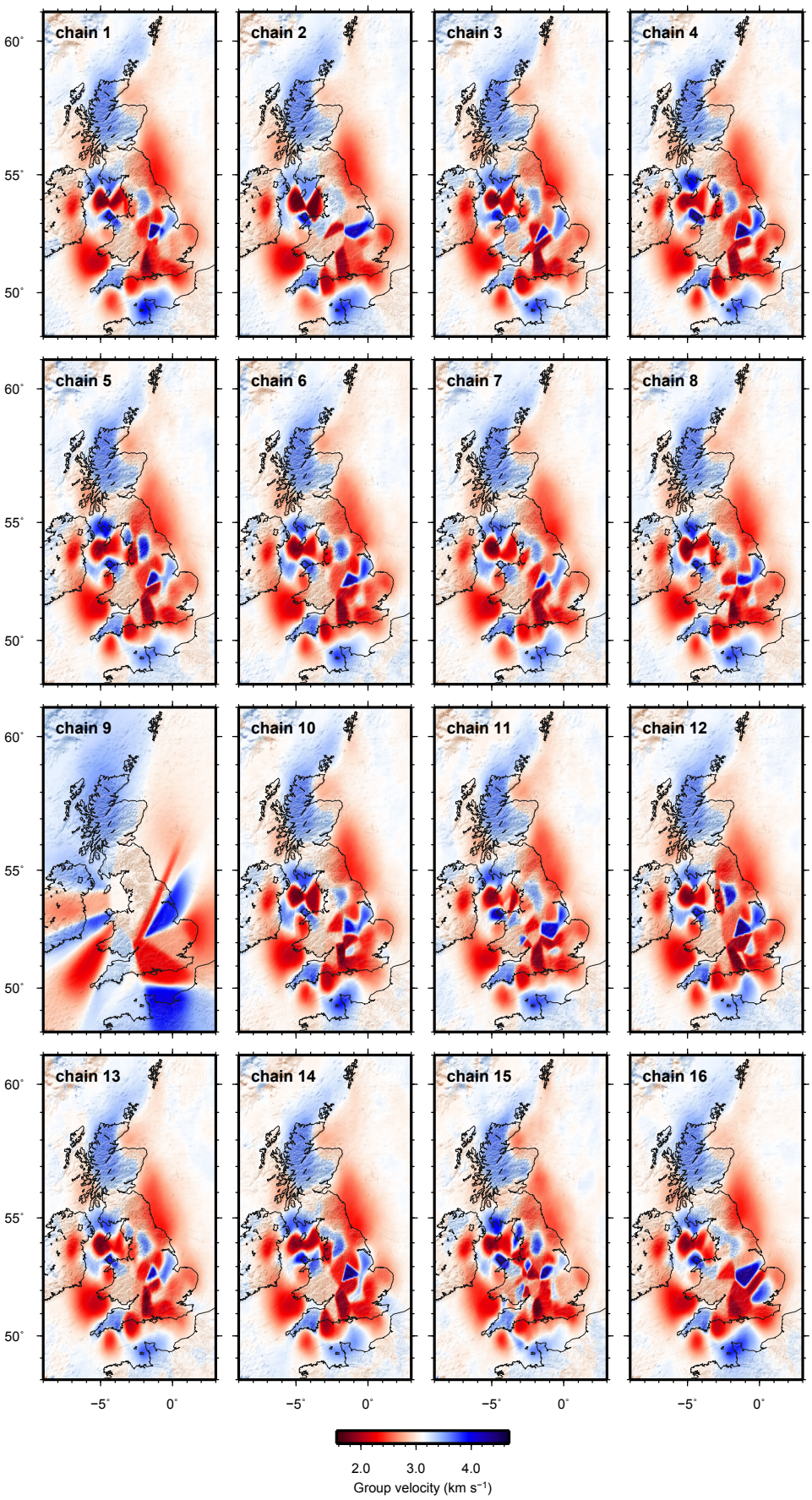

Figure 8.29. Average Love-wave group-velocity maps at 9 seconds period for each of the 16 Markov chains run in rj-McMC inversion.

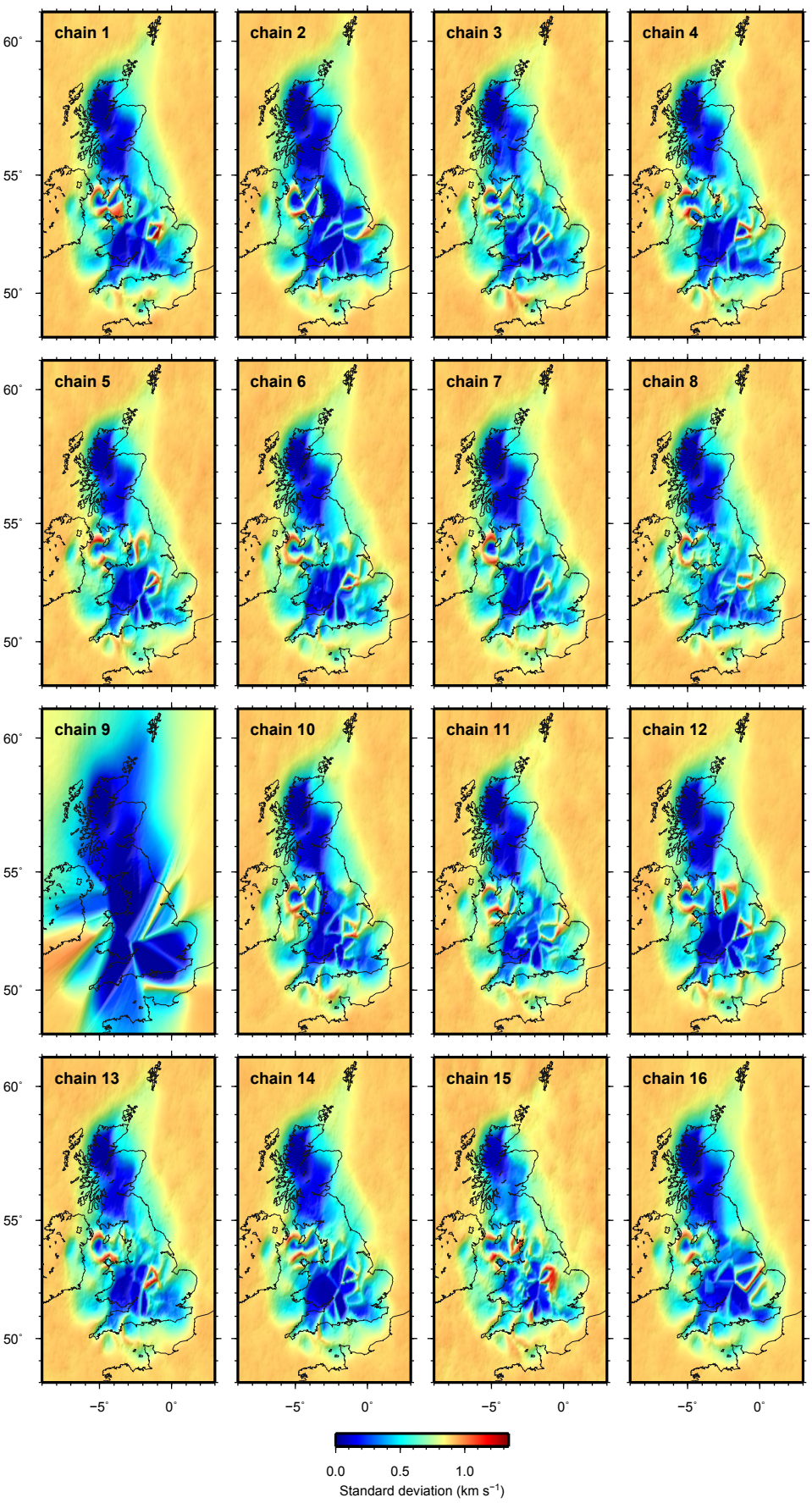

Figure 8.30. Standard deviation maps associated with the average group-velocity maps in Fig. 8.29.

were run to perform the inversion. While 14 Markov chains seem to converge around a similar number of Voronoi cells, one chain (the grey line near the bottom edge of the plot, corresponding to chain 9) does not convergence to the same region of high probability, while another Markov chain (the green line near the top of the plot, corresponding to chain 15) moves in and out of the convergence zone during 3 million iterations. Figures 8.29 and 8.30 show the average and standard deviation maps obtained by processing each Markov chain separately. Clearly, the results obtained for chain 9 (first plot in the third row) are substantially different from those obtained from the other Markov chains. On the other hand, the results obtained for chain 15 are relatively similar to those from the other Markov chains despite this chain's distinct behaviour. Figure 8.31 shows the average map, standard deviation map and posteriors on a, b and number of Voronoi cells that would be obtained if the models from chain 9 were included in the ensemble, together with a map showing the difference between the averages obtained in the two cases. Although the differences between the average map obtained by excluding (Fig. 7.10(a)) and including (Fig. 8.31(a)) Markov chain 9 are relatively small, the posterior distributions on noise hyperparameter a and number of Voronoi cells clearly show the distinct behaviour of this chain as a separate small peak in both distributions.

Finally, the choice of the prior also plays a role on Markov chain convergence, with wider priors normally causing convergence to be slower. This is intuitive since, for the same Markov chain length, wider prior boundaries imply that a larger part of model space must be explored. We observed this behaviour when performing tomography of the British Isles using wider priors on velocity compared to those listed in Table 7.1. At all of the analysed periods, convergence occurred much more slowly, the posterior distributions on the number of cells had multiple peaks, and in many cases the Voronoi cell boundaries were still visible in the final average and standard deviation maps. Hence, although the use of a wider prior ensures that no prior-related biases are introduced into the solution (i.e., at 8–11 seconds period, the maximum probability maps in Chapter 7 show that the group-velocities within the Irish Sea anomaly hit the lower bound of the priors), it also means that Markov chains need to be run for a longer time in order to reach convergence. For the inversions presented in Chapter 7 we therefore chose the narrower priors in Table 7.1 given the practical limitations on the available computing time.

8.4 rj-McMC group-velocity inversion: issues and challenges

As discussed in Section 7.6, the forward problem in group-velocity inversion consists of calculating a group-velocity dispersion curve for a given layered velocity model. Within this project, forward modelling was performed using the DISPER80 subroutines by Saito (1988), which are well known within seismology and have so far been used in more than one hundred published studies since their release, including the first applications of the

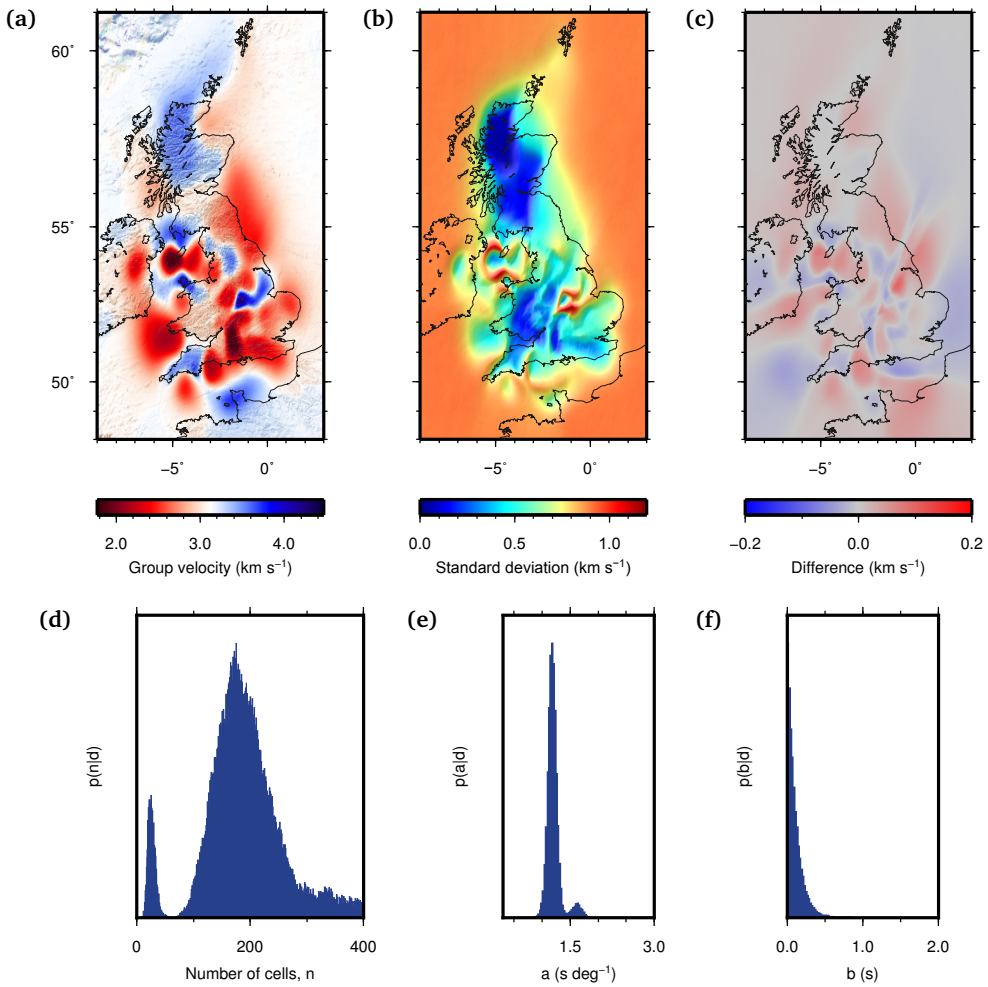

Figure 8.31. Results of Love-wave rj-McMC tomography at 9 seconds period obtained by including the models from Markov chain 9 in the ensemble. (a) Average group-velocity map. (b) Standard deviation map. (c) Difference between the map in (a) and that obtained by excluding the models from Markov chain 9 from the analysis (Fig. 7.10(a)). Posterior distributions on (d) number of Voronoi cells, (e) noise hyperparameter a, (f) noise hyperparameter b.

rj-McMC algorithm to group- and phase-velocity inversion (Bodin et al., 2012c; Young et al., 2013a). These Fortran subroutines require values for compressional velocity v_P, shear velocity v_S and density ρ to be defined for each layer in order to compute Love- or Rayleigh-wave phase- or group-velocities, and can easily be integrated into the rj-McMC inversion code. However, although they are ideal for application in a Markov chain Monte Carlo setting thanks to their fast execution time, we found that they may yield an incorrect dispersion curve when the velocity structure of the layered model is relatively unusual. For instance, we tested the code on a number of synthetic models and found that unrealiable results were produced when one or more layers of particularly low velocity were present at large depths in the model. Examples of some of these tests are given below, where DISPER80 is used to compute Love-wave group-velocity dispersion by using a fixed value of 1.76 for v_P/v_S, and by letting density vary as a function of v_P as in equation (7.3).

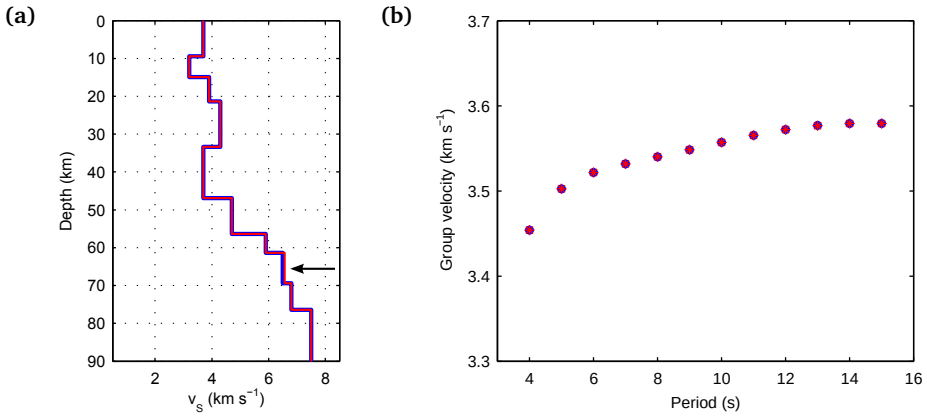

Figure 8.32. Example of Love-wave group-velocity dispersion modelling using DISPER80 on a normal shear-velocity profile in which v_S generally increases with depth. The blue and red v_S profiles in panel (a) produce the dispersion curves denoted by the blue circles and red asterisks, respectively, in panel (b). The red profile in (a) is obtained by increasing the shear-velocity of the layer near 65 km depth (indicated by the arrow) by 1% relative to that of the same layer in the blue profile.

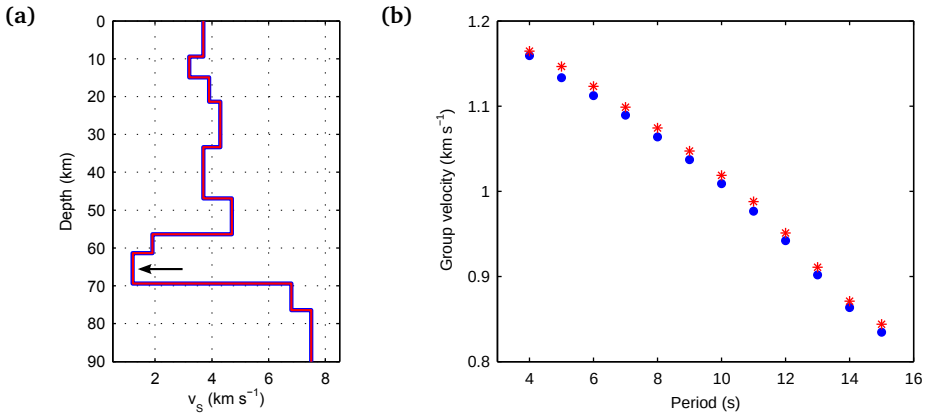

Figure 8.33. Example of Love-wave group-velocity dispersion modelling using DISPER80 on an inverted shear-velocity profile which contains a low-velocity layer at large depths. The blue and red v_S profiles in panel (a) produce the dispersion curves denoted by the blue circles and red asterisks, respectively, in panel (b). The red profile in (a) is obtained by increasing the shear-velocity of the layer near 65 km depth (indicated by the arrow) by 1% relative to that of the same layer in the blue profile.

Consider first the case of a normal velocity profile in which v_S generally increases with depth, as illustrated in Fig. 8.32. The blue shear-velocity profile in panel (a) produces the Love-wave group-velocity dispersion curve denoted by the blue circles in panel (b). When the shear-velocity of the layer near 65 km depth is perturbed by +1% (red profile in (a)), the dispersion curve denoted by the red asterisks in panel (b) is obtained. As expected, since the amount of velocity perturbation is small and is applied at a very large depth at which the analysed periods have very little sensitivity, the group velocities obtained in the two cases match almost perfectly.

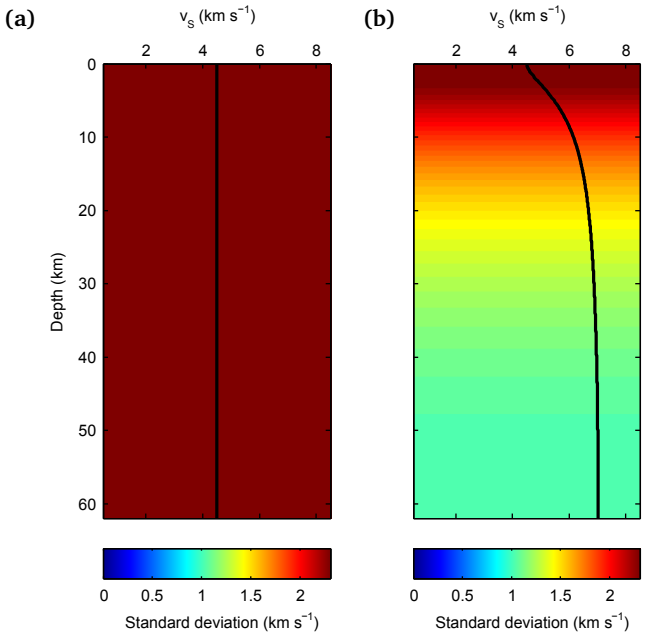

Figure 8.34. Shear-velocity priors obtained (a) when no limit on velocity drop is imposed between layers, and (b) when an 80% limit on velocity drop is imposed between any two consecutive layers of increasing depth. In both cases the black line denotes the a priori average shear-velocity v_S, while the background image represents the a priori standard deviation. The average and standard deviation profiles in (a) were computed analytically from a Uniform distribution with shear-velocity bounds at [0.5 8.5] km s^{-1}, using equation (7.2) to evaluate the a priori standard deviation. The average and standard deviation profiles in (b) were computed numerically across an ensemble of 1 million randomly-generated models using the same bounds on v_S, number of layers, and depth of Voronoi nuclei as in Section 7.6.

The case of an inverted velocity profile, in which a layer of particularly low velocity is present at large depths, is illustrated in Fig. 8.33. As in the previous case, the blue shear-velocity profile in panel (a) produces the Love-wave group-velocity dispersion curve denoted by the blue circles in panel (b). When the shear-velocity of the layer near 65 km depth is perturbed by +1% (red profile in (a)), the dispersion curve denoted by the red asterisks in panel (b) is obtained. In this case, although the amount of perturbation is of the same order of magnitude as that in the previous example, the change in group velocities is larger than 1%. Given the large depth at which the perturbation was applied and that the sensitivity of the analysed periods at the perturbation depth should be very limited, this large change is likely to be due to errors introduced by the DISPER80 modelling code.

Although models such as the one in Fig. 8.33(a) are relatively unusual in real scenarios, they might occur in a Markov chain Monte Carlo setting in which models are generated and perturbed randomly. Hence, in order to prevent modelling errors such as those described above from occurring during the rj-McMC inversion, after a number of trials we imposed an 80% limit on the velocity drop between any two consecutive layers of increasing depth (i.e., in each proposed model the shear-velocity of layer i must be at least 80% of the shear-velocity of layer $i-1$ above it). This ensured that only reliable models such as

the one in Fig. 8.32 were proposed, while still allowing velocity to decrease with depth if needed. However, this also implied that the prior on shear-velocity was not uniform across the model space (e.g., Fig. 8.34(a)) but varied with depth.

We therefore produced an estimate of the new prior by generating 1 million random velocity models, all of which respected the 80% limit on velocity drop between consecutive layers and used the same bounds on v_S, number of layers, and depth of Voronoi nuclei as described in Section 7.6. The average velocity profile (black line) and the standard deviation (background image) across this ensemble of random models are shown in Fig. 8.34(b). As expected, while the average and standard deviation profiles are constant when no limits on velocity drop are imposed (Fig. 8.34(a)), the values of average shear-velocity and standard deviation vary as a function of depth when a limit on velocity drop between layers is introduced. In particular, the average v_S increases with increasing depth, while the standard deviation progressively decreases. However, the rate of change of both quantities also decreases with depth, and the two quantities become almost constant below 50 km. This is likely to be due to the fact that the lower bound on v_S progressively increases with depth, which in turn causes the range of possible values for v_S to narrow.

The velocity prior in Fig. 8.34(b) can be used to properly interpret the results obtained from the group-velocity inversions presented in Section 7.6. For instance, with respect to the results of the 1D inversion at $-4°$E, $54°$N displayed in Fig. 7.20, the posterior standard deviation in Fig. 7.20(b) is lower than the prior down to the limit of significant resolution at ~ 25 km, while it is larger than the prior standard deviation below this depth.

Although this type of prior parametrisation allowed us to conduct the preliminary study described in Section 7.6, we are aware that a more detailed investigation is needed in order to identify and understand the exact causes of this behaviour in the DISPER80 subroutines. Such investigation may include testing the code over a wider range of periods, analysing the relationship between low-velocity layer thickness and available wavelengths, and identifying any assumptions and approximations in the theory that the code uses.

CHAPTER 9

Conclusions

Seismic records contain information that allows geoscientists to make inferences about the properties and structure of the Earth's subsurface. Traditionally, seismic imaging and tomography methods require the use of identifiable impulsive sources such as earthquakes or explosions, while seismic ambient noise is regarded as a nuisance and removed from active-source datasets in order to enhance data quality. However, in recent years the method of seismic interferometry has revolutionised earthquake seismology by allowing useful information to be extracted from ambient noise. In fact, cross-correlation of ambient-noise waveforms recorded by a pair of receivers yields the Green's function (i.e., impulse response) between the two receiver locations, as if an active seismic source had been co-located with one of the receivers and recorded by the other. Later developments in interferometric theory allowed Green's functions to be constructed between source-source and source-receiver pairs, using either cross-correlation, convolution or deconvolution of wavefields. In all of these formulations, energy is recorded and/or produced by surrounding boundaries of receivers and sources, respectively.

In Part I of this thesis I provided a comprehensive overview of the field of seismic interferometry, its background theory, and examples of its application. Since its initial appearance in the early 2000s, the field of interferometry has expanded, and is now commonly used in various branches of seismology. What makes interferometry particularly appealing to seismologists is the fact that it obviates the need for earthquakes to be recorded directly (or at all), making traditional earthquake seismology studies possible even in non-seismic areas. In addition, since ambient noise can normally be recorded continuously for long periods of time, changes in the Earth's subsurface may be

regularly monitored, allowing us to gain a better understanding about dynamic processes occurring within the Earth's interior.

In Chapter 2, I presented an exact, error-free waveform modelling code which I developed specifically for applications to interferometry. I then used this code to test interferometric theory and quantify the effects of approximations that are commonly made when the interferometric formulae are applied to real datasets. In Section 4.1 I provided further examples of the use of this modelling code to test existing and new theory in interferometry and scattering in a number of published studies by the Edinburgh Interferometry Project (EIP) research group. In all of these examples, the use of exact, error-free data allowed physical and non-physical events in the results to be related to specific origins in interferometric theory, enhancing our understanding of how interferometry works in simple scattering acoustic media. The knowledge and understanding obtained from these tests provided a solid base for applications of interferometry and scattering theory to more complex datasets.

In Chapter 3 I discussed the ability of interferometry to redatum seismic energy in both space and time. This is achieved using source-receiver interferometry (SRI) to construct virtual seismograms at new locations where receivers may not have been present at the time of occurrence of the associated seismic source. The method was tested on synthetic and real datasets spanning different length scales, and satisfactory results were obtained in all cases. Although the two real-data examples presented in Chapter 3 are currently restricted to relatively narrow bandwidths, they demonstrate the potential of this technique, which constitutes a new powerful tool in the seismologist's arsenal. In fact, these results pave the way for a new type of 'retrospective' seismology where sensors may be installed at any desired location at any time, and recordings of seismic events occurring at any other time can be constructed retrospectively – even long after their energy has dissipated.

Within crustal seismology, a very common application of seismic interferometry is ambient-noise tomography (ANT). This method allows one to image the Earth's subsurface tomographically using Green's functions constructed from inter-receiver interferometry, and is particularly useful in seismically quiescent areas where traditional tomography methods that rely on local earthquake sources would fail to produce interpretable results due to the lack of available data. Once a set of inter-receiver Green's functions have been constructed, inter-station traveltimes may be obtained from standard surface-wave analysis and inverted for group-velocity structure using more or less traditional imaging methods.

In Part II of this thesis, I discussed the development and application of a fully non-linear inversion method which I used to perform ANT across the British Isles. Compared to the majority of currently-available tomography methods, this inversion scheme can be considered fully non-linear in that both raypaths and model parametrisation are allowed to vary freely during the inversion. In addition, being a stochastic scheme which uses Bayes'

theorem and Markov chain Monte Carlo, it produces not only one but several solutions to the tomographic inverse problem, all of which fit the recorded data to within uncertainties. Statistical moments of different order such as the mean or average model, or the standard deviation of seismic velocity structures across the ensemble, may be extracted from the ensemble of solutions: while the average map provides a smooth representation of the velocity field, a measure of uncertainty on the estimated velocities can be obtained from the standard deviation map. In addition, since the number of model parameters is itself an inversion parameter, its posterior distribution may also be derived from the ensemble, providing an indication on the level of detail which is expected from the inversion.

The combination of variable raypaths and model parametrisation is key to the emergence of the previously-unobserved, loop-like uncertainty topologies which were discussed in Chapter 6. These uncertainty loops surround low- or high-velocity anomalies indicating that, while the velocity of each anomaly may be fairly well reconstructed, its exact size and location tend to remain uncertain. These structures were initially noticed while performing ANT of the British Isles at 10 seconds period, but were later studied in detail through a number of synthetic tests. Such tests showed that the emergence of loops is related to the variation in raypaths with velocity structure, and hence to 2^{nd} and higher order wave-physics. Thus, loops can only be observed using non-linear inversion methods such as the one described in Part II of this thesis, explaining why these topologies have never been observed previously.

In Chapter 7 I then presented Love-wave group-velocity maps of the British Isles in a number of frequency bands. Between 4 and 11 seconds period, the maps show a good correlation between visible high- and low-velocity structures and known geology in the upper crustal layers. Particularly, high velocities are observed in the Scottish Highlands, in the Southern Uplands, in the Pennines and near granitic intrusions in Wales and Cornwall, while low velocities are observed in a number of sedimentary basins such as those in the south of England, the Moray Firth, the Midland Valley and the Irish Sea. A robust high-velocity feature was also detected in the East Midlands, and may be related to the presence of granitic batholiths and dykes in the subsurface. At larger depths sampled by the 12 and 15 seconds period maps, most sedimentary basins are no longer visible, hence these maps are mainly representative of basement rocks. A preliminary investigation of the shear-velocity structure of the Irish Sea from inversion of Love-wave group-velocities was also conducted, and showed an approximate depth to basement of 5 km in this basin.

Finally, in Chapter 8 I discussed the advantages and current limitations of the fully non-linear tomography method presented in Chapter 5. In light of the results presented in Part II of this thesis, this method can be regarded as extremely powerful and fruitful since it not only produces reliable group-velocity maps, but also requires little a priori knowledge of the area of study and robustly assesses model uncertainty. As an added benefit, the estimation of model uncertainty does not require the inversion of large matrices since uncertainties are simply evaluated as the standard deviation of group velocities across

the ensemble of models. In terms of limitations and possible improvements, a current drawback of the code is the long computation time, which is mainly due to the complete recalculation of raypath geometries at each step of the Markov chain. Meanwhile, the algorithm allows further parallelisation of processes leveraging recent advances in parallel computing. In fact, experimental parallelisation of the raytracing subroutine over sources has been shown to reduce computation time quite dramatically, making the use of this code more realistic in cases where computing time is an issue or when much denser arrays of sources and receivers are available compared to those used in this thesis. However, the successful application of this method demonstrates how fully non-linear tomography is now a possibility, eliminating the need for any linearised approximations to be made during the inversion.

Within the context of crustal seismology, the network of seismometers used for this study was relatively limited, and the tomographic maps presented in this thesis were unable to resolve features less than tens of kilometers across. However, because seismic interferometry allows classical earthquake seismology methods to be used even in seismically quiescent areas, much interest is currently given to the deployment of dense arrays of seismometers to record the ambient-noise field. In the United States, such a project was launched in 2004 with the deployment of the USArray, a dense network of permanent and semi-permanent seismometers which aims at recording local and teleseismic earthquakes as well as continuous ambient noise. Thanks to the availability of near real-time data at such a large number of closely-spaced stations, high-resolution models of the crust and upper mantle across the United States have successfully been produced in a number of published studies. The success of the USArray project and the wide use of its data have prompted the installation of similar arrays in other parts of the world. Within the United Kingdom, the recent deployment of the UKArray (which includes 40 seismometers, of which 25 permanent and 15 temporary), together with the implementation of the TerraCorrelator at the University of Edinburgh (two 1 Tb machines capable of cross-correlating and analysing seismic waveforms in real-time), sets the basis for significant advances in UK seismology. These advances are expected to benefit many of the branches of seismology from natural hazard assessment to subsurface monitoring, and are likely to increase our understanding of the dynamic processes occurring in the Earth's interior at a variety of scales.

Bibliography

Aki, K. & Richards, P., 2002. *Quantitative seismology*, University Science Books, 2nd edn.

Arroucau, P., Rawlinson, N., & Sambridge, M., 2010. New insight into Cainozoic sedimentary basins and Palaeozoic suture zones in southeast Australia from ambient noise surface wave tomography, *Geophysical Research Letters*, **37**(7), L07303.

Arrowsmith, S. J., Kendall, M., White, N., VanDecar, J. C., & Booth, D. C., 2005. Seismic imaging of a hot upwelling beneath the British Isles, *Geology*, **33**(5), 345–348.

Asencio, E., Knapp, J. H., Owens, T. J., & Helffrich, G., 2003. Mapping fine-scale heterogeneities within the continental mantle lithosphere beneath Scotland: Combining active- and passive-source seismology, *Geology*, **31**(6), 477–480.

Bakulin, A. & Calvert, R., 2004. Virtual source: new method for imaging and 4D below complex overburden, *SEG Technical Program Expanded Abstracts 2004*, pp. 2477–2480.

Bakulin, A. & Calvert, R., 2006. The virtual source method: Theory and case study, *Geophysics*, **71**(4), SI139–SI150.

Bakulin, A., Mateeva, A., Mehta, K., Jorgensen, P., Ferrandis, J., Herhold, I. S., & Lopez, J., 2007. Virtual source applications to imaging and reservoir monitoring, *The Leading Edge*, **26**(6), 732–740.

Baptie, B., 2010. Seismogenesis and state of stress in the UK, *Tectonophysics*, **482**(1–4), 150–159.

Bastow, I. D., Owens, T. J., Helffrich, G., & Knapp, J. H., 2007. Spatial and temporal constraints on sources of seismic anisotropy: Evidence from the Scottish highlands, *Geophysical Research Letters*, **34**(5), L05305.

Bayes, M. & Price, M., 1763. An Essay towards Solving a Problem in the Doctrine of Chances. By the Late Rev. Mr. Bayes, F. R. S. Communicated by Mr. Price, in a Letter to John Canton, A. M. F. R. S., *Philosophical Transactions*, **53**, 370–418.

Beaumont, M. & Rannala, B., 2004. The Bayesian revolution in genetics, *Nature Reviews Genetics*, **5**(4), 251–261.

Behura, J. & Snieder, R., 2013. Virtual Real Source: Source signature estimation using seismic interferometry, *Geophysics*, **78**(5), Q57–Q68.

Bensen, G. D., Ritzwoller, M. H., Barmin, M. P., Levshin, A. L., Lin, F., Moschetti, M. P., Shapiro, N. M., & Yang, Y., 2007. Processing seismic ambient noise data to obtain reliable broad-band surface wave dispersion measurements, *Geophysical Journal International*, **169**(3), 1239–1260.

Bensen, G. D., Ritzwoller, M. H., & Shapiro, N. M., 2008. Broadband ambient noise surface wave tomography across the United States, *Journal of Geophysical Research*, **113**(B5), B05306.

Berkhout, A. J. & Wapenaar, C. P. A., 1989. One-way versions of the Kirchhoff Integral, *Geophysics*, **54**(4), 460–467.

Bluck, B. J., Gibbons, W., & Ingham, J. K., 1992. *Atlas of Palaeogeography and Lithofacies*, The Geological Society.

Bodin, T. & Sambridge, M., 2009. Seismic tomography with the reversible jump algorithm, *Geophysical Journal International*, **178**(3), 1411–1436.

Bodin, T., Salmon, M., Kennett, B. L. N., & Sambridge, M., 2012a. Probabilistic surface reconstruction from multiple data sets: An example for the Australian Moho, *Journal of Geophysical Research: Solid Earth*, **117**, B10307.

Bodin, T., Sambridge, M., Rawlinson, N., & Arroucau, P., 2012b. Transdimensional tomography with unknown data noise, *Geophysical Journal International*, **189**(3), 1536–1556.

Bodin, T., Sambridge, M., Tkalčić, H., Arroucau, P., Gallagher, K., & Rawlinson, N., 2012c. Transdimensional inversion of receiver functions and surface wave dispersion, *Journal of Geophysical Research: Solid Earth*, **117**(B2), B02301.

Born, M. & Wolf, E., 1999. *Principles of Optics*, Cambridge University Press, Cambridge, 7th edn.

Brandon, C. & Romanowicz, B., 1986. A "No-Lid" Zone in the Central Chang-Thang Platform of Tibet: Evidence from Pure Path Phase Velocity Measurements of Long Period Rayleigh Waves, *Journal of Geophysical Research*, **91**(B6), 6547–6564.

Brenguier, F., Shapiro, N. M., Campillo, M., Nercessian, A., & Ferrazzini, V., 2007. 3-D surface wave tomography of the Piton de la Fournaise volcano using seismic noise correlations, *Geophysical Research Letters*, **34**(2), L02305.

Brenguier, F., Campillo, M., Hadziioannou, C., Shapiro, N. M., Nadeau, R. M., & Larose, E., 2008a. Postseismic Relaxation Along the San Andreas Fault at Parkfield from Continuous Seismological Observations, *Science*, **321**(5895), 1478–1481.

Brenguier, F., Shapiro, N. M., Campillo, M., Ferrazzini, V., Duputel, Z., Coutant, O., & Nercessian, A., 2008b. Towards forecasting volcanic eruptions using seismic noise, *Nature Geoscience*, **1**(2), 126–130.

Bunch, J. R. & Hopcroft, J. E., 1974. Triangular Factorization and Inversion by Fast Matrix Multiplication, *Mathematics of Computation*, **28**(125), 231–236.

Campillo, M. & Paul, A., 2003. Long-Range Correlations in the Diffuse Seismic Coda, *Science*, **299**(5606), 547–549.

Cassereau, D. & Fink, M., 1993. Focusing with plane time-reversal mirrors: An efficient alternative to closed cavities, *The Journal of the Acoustical Society of America*, **94**(4), 2373–2386.

Chadwick, R. & Pharaoh, T., 1998. The seismic reflection Moho beneath the United Kingdom and adjacent areas, *Tectonophysics*, **299**(4), 255–279.

Cho, K. H., Herrmann, R. B., Ammon, C. J., & Lee, K., 2007. Imaging the Upper Crust of the Korean Peninsula by Surface-Wave Tomography, *Bulletin of the Seismological Society of America*, **97**(1B), 198–207.

Claerbout, J. F., 1968. Synthesis of a layered medium from its acoustic transmission response, *Geophysics*, **33**(2), 264–269.

Claerbout, J. F., 1976. *Fundamentals of Geophysical Data Processing*, Blackwell Scientific Publications.

Cole, S., 1995. *Passive seismic and drill-bit experiments using 2-D arrays*, Ph.D. Thesis, Stanford University.

Curtis, A., 2009. Source-receiver seismic interferometry, *SEG Technical Program Expanded Abstracts 2009*, pp. 3655–3659.

Curtis, A. & Halliday, D., 2010a. Source-receiver wave field interferometry, *Physical Review E*, **81**(4), 046601.

Curtis, A. & Halliday, D., 2010b. Directional balancing for seismic and general wavefield interferometry, *Geophysics*, **75**(1), SA1–SA14.

Curtis, A. & Woodhouse, J. H., 1997. Crust and upper mantle shear velocity structure beneath the Tibetan plateau and surrounding regions from interevent surface wave phase velocity inversion, *Journal of Geophysical Research*, **102**(B6), 11789–11813.

Curtis, A., Gerstoft, P., Sato, H., Snieder, R., & Wapenaar, K., 2006. Seismic interferometry—turning noise into signal, *The Leading Edge*, **25**(9), 1082–1092.

Curtis, A., Nicolson, H., Halliday, D., Trampert, J., & Baptie, B., 2009. Virtual seismometers in the subsurface of the Earth from seismic interferometry, *Nature Geoscience*, **2**(10), 700–704.

Curtis, A., Behr, Y., Entwistle, E., Galetti, E., Townend, J., & Bannister, S., 2012. The benefit of hindsight in observational science: Retrospective seismological observations, *Earth and Planetary Science Letters*, **345–348**, 212–220.

D'Ariano, G., Paris, M., Sacchi, M., & Hawkes, P., 2003. Quantum tomography, *Advances in Imaging and Electron Physics*, **128**, 205–308.

de Hoop, A. T., 1988. Time-domain reciprocity theorems for acoustic wave fields in fluids with relaxation, *The Journal of the Acoustical Society of America*, **84**(5), 1877–1882.

de Ridder, S. & Dellinger, J., 2011. Ambient seismic noise eikonal tomography for near-surface imaging at Valhall, *The Leading Edge*, **30**(5), 506–512.

de Ridder, S. A. L., Biondi, B. L., & Clapp, R. G., 2014. Time-lapse seismic noise correlation tomography at Valhall, *Geophysical Research Letters*, **41**(17), 6116–6122.

Dentith, M. C. & Hall, J., 1989. MAVIS – an upper crustal seismic refraction experiment in the Midland Valley of Scotland, *Geophysical Journal International*, **99**(3), 627–643.

Dentith, M. C. & Hall, J., 1990. MAVIS: Geophysical constraints on the structure of the Carboniferous basin of West Lothian, Scotland, *Earth and Environmental Science Transactions of the Royal Society of Edinburgh*, **81**, 117–126.

Derode, A., Larose, E., Campillo, M., & Fink, M., 2003a. How to estimate the Green's function of a heterogeneous medium between two passive sensors? Application to acoustic waves, *Applied Physics Letters*, **83**(15), 3054–3056.

Derode, A., Larose, E., Tanter, M., de Rosny, J., Tourin, A., Campillo, M., & Fink, M., 2003b. Recovering the Green's function from field-field correlations in an open scattering medium (L), *The Journal of the Acoustical Society of America*, **113**(6), 2973–2976.

Dong, S., He, R., & Schuster, G. T., 2006. Interferometric predcition and least squares subtraction of surface waves, *SEG Technical Program Expanded Abstracts 2006*, pp. 2783–2786.

Douma, H. & Snieder, R., 2006. Correcting for bias due to noise in coda wave interferometry, *Geophysical Journal International*, **164**(1), 99–108.

Douma, H., Vasconcelos, I., & Snieder, R., 2011. The reciprocity theorem for the scattered field is the progenitor of the generalized optical theorem, *The Journal of the Acoustical Society of America*, **129**(5), 2765–2771.

Draganov, D., Wapenaar, K., & Thorbecke, J., 2006. Seismic interferometry: Reconstructing the Earth's reflection response, *Geophysics*, **71**(4), SI61–SI70.

Draganov, D., Wapenaar, K., Mulder, W., Singer, J., & Verdel, A., 2007. Retrieval of reflections from seismic background-noise measurements, *Geophysical Research Letters*, **34**(4), L04305, 0094–8276.

Draganov, D., Campman, X., Thorbecke, J., Verdel, A., & Wapenaar, K., 2009. Reflection images from ambient seismic noise, *Geophysics*, **74**(5), A63–A67.

Duguid, C., 2010. *Applied Seismic Interferometry: Directional Balancing Investigation and a Source-Receiver Data Example*, M.Sc. Thesis, University of Edinburgh.

Duguid, C., Halliday, D., & Curtis, A., 2011. Source-Receiver Interferometry for Seismic Wavefield Construction and Ground Roll Removal, *The Leading Edge*, **30**(8), 838–843.

Duvall, T. L., Jeffferies, S. M., Harvey, J. W., & Pomerantz, M. A., 1993. Time-distance helioseismology, *Nature*, **362**(6419), 430–432.

Entwistle, E., Curtis, A., Galetti, E., Baptie, B., & Meles, G. A., 2015. Constructing new seismograms from old earthquakes: Retrospective seismology at multiple length scales, *Journal of Geophysical Research*, **120**(4), 2466–2490.

Fink, M., 2006. Time-reversal acoustics in complex environments, *Geophysics*, **71**(4), SI151–SI164.

Fink, M. & Prada, C., 2001. Acoustic time-reversal mirrors, *Inverse Problems*, **17**(1), R1.

Fokkema, J. & van den Berg, P., 1993. *Seismic applications of acoustic reciprocity*, Elsevier Science Publishing Company, Inc.

Foldy, L. L., 1945. The Multiple Scattering of Waves. I. General Theory of Isotropic Scattering by Randomly Distributed Scatterers, *Physical Review*, **67**(3–4), 107–119.

Forghani, F. & Snieder, R., 2010. Underestimation of body waves and feasibility of surface-wave reconstruction by seismic interferometry, *The Leading Edge*, **29**(7), 790–794.

Fridman, K., Mader, A., Zwerger, M., Elia, N., & Medalia, O., 2012. Advances in tomography: probing the molecular architecture of cells, *Nature Reviews Molecular Cell Biology*, **13**(11), 736–742.

Galetti, E. & Curtis, A., 2012. Generalised receiver functions and seismic interferometry, *Tectonophysics*, **532–535**, 1–26.

Galetti, E., Curtis, A., Baptie, B., Jenkins, D., & Nicolson, H., 2013a. Novel Uncertainty Structures Observed in UK Ambient Noise Tomography, *AGU Fall Meeting, San Francisco*.

Galetti, E., Curtis, A., & Halliday, D., 2013b. An exact wavefield modelling method for data processing, imaging, and interferometry applications in scattering acoustic media, *SEG Technical Program Expanded Abstracts 2013*, pp. 3330–3334.

Galetti, E., Halliday, D., & Curtis, A., 2013c. A simple and exact acoustic wavefield modeling code for data processing, imaging, and interferometry applications, *Geophysics*, **78**(6), F17–F27.

Galetti, E., Halliday, D., & Curtis, A., 2013d. An Exact Modelling Method for Data Processing, Imaging and Interferometry Applications in Scattering Acoustic Media, *EAGE, Extended Abstracts, 75th EAGE Conference & Exhibition*.

Galetti, E., Jenkins, D., Nicolson, H., Curtis, A., & Baptie, B., 2013e. Transdimensional Love-wave tomography of the British Isles, *EGU General Assembly, Vienna*.

Galetti, E., Curtis, A., & Baptie, B., 2015a. Transdimensional Love-wave tomography and depth inversion of the British Isles from ambient-noise interferometry, in preparation.

Galetti, E., Curtis, A., Meles, G. A., & Baptie, B., 2015b. Uncertainty loops in travel-time tomography from nonlinear wave physics, *Physical Review Letters*, **114**(14), 148501.

Gallagher, K., Charvin, K., Nielsen, S., Sambridge, M., & Stephenson, J., 2009. Markov chain Monte Carlo (MCMC) sampling methods to determine optimal models, model resolution and model choice for Earth Science problems, *Marine and Petroleum Geology*, **26**(4), 525–535.

Gallagher, K., Bodin, T., Sambridge, M., Weiss, D., Kylander, M., & Large, D., 2011. Inference of abrupt changes in noisy geochemical records using transdimensional changepoint models, *Earth and Planetary Science Letters*, **311**, 182–194.

Gerstoft, P., Sabra, K. G., Roux, P., Kuperman, W. A., & Fehler, M. C., 2006. Green's functions extraction and surface-wave tomography from microseisms in southern California, *Geophysics*, **71**(4), SI23–SI31.

Grechka, V. & Dewangan, P., 2003. Generation and processing of pseudo-shear-wave data: Theory and case study, *Geophysics*, **68**(6), 1807–1816.

Grechka, V. & Tsvankin, I., 2002. PP + PS = SS, *Geophysics*, **67**(6), 1961–1971.

Grêt, A., Snieder, R., Aster, R. C., & Kyle, P. R., 2005. Monitoring rapid temporal change in a volcano with coda wave interferometry, *Geophysical Research Letters*, **32**(6), L06304.

Grêt, A., Snieder, R., & Özbay, U., 2006a. Monitoring in situ stress changes in a mining environment with coda wave interferometry, *Geophysical Journal International*, **167**(2), 504–508.

Grêt, A., Snieder, R., & Scales, J., 2006b. Time-lapse monitoring of rock properties with coda wave interferometry, *Journal of Geophysical Research*, **111**(B3), B03305.

Groenenboom, J. & Snieder, R., 1995. Attenuation, dispersion, and anisotropy by multiple scattering of transmitted waves through distributions of scatterers, *The Journal of the Acoustical Society of America*, **98**(6), 3482–3492.

Gudmundsson, O., Khan, A., & Voss, P., 2007. Rayleigh-wave group-velocity of the Icelandic crust from correlation of ambient seismic noise, *Geophysical Research Letters*, **34**(14), L14314.

Gurrola, H., Minster, J. B., & Owens, T., 1994. The Use of Velocity Spectrum For Stacking Receiver Functions and Imaging Upper Mantle Discontinuities, *Geophysical Journal International*, **117**(2), 427–440.

Halliday, D., 2010. Adaptive model-driven interferometry for ground-roll attenuation, *SEG Technical Program Expanded Abstracts 2010*, pp. 3550–3554.

Halliday, D. & Curtis, A., 2008. Seismic interferometry, surface waves and source distribution, *Geophysical Journal International*, **175**(3), 1067–1087.

Halliday, D. & Curtis, A., 2009a. Seismic interferometry of scattered surface waves in attenuative media, *Geophysical Journal International*, **178**(1), 419–446.

Halliday, D. & Curtis, A., 2009b. Generalized optical theorem for surface waves and layered media, *Physical Review E*, **79**(5), 056603.

Halliday, D. & Curtis, A., 2010. An interferometric theory of source-receiver scattering and imaging, *Geophysics*, **75**(6), SA95–SA103.

Halliday, D., Curtis, A., & Kragh, E., 2008. Seismic surface waves in a suburban environment: Active and passive interferometric methods, *The Leading Edge*, **27**(2), 210–218.

Halliday, D., Curtis, A., & Wapenaar, K., 2010a. Generalized PP + PS = SS from seismic interferometry, *SEG Technical Program Expanded Abstracts 2010*, pp. 4029–4033.

Halliday, D., Curtis, A., & Wapenaar, K., 2012. Generalized PP+PS=SS from seismic interferometry, *Geophysical Journal International*, **189**(2), 1015–1024.

Halliday, D. F., Curtis, A., Robertsson, J. O. A., & van Manen, D.-J., 2007. Interferometric surface-wave isolation and removal, *Geophysics*, **72**(5), A69–A73.

Halliday, D. F., Curtis, A., Vermeer, P., Strobbia, C., Glushchenko, A., van Manen, D., & Robertsson, J., 2010b. Interferometric ground-roll removal: Attenuation of scattered surface waves in single-sensor data, *Geophysics*, **75**(2), SA15–SA25.

Haney, M. M. & Douma, H., 2010. Imaging lateral heterogeneity at Coronation Field with surface waves, *SEG Technical Program Expanded Abstracts 2010*, pp. 1851–1855.

Haney, M. M. & Douma, H., 2012. Rayleigh-wave tomography at Coronation Field, Canada: The topography effect, *The Leading Edge*, **31**(1), 54–61.

Harmon, N., Rychert, C., & Gerstoft, P., 2010. Distribution of noise sources for seismic interferometry, *Geophysical Journal International*, **183**(3), 1470–1484.

Heit, B., Yuan, X., Bianchi, M., Sodoudi, F., & Kind, R., 2008. Crustal thickness estimation beneath the southern central Andes at 30°S and 36°S from *S* wave receiver function analysis, *Geophysical Journal International*, **174**(1), 249–254.

Herman, G. T., 2009. *Fundamentals of Computerized Tomography: Image Reconstruction from Projections, Second Edition*, Springer.

Herrin, E. & Goforth, T., 1977. Phase-matched filters: Application to the study of Rayleigh waves, *Bulletin of the Seismological Society of America*, **67**(5), 1259–1275.

Herrmann, R. B. & Ammon, C. J., 2002. *Computer Programs in Seismology - Surface Waves, Receiver Functions and Crustal Structure*.

Hong, T.-K. & Menke, W., 2006. Tomographic investigation of the wear along the San Jacinto fault, southern California, *Physics of The Earth and Planetary Interiors*, **155**(3–4), 236–248.

Jay, J., Pritchard, M., West, M., Christensen, D., Haney, M., Minaya, E., Sunagua, M., McNutt, S., & Zabala, M., 2012. Shallow seismicity, triggered seismicity, and ambient noise tomography at the long-dormant Uturuncu Volcano, Bolivia, *Bulletin of Volcanology*, **74**, 817–837.

Kevles, B. H., 1996. *Naked to the Bone: Medical Imaging in the Twentieth Century*, Rutgers University Press.

Kim, C., Favazza, C., & Wang, L. H. V., 2010. In Vivo Photoacoustic Tomography of Chemicals: High-Resolution Functional and Molecular Optical Imaging at New Depths, *Chemical Reviews*, **110**(5), 2756–2782.

Kind, R. & Vinnik, L., 1988. The upper mantle discontinuities underneath the GRF array from P-to-S converted phases, *Journal of Geophysics*, **62**(3), 138–147.

King, S. & Curtis, A., 2012. Suppressing nonphysical reflections in Green's function estimates using source-receiver interferometry, *Geophysics*, **77**(1), Q15–Q25.

King, S., Curtis, A., & Poole, T. L., 2011. Interferometric velocity analysis using physical and nonphysical energy, *Geophysics*, **76**(1), SA35–SA49.

Kraeva, N., Pinsky, V., & Hofstetter, A., 2009. Seasonal variations of cross correlations of seismic noise in Israel, *Journal of Seismology*, **13**(1), 73–87.

Kumar, P., Kind, R., & Yuan, X., 2010. Receiver function summation without deconvolution, *Geophysical Journal International*, **180**(3), 1223–1230.

Kurita, T., 1973. Regional variations in the structure of the crust in the central United States from P-wave spectra, *Bulletin of the Seismological Society of America*, **63**(5), 1663–1687.

Kwon, O. H. & Zewail, A. H., 2010. 4D Electron Tomography, *Science*, **328**(5986), 1668–1673.

Lagendijk, A. & van Tiggelen, B. A., 1996. Resonant multiple scattering of light, *Physics Reports*, **270**(3), 143–215.

Langston, C. A., 1979. Structure Under Mount Rainier, Washington, Inferred From Teleseismic Body Waves, *Journal of Geophysical Research*, **84**(B9), 4749–4762.

Larose, E., Margerin, L., van Tiggelen, B. A., & Campillo, M., 2004. Weak Localization of Seismic Waves, *Physical Review Letters*, **93**, 048501.

Larose, E., Derode, A., Clorennec, D., Margerin, L., & Campillo, M., 2005. Passive retrieval of Rayleigh waves in disordered elastic media, *Physical Review E*, **72**(4), 046607.

Li, H., Su, W., Wang, C.-Y., & Huang, Z., 2009. Ambient noise Rayleigh wave tomography in western Sichuan and eastern Tibet, *Earth and Planetary Science Letters*, **282**(1–4), 201–211.

Li, H., Bernardi, F., & Michelini, A., 2010a. Love wave tomography in Italy from seismic ambient noise, *Earthquake Science*, **23**(5), 487–495.

Li, H., Su, W., Wang, C.-Y., Huang, Z., & Lv, Z., 2010b. Ambient noise Love wave tomography in the eastern margin of the Tibetan plateau, *Tectonophysics*, **491**(1–4), 194–204.

Liang, C. & Langston, C. A., 2008. Ambient seismic noise tomography and structure of eastern North America, *Journal of Geophysical Research*, **113**(B3), B03309.

Lin, F.-C., Ritzwoller, M. H., Townend, J., Bannister, S., & Savage, M. K., 2007. Ambient noise Rayleigh wave tomography of New Zealand, *Geophysical Journal International*, **170**(2), 649–666.

Lin, F.-C., Moschetti, M. P., & Ritzwoller, M. H., 2008. Surface wave tomography of the western United States from ambient seismic noise: Rayleigh and Love wave phase velocity maps, *Geophysical Journal International*, **173**(1), 281–298.

Lobkis, O. I. & Weaver, R. L., 2001. On the emergence of the Green's function in the correlations of a diffuse field, *The Journal of the Acoustical Society of America*, **110**(6), 3011–3017.

Löer, K., Meles, G. A., & Curtis, A., 2013. Incomplete boundaries and partial equations in source-receiver interferometry (SRI), *SEG Technical Program Expanded Abstracts 2013*, pp. 4579–4583.

Löer, K., Meles, G. A., Curtis, A., & Vasconcelos, I., 2014. Diffracted and pseudo-physical waves from spatially limited arrays using source-receiver interferometry (SRI), *Geophysical Journal International*, **196**(2), 1043–1059.

Löer, K., Meles, G. A., & Curtis, A., 2015. Automatic identification of multiply diffracted waves and their ordered scattering paths, *The Journal of the Acoustical Society of America*, in press.

Lu, R., Willis, M., Campman, X., Ajo-Franklin, J., & Toksoz, M. N., 2008. Redatuming through a salt canopy and target-oriented salt-flank imaging, *Geophysics*, **73**(3), S63–S71.

Luckett, R. & Baptie, B., 2015. Local earthquake tomography of Scotland, *Geophysical Journal International*, **200**(3), 1538–1554.

Maret, G., 1995. in *Mesoscopic Quantum Physics*, Les Houches Summer School, Elsevier Science, Amsterdam.

Masterlark, T., Haney, M., Dickinson, H., Fournier, T., & Searcy, C., 2010. Rheologic and structural controls on the deformation of Okmok volcano, Alaska: FEMs, InSAR, and ambient noise tomography, *Journal of Geophysical Research*, **115**(B2), B02409.

MathWorks, 2012. Systems of Linear Equations, http://www.mathworks.co.uk/help/matlab/math/systems-of-linear-equations.html, Online; last accessed: 08 February 2013.

Maurer, H., Curtis, A., & Boerner, D. E., 2010. Recent advances in optimized geophysical survey design, *Geophysics*, **75**(5), 75A177–75A194.

Mehta, K., Bakulin, A., Sheiman, J., Calvert, R., & Snieder, R., 2007. Improving the virtual source method by wavefield separation, *Geophysics*, **72**(4), V79–V86.

Mehta, K., Sheiman, J. L., Snieder, R., & Calvert, R., 2008. Strengthening the virtual-source method for time-lapse monitoring, *Geophysics*, **73**(3), S73–S80.

Meles, G. & Curtis, A., 2013a. Finger-printing Diffractors Encountered by Multiply-scattered Waves, *EAGE, Extended Abstracts, 75th EAGE Conference & Exhibition*.

Meles, G. & Curtis, A., 2013b. Discriminating Physical and Non-physical Energy in Wavefield Interferometry, *EAGE, Extended Abstracts, 75th EAGE Conference & Exhibition*.

Meles, G., Löer, K., & Curtis, A., 2013. Why scattered wave source-receiver interferometry (SRI) may out-perform inter-receiver interferometry, *EAGE, Extended Abstracts, 75th EAGE Conference & Exhibition*.

Meles, G. A. & Curtis, A., 2013c. Physical and non-physical energy in scattered wave source-receiver interferometry, *The Journal of the Acoustical Society of America*, **133**(6), 3790–3801.

Meles, G. A. & Curtis, A., 2014a. Discriminating physical and non-physical diffracted energy in source-receiver interferometry, *Geophysical Journal International*, **197**(3), 1642–1659.

Meles, G. A. & Curtis, A., 2014b. Fingerprinting ordered diffractions in multiply diffracted waves, *Geophysical Journal International*, **198**(3), 1701–1713.

Midgley, P. & Dunin-Borkowski, R., 2009. Electron tomography and holography in materials science, *Nature Materials*, **8**(4), 271–280.

Mikesell, D., van Wijk, K., Calvert, A., & Haney, M., 2009. The virtual refraction: Useful spurious energy in seismic interferometry, *Geophysics*, **74**(3), A13–A17.

Milne, J. L. S. & Subramaniam, S., 2009. Cryo-electron tomography of bacteria: progress, challenges and future prospects, *Nature Reviews Microbiology*, **7**(9), 666–675.

Minato, S., Matsuoka, T., Tsuji, T., Draganov, D., Hunziker, J., & Wapenaar, K., 2011. Seismic interferometry using multidimensional deconvolution and crosscorrelation for crosswell seismic reflection data without borehole sources, *Geophysics*, **76**(1), SA19–SA34.

Mishchenko, M. I., 2006. Far-field approximation in electromagnetic scattering, *Journal of Quantitative Spectroscopy and Radiative Transfer*, **100**(1–3), 268–276.

Miyazawa, M., Snieder, R., & Venkataraman, A., 2008. Application of seismic interferometry to extract P- and S-wave propagation and observation of shear-wave splitting from noise data at Cold Lake, Alberta, Canada, *Geophysics*, **73**(4), D35–D40.

Moldoveanu, N., Combee, L., Egan, M., Hampson, G., Sydora, L., & Abriel, W., 2007. Over/under towed-streamer acquisition, *The Leading Edge*, **26**(1), 41–58.

Mordret, A., Landès, M., Shapiro, N. M., Singh, S. C., Roux, P., & Barkved, O. I., 2013a. Near-surface study at the Valhall oil field from ambient noise surface wave tomography, *Geophysical Journal International*, pp. 1–17.

Mordret, A., Shapiro, N. M., Singh, S. S., Roux, P., & Barkved, O. I., 2013b. Helmholtz tomography of ambient noise surface wave data to estimate Scholte wave phase velocity at Valhall Life of the Field, *Geophysics*, **78**(2), WA99–WA109.

Moschetti, M. P., Ritzwoller, M. H., & Shapiro, N. M., 2007. Surface wave tomography of the western United States from ambient seismic noise: Rayleigh wave group velocity maps, *Geochemistry, Geophysics, Geosystems*, **8**(8), Q08010.

Musson, R. M. W., 1996. The seismicity of the British Isles, *Annals of Geophysics*, **39**(3).

Nagaoka, Y., Nishida, K., Aoki, Y., & Takeo, M., 2010. Temporal change of phase velocity beneath Mt. Asama, Japan, inferred from coda wave interferometry, *Geophysical Research Letters*, **37**(22), L22311, 0094–8276.

Nagaoka, Y., Nishida, K., Aoki, Y., Takeo, M., & Ohminato, T., 2012. Seismic imaging of magma chamber beneath an active volcano, *Earth and Planetary Science Letters*, **333–334**(0), 1–8.

Neidell, N. S. & Taner, M. T., 1971. Semblance and other coherency measures for multichannel data, *Geophysics*, **36**(3), 482–497, 10.1190/1.1440186.

Nicolson, H., 2011. *Exploring the Earth's Subsurface with Virtual Seismic Sources and Receivers*, Ph.D. Thesis, University of Edinburgh.

Nicolson, H., Curtis, A., Baptie, B., & Galetti, E., 2012. Seismic interferometry and ambient noise tomography in the British Isles, *Proceedings of the Geologists' Association*, **123**(1), 74–86.

Nicolson, H., Curtis, A., & Baptie, B., 2014. Rayleigh Wave Tomography of the British Isles from Ambient Seismic Noise, *Geophysical Journal International*, **198**(2), 637–655.

Nolet, G., 2008. *A Breviary of Seismic Tomography: Imaging the Interior of the Earth and Sun*, Cambridge University Press.

Ohmi, S., Hirahara, K., Wada, H., & Ito, K., 2008. Temporal variations of crustal structure in the source region of the 2007 Noto Hanto Earthquake, central Japan, with passive image interferometry, *Earth Planets Space*, **60**, 1069–1074.

Oristaglio, M. L., 1989. An inverse scattering formula that uses all the data, *Inverse Problems*, **5**, 1097–1105.

Pandolfi, D., Bean, C. J., & Saccorotti, G., 2006. Coda wave interferometric detection of seismic velocity changes associated with the 1999 M = 3.6 event at Mt. Vesuvius, *Geophysical Research Letters*, **33**(6), L06306.

eds Paris, M. & Řeháček, J., 2004. *Quantum state estimation*, vol. 649 of **Lecture Notes in Physics**, Springer Berlin Heidelberg.

Phinney, R. A., 1964. Structure of the Earth's Crust from Spectral Behavior of Long-Period Body Waves, *Journal of Geophysical Research*, **69**(14), 2997–3017.

Picozzi, M., Parolai, S., Bindi, D., & Strollo, A., 2009. Characterization of shallow geology by high-frequency seismic noise tomography, *Geophysical Journal International*, **176**(1), 164–174.

Pilz, M., Parolai, S., Picozzi, M., & Bindi, D., 2012. Three-dimensional shear wave velocity imaging by ambient seismic noise tomography, *Geophysical Journal International*, **189**(1), 501–512.

Poliannikov, O. V., 2011. Retrieving reflections by source-receiver wavefield interferometry, *Geophysics*, **76**(1), SA1–SA8.

Ravasi, M. & Curtis, A., 2013. Nonlinear scattering based imaging in elastic media: Theory, theorems, and imaging conditions, *Geophysics*, **78**(3), S137–S155.

Rawlinson, N. & Sambridge, M., 2003. Seismic Traveltime Tomography of the Crust and Lithosphere, vol. 46 of **Advances in Geophysics**, pp. 81–198, Elsevier.

Rawlinson, N. & Sambridge, M., 2004. Wave front evolution in strongly heterogeneous layered media using the fast marching method, *Geophysical Journal International*, **156**(3), 631–647.

Rawlinson, N. & Sambridge, M., 2005. The fast marching method: an effective tool for tomographic imaging and tracking multiple phases in complex layered media, *Exploration Geophysics*, **36**(4), 341–350.

Rawlinson, N., Sambridge, M., & Saygin, E., 2008. A dynamic objective function technique for generating multiple solution models in seismic tomography, *Geophysical Journal International*, **174**(1), 295–308.

Rawlinson, N., Pozgay, S., & Fishwick, S., 2010. Seismic tomography: A window into deep Earth, *Physics of the Earth and Planetary Interiors*, **178**(3–4), 101–135.

Ray, A., Key, K., Bodin, T., Myer, D., & Constable, S., 2014. Bayesian inversion of marine CSEM data from the Scarborough gas field using a transdimensional 2-D parametrization, *Geophysical Journal International*, **199**(3), 1847–1860.

Rayleigh, J., 1878. *The Theory of Sound*, vol. 2, Dover Publications Inc., New York, (reprint 1945) edn.

Rickett, J. & Claerbout, J., 1999. Acoustic daylight imaging via spectral factorization; helioseismology and reservoir monitoring, *The Leading Edge*, **18**(8), 957–960.

Rodberg, L. S. & Thaler, R. M., 1967. *Introduction to the Quantum Theory of Scattering*, Academic Press.

Romanowicz, B. A., 1982. Constraints on the structure of the Tibet Plateau from pure path phase velocities of Love and Rayleigh waves, *Journal of Geophysical Research*, **87**(B8), 6865–6883.

Roux, P., 2009. Passive seismic imaging with directive ambient noise: application to surface waves and the San Andreas Fault in Parkfield, CA, *Geophysical Journal International*, **179**(1), 367–373.

Ruigrok, E., Campman, X., Draganov, D., & Wapenaar, K., 2010. High-resolution lithospheric imaging with seismic interferometry, *Geophysical Journal International*, **183**(1), 339–357.

Ryberg, T. & Weber, M., 2000. Receiver function arrays: a reflection seismic approach, *Geophysical Journal International*, **141**(1), 1–11.

Sabra, K. G., Gerstoft, P., Roux, P., Kuperman, W. A., & Fehler, M. C., 2005. Surface wave tomography from microseisms in Southern California, *Geophysical Research Letters*, **32**(14), L14311.

Saito, M., 1988. DISPER80: A Subroutine Package for the Calculations of Seismic Normal-Mode Solutions, in *Seismological Algorithms – Computational Mehtods and Computer Programs*, chap. 4.1, pp. 293–319, ed. Doornbos, D. J., Academic Press.

Sambridge, M., Beghein, C., Simons, F., & Snieder, R., 2006. How do we understand and visualize uncertainty?, *The Leading Edge*, **25**(5), 542–546.

Sava, P. & Vasconcelos, I., 2009. Efficient computation of extended images by wavefield-based migration, *SEG Technical Program Expanded Abstracts 2009*, pp. 2824–2828.

Saygin, E. & Kennett, B. L. N., 2010. Ambient seismic noise tomography of Australian continent, *Tectonophysics*, **481**(1–4), 116–125.

Schuster, G. T., 2001. Theory of Daylight/Interferometric Imaging – Tutorial, *EAGE, Extended Abstracts, 63rd EAGE Conference & Exhibition*, **A32**.

Schuster, G. T., 2009. *Seismic Interferometry*, Cambridge University Press.

Schuster, G. T., Yu, J., Sheng, J., & Rickett, J., 2004. Interferometric/daylight seismic imaging, *Geophysical Journal International*, **157**(2), 838–852.

Sens-Schönfelder, C. & Wegler, U., 2006. Passive image interferometry and seasonal variations of seismic velocities at Merapi Volcano, Indonesia, *Geophysical Research Letters*, **33**(21), L21302.

Sethian, J. A., 1996. A fast marching level set method for monotonically advancing fronts, *Proceedings of the National Academy of Sciences*, **93**(4), 1591–1595.

Sethian, J. A. & Popovici, A. M., 1999. 3-D traveltime computation using the fast marching method, *Geophysics*, **64**(2), 516–523.

Shapiro, N. M. & Campillo, M., 2004. Emergence of broadband Rayleigh waves from correlations of the ambient seismic noise, *Geophysical Research Letters*, **31**(7), L07614.

Shapiro, N. M., Campillo, M., Stehly, L., & Ritzwoller, M. H., 2005. High-Resolution Surface-Wave Tomography from Ambient Seismic Noise, *Science*, **307**(5715), 1615–1618.

Slob, E. & Wapenaar, K., 2007. Electromagnetic Green's functions retrieval by cross-correlation and cross-convolution in media with losses, *Geophysical Research Letters*, **34**(5), L05307.

Slob, E., Draganov, D., & Wapenaar, K., 2007. Interferometric electromagnetic Green's functions representations using propagation invariants, *Geophysical Journal International*, **169**(1), 60–80.

Snieder, R., 1988a. Large-Scale Waveform Inversions of Surface Waves for Lateral Heterogeneity 1. Theory and Numerical Examples, *Journal of Geophysical Research*, **93**(B10), 12055–12065.

Snieder, R., 1988b. Large-Scale Waveform Inversions of Surface Waves for Lateral Heterogeneity 2. Application to Surface Waves in Europe and the Mediterranean, *Journal of Geophysical Research*, **93**, 12067–12080.

Snieder, R., 1999. Imaging and averaging in complex media, in *Diffuse waves in complex media*, vol. 531 of **NATO Science Series - Series C: Mathematical and Physical Sciences**, pp. 405–454, ed. Fouque, J.-P., Kluwer Academic Publishers, Dordrecht, The Netherlands.

Snieder, R., 2003. Coda wave interferometry, in *McGraw-Hill 2004 Yearbook of Science & Technology*, ed. Hill, M., McGraw-Hill, New York.

Snieder, R., 2004. Extracting the Green's function from the correlation of coda waves: A derivation based on stationary phase, *Physical Review E*, **69**(4), 046610.

Snieder, R., 2006. The Theory of Coda Wave Interferometry, *Pure and Applied Geophysics*, **163**(2), 455–473.

Snieder, R., 2007. Extracting the Green's function of attenuating heterogeneous acoustic media from uncorrelated waves, *Journal of the Acoustical Society of America*, **121**(5), 2637–2643.

Snieder, R., 2009. *A Guided Tour of Mathematical Methods For the Physical Sciences*, Cambridge University Press, 2nd edn.

Snieder, R. & Hagerty, M., 2004. Monitoring change in volcanic interiors using coda wave interferometry: Application to Arenal Volcano, Costa Rica, *Geophysical Research Letters*, **31**(9), L09608.

Snieder, R., Grêt, A., Douma, H., & Scales, J., 2002. Coda Wave Interferometry for Estimating Nonlinear Behavior in Seismic Velocity, *Science*, **295**(5563), 2253–2255.

Snieder, R., Wapenaar, K., & Larner, K., 2006. Spurious multiples in seismic interferometry of primaries, *Geophysics*, **71**(4), SI111–SI124.

Snieder, R., Wapenaar, K., & Wegler, U., 2007. Unified Green's function retrieval by cross-correlation; connection with energy principles, *Physical Review E*, **75**(3), 036103.

Snieder, R., van Wijk, K., Haney, M., & Calvert, R., 2008. Cancellation of spurious arrivals in Green's function extraction and the generalized optical theorem, *Physical Review E*, **78**, 036606.

Snieder, R., Miyazawa, M., Slob, E., Vasconcelos, I., & Wapenaar, K., 2009. A Comparison of Strategies for Seismic Interferometry, *Surveys in Geophysics*, **30**(4), 503–523, 0169–3298.

Song, W. Y., Chiu, B., Bauman, G. S., Lock, M., Rodrigues, G., Ash, R., Lewis, C., Fenster, A., Battista, J. J., & Van Dyk, J., 2006. Prostate contouring uncertainty in megavoltage computed tomography images acquired with a helical tomotherapy unit during image-guided radiation therapy, *International Journal of Radiation Oncology Biology Physics*, **65**(2), 595–607.

Spindel, R. C. & Worcester, P. F., 1990. Ocean Acoustic Tomography, *Scientific American*, **263**(4), 94–99.

Stark, P. B., 2008. Generalizing resolution, *Inverse Problems*, **24**(3), 034014.

Stehly, L., Campillo, M., Froment, B., & Weaver, R. L., 2008. Reconstructing Green's function by correlation of the coda of the correlation (C3) of ambient seismic noise, *Journal of Geophysical Research*, **113**(B11), B11306, 0148–0227.

Stehly, L., Fry, B., Campillo, M., Shapiro, N. M., Guilbert, J., Boschi, L., & Giardini, D., 2009. Tomography of the Alpine region from observations of seismic ambient noise, *Geophysical Journal International*, **178**(1), 338–350.

Stolt, R. & Benson, A., 1986. Seismic migration: Theory and practice, in *Handbook of Geophysical Exploration*, vol. 5, Geophysical Press.

Taira, T. a., Silver, P. G., Niu, F., & Nadeau, R. M., 2009. Remote triggering of fault-strength changes on the San Andreas fault at Parkfield, *Nature*, **461**(7264), 636–639.

Tanimoto, T. & Lay, T., 2000. Mantle dynamics and seismic tomography, *Proceedings of the National Academy of Sciences of the United States of America*, **97**(23), 12409–12410.

Thorbecke, J. & Wapenaar, K., 2007. On the relation between seismic interferometry and the migration resolution function, *Geophysics*, **72**(6), T61–T66, 10.1190/1.2785850.

Thorbecke, J. W. & Draganov, D., 2011. Finite-difference modeling experiments for seismic interferometry, *Geophysics*, **76**(6), H1–H18.

Tomlinson, J. P., Denton, P., Maguire, P. K. H., & Booth, D. C., 2006. Analysis of the crustal velocity structure of the British Isles using teleseismic receiver functions, *Geophysical Journal International*, **167**(1), 223–237.

Tonegawa, T. & Nishida, K., 2010. Inter-source body wave propagations derived from seismic interferometry, *Geophysical Journal International*, **183**(2), 861–868.

Tonegawa, T., Nishida, K., Watanabe, T., & Shiomi, K., 2009. Seismic interferometry of teleseicmic S-wave coda for retrieval of body waves: an application to the Philippine Sea slab underneath the Japanese Islands, *Geophysical Journal International*, **178**(3), 1574–1586.

van der Neut, J. & Bakulin, A., 2008. The effects of time-gating and radiation correction on virtual source data, *SEG Technical Program Expanded Abstracts 2008*, **27**(1), 2922–2926.

van Manen, D.-J., 2006. *Time reversal and Interferometry with applications to forward modeling of wave propagation and a chapter on receiver functions*, Ph.D. Thesis, University of Edinburgh.

van Manen, D.-J., Robertsson, J. O. A., Curtis, A., Ferber, R., & Paulssen, H., 2003. Shear wave statics using receiver functions, *Geophysical Journal International*, **153**(3), F1–F5.

van Manen, D.-J., Robertsson, J. O. A., & Curtis, A., 2005. Modeling of Wave Propagation in Inhomogeneous Media, *Physical Review Letters*, **94**(16), 164301.

van Manen, D.-J., Curtis, A., & Robertsson, J. O. A., 2006. Interferometric modeling of wave propagation in inhomogeneous elastic media using time reversal and reciprocity, *Geophysics*, **71**(4), SI47–SI60.

van Manen, D.-J., Robertsson, J. O. A., & Curtis, A., 2007. Exact wave field simulation for finite-volume scattering problems, *The Journal of the Acoustical Society of America*, **122**(4), EL115–EL121.

Vasco, D., Johnson, L., & Marques, O., 2003. Resolution, uncertainty, and whole Earth tomography, *Journal of Geophysical Research-Solid Earth*, **108**(B1), ESE 9–1–ESE 9–26.

Vasconcelos, I., 2008. Generalized representations of perturbed fields – applications in seismic interferometry and migration, *SEG Technical Program Expanded Abstracts 2008*, pp. 2927–2931.

Vasconcelos, I., 2013. Source-receiver, reverse-time imaging of dual-source, vector-acoustic seismic data, *Geophysics*, **78**(2), WA123–WA145.

Vasconcelos, I. & Snieder, R., 2008a. Interferometry by deconvolution: Part 1 – Theory for acoustic waves and numerical examples, *Geophysics*, **73**(3), S115–128.

Vasconcelos, I. & Snieder, R., 2008b. Interferometry by deconvolution: Part 2 – Theory for elastic waves and application to drill-bit seismic imaging, *Geophysics*, **73**(3), S129–141.

Vasconcelos, I., Sava, P., & Douma, H., 2009a. Wave-equation extended images via image-domain interferometry, *SEG Technical Program Expanded Abstracts 2009*, pp. 2839–2843.

Vasconcelos, I., Snieder, R., & Douma, H., 2009b. Representation theorems and Green's function retrieval for scattering in acoustic media, *Physical Review E*, **80**(3), 036605.

Vasconcelos, I., Sava, P., & Douma, H., 2010. Nonlinear extended images via image-domain interferometry, *Geophysics*, **75**(6), SA105–SA115.

Villaseñor, A., Yang, Y., Ritzwoller, M. H., & Gallart, J., 2007. Ambient noise surface wave tomography of the Iberian Peninsula: Implications for shallow seismic structure, *Geophysical Research Letters*, **34**(11), L11304.

Vinnik, L. P., 1977. Detection of waves converted from P to SV in the mantle, *Physics of The Earth and Planetary Interiors*, **15**(1), 39–45.

Wang, G., Yu, H. Y., & De Man, B., 2008. An outlook on x-ray CT research and development, *Medical Physics*, **35**(3), 1051–1064.

Wang, L. & Hu, S., 2012. Photoacoustic Tomography: In Vivo Imaging from Organelles to Organs, *Science*, **335**(6075), 1458–1462.

Wapenaar, C. P. A., 1993. Kirchhoff-Helmholtz downward extrapolation in a layered medium with curved interfaces, *Geophysical Journal International*, **115**(2), 445–455.

Wapenaar, K., 2003. Synthesis of an inhomogeneous medium from its acoustic transmission response, *Geophysics*, **68**(5), 1756–1759.

Wapenaar, K., 2004. Retrieving the Elastodynamic Green's Function of an Arbitrary Inhomogeneous Medium by Cross Correlation, *Physical Review Letters*, **93**(25), 254301.

Wapenaar, K., 2007. General representations for wavefield modeling and inversion in geophysics, *Geophysics*, **72**(5), SM5–SM17.

Wapenaar, K. & Douma, H., 2012. A unified optical theorem for scalar and vectorial wave fields, *The Journal of the Acoustical Society of America*, **131**(5), 3611–3626.

Wapenaar, K. & Fokkema, J., 2006. Green's function representations for seismic interferometry, *Geophysics*, **71**(4), SI33–SI46.

Wapenaar, K. & van der Neut, J., 2010. A representation for Green's function retrieval by multidimensional deconvolution, *The Journal of the Acoustical Society of America*, **128**(6), EL366–EL371.

Wapenaar, K., Fokkema, J., & Snieder, R., 2005. Retrieving the Green's function in an open system by cross correlation: A comparison of approaches (L), *The Journal of the Acoustical Society of America*, **118**(5), 2783–2786.

Wapenaar, K., Slob, E., & Snieder, R., 2006. Unified Green's Function Retrieval by Cross Correlation, *Physical Review Letters*, **97**, 234301.

Wapenaar, K., van der Neut, J., & Ruigrok, E., 2008. Passive seismic interferometry by multidimensional deconvolution, *Geophysics*, **73**(6), A51–A56.

Wapenaar, K., Draganov, D., Snieder, R., Campman, X., & Verdel, A., 2010a. Tutorial on seismic interferometry: Part 1 – Basic principles and applications, *Geophysics*, **75**(5), 75A195–75A209.

Wapenaar, K., Slob, E., & Snieder, R., 2010b. On seismic interferometry, the generalized optical theorem, and the scattering matrix of a point scatterer, *Geophysics*, **75**(3), SA27–SA35.

Wapenaar, K., Slob, E., Snieder, R., & Curtis, A., 2010c. Tutorial on seismic interferometry: Part 2 – Underlying theory and new advances, *Geophysics*, **75**(5), 75A211–75A227.

Wapenaar, K., Ruigrok, E., van der Neut, J., & Draganov, D., 2011. Improved surface-wave retrieval from ambient seismic noise by multi-dimensional deconvolution, *Geophysical Research Letters*, **38**(1), L01313.

Weaver, R. L. & Lobkis, O. I., 2001. Ultrasonics without a Source: Thermal Fluctuation Correlations at MHz Frequencies, *Physical Review Letters*, **87**(13), 134301.

Wegler, U. & Sens-Schönfelder, C., 2007. Fault zone monitoring with passive image interferometry, *Geophysical Journal International*, **168**(3), 1029–1033.

Wegler, U., Nakahara, H., Sens-Schönfelder, C., Korn, M., & Shiomi, K., 2009. Sudden drop of seismic velocity after the 2004 M_w 6.6 mid-Niigata earthquake, Japan, observed with Passive Image Interferometry, *Journal of Geophysical Research*, **114**(B6), B06305.

Woodcock, N. H. & Strachan, R., 2012. *Geological History of Britain and Ireland*, Wiley-Blackwell, 2nd edn.

Yang, Y., Ritzwoller, M. H., Levshin, A. L., & Shapiro, N. M., 2007. Ambient noise Rayleigh wave tomography across Europe, *Geophysical Journal International*, **168**(1), 259–274.

Yang, Y., Li, A., & Ritzwoller, M. H., 2008. Crustal and uppermost mantle structure in southern Africa revealed from ambient noise and teleseismic tomography, *Geophysical Journal International*, **174**(1), 235–248.

Yao, H., Van Der Hilst, R. D., & De Hoop, M. V., 2006. Surface-wave array tomography in SE Tibet from ambient seismic noise and two-station analysis – I. Phase velocity maps, *Geophysical Journal International*, **166**(2), 732–744.

Yao, H., Beghein, C., & Van Der Hilst, R. D., 2008. Surface wave array tomography in SE Tibet from ambient seismic noise and two-station analysis – II. Crustal and upper-mantle structure, *Geophysical Journal International*, **173**(1), 205–219.

Young, M., Rawlinson, N., & Bodin, T., 2013a. Transdimensional inversion of ambient seismic noise for 3D shear velocity structure of the Tasmanian crust, *Geophysics*, **78**(3), WB49–WB62.

Young, M. K., Tkalčić, H., Bodin, T., & Sambridge, M., 2013b. Global P wave tomography of Earth's lowermost mantle from partition modeling, *Journal of Geophysical Research: Solid Earth*, **118**(10), 5467–5486.

Zhan, Z., Ni, S., Helmberger, D. V., & Clayton, R. W., 2010. Retrieval of Moho-reflected shear wave arrivals from ambient seismic noise, *Geophysical Journal International*, **182**(1), 408–420.

Zheng, S., Sun, X., Song, X., Yang, Y., & Ritzwoller, M. H., 2008. Surface wave tomography of China from ambient seismic noise correlation, *Geochemistry, Geophysics, Geosystems*, **9**(5), Q05020.

Zheng, X., Jiao, W., Zhang, C., & Wang, L., 2010. Short-Period Rayleigh-Wave Group Velocity Tomography through Ambient Noise Cross-Correlation in Xinjiang, Northwest China, *Bulletin of the Seismological Society of America*, **100**(3), 1350–1355.

Zhou, R., Huang, L., Rutledge, J. T., Fehler, M., Daley, T. M., & Majer, E. L., 2010. Coda-wave interferometry analysis of time-lapse VSP data for monitoring geological carbon sequestration, *International Journal of Greenhouse Gas Control*, **4**(4), 679–686.

APPENDIX A

Acoustic Green's function retrieval from seismic interferometry

Mathematical proofs of the theory of seismic interferometry in the acoustic domain have so far been derived by Wapenaar & Fokkema (2006) and van Manen et al. (2005). However, due to a different approach in the derivation and to a difference in the source term used by the two authors, the resulting reciprocity theorems and interferometric formulae present some minor differences. The aim of this appendix is to highlight such differences and to present the full derivations by the two authors. Within the context of this thesis, this is particularly important with respect to the acoustic wavefield modelling code presented in Chapter 2, which allows different source types to be defined.

A.1 Acoustic reciprocity theorems

A.1.1 Derivation from the interaction quantity

The derivation of the acoustic reciprocity theorems by Wapenaar & Fokkema (2006) begins by considering the *interaction quantity* (de Hoop, 1988), relating acoustic pressure $p(\mathbf{x},\omega)$ and particle velocity $v_j(\mathbf{x},\omega)$ in an acoustic wavefield:

$$\partial_j \left\{ p_A(\mathbf{x},\omega) v_{j,B}(\mathbf{x},\omega) - v_{j,A}(\mathbf{x},\omega) p_B(\mathbf{x},\omega) \right\} , \tag{A.1}$$

where A and B indicate two independent acoustic states and ∂_j represents the partial derivative in the x_j-direction. The acoustic pressure and particle velocity in a lossless

arbitrary inhomogeneous medium obey the following equations in the frequency domain:

$$\textit{equation of motion: } \iota\omega\rho v_j(\mathbf{x},\omega) + \partial_j p(\mathbf{x},\omega) = f_j(\mathbf{x},\omega) \tag{A.2}$$

$$\textit{stress-strain relation: } \iota\omega\kappa p(\mathbf{x},\omega) + \partial_j v_j(\mathbf{x},\omega) = \hat{\hat{q}}(\mathbf{x},\omega) \tag{A.3}$$

where ρ is the medium mass density, κ is the medium compressibility, f_j is the external volume force density, and $\hat{\hat{q}}$ is an impulsive point-source of positive volume injection rate (the double hat symbol $\hat{}$ over q is used to identify this particular type of source).

Wapenaar & Fokkema (2006) derive the acoustic reciprocity theorems of the convolution and correlation type by substituting equations (A.2) and (A.3) into equation (A.1). This is done by following the steps below (for simplicity, the dependence notation $(\mathbf{x},\omega)$ is dropped in the rest of this section):

1. Apply differentiation to equation (A.1), obtaining

$$\partial_j \left\{ p_A v_{j,B} - v_{j,A} p_B \right\} = (\partial_j p_A) v_{j,B} + (\partial_j v_{j,B}) p_A - (\partial_j v_{j,A}) p_B - (\partial_j p_B) v_{j,A} \tag{A.4}$$

2. Substitute $\partial_j p$ and $\partial_j v_j$ from equations (A.2) and (A.3) into the right-hand side of equation (A.4) and integrate over volume V:

$$\int_V \partial_j \left\{ p_A v_{j,B} - v_{j,A} p_B \right\} \mathrm{d}V = \int_V \left\{ p_A \hat{\hat{q}}_B - v_{j,A} f_{j,B} - \hat{\hat{q}}_A p_B + f_{j,A} v_{j,B} \right\} \mathrm{d}V \tag{A.5}$$

3. The *reciprocity theorem of the convolution type* is finally obtained by applying Gauss's theorem to the left-hand side of equation (A.5):

$$\int_S \left\{ p_A v_{j,B} - v_{j,A} p_B \right\} n_j \, \mathrm{d}S = \int_V \left\{ p_A \hat{\hat{q}}_B - v_{j,A} f_{j,B} - \hat{\hat{q}}_A p_B + f_{j,A} v_{j,B} \right\} \mathrm{d}V \, . \tag{A.6}$$

   The theorem in equation (A.6) is said to be of the convolution type because the products under the integral in the frequency domain (e.g., $p_A v_{j,B}$) correspond to convolutions in the time domain.

4. Since the medium is assumed to be lossless, the principle of time-reversal invariance (i.e., the wave equation is invariant under time reversal since it only contains even-order time derivatives) can be applied: just as p and v_j are solutions of the equation of motion (A.2) and the stress-strain relation (A.3) with source terms f_j and $\hat{\hat{q}}$, p^* and $-v_j^*$ are solutions to the same equations with source terms f_j^* and $-\hat{\hat{q}}^*$ (where the asterisk * denotes complex conjugation, corresponding to time-reversal in the time domain). By making these substitutions for state A to equation (A.6) we obtain

the *reciprocity theorem of the correlation type*:

$$\int_S \left\{ p_A^* v_{j,B} + v_{j,A}^* p_B \right\} n_j \, \mathrm{d}S = \int_V \left\{ p_A^* \hat{\hat{q}}_B + v_{j,A}^* f_{j,B} + \hat{\hat{q}}_A^* p_B + f_{j,A}^* v_{j,B} \right\} \mathrm{d}V \, . \tag{A.7}$$

The theorem in equation (A.7) is said to be of the correlation type because the products under the integral in the frequency domain (e.g., $p_A^* v_{j,B}$) correspond to correlations in the time domain.

Note that in both theorems the medium parameters in states A and B are assumed to be identical. For more general reciprocity theorems that account for different medium parameters in the two states, the reader can refer to de Hoop (1988) and Fokkema & van den Berg (1993).

A.1.2 Derivation from the wave equation

The derivation of the acoustic reciprocity theorems by van Manen et al. (2005) starts by considering the acoustic wave equation in the space-frequency domain:

$$\partial_j \left(\frac{1}{\rho} \partial_j p(\mathbf{x}, \omega) \right) + \left(\frac{\omega^2}{\rho c^2} p(\mathbf{x}, \omega) \right) = \breve{q}(\mathbf{x}, \omega) \, , \tag{A.8}$$

where $p(\mathbf{x}, \omega)$ is the pressure at location $\mathbf{x}$ and frequency ω, and $\breve{q}(\mathbf{x}, \omega)$ is an impulsive source of negative volume injection. The source terms used by Wapenaar & Fokkema (2006) and van Manen et al. (2005) are related by

$$\breve{q}(\mathbf{x}, \omega) = -\frac{\hat{\hat{q}}(\mathbf{x}, \omega)}{\imath \omega} \, , \tag{A.9}$$

where the division by $\imath\omega$ corresponds to integration in the time domain. Note that van Manen et al. (2005) denote the source term with the letter f, while here the source is denoted by q for consistency with the notation of Wapenaar & Fokkema (2006).

Now consider two independent acoustic states, A and B, which can occur in the same medium. For these two states, the wave equations are the following:

$$\partial_j \left(\frac{1}{\rho} \partial_j p_A(\mathbf{x}, \omega) \right) + \left(\frac{\omega^2}{\rho c^2} p_A(\mathbf{x}, \omega) \right) = \breve{q}_A(\mathbf{x}, \omega) \tag{A.10}$$

$$\partial_j \left(\frac{1}{\rho} \partial_j p_B(\mathbf{x}, \omega) \right) + \left(\frac{\omega^2}{\rho c^2} p_B(\mathbf{x}, \omega) \right) = \breve{q}_B(\mathbf{x}, \omega) \, . \tag{A.11}$$

Note that in van Manen et al. (2005) the coefficient of $p(\mathbf{x}, \omega)$ is given by the ratio ω/κ where κ is the incompressibility (bulk modulus), while κ denotes compressibility (the inverse of bulk modulus) in Wapenaar & Fokkema (2006).

From these two equations, van Manen et al. (2005) derive the acoustic reciprocity theorems of the convolution and correlation type by following the steps below (for simplicity, the dependence notation $(\mathbf{x}, \omega)$ is dropped in the rest of this section):

1. Multiply equation (A.10) by p_B and equation (A.11) by p_A and get:

$$p_B \partial_j \left(\frac{1}{\rho} \partial_j p_A \right) + \left(\frac{\omega^2}{\rho c^2} p_A p_B \right) = \check{q}_A p_B \tag{A.12}$$

$$p_A \partial_j \left(\frac{1}{\rho} \partial_j p_B \right) + \left(\frac{\omega^2}{\rho c^2} p_B p_A \right) = \check{q}_B p_A \tag{A.13}$$

2. Subtract equation (A.13) from equation (A.12) and obtain:

$$p_B \partial_j \left(\frac{1}{\rho} \partial_j p_A \right) - p_A \partial_j \left(\frac{1}{\rho} \partial_j p_B \right) = \check{q}_A p_B - \check{q}_B p_A \tag{A.14}$$

3. Integrate equation (A.14) over volume V:

$$\int_V p_B \partial_j \left(\frac{1}{\rho} \partial_j p_A \right) \mathrm{d}V - \int_V p_A \partial_j \left(\frac{1}{\rho} \partial_j p_B \right) \mathrm{d}V = \int_V \left\{ \check{q}_A p_B - \check{q}_B p_A \right\} \mathrm{d}V \tag{A.15}$$

4. Apply the following identity to both terms on the left-hand side of equation (A.15):

$$\begin{aligned} \int_V v \partial_j \left(\frac{1}{\rho} \partial_j u \right) \mathrm{d}V &= \int_V \partial_j \left\{ v \left(\frac{1}{\rho} \partial_j u \right) \right\} \mathrm{d}V - \int_V \left\{ \frac{1}{\rho} \partial_j u \right\} \partial_j v \, \mathrm{d}V \\ &= \int_S \left\{ v \left(\frac{1}{\rho} \partial_j u \right) \right\} n_j \, \mathrm{d}S - \int_V \left\{ \frac{1}{\rho} \partial_j u \right\} \partial_j v \, \mathrm{d}V \, , \end{aligned} \tag{A.16}$$

where Gauss's theorem is applied to the first term on the right-hand side. In equation (A.16), letters u and v simply denote two different variables that in this specific case correspond to pressure in the two states. By applying the identity in equation (A.16) to equation (A.15) we obtain:

$$\begin{aligned} &\int_S \left\{ p_B \left(\frac{1}{\rho} \partial_j p_A \right) \right\} n_j \, \mathrm{d}S - \int_V \left\{ \frac{1}{\rho} \partial_j p_A \right\} \partial_j p_B \, \mathrm{d}V \\ &- \int_S \left\{ p_A \left(\frac{1}{\rho} \partial_j p_B \right) \right\} n_j \, \mathrm{d}S + \int_V \left\{ \frac{1}{\rho} \partial_j p_B \right\} \partial_j p_A \, \mathrm{d}V \\ &= \int_V \left\{ \check{q}_A p_B - \check{q}_B p_A \right\} \mathrm{d}V \, . \end{aligned} \tag{A.17}$$

5. The second terms in the first and second line of equation (A.17) vanish, giving the *reciprocity theorem of the convolution type*:

$$\int_S \left\{ p_B \left(\frac{1}{\rho} \partial_j p_A \right) - p_A \left(\frac{1}{\rho} \partial_j p_B \right) \right\} n_j \, \mathrm{d}S = \int_V \left\{ \check{q}_A p_B - \check{q}_B p_A \right\} \mathrm{d}V \tag{A.18}$$

6. The *reciprocity theorem of the correlation type* is obtained by applying the principle of time-reversal invariance (since the medium is assumed to be lossless): just as p is the solution of the wave equation (A.8) with source term $\check{q}$, p^* is the solution of the wave equation with source term $-\check{q}^*$ (where the asterisk * denotes complex conjugation, corresponding to time-reversal in the time domain). By applying these substitutions for state A to equation (A.18) we get:

$$\int_S \left\{ p_B \left(\frac{1}{\rho} \partial_j p_A^* \right) - p_A^* \left(\frac{1}{\rho} \partial_j p_B \right) \right\} n_j \, \mathrm{d}S = \int_V \left\{ \check{q}_A^* p_B - \check{q}_B p_A^* \right\} \mathrm{d}V \tag{A.19}$$

Although they look different, the reciprocity theorems obtained by van Manen et al. (2005) and Wapenaar & Fokkema (2006) are exactly the same. To go from equations (A.18) and (A.19) to equations (A.6) and (A.7), the following substitutions need to be made:

- The derivative of pressure in the x_j-direction can be expressed in terms of particle velocity v_j in the x_j-direction using the equation of conservation of momentum:

$$\partial_j p = -\rho \frac{\partial v_j}{\partial t} \tag{A.20}$$

  in the time domain, and

$$\partial_j p = -\rho \iota \omega v_j \tag{A.21}$$

  in the frequency domain.

- Equation (A.9) can be used to change the source distribution term $\check{q}$ used by van Manen et al. (2005) to the source distribution term $\hat{\check{q}}$ used by Wapenaar & Fokkema (2006).

A.2 Acoustic Green's function representations

A.2.1 Derivation by Wapenaar & Fokkema (2006)

Wapenaar & Fokkema (2006) derive acoustic Green's function representations for seismic interferometry by substituting Green's functions as wavefields in the acoustic reciprocity

theorem of the correlation type – equation (A.7). They choose positive impulsive point sources of volume injection rate in both states, which in the frequency domain are given by:

$$\hat{\hat{q}}_A(\mathbf{x},\omega) = \delta(\mathbf{x}-\mathbf{x}_A) \tag{A.22}$$

$$\hat{\hat{q}}_B(\mathbf{x},\omega) = \delta(\mathbf{x}-\mathbf{x}_B) \tag{A.23}$$

with $\mathbf{x}_A$ and $\mathbf{x}_B$ both in volume V bounded by surface S; the external forces f are chosen equal to zero in both states.

The wavefields in the two states can be expressed in terms of acoustic Green's functions:

$$p_A(\mathbf{x},\omega) = \hat{\hat{G}}(\mathbf{x},\mathbf{x}_A,\omega) \tag{A.24}$$

$$v_{j,A}(\mathbf{x},\omega) = -\frac{1}{\iota\omega\rho(\mathbf{x})}\partial_j\hat{\hat{G}}(\mathbf{x},\mathbf{x}_A,\omega) \tag{A.25}$$

$$p_B(\mathbf{x},\omega) = \hat{\hat{G}}(\mathbf{x},\mathbf{x}_B,\omega) \tag{A.26}$$

$$v_{j,B}(\mathbf{x},\omega) = -\frac{1}{\iota\omega\rho(\mathbf{x})}\partial_j\hat{\hat{G}}(\mathbf{x},\mathbf{x}_B,\omega) \tag{A.27}$$

where the Green's function $\hat{\hat{G}}(\mathbf{x},\mathbf{x}_A,\omega)$ is the acoustic pressure measured at $\mathbf{x}$ due to a volume injection rate source located at $\mathbf{x}_A$ (as indicated by equation (A.22)). The same remarks apply to sources and Green's functions in state B.

By substituting equations (A.22), (A.24), (A.25) and (A.23), (A.26), (A.27) into the stress-strain relation in equation (A.3), and multiplying both sides by $-\iota\omega$, the wave equations for state A and B are obtained:

$$\partial_j\left(\frac{1}{\rho(\mathbf{x})}\partial_j\hat{\hat{G}}(\mathbf{x},\mathbf{x}_A,\omega)\right) + \left(\frac{\omega^2}{\rho c^2}\hat{\hat{G}}(\mathbf{x},\mathbf{x}_A,\omega)\right) = -\iota\omega\delta(\mathbf{x}-\mathbf{x}_A) \tag{A.28}$$

$$\partial_j\left(\frac{1}{\rho(\mathbf{x})}\partial_j\hat{\hat{G}}(\mathbf{x},\mathbf{x}_B,\omega)\right) + \left(\frac{\omega^2}{\rho c^2}\hat{\hat{G}}(\mathbf{x},\mathbf{x}_B,\omega)\right) = -\iota\omega\delta(\mathbf{x}-\mathbf{x}_B) \tag{A.29}$$

By comparing equations (A.28) and (A.29) with the wave equation in the frequency domain given in Appendix B (equation (B.1)), we can see that the source term on the right-hand side of equations (A.28) and (A.29) contains an extra factor $\iota\omega$ (corresponding to differentiation in the time domain), explaining the definition of the source distribution term $\hat{\hat{q}}$ as a volume injection *rate* source. It follows that the Green's functions considered

by Wapenaar & Fokkema (2006) are related to those used in the Foldy modelling code given in Appendix B (equations (B.2)–(B.5)) by

$$\hat{\tilde{G}} = \imath\omega G \,. \tag{A.30}$$

By substituting equations (A.22)–(A.27) into the acoustic reciprocity theorem of the correlation type (equation (A.7)) and applying source-receiver reciprocity (i.e., interchanging the coordinates $\mathbf{x} \longleftrightarrow \mathbf{x}_A$, $\mathbf{x} \longleftrightarrow \mathbf{x}_B$ and $\mathbf{x}_B \longleftrightarrow \mathbf{x}_A$), Wapenaar & Fokkema (2006) derive an expression for the acoustic Green's function $\hat{\tilde{G}}(\mathbf{x}_B, \mathbf{x}_A, \omega)$ between a source at $\mathbf{x}_A$ and a receiver at $\mathbf{x}_B$:

$$\begin{aligned}\hat{\tilde{G}}(\mathbf{x}_B, \mathbf{x}_A, \omega) + \hat{\tilde{G}}^*(\mathbf{x}_B, \mathbf{x}_A, \omega) \\ = -\frac{1}{\imath\omega} \int_S \frac{1}{\rho(\mathbf{x})} \Big[\Big(\partial_j \hat{\tilde{G}}(\mathbf{x}_B, \mathbf{x}, \omega) \Big) \hat{\tilde{G}}^*(\mathbf{x}_A, \mathbf{x}, \omega) \\ - \hat{\tilde{G}}(\mathbf{x}_B, \mathbf{x}, \omega) \Big(\partial_j \hat{\tilde{G}}^*(\mathbf{x}_A, \mathbf{x}, \omega) \Big) \Big] \, n_j \, \mathrm{d}S\end{aligned} \tag{A.31}$$

in the frequency domain, and

$$\begin{aligned}\hat{\tilde{G}}(\mathbf{x}_B, \mathbf{x}_A, t) + \hat{\tilde{G}}(\mathbf{x}_B, \mathbf{x}_A, -t) \\ = -\int \Bigg\{ \int_S \frac{1}{\rho(\mathbf{x})} \Big[\Big(\partial_j \hat{\tilde{G}}(\mathbf{x}_B, \mathbf{x}, t) \Big) \otimes \hat{\tilde{G}}(\mathbf{x}_A, \mathbf{x}, -t) \\ - \hat{\tilde{G}}(\mathbf{x}_B, \mathbf{x}, t) \otimes \Big(\partial_j \hat{\tilde{G}}(\mathbf{x}_A, \mathbf{x}, -t) \Big) \Big] \, n_j \, \mathrm{d}S \Bigg\} \, \mathrm{d}t\end{aligned} \tag{A.32}$$

in the time domain, where $\otimes$ denotes convolution and integration over time arises as a consequence of there being a $1/\imath\omega$ factor in front of the surface integral in the frequency domain.

Assuming surface S is a sphere with very large radius and that the medium outside S is homogeneous, Wapenaar & Fokkema (2006) also show that the integrand on the right-hand side can be simplified by approximating the dipole responses as

$$\partial_j \hat{\tilde{G}}(\mathbf{x}_A, \mathbf{x}, \omega) \, n_j \approx -\imath \frac{\omega}{c} \hat{\tilde{G}}(\mathbf{x}_A, \mathbf{x}, \omega) \,. \tag{A.33}$$

Using this approximation, the following simplified Green's functions are obtained:

$$\hat{\tilde{G}}(\mathbf{x}_B, \mathbf{x}_A, \omega) + \hat{\tilde{G}}^*(\mathbf{x}_B, \mathbf{x}_A, \omega) \approx \frac{2}{\rho c} \int_S \hat{\tilde{G}}(\mathbf{x}_B, \mathbf{x}, \omega) \hat{\tilde{G}}^*(\mathbf{x}_A, \mathbf{x}, \omega) \, \mathrm{d}S \tag{A.34}$$

in the frequency domain, and

$$\hat{\check{G}}(\mathbf{x}_B, \mathbf{x}_A, t) + \hat{\check{G}}(\mathbf{x}_B, \mathbf{x}_A, -t) \approx \frac{2}{\rho c} \int_S \hat{\check{G}}(\mathbf{x}_B, \mathbf{x}, t) \otimes \hat{\check{G}}(\mathbf{x}_A, \mathbf{x}, -t)\, \mathrm{d}S \tag{A.35}$$

in the time domain.

A.2.2 Alternative derivation by Wapenaar & Fokkema (2006)

The Green's function $\hat{\check{G}}(\mathbf{x}_B, \mathbf{x}_A, \omega)$ in the previous section represents the acoustic pressure due to a *positive* point source of volume injection rate, and obeys equation (A.28) which has a source term given by $-\imath\omega\delta(\mathbf{x} - \mathbf{x}_A)$. A new Green's function $\hat{G}(\mathbf{x}_B, \mathbf{x}_A, \omega)$ which represents the acoustic pressure due to a *positive* point source of volume injection (rather than volume injection *rate*) can be obtained by defining new source distribution terms in both states A and B:

$$\hat{q}_A(\mathbf{x}, \omega) = \frac{\delta(\mathbf{x} - \mathbf{x}_A)}{\imath\omega} \tag{A.36}$$

$$\hat{q}_B(\mathbf{x}, \omega) = \frac{\delta(\mathbf{x} - \mathbf{x}_B)}{\imath\omega} \tag{A.37}$$

with $\mathbf{x}_A$ and $\mathbf{x}_B$ both in volume V bounded by surface S; again, the external forces f are chosen equal to zero in both states.

The wavefields in the two states can be expressed in terms of acoustic Green's functions:

$$p_A(\mathbf{x}, \omega) = \hat{G}(\mathbf{x}, \mathbf{x}_A, \omega) \tag{A.38}$$

$$v_{j,A}(\mathbf{x}, \omega) = -\frac{1}{\imath\omega\rho(\mathbf{x})} \partial_j \hat{G}(\mathbf{x}, \mathbf{x}_A, \omega) \tag{A.39}$$

$$p_B(\mathbf{x}, \omega) = \hat{G}(\mathbf{x}, \mathbf{x}_B, \omega) \tag{A.40}$$

$$v_{j,B}(\mathbf{x}, \omega) = -\frac{1}{\imath\omega\rho(\mathbf{x})} \partial_j \hat{G}(\mathbf{x}, \mathbf{x}_B, \omega) \tag{A.41}$$

where the Green's function $\hat{G}(\mathbf{x}, \mathbf{x}_A, \omega)$ is the acoustic pressure measured at $\mathbf{x}$ due to a *positive* volume injection source located at $\mathbf{x}_A$ (as indicated by equation (A.36)). The same remarks apply to sources and Green's functions in state B.

By substituting equations (A.36), (A.38), (A.39) and (A.37), (A.40), (A.41) into the stress-strain relation in equation (A.3), and multiplying both sides by $-\imath\omega$, the wave

equations for state A and B are obtained:

$$\partial_j \left(\frac{1}{\rho(\mathbf{x})} \partial_j \hat{G}(\mathbf{x}, \mathbf{x}_A, \omega) \right) + \left(\frac{\omega^2}{\rho c^2} \hat{G}(\mathbf{x}, \mathbf{x}_A, \omega) \right) = -\delta(\mathbf{x} - \mathbf{x}_A) \tag{A.42}$$

$$\partial_j \left(\frac{1}{\rho(\mathbf{x})} \partial_j \hat{G}(\mathbf{x}, \mathbf{x}_B, \omega) \right) + \left(\frac{\omega^2}{\rho c^2} \hat{G}(\mathbf{x}, \mathbf{x}_B, \omega) \right) = -\delta(\mathbf{x} - \mathbf{x}_B) \,. \tag{A.43}$$

Equations (A.42) and (A.43) correspond to the wave equation given in Appendix B (equation (B.1)), and do not contain the extra factor $\imath\omega$ which is present in equations (A.28) and (A.29), explaining how the source distribution term $\hat{q}$ represents a volume injection source (rather than volume injection rate). It follows that the modified Green's functions considered by Wapenaar & Fokkema (2006) are related to those used in the Foldy modelling code given in Appendix B (equations (B.2)–(B.5)) by

$$\hat{G} = G \,, \tag{A.44}$$

and to those in equations (A.24)–(A.35) by

$$\hat{G} = \frac{\hat{\hat{G}}}{\imath\omega} \,. \tag{A.45}$$

By substituting equations (A.36)–(A.41) into the acoustic reciprocity theorem of the correlation type (equation (A.7)) and applying source-receiver reciprocity (i.e. interchanging the coordinates $\mathbf{x} \longleftrightarrow \mathbf{x}_A$, $\mathbf{x} \longleftrightarrow \mathbf{x}_B$ and $\mathbf{x}_B \longleftrightarrow \mathbf{x}_A$), Wapenaar & Fokkema (2006) derive an expression for the acoustic Green's function $\hat{G}(\mathbf{x}_B, \mathbf{x}_A, \omega)$ between a source at $\mathbf{x}_A$ and a receiver at $\mathbf{x}_B$:

$$\begin{aligned} &\hat{G}(\mathbf{x}_B, \mathbf{x}_A, \omega) - \hat{G}^*(\mathbf{x}_B, \mathbf{x}_A, \omega) \\ &\qquad = \int_S \frac{1}{\rho(\mathbf{x})} \Big[\left(\partial_j \hat{G}(\mathbf{x}_B, \mathbf{x}, \omega) \right) \hat{G}^*(\mathbf{x}_A, \mathbf{x}, \omega) \\ &\qquad\quad - \hat{G}(\mathbf{x}_B, \mathbf{x}, \omega) \left(\partial_j \hat{G}^*(\mathbf{x}_A, \mathbf{x}, \omega) \right) \Big] \, n_j \, \mathrm{d}S \end{aligned} \tag{A.46}$$

in the frequency domain, and

$$\begin{aligned} &\hat{G}(\mathbf{x}_B, \mathbf{x}_A, t) - \hat{G}(\mathbf{x}_B, \mathbf{x}_A, -t) \\ &\qquad = \int_S \frac{1}{\rho(\mathbf{x})} \Big[\left(\partial_j \hat{G}(\mathbf{x}_B, \mathbf{x}, t) \right) \otimes \hat{G}(\mathbf{x}_A, \mathbf{x}, -t) \\ &\qquad\quad - \hat{G}(\mathbf{x}_B, \mathbf{x}, t) \otimes \left(\partial_j \hat{G}(\mathbf{x}_A, \mathbf{x}, -t) \right) \Big] \, n_j \, \mathrm{d}S \end{aligned} \tag{A.47}$$

in the time domain, where $\otimes$ denotes convolution.

By applying an approximation similar to that in equation (A.33), Wapenaar & Fokkema (2006) also show that the integrand on the right-hand side can be reduced to monopole sources only, giving the following simplified Green's function:

$$\hat{G}(\mathbf{x}_B, \mathbf{x}_A, \omega) - \hat{G}^*(\mathbf{x}_B, \mathbf{x}_A, \omega) \approx -\frac{2\iota\omega}{\rho c} \int_S \hat{G}(\mathbf{x}_B, \mathbf{x}, \omega)\hat{G}^*(\mathbf{x}_A, \mathbf{x}, \omega)\,\mathrm{d}S \tag{A.48}$$

in the frequency domain, and

$$\hat{G}(\mathbf{x}_B, \mathbf{x}_A, t) - \hat{G}(\mathbf{x}_B, \mathbf{x}_A, -t) \approx -\frac{2}{\rho c}\frac{\mathrm{d}}{\mathrm{d}t}\left\{\int_S \hat{G}(\mathbf{x}_B, \mathbf{x}, t) \otimes \hat{G}(\mathbf{x}_A, \mathbf{x}, -t)\,\mathrm{d}S\right\} \tag{A.49}$$

in the time domain, where time differentiation arises as a consequence of there being a $\iota\omega$ factor in front of the surface integral in the frequency domain.

A.2.3 Derivation by van Manen et al. (2005)

Similarly to the modified Green's function $\hat{G}(\mathbf{x}_B, \mathbf{x}_A, \omega)$ derived by Wapenaar & Fokkema (2006), van Manen et al. (2005) derive a Green's function $\check{G}(\mathbf{x}_B, \mathbf{x}_A, \omega)$ which represents the acoustic pressure due to a *negative* point source of volume injection. This Green's function obeys equation (A.8), which has a source term given by $\delta(\mathbf{x} - \mathbf{x}_A)$, and can be obtained by defining new source distribution terms in both states A and B:

$$\check{q}_A(\mathbf{x}, \omega) = -\frac{\delta(\mathbf{x} - \mathbf{x}_A)}{\iota\omega} \tag{A.50}$$

$$\check{q}_B(\mathbf{x}, \omega) = -\frac{\delta(\mathbf{x} - \mathbf{x}_B)}{\iota\omega} \tag{A.51}$$

with $\mathbf{x}_A$ and $\mathbf{x}_B$ both in volume V bounded by surface S; again, the external forces f are chosen equal to zero in both states.

The wavefields in the two states can be expressed in terms of acoustic Green's functions:

$$p_A(\mathbf{x}, \omega) = \check{G}(\mathbf{x}, \mathbf{x}_A, \omega) \tag{A.52}$$

$$v_{j,A}(\mathbf{x}, \omega) = -\frac{1}{\iota\omega\rho(\mathbf{x})}\partial_j\check{G}(\mathbf{x}, \mathbf{x}_A, \omega) \tag{A.53}$$

$$p_B(\mathbf{x}, \omega) = \check{G}(\mathbf{x}, \mathbf{x}_B, \omega) \tag{A.54}$$

$$v_{j,B}(\mathbf{x},\omega) = -\frac{1}{\iota\omega\rho(\mathbf{x})}\partial_j \check{G}(\mathbf{x},\mathbf{x}_B,\omega) \tag{A.55}$$

where the Green's function $\check{G}(\mathbf{x},\mathbf{x}_A,\omega)$ is the acoustic pressure measured at $\mathbf{x}$ due to a *negative* volume injection source located at $\mathbf{x}_A$ (as indicated by equation (A.50)). The same remarks apply to sources and Green's functions in state B.

By substituting equations (A.50), (A.52), (A.53) and (A.51), (A.54), (A.55) into the stress-strain relation in equation (A.3), and multiplying both sides by $-\iota\omega$, the wave equations for state A and B are obtained:

$$\partial_j\left(\frac{1}{\rho(\mathbf{x})}\partial_j \check{G}(\mathbf{x},\mathbf{x}_A,\omega)\right) + \left(\frac{\omega^2}{\rho c^2}\check{G}(\mathbf{x},\mathbf{x}_A,\omega)\right) = \delta(\mathbf{x}-\mathbf{x}_A) \tag{A.56}$$

$$\partial_j\left(\frac{1}{\rho(\mathbf{x})}\partial_j \check{G}(\mathbf{x},\mathbf{x}_B,\omega)\right) + \left(\frac{\omega^2}{\rho c^2}\check{G}(\mathbf{x},\mathbf{x}_B,\omega)\right) = \delta(\mathbf{x}-\mathbf{x}_B)\,. \tag{A.57}$$

Equations (A.56) and (A.57) correspond to the wave equation given in Appendix B (equation (B.1)) with an extra -1 factor on the right-hand side, explaining how the source distribution term $\check{q}$ represents a *negative* volume injection source. It follows that the Green's functions derived by van Manen et al. (2005) are related to those used in the Foldy modelling code given in Appendix B (equations (B.2)–(B.5)) by

$$\check{G} = -G\,, \tag{A.58}$$

to those in equations (A.24)–(A.35) by

$$\check{G} = -\frac{\hat{\hat{G}}}{\iota\omega}\,, \tag{A.59}$$

and to those in equations (A.38)–(A.49) by

$$\check{G} = -\hat{G}\,. \tag{A.60}$$

By substituting equations (A.50)–(A.55) into the acoustic reciprocity theorem of the correlation type (equation (A.7)) and applying source-receiver reciprocity (i.e. interchanging the coordinates $\mathbf{x} \longleftrightarrow \mathbf{x}_A$, $\mathbf{x} \longleftrightarrow \mathbf{x}_B$ and $\mathbf{x}_B \longleftrightarrow \mathbf{x}_A$), an expression for the acoustic Green's function $\check{G}(\mathbf{x}_B,\mathbf{x}_A,\omega)$ between a source at $\mathbf{x}_A$ and a receiver at $\mathbf{x}_B$ is obtained:

$$\begin{aligned}\check{G}^*(\mathbf{x}_B,\mathbf{x}_A,\omega) - \check{G}(\mathbf{x}_B,\mathbf{x}_A,\omega)& \\ = \int_S \frac{1}{\rho(\mathbf{x})}\Big[\left(\partial_j\check{G}(\mathbf{x}_B,\mathbf{x},\omega)\right)\check{G}^*(\mathbf{x}_A,\mathbf{x},\omega)& \\ - \check{G}(\mathbf{x}_B,\mathbf{x},\omega)\left(\partial_j\check{G}^*(\mathbf{x}_A,\mathbf{x},\omega)\right)\Big]\, n_j\,\mathrm{d}S&\end{aligned} \tag{A.61}$$

in the frequency domain, and

$$\begin{aligned}\check{G}(\mathbf{x}_B,\mathbf{x}_A,-t)-\check{G}(\mathbf{x}_B,\mathbf{x}_A,t)&\\ =\int_S \frac{1}{\rho(\mathbf{x})}\Big[\Big(\partial_j\check{G}(\mathbf{x}_B,\mathbf{x},t)\Big)\otimes\check{G}(\mathbf{x}_A,\mathbf{x},-t)&\\ -\check{G}(\mathbf{x}_B,\mathbf{x},t)\otimes\Big(\partial_j\check{G}(\mathbf{x}_A,\mathbf{x},-t)\Big)\Big]\,n_j\,\mathrm{d}S&\end{aligned} \tag{A.62}$$

in the time domain, where $\otimes$ denotes convolution.

By applying an approximation similar to that in equation (A.33), the integrand on the right-hand side can be reduced to monopole sources only, giving the following simplified Green's function:

$$\check{G}^*(\mathbf{x}_B,\mathbf{x}_A,\omega)-\check{G}(\mathbf{x}_B,\mathbf{x}_A,\omega)\approx-\frac{2\imath\omega}{\rho c}\int_S\check{G}(\mathbf{x}_B,\mathbf{x},\omega)\check{G}^*(\mathbf{x}_A,\mathbf{x},\omega)\,\mathrm{d}S \tag{A.63}$$

in the frequency domain, and

$$\check{G}(\mathbf{x}_B,\mathbf{x}_A,-t)-\check{G}(\mathbf{x}_B,\mathbf{x}_A,t)\approx-\frac{2}{\rho c}\frac{\mathrm{d}}{\mathrm{d}t}\left\{\int_S\check{G}(\mathbf{x}_B,\mathbf{x},t)\otimes\check{G}(\mathbf{x}_A,\mathbf{x},-t)\,\mathrm{d}S\right\} \tag{A.64}$$

in the time domain, where time differentiation arises as a consequence of there being a $\imath\omega$ factor in front of the surface integral in the frequency domain.

Compared to equations (A.46)–(A.49), equations (A.61)–(A.64) have the same integrand on the right-hand side, but opposite sign on the left-hand side. This is due to the opposite sign in the source distribution terms used (cfr. equations (A.36)–(A.37) and (A.50)-(A.51)).

Similarly, the presence of a difference on the left-hand side of equations (A.46)–(A.49) and (A.61)–(A.64), as opposed to a sum as in equations (A.31)–(A.32) and (A.34)–(A.35), is due the presence of the factor $1/\imath\omega$ in the source distribution terms in equations (A.36)–(A.37) and (A.50)–(A.51), which also accounts for the different factors outside the integrals on the right-hand side of equations (A.31)–(A.32) and (A.34)–(A.35).

APPENDIX B

Exact wavefield modelling in scattering acoustic media – Appendix[1]

B.1 Analytic monopole and dipole Green's functions

The monopole Green's function (impulse response) in a medium with constant velocity c satisfies the following equation in the frequency domain (the *Helmholtz equation*):

$$\nabla^2 G(\mathbf{x}, \mathbf{x}_0, \omega) + k^2 G(\mathbf{x}, \mathbf{x}_0, \omega) = -\delta(\mathbf{x} - \mathbf{x}_0)\,, \tag{B.1}$$

where $G(\mathbf{x}, \mathbf{x}_0, \omega)$ is the Green's function at location $\mathbf{x}$ due to a source at location $\mathbf{x}_0$, k is the wavenumber (which satisfies $k = \omega/c$, where ω is angular frequency), and the term $\delta(\mathbf{x} - \mathbf{x}_0)$ represents the source defined as a spatio-temporal impulse (delta function) acting at location $\mathbf{x}_0$ at time $t = 0$. The Helmholtz equation can be solved for the Green's function in N dimensions, and full derivations in one, two or three dimensions can be found in Snieder (2009). For consistency with interferometric theory (van Manen et al., 2005, 2006; Wapenaar & Fokkema, 2006), compared to Snieder (2009) we use a negative delta function as a source term on the right-hand side of the Helmholtz equation; in addition, we assume the exponential term in the Fourier transform from frequency to time domain to be $e^{\iota\omega t}$, which is the sign convention used by Matlab (as opposed to $e^{-\iota\omega t}$, which is more usual in geophysics, for example). For these reasons, the following Green's functions are the negative complex conjugates of those given in Snieder (2009).

[1] This chapter has been published as the appendix of Galetti et al. (2013c).

The solution to the Helmholtz equation is given in one dimension by

$$\begin{aligned} G^{1D}(x,x_0) &= -\frac{\iota}{2k}\mathrm{e}^{-\iota k|x-x_0|} \\ &= -\frac{1}{2k}\mathrm{e}^{-\iota\left(k|x-x_0|-\frac{\pi}{2}\right)}, \end{aligned} \tag{B.2}$$

in two dimensions by

$$G^{2D}(\mathbf{x},\mathbf{x}_0) = -\frac{\iota}{4}H_0^{(2)}(k|\mathbf{x}-\mathbf{x}_0|), \tag{B.3}$$

in two dimensions (far-field case) by

$$\begin{aligned} G^{2D\_far}(\mathbf{x},\mathbf{x}_0) &= -\frac{\iota}{4}\mathrm{e}^{-\iota\left(k|\mathbf{x}-\mathbf{x}_0|-\frac{\pi}{4}\right)}\sqrt{\frac{2}{\pi k|\mathbf{x}-\mathbf{x}_0|}} \\ &= -\frac{1}{4}\mathrm{e}^{-\iota\left(k|\mathbf{x}-\mathbf{x}_0|-\frac{3\pi}{4}\right)}\sqrt{\frac{2}{\pi k|\mathbf{x}-\mathbf{x}_0|}}, \end{aligned} \tag{B.4}$$

and in three dimensions by

$$G^{3D}(\mathbf{x},\mathbf{x}_0) = \frac{1}{4\pi}\frac{\mathrm{e}^{-\iota k|\mathbf{x}-\mathbf{x}_0|}}{|\mathbf{x}-\mathbf{x}_0|}, \tag{B.5}$$

where $H_0^{(2)}$ is the Hankel function of the second kind and order 0, and the imaginary unit $\iota = \sqrt{-1}$ has been taken inside the exponential term in the second line of equations (B.2) and (B.4).

Dipole Green's functions may be obtained from spatial differentiation of equations (B.2)–(B.5) and are given by

$$\partial G^{1D}(x,x_0) = -\iota k G^{1D}(x,x_0) \tag{B.6}$$

in one dimension, by

$$\partial_m G^{2D}(\mathbf{x},\mathbf{x}_0) = \frac{\iota k}{4}\cos(\phi_m)H_1^{(2)}(k|\mathbf{x}-\mathbf{x}_0|), \tag{B.7}$$

in two dimensions, by

$$\partial_m G^{2D\_far}(\mathbf{x},\mathbf{x}_0) = -G^{2D\_far}(\mathbf{x},\mathbf{x}_0)\cos(\phi_m)\left[\iota k + \frac{1}{2|\mathbf{x}-\mathbf{x}_0|}\right], \tag{B.8}$$

in two dimensions (far-field case), and by

$$\partial_m G^{3D}(\mathbf{x},\mathbf{x}_0) = -G^{3D}(\mathbf{x},\mathbf{x}_0)\cos(\phi_m)\left[\iota k + \frac{1}{|\mathbf{x}-\mathbf{x}_0|}\right], \tag{B.9}$$

in three dimensions. $H_1^{(2)}$ is the Hankel function of the second kind and order 1, and the term $\cos(\phi_m)$ is the direction cosine of the receiver position $\mathbf{x}$ with respect to the source

location $\mathbf{x}_0$ along the m-direction, i.e., the cosine of the angle between vector $\mathbf{x} - \mathbf{x}_0$ and the m-direction.

B.2 Scattering amplitude in D-dimensions

For a certain distribution of N isotropic point scatterers, the scattering amplitude $A^{(i)}$ of scatterer (i) located at $\mathbf{x}^{(i)}$ is a complex quantity that relates the total wavefield $\Psi_0(\mathbf{x}^{(i)})$ incident on the scatterer to the scattered wavefield $\Psi_S(\mathbf{x})$ measured at $\mathbf{x}$, according to

$$\Psi_S(\mathbf{x}) = \Psi_0(\mathbf{x}^{(i)})A^{(i)}G(\mathbf{x}, \mathbf{x}^{(i)}) \,, \tag{B.10}$$

where $G(\mathbf{x}, \mathbf{x}^{(i)})$ is the Green's function between $\mathbf{x}^{(i)}$ and $\mathbf{x}$. As shown by Snieder (1999), the scattering amplitude contains the superposition of all possible multiple scattering interactions with the same scatterer and, since scattering is assumed to be isotropic, is independent of the angle of incidence.

The real and imaginary parts of the scattering amplitude are related via the optical theorem (generally, an optical theorem describes the conservation of energy between a wave incident on a scattering object and the resulting wave scattered by that object). In simple acoustic media with uniform background velocity, the relationship between the real and imaginary part of the scattering amplitude can be derived by equating the total energy loss for unit incident wavefield (the so-called *total cross-section* Ω_T) to the total scattered energy (the so-called *scattering cross-section* Ω_S). This approach assumes that no energy is lost to anelastic attenuation, hence the energy loss of the incident wavefield is due to scattering alone.

In two dimensions, the total and scattering cross-sections are given respectively by (Groenenboom & Snieder, 1995)

$$\Omega_T = -\frac{\Im(A)}{k} \tag{B.11}$$

and

$$\Omega_S = \frac{|A|^2}{4k} \,, \tag{B.12}$$

where the latter expression is obtained by using the far-field Green's function (equation (B.4)) to get Ψ_S in equation (B.10) and integrating the power of the scattered field $|\Psi_S|^2 = \Psi_S \Psi_S^*$ over 2π. Using a similar approach, expressions similar to those in the above equations can be derived in one and three dimensions, and by equating the total and scattering cross-sections the relationships between the real and imaginary parts of the

scattering amplitude can be obtained in one, two and three dimensions (Snieder, 1999):

$$\Re(A) = \pm \begin{cases} (-\Im(A)\,[2k + \Im(A)])^{1/2} & \text{in 1D} \\ (-\Im(A)\,[4 + \Im(A)])^{1/2} & \text{in 2D} \\ \left(-\Im(A)\left[\dfrac{4\pi}{k} + \Im(A)\right]\right)^{1/2} & \text{in 3D} \end{cases} \tag{B.13}$$

These expressions impose the following constraints on the value of the imaginary part of the scattering amplitude:

$$\begin{aligned} -2k \leq \Im(A) \leq 0 \quad & \text{in 1D} \\ -4 \leq \Im(A) \leq 0 \quad & \text{in 2D} \\ -\frac{4\pi}{k} \leq \Im(A) \leq 0 \quad & \text{in 3D} \end{aligned} \tag{B.14}$$

The relationships between the real and imaginary components of A are of particular importance as they ensure that the scattering strength of each scatterer satisfies the requirement of energy conservation. Optical theorems for more complex scattering media also exist (Halliday & Curtis, 2009b; Douma et al., 2011; Wapenaar & Douma, 2012) and can be applied to obtain a correct estimate of the scattering amplitude. However, the details of these theorems will not be discussed here as their application is beyond the scope of our simple modelling code.